LBL-1690
c.1

SYSTEMATICS OF THE $(\alpha, 2\alpha)$ REACTION AT E_α = 90 MeV

Joseph Donald Sherman
(Ph. D. Thesis)

May 1973

Prepared for the U. S. Atomic Energy Commission
under Contract W-7405-ENG-48

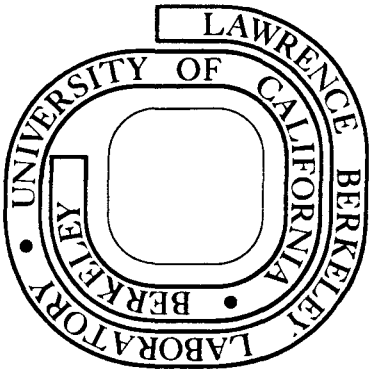

LBL-1690
c.1

DISCLAIMER

Contents

SYSTEMATICS OF THE $(\alpha, 2\alpha)$ REACTION AT E_α = 90 MeV

Joseph Donald Sherman

Lawrence Berkeley Laboratory
University of California
Berkeley, California 94720

Abstract

A coincidence technique has been used to study the $(\alpha, 2\alpha)$ reaction on a series of nuclei at E_α = 90 MeV. Typically, resolutions of 250-300 keV FWHM have been achieved for the kinematic bands lying in the $T_3 + T_4$ vs. T_3 kinetic energy plane. Nine targets from ^{12}C to ^{66}Zn have been studied. The most complete experimental data were taken on the ^{12}C and ^{16}O targets in order to define the angular correlation shape so that a three body reaction theory could be more completely tested. The $^{12}C(\alpha, 2\alpha)^8Be$ and $^{16}O(\alpha, 2\alpha)^{12}C$ reactions included symmetric angle measurements from 19° to 47° in approximate 4° steps; also, an asymmetric angular correlation with one counter fixed at 42° and the other counter ranging from 25° to 47° in 3° steps was taken. Since data were obtained in the energy plane, energy and momentum correlations were also extracted.

The seven remaining targets studied by the $(\alpha, 2\alpha)$ reaction were ^{24}Mg, ^{26}Mg, ^{28}Si, ^{30}Si, ^{40}Ca, ^{44}Ca, and ^{66}Zn. Symmetric angular correlations were taken in the 28° to 47° range for these nuclei, typically taking four angular settings for each target. In all cases data were taken at the symmetric quasi-elastic angle. A prominent systematic feature to emerge from this study was the predominance of the ground state transitions. The $^{40}Ca(\alpha, 2\alpha)^{36}Ar$ reaction was the only nucleus to yield excited state cross sections that were comparable to

the ground state transition. Another systematic item was that after a rapid fall of cross section from the p-shell nuclei to the sd-shell nuclei, the $(\alpha, 2\alpha)$ cross sections were found to be nearly constant from the Si isotopes to ^{66}Zn. The angular correlations for transitions to the ground states of these nuclei are very similar.

A distorted wave impulse approximation (DWIA) calculation was developed; the distortions were described by McCarthy-Pursey wave functions with the focus term set equal to zero. The DWIA was found to fit the angular correlations in shape and magnitude. Systematic features of the energy correlations were also described quite well, although the momentum correlations were fit in shape and magnitude only for $q \leq 0.5$ (fm)$^{-1}$. The model was used to extract relative spectroscopic factors from ^{12}C to ^{66}Zn, and these results were in good agreement with spectroscopic factors obtained from a DWBA analysis of a systematic (^{3}He, ^{7}Be) study.

The ^{16}O$(\alpha, 2\alpha)^{12}$C reaction was found to populate the ^{12}C ground state most strongly, whereas the (d, ^{6}Li) and (^{3}He, ^{7}Be) reactions have preferentially populated the ^{12}C(4.44) level. Also, theoretical calculations have shown that the $\{^{12}\text{C}(4.44)+\alpha\}$ configuration is the principal parent of the ^{16}O nucleus in an alpha cluster model. Analysis within the plane wave impulse approximation (PWIA) of the ^{16}O$(\alpha, 2\alpha)^{12}$C reaction still indicated that the ^{12}C(0.0) was receiving most of the $(\alpha, 2\alpha)$ transition strength. This result indicates that the $(\alpha, 2\alpha)$ and alpha pickup reactions are probing four particle correlations in different manners, and a careful theoretical analysis of the $(\alpha, 2\alpha)$ reaction mechanism would be very valuable to nuclear structure studies if these differences were elucidated.

I. Introduction

A. Alpha Clustering

Alpha clustering in nuclei has been a recurring theme in nuclear physics. Early experimental evidence which favors alpha clustering includes alpha decay [Gam 28] and binding energy systematics. Neutron binding energy systematics have been summarized by Soloviev [Sol 60], and Fig. I-1 indicates that a maximum in the experimental neutron binding energy occurs at the 4N nuclei. The binding energy systematics are understood within the supermultiplet scheme. In this description [Eis 58] it is seen that the alpha particle wave function is completely spatially symmetric, and thus takes full advantage of the attractive spin and isospin independent nuclear forces.

Alpha decay and binding energy systematics helped stimulate early development of α-cluster models [Whe 37, Mar 41], and there has been steady development since (cf. [Ari 72] for references). The increasing complication of shell model calculations with residual interactions led to the suggestion that refined clustering models provide an alternative description of nuclear states [Bri 66], and much theoretical effort has recently been expended in developing cluster models [Ari 72].

The quartet model [Ari 71] and quadruple model [Eic 72] provide microscopic descriptions which emphasize alpha-like clustering in nuclei. Pairing as well as "quartetting" or "quadrupling" is included in the model development; Fig. I-1 indicates that discontinuities in neutron binding energies also exist for paired nuclei. Whether these models will provide insight into nuclear properties is controversial [Rob 72], and the relation of these models with other alpha-clustering theories remains largely uninvestigated[Ari 72].

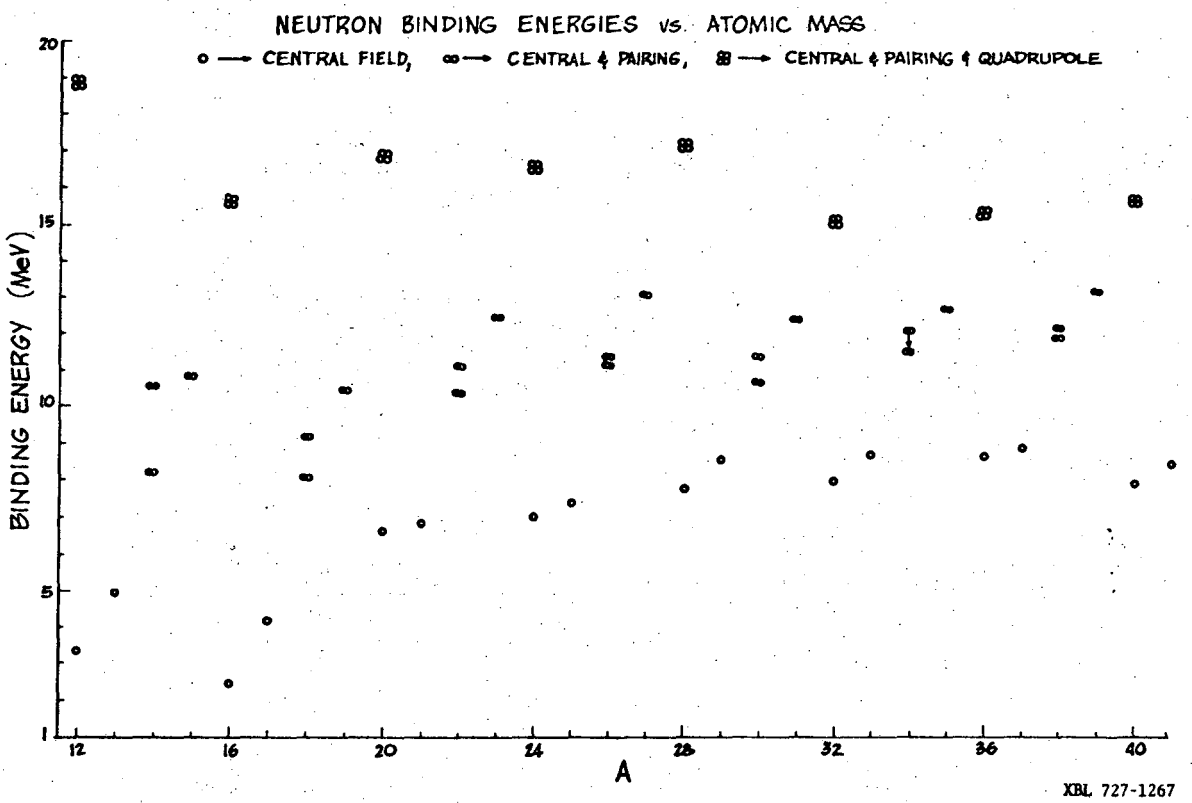

Fig. I-1. Experimental neutron binding energy systematics as a function of nuclear mass.

B. Recent Experiments

Considerable experimental effort has been applied to the study of clustering phenomena, and much more diversified information has become available. Alpha capture reactions have been investigated [Ball 59]. These authors studied the ^{58}Ni, ^{136}Xe (α,γ) reactions, and found the maximum cross section at about 20 MeV excitation in the residual nuclei. This result has been interpreted as evidence for the possibility of alpha clustering at high excitation in these nuclei [Phi 60].

Another experiment which has been interpreted as evidence of α-clustering in nuclei is the enhanced elastic alpha scattering from the ^{40}Ca target relative to the ^{44}Ca target in the backward hemisphere [Sto 72]. The enhanced scattering was attributed to existence of alpha clusters in the nuclear surface of ^{40}Ca. It was postulated [Sch 70] that the incident alpha undergoes repulsive scattering from the discrete alpha clusters, and sufficient momentum is transferred to the core-cluster system so that the incident alpha is scattered at large angles. The bond in the core-cluster system is not broken, and the whole nuclear mass is available to absorb the momentum transfer. This picture is analogous to the Mössbauer effect.

Alternative explanations were soon developed in terms of an ℓ-dependent optical model [Eber 70]. Since the (α,n) Q-value is more negative for ^{40}Ca than ^{44}Ca, the partial waves contributing to absorption in ^{40}Ca via the (α,n) reaction are cut off at approximately $l_n = 12$, whereas the cut off for ^{44}Ca is $l_n = 15$. Thus partial waves with $l_n \geq 12$ for ^{40}Ca could contribute only to the elastic channel, which gave an alternative explanation not involving alpha clustering for enhanced scattering at $\theta_L > 90°$.

In the most recent elastic scattering study over a broad angular range [Oes 72] at E_α = 20-30 MeV additional targets were studied. The conclusions were: First, N = Z or N = Z + 1 nuclei showed back angle enhancements. Second, excess neutrons do not destroy this enhancement if the neutrons occupy the same major shell as the outer nucleons of the N = Z and N = Z + 1 isotopes. Third, the enhancement was reduced if the excess neutrons entered the next higher shell. The authors point out that the ℓ-dependent optical model is not consistent with their conclusions for nuclei in the second category. Summarizing, it seems that a more consistent picture of large angle elastic alpha scattering in terms of α-clustering may be emerging, although problems and ambiguities remain.

A more direct procedure for determining cluster structure is to study four nucleon pickup and stripping reactions. These methods are relatively recent, since they involve good resolution work with heavy ions (A > 4) in either the incident or exit channel, or both. The (d, ^{6}Li) [Den 66, Gut 71, McG 71, Bed 72] and (^{3}He, ^{7}Be) [Zaf 71, Det 72, Det 70, Zaf 72] pickup reactions have been the most popular probes in investigating the parentage of target nuclei in terms of {residual core + cluster} configurations [La 55]. Four particle stripping reactions provide information concerning parentage relations between the final nucleus' spectrum and the {target (g. s.) + cluster} system. Some of the earliest (^{16}O, ^{12}C) work [Fai 70] on Fe isotopes picked out discrete states at comparatively high excitation energies in the Ni isotopes; these results were interpreted as experimental evidence supporting quartet states. The (^{16}O, ^{12}C) reaction has also been studied

in the 2s-1d shell [Mah 72, Mun 72]. Other four nucleon stripping reactions include the (^{7}Li, t), (^{6}Li, d), (^{12}C, ^{8}Be), and (^{20}Ne, ^{16}O) reactions. A summary of alpha-particle transfer reactions has been published [Bet 70]. The DWBA analysis [Kubo 72] of four particle transfers is more complicated than the DWBA treatment for projectiles and products with $A \leq 4$, and it seems unlikely that the transferred cluster in four nucleon stripping and pickup reactions maintain the high spatial symmetry of a free alpha particle.

The knock-out reaction has been of continuing interest in clustering studies. The alpha knock-out process is written $(x, x\alpha)$ where x is typically a proton or alpha particle. This reaction requires the measurement of energies and angles of two exit particles to completely specify the kinematics. The required coincidence technique gives strong control of the kinematics, and the detector geometry can be arranged so that the residual nucleus receives small or zero recoil energy. The residual nucleus may then be described as a spectator to the x-α collision: this is the basis for the impulse approximation.

The ^{12}C, ^{16}O $(p, p\alpha)$ reactions at energies greater than 100 MeV have been investigated by several workers. James and Pugh [Jam 63] studied the ^{12}C $(p, p\alpha)$ reaction at E_p = 150 MeV. They concluded that many events left the residual ^{8}Be at 11 MeV excitation. Later work [Gott 70] with better energy resolution and statistics for ^{12}C $(p, p\alpha)$ at E_p = 160 MeV did not agree with the earlier James and Pugh result. The latter authors found ^{8}Be (0.0) most strongly excited, with considerable excitation of ^{8}Be (2.90). Gottschalk and Kannenberg also studied the ^{16}O $(p, p\alpha)$ process [Kann 68]. A recent $(p, p\alpha)$ experiment at

E_p = 156 MeV was studied on six targets from ^{6}Li to ^{232}Th [Bach 73]. They emphasized the quasi-elastic condition, and found a mass dependence for the α knock-out process. An unfortunate feature of the higher energy (p, pα) experiments, to date, is the poor energy resolution: it is difficult to resolve final states even in light nuclei ($\leq$ ^{16}O).

The (p, pα) reaction has also been studied in the 40-60 MeV proton energy range. The ^{9}Be (p, pα)^{5}He reaction [Roos 68] at E_p = 57 MeV was analyzed within the impulse approximation, but reactions on ^{12}C at E_p = 57 MeV [Eps 68] and ^{16}O and ^{20}Ne at E_p = 47 MeV [Eps 71] were found to be dominated by sequential processes.

The (α, 2α) reaction history is similar to that of the (p, pα) work. Several light targets (^{6}Li in particular) have been studied in the E_α = 40 - 70 MeV range, and have been interpreted within the impulse approximation [Pugh 69, Gail 70]. Success in interpreting the ^{6}Li, ^{7}Li, ^{9}Be, and ^{12}C (α, 2α) reactions at E_α = 25 MeV within the impulse approximation has also been reported [Dol 69, Dol 69a].

A study of the (α, 2α) reaction at 0.91 GeV indicated that all nucleons in the density region $\rho < \rho_0/20$ were clustered [Igo 63]. The quantity ρ_0 is the nuclear density within the nucleus. The ^{28}Si(α, 2α) reaction was studied at E_α = 104 MeV [Pli 69]. These authors concluded that the 4.12 (4^+) state in ^{24}Mg was more strongly populated than the ground (0^+) or first excited (2^+) states. As in the high energy (p, pα) work, detailed spectroscopy was difficult because of poor energy resolution.

II. Theory

A. Kinematics and Three Body Correlations

Figure II-1 displays the coplanar geometry used throughout this experiment as well as kinematical definitions. Most measurements maintained a symmetric angle geometry, $\theta_1 = -\theta_2$. The notation used is that the initial system is composed of the incident beam labelled by the four-momenta $\underline{P_1}$ and stationary target labelled $\underline{P_2}$. The final system is composed of detected particles 3 and 4 ($\underline{P_3}$ and $\underline{P_4}$) at angles θ_1 and θ_2. The recoiling nucleus ($\underline{P_5}$) is undetected. The kinematic quantities characterizing the recoil motion are completely determined (except for uncertainties introduced by finite detector sizes) by the energy and angle measurements performed on particles 3 and 4. In four-vector notation the conservation of momentum and energy is

$$\underline{P_1} + \underline{P_2} = \underline{P_3} + \underline{P_4} + \underline{P_5}. \qquad \text{(II-1)}$$

A derivation leading to $\underline{P_5}$ and other kinematic quantities of interest as a function of $\underline{P_3}$ and $\underline{P_4}$ is given in Appendix I.A. A development of relativistic and non-relativistic three-body kinematics is found in [Zup 67]. Relating specifically to the $(\alpha, 2\alpha)$ experiment, particle 1 is the incident α beam, 2 is the target, 3 and 4 are the detected final state alphas, and 5 is the recoiling nucleus. The symbol $\vec{q}$ is used for the bound alpha's initial momentum. It is attempted to maintain this notation throughout, although certain instances benefit from a change in terms.

The experimental geometry is arranged so that the accepted coincidence events correspond to a small recoil energy, and it is possible for T_5 to be zero at some symmetric angle, which is subsequently referred to as the quasi-elastic angle. In the non-relativistic limit the

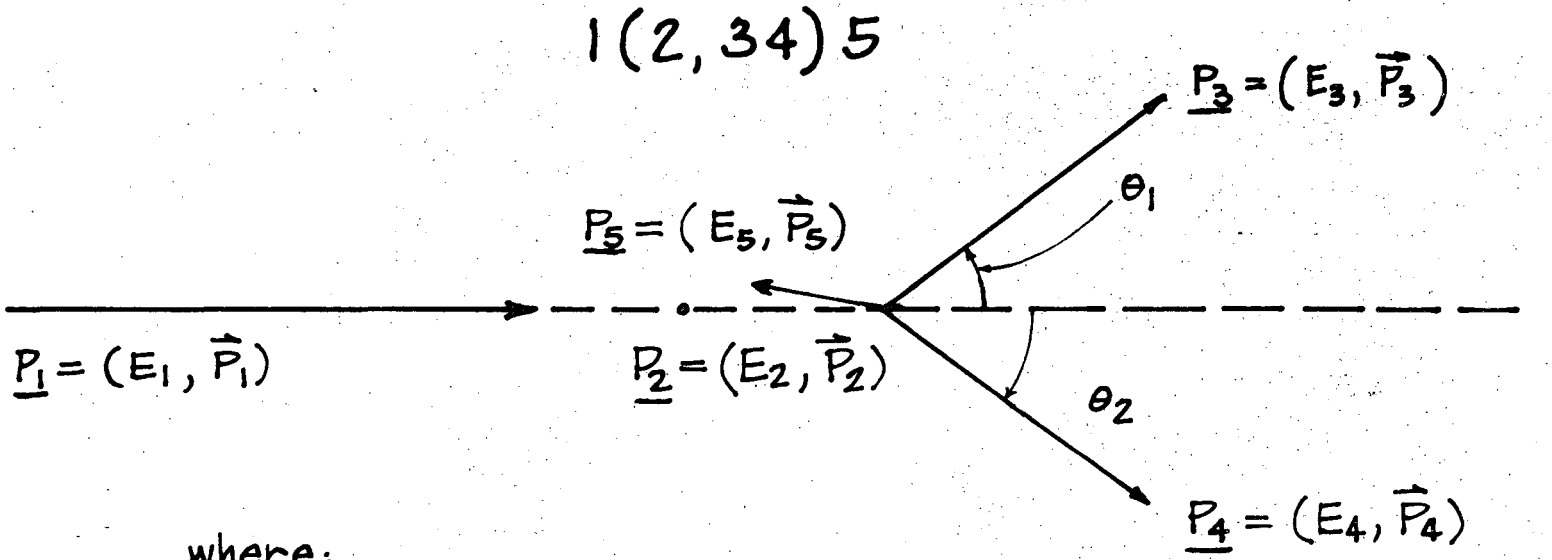

where:

$\underline{P_i}$ = 4 MOMENTA OF i^{th} PARTICLE.

E_i = $T_i + m_i c^2$ = TOTAL ENERGY OF i^{th} PARTICLE.

T_i = KINETIC ENERGY OF i^{th} PARTICLE.

m_i = REST MASS OF i^{th} PARTICLE.

$\theta 1$ = DETECTION ANGLE OF PARTICLE 3.

$\theta 2$ = DETECTION ANGLE OF PARTICLE 4.

XBL 727-1234

Fig. II-1. Definition of notation for the three body kinematics problem.

symmetric quasi-elastic angle is a function of T_3, T_4, and the reaction Q-value, and is given by:

$$\cos(2\theta_{Q.E.}) = - Q/2\, T_3 \qquad \text{(II-2)}$$

where it has been assumed $T_3 = T_4$ and $\theta_1 = -\theta_2 = \theta_{Q.E.}$. This angle is of considerable importance in three-body reaction theory [Holm 69]. A derivation of the relativistic and non-relativistic formulae for II-2 is given in Appendix I.B.

Examples of the three body kinematics are given in Fig. II-2. The kinetic energies of particles 3 and 4 are given by T_3 and T_4. The T_3 versus T_4 plot is a common technique used to display coincidence data, but the plot of $T_3 + T_4$ vs. T_3 is more convenient for data analysis in this experiment. The triple differential cross section ($\sigma^3(\theta)$ or $d^3\sigma/d\Omega_1 d\Omega_2 dT_3$) is extracted from events distributed along these kinematic bands. This cross section can then by plotted versus the appropriate kinematic variable to obtain the desired correlation.

The energy correlation is a plot of $\sigma^3(\theta)$ versus T_3, while the momentum correlation refers to a plot of $\sigma^3(\theta)$ versus the recoiling wave number, $\vec{k}_5$. A symmetric angular correlation can be defined by requiring $\theta_1 = -\theta_2 = \theta$, $T_3 = T_4$, and then plotting the $\sigma^3(\theta)$ extracted under these restraints versus θ. An asymmetric angular correlation utilized in these experiments is obtained by plotting $\sigma^3(\theta)$ vs. θ_2 where θ_2 varies and θ_1 remains stationary. This last correlation is kinematically restricted by taking $\sigma^3(\theta)$ at the value of T_3 that requires the recoiling nucleus to be collinear with the beam axis.

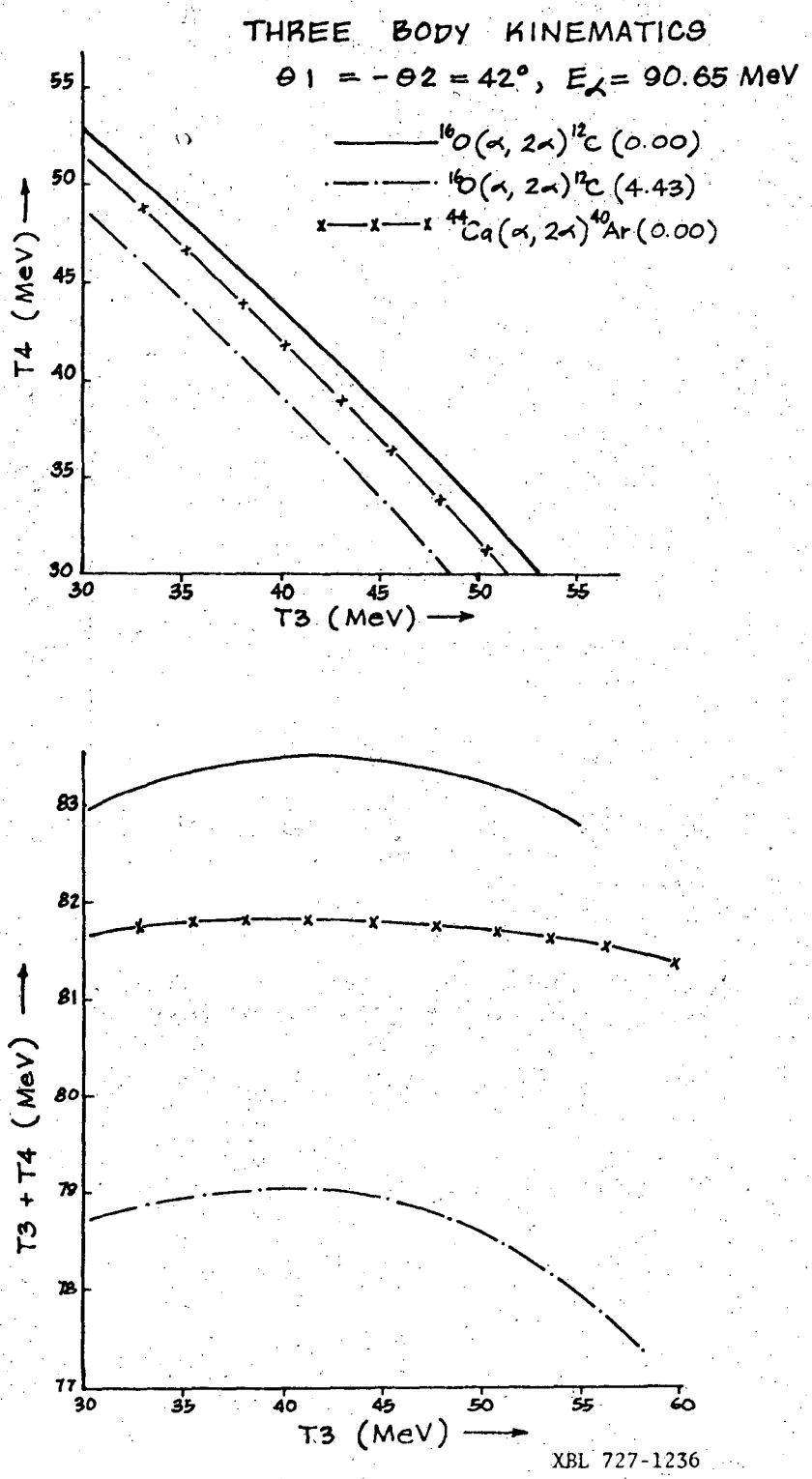

Fig. II-2. Examples of three body kinematics calculations in the T_3 vs. T_4 plane (top) and in the $T_3 + T_4$ vs. T_3 plane (bottom). The notation is that given in Fig. II-1 and Appendix I.

B. Competing Reaction Mechanisms

The behavior of $\sigma^3(\theta)$ along the kinematic band is an indication of the reaction mechanism. A sequential process is an inelastic scattering to a level at high excitation in the target nucleus which then decays by α-emission to the ground or low-lying state of the final nucleus:

$$\begin{array}{l} 1 + 2 \longrightarrow 2^* + 3 \\ \qquad\qquad\quad \hookrightarrow\ 4 + 5. \end{array} \qquad \text{(II-3)}$$

Such a process obeys three body kinematics, and events corresponding to such a mechanism usually appear as sharp structure in a kinematic band. These sharp structures are due to the particle unbound levels in 2^*; very highly excited overlapping levels could contribute but have been considered negligible in the $(\alpha, 2\alpha)$ analysis.

A second mechanism, referred to as quasi-elastic scattering, is viewed as a one-step process:

$$1 + 2 \longrightarrow 3 + 4 + 5. \qquad \text{(II-4)}$$

This cross section is manifested by a large comparatively smooth structure centered about equal energy sharing on the kinematic band [Holm 69]. Analysis problems ensue when both mechanisms coexist as in the $^{16}O(\alpha, 2\alpha)^{12}C(0.00)$ at E_α = 25 MeV [Park 68], where the plots demonstrate several sequential peaks, as well as broad structure lying under the sequential peaks. Alpha-cluster removal in ^{16}O and ^{20}Ne targets with the $(p, p\alpha)$ reaction at E_p = 46.8 MeV were also thought to be dominated by sequential processes [Eps 71]. This work is directed to a study of quasi-elastic processes, so a reasonably high alpha beam energy (90 MeV) from the 88-in. cyclotron was chosen in an effort to separate the sequential and quasi-elastic mechanisms.

C. Selection Rules

1. Total spin and isospin

The following discussion of $(\alpha, 2\alpha)$ selection rules assumes a one step process characteristic of a simple direct nuclear reaction mechanism. In the α knock-out picture the incident alpha particle strikes an alpha cluster initially bound to a nuclear core. The results of the collision are the rupturing of the bound alpha-nucleus bond and the appearance of two fast alpha particles in the exit channel. For the one step assumption to be valid, it is necessary that the struck cluster be an alpha particle. If the beam particle struck a correlated four particle group which was not an alpha particle and this cluster was released from the core with no other interaction, the event could not be observed in this experiment. This is true since such a four particle correlation must correspond to an excited particle-unstable state of the ^{4}He nucleus which would decay by particle emission before reaching the detectors. More complicated reaction mechanisms may be proposed, but it would seem difficult to test these hypotheses.

Conservation of total angular momentum states that

$$\vec{J}_t = \vec{J}_f - \vec{J}_i \qquad \text{(II-5)}$$

where $\vec{J}_t$ is the transferred angular momentum and $\vec{J}_f$ and $\vec{J}_i$ are the total nuclear spins for the final and initial states. For an even-even target nucleus $\vec{J}_i = 0$, and if $\vec{J}_t$ is decomposed into a sum of intrinsic spin $(\vec{S}_t)$ and orbital angular momentum $(\vec{L}_t)$, then

$$\vec{J}_f = \vec{L}_t + \vec{S}_t = \vec{L}_t \qquad \text{(II-6)}$$

since the transferred alpha particle has intrinsic spin equal to zero. Thus, the final nuclear spin equals the transferred orbital angular momentum.

An equation for isospin transfer can be written analogous to II-5. Since the isospin of the transferred alpha is zero, the reaction will populate only residual states whose isospin equals the target isospin.

2. Parity

Parity is a conserved quantity in strong interactions [Bohr 69]. This implies that the total parity of the initial state must equal the total parity of the final state. The total parity of a physical system includes intrinsic parities as well as relative motion parity. A statement of this conservation law is

$$\pi_i = \pi_f(-1)^L \qquad \text{(II-7)}$$

where L is the angular momentum of the bound alpha with respect to the core. Assuming an even-even target and an incident α particle, π_i is positive. Thus

$$\pi_f = (-1)^L = (-1)^{J_f} \qquad \text{(II-8)}$$

by Eq. II-6. Thus the one-step $(\alpha, 2\alpha)$ reaction populates only natural parity states. Unnatural parity states could appear in sequential reactions.

The 3^+ state at 5.23 MeV in ^{24}Mg was weakly excited in the ^{28}Si$(\alpha, 2\alpha)^{24}$Mg reaction. However, the 4.97 MeV 2^- level in ^{20}Ne was not observed in ^{24}Mg$(\alpha, 2\alpha)^{20}$Ne (see Sec. IV). Unnatural parity states have been excited in inelastic alpha particle scattering, and explanations for the occurrence of these states have been given in terms of multi-step reaction processes [Reed 68, Eid 62]. It is encouraging from the $(\alpha, 2\alpha)$ reaction theory point of view that unnatural parity states are weakly excited in the $(\alpha, 2\alpha)$ process.

D. Kinematical Effects in Knock-Out Reactions

1. Sensitivity to low momentum components

Knock-out reactions at or near the quasi-free condition [Jac 71, Riou 70] are most sensitive to low momentum components of the nuclear wave function. The arguments are based on the impulse approximation, which predicts that the initial bound alpha momentum ($\vec{q}$) equals the recoil momentum ($\vec{k}_5$) in magnitude but is oppositely directed, i.e.,

$$\vec{q} = -\vec{k}_5 . \qquad \text{(II-9)}$$

The quasi-elastic geometry is arranged so that k_5 is small; so, by kinematic limitations the range of q is also small. Figure II-3 gives a plot of the minimum q allowed at symmetric angles for the $^{16}O(\alpha, 2\alpha)^{12}C(0.0)$ reaction. The maximum q is about 1 $(fm)^{-1}$ for the symmetric angles indicated.

2. Angular momentum transfer

The preceding section has shown that the linear momentum transfer to the core is small. By constructing a classical model in which the interaction occurs on the nuclear surface a prediction for the angular momentum transfer can be made. The model follows.

Particle 1 with wave number k_1 is incident on the target nucleus with radius R, and two emergent alphas are detected at θ_1 and θ_2 with wave numbers k_3 and k_4. In the symmetric case, where $k_3 = k_4$ and $\theta_1 = -\theta_2$, the recoiling nucleus is collinear with the beam, and its wave number is k_5. In the lab system the conservation of angular momentum states:

$$\vec{k}_1 \times \vec{R} = \vec{k}_3 \times \vec{R} + \vec{k}_4 \times \vec{R} + \vec{k}_5 \times \vec{R} . \qquad \text{(II-10)}$$

By taking the symmetric case (II-10) becomes

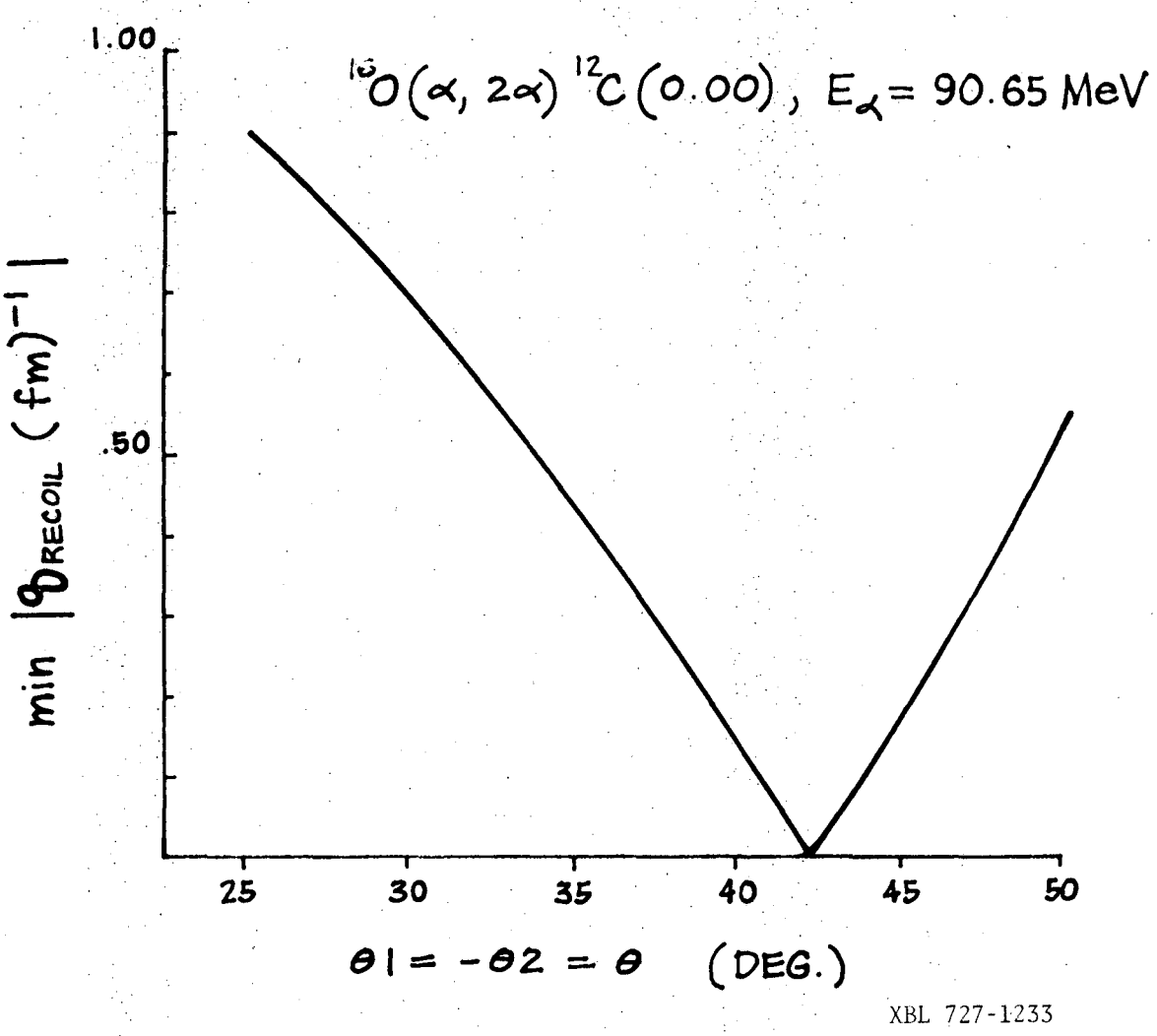

Fig. II-3. A plot of the minimum recoil momentum versus correlation angle.

$$L = k_5 R = - k_1 R + R \cos(\theta)(k_3 + k_4) \qquad \text{(II-11)}$$

and L assumes non zero values as a function of the correlation angle. If R = 3.28 fm, then the product $k_5 R$ (which is dimensionless and equals the number of angular momentum units, L) has the range

$$0.0 \leq k_5 R \leq 3.6 \qquad \text{(II-12)}$$

over the correlation angles extending from 42° to 19°. The conclusion is that the $(\alpha, 2\alpha)$ reaction at E_α = 90 MeV would favor excitation of low angular momentum states.

If the restriction to the symmetric case (where $k_3 = k_4$) is removed, then the recoil momentum assumes a larger range for most angles studied in this experiment. For example the $^{16}O(\alpha, 2\alpha)^{12}C(0.00)$ reaction at 42° - 42° has recoil momentum in the range $0.0 \leq k_5 \leq 0.90$ $(fm)^{-1}$, whereas in the symmetric case ($k_3 = k_4$) $k_5 = 0.00$. Moving away from the symmetric correlation means $k_3 \neq k_4$ and the $\vec{k}_5$ is no longer collinear with the beam axis.

E. Derivation of Plane Wave Impulse Approximation (PWIA)

1. General assumptions

A general expression for a scattering cross section is [Rod 67]

$$d\sigma_{f'i} = \frac{2\pi}{\hbar v_i} \left| \langle \phi_{f'} \left| V' \right| \psi_i^{(+)} \rangle \right|^2 \rho_{f'}(E_i) \qquad \text{(II-13)}$$

The quantity $\psi_i^{(+)}$ is the exact solution for the scattering wave in the entrance channel, and $\phi_{f'}$ is the wave function describing free motion in the exit channel. The post form of the T-matrix is given here [Tay 72]. If the total Hamiltonian is written

$$H = H_0 + V = H_0' + V' \qquad \text{(II-14)}$$

where primes indicate the final channel, then

$$H'_0 \phi_{f'} = E_f \phi_{f'}$$

$$H\psi_i^{(+)} = (H_0 + V)\, \psi_i^{(+)} = E_i \psi_i^{(+)} \qquad \text{(II-15)}$$

In the present form of $d\sigma_{fi}'$ it is the final state potential which accounts for the transition. The remaining factors are v_i the relative velocity in the entrance channel, and $\rho_{f'}(E_i)$ the phase space factor. A general expression for the phase space factor which contains momentum and energy conservation is:

$$\rho_{f'}(E_i) = \prod_{i=1}^{N} \int \frac{d^3 p_i}{(2\pi\hbar)^{3N-3}}\, \delta\left(\sum_{j=1}^{N} p_j\right) \delta\left(E - \sum_{j=1}^{N} E_j\right) \qquad \text{(II-16)}$$

[Rod 67]. Discussions of three body final states phase space factors exist in the literature [Skj 64, Will 71].

The PWIA makes several extreme assumptions to evaluate (II-13):

(i) Incoming and outgoing waves are represented by plane waves.

(ii) The target is decomposed into core + bound cluster system.

(iii) The interaction is assumed to be a function of the relative coordinate between the incident particle and bound cluster.

(iv) The interaction is assumed to be derivable from the free cluster - cluster scattering cross sections.

(v) No exchange terms are explicitly included, although use of free (α,α) scattering automatically includes projectile exchange effects [Roos 68, Jac 65].

The derivation of PWIA from (II-13) is separated into two parts: first, the treatment of phase space; and second, the application of assumptions (i) - (v) in the evaluation of the transition matrix.

2. Phase space

The notation of Fig. (II-1) is used in this section, and the quantity $|M|^2$ is substituted for $|\langle \phi_{f'} | V' | \psi_i^{(+)} \rangle|^2$. The cross section for the three body final state in the lab system is

$$d\sigma = \frac{2\pi}{\hbar v_i} |M|^2 \int \frac{d^3\vec{p}_3\, d^3\vec{p}_4\, d^3\vec{p}_5}{(2\pi\hbar)^6} \delta(\vec{p}_3 + \vec{p}_4 + \vec{p}_5 - \vec{p}_1)\, \delta(E_i - E_f) \qquad \text{(II-17)}$$

The delta function expressing momentum conservation allows integration over the recoil (unobserved) momentum. Performing this integration and substituting

$$d^3\vec{p} = p^2 dp d\Omega \qquad \text{(II-18)}$$

one finds

$$\frac{d^2\sigma}{d\Omega_1 d\Omega_2} = \frac{2\pi}{\hbar v_i} \frac{|M|^2}{(2\pi\hbar c)^6} \int (cp_3)^2\, d(cp_3)\, (cp_4)^2 d(cp_4)\, \delta(E_i - E_f). \qquad \text{(II-19)}$$

The angular variables are subscripted with 1 and 2, and (II-19) momentum units are in MeV.

The next step involves changing the momenta differentials of (II-19) to the energy differentials dE_3 and $d(E_3 + E_4)$. It is asserted that

$$cp_3\, dp_3 = E_3 dE_3 \qquad \text{(II-20)}$$

This equality is shown by solving for the Jacobian (J)

$$\frac{d^4\sigma}{d\Omega_1 d\Omega_2 d(cp_3) d(cp_4)}\, J = \frac{d^4\sigma}{d\Omega_1 d\Omega_2 d(cp_4) dE_3} \qquad \text{(II-21)}$$

where

$$J = \partial(cp_3)/\partial E_3 .$$

By using the relativistic relation between momentum and energy it is found that $J = E_3/(cp_3)$ and consequently

$$\frac{d^4\sigma}{d\Omega_1 d\Omega_2 cp_3 d(cp_3) d(cp_4)} = \frac{d^4\sigma}{d\Omega_1 d\Omega_2 E_3 dE_3 d(cp_4)}$$

thus

$$cp_3 d(cp_3) = E_3 dE_3.$$

A similar argument shows that

$$cp_4 d(cp_4) = E_4 d(E_3 + E_4).$$

Making these substitutions for $cp_3 d(cp_3)$ and $cp_4 d(cp_4)$ in (II-19)

$$\frac{d^2\sigma}{d\Omega_1 d\Omega_2} = \frac{2\pi}{\hbar v_i} \quad \frac{|M|^2}{(2\pi\hbar c)^6} \int cp_3 E_3 dE_3 cp_4 dE_4 d(E_3 + E_4) \delta(E_i - E_f) \tag{II-22}$$

The differential $d(E_3 + E_4)$ is rewritten as:

$$d(E_3 + E_4) = \frac{d(E_3 + E_4)}{d(cp_4)} \quad \frac{d(cp_4)}{dE_f} \, dE_f \tag{II-23}$$

where

$$E_f = E_3 + E_4 + E_5 .$$

Substituting (II-23) into (II-22), using the energy delta function to integrate over dE_f, and dividing by dE_3 finishes the integrations and yields an expression for the triple differential cross section:

$$\frac{d^3\sigma}{d\Omega_1 d\Omega_2 dE_3} = \frac{2\pi}{\hbar v_i} \quad \frac{|M|^2}{(2\pi\hbar c)^6} \, (cp_3) \, (cp_4) \, E_3 E_4 \quad \frac{d(E_3 + E_4)}{d(cp_4)} \quad \frac{d(cp_4)}{dE_f} \tag{II-24}$$

Using relativistic expressions, the differentials in (II-24) are solved:

$$\frac{d(E_3 + E_4)}{d(cp_4)} = \frac{cp_4}{E_4}$$

$$\frac{d(cp_4)}{d(E_f)} = \frac{E_4 E_5}{(cp_4)E_5 + E_4(cp_4 + cp_3 \cos\theta_{12} - cp_1 \cos\theta_2)} \tag{II-25}$$

and

$$dE_3 = dT_3.$$

So, the triple differential cross section becomes

$$\frac{d^3\sigma}{d\Omega_1 d\Omega_2 dT_3} = \frac{2\pi}{\hbar v_i} |M|^2 \left\{ \frac{(cp_3)(cp_4)^2 E_3 E_4 E_5}{(2\pi\hbar c)^6 [cp_4 E_5 + E_4(cp_4 + cp_3 \cos\theta_{12} - cp_1 \cos\theta_2)]} \right\} \quad \text{(II-26)}$$

The bracketed quantity is the contribution of three body phase space to the triple differential cross section. In the non-relativistic limit this expression reduces to a non-relativistic expression used in the literature [Mit 72]. Further comparisons between the relativistic and non-relativistic phase space factors have shown the same shape along the T_3 axis using energies appropriate to the present experiment.

3. Evaluation of $|M|^2$

Evaluation of M follows the assumptions outlined in II.E.1. The PWIA has been studied in detail in the literature, and the description followed most closely here is that given by Y. Kudo [Kudo 65] and I. McCarthy [McC 65].

The initial and final coordinate systems are given in Fig. II-4. Using assumptions (i) → (iii) and (v) the transition matrix element becomes:

$$M = \int d\tau\, e^{-i\vec{k}_3\cdot\vec{r}_1} \phi_{\alpha_1}(\xi_1) e^{-i\vec{k}_4\cdot\vec{r}_2} \phi_{\alpha_2}(\xi_2) \psi_R^*(\xi_R) V[|(\vec{r}_1 - \vec{r}_2)|] e^{i\vec{k}_1\cdot\vec{r}_1} \times \phi_{\alpha_1}(\xi_1) \psi_T(\vec{r}_2, \xi_2; \xi_R) \quad \text{(II-27)}$$

where

$\phi_{\alpha_1}(\xi_1)$ = internal wave function of incident alpha

$\phi_{\alpha_2}(\xi_2)$ = internal wave function of ejected cluster

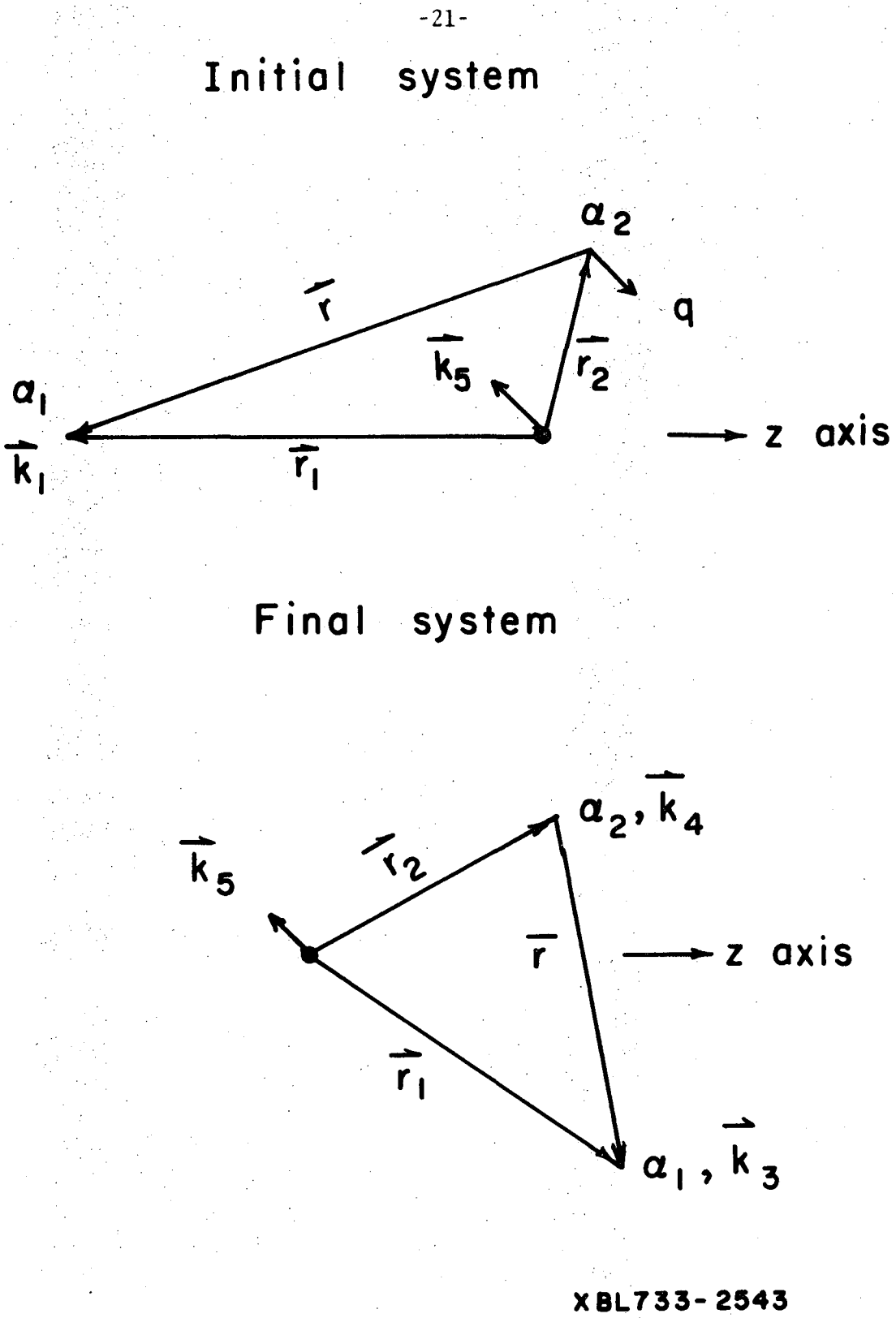

Fig. II-4. Coordinate system for the $(\alpha, 2\alpha)$ reaction theory.

$\psi_R(\xi_R)$ = residual nucleus' wave function

$\psi_T(\vec{r}_2\,\xi_2;\,\xi_R)$ = target nucleus' wave function

$$= \sum_{L,M} (I_R L M_R M \mid I_T M_T)\, S_\alpha^{1/2}\, \psi_R(\xi_R)\, \phi_{\alpha_2}(\xi_2) R_{NL}(\rho) Y_L^M(\theta, \phi)$$

where

$$\vec{\rho} = \vec{r}_2, \quad \vec{r} = \vec{r}_1 - \vec{r}_2,$$

$S_\alpha^{1/2}$ is a spectroscopic factor, and I_T equals target spin, I_R equals residual nucleus' spin, L equals orbital angular momentum of α_2 and M_T, M_R, and M are the corresponding z projections. Substituting for r_1 and r_2 in terms of ρ and r, and integrating over the internal coordinates the following separation is effected:

$$M = \int d\vec{r}\; e^{i(\vec{k}_1 - \vec{k}_3)\cdot\vec{r}}\, V(|\vec{r}|) \int d\vec{\rho}\; e^{i(\vec{k}_1 - \vec{k}_3 - \vec{k}_4)\cdot\vec{\rho}}\, f_{NL}(\vec{\rho}) \qquad \text{(II-28)}$$

where

$$f_{NL}(\rho) = \sum_{L,M} S_\alpha^{1/2} (I_R L M_R M \mid I_T M_T)\, R_{NL}(\rho)\, Y_L^M(\theta, \phi) \qquad \text{(II-29)}$$

and $f_{NL}(\vec{\rho})$ may be referred to as the form factor.

The first integral of (II-28) is seen to depend only on the α-α relative coordinate and the momentum transferred from α to α by the incident particle. This integral is equivalent to the plane wave Born approximation description of free α-α scattering, so

$$\left| \int d\vec{r}\; e^{i(\vec{k}_1 - \vec{k}_3)\cdot\vec{r}}\, V(|\vec{r}|) \right|^2 = \sigma_{\alpha\alpha}(T, \theta) \cdot \frac{(2\pi)^2 (\hbar c)^4}{(\mu_\alpha c^2)^2} \qquad \text{(II-30)}$$

where $\sigma_{\alpha\alpha}(T, \theta)$ = free α-α scattering differential cross section and $\mu_\alpha c^2$ = reduced α-α mass (MeV) = $m_\alpha c^2/2$. The additional factors in (II-30) are found in books dealing with two body scattering problems

[Tob 61]. The relation (II-30) provides a method for introducing free α-α scattering information and its use in II-28 is the impulse approximation. A future section will discuss this approximation in more detail.

The second integral of (II-28) is the Fourier transform of the bound state wave function with respect to the recoil momentum:

$$\phi_{NL}(\vec{k}_5) = \int d\vec{\rho}\ e^{i\vec{k}_5 \cdot \vec{\rho}} f_{NL}(\vec{\rho}) \qquad \text{(II-31)}$$

and $\vec{k}_5 = \vec{k}_1 - \vec{k}_3 - \vec{k}_4$ (in the lab frame). In the PWIA, θ is defined as the angle between the relative coordinate ρ and the z-axis, defined by the beam direction. For $0^+ \rightarrow 0^+$ transitions the summation over Clebsch-Gordan coefficients in (II-29) yields unity. (In this case $I_R = L = I_T = 0$). For $0^+ \rightarrow 2^+$ transitions $I_R = L = 2$ for even-even targets where $I_T = 0$. The z-projection of L (M) is restricted to zero in the symmetric case because of the orthogonality of the spherical harmonics (cf. integration in II-31). Thus $M_R = M = M_T = 0$ for even-even target nuclei, the the Clebsch-Gordan coefficient yields the factor $(2L+1)^{-1/2}$.

Consider the non-symmetric case with $T_3 \neq T_4$ but with $\theta_1 = -\theta_2$. In this case $\vec{k}_5$ is no longer collinear with the z-axis and II-31 becomes:

$$\phi_{NL}(\vec{k}_5) = \int e^{ik_5\rho \cos\theta'} f_{NL}(\rho, \theta, \phi) \sin\theta d\theta d\phi \rho^2 d\rho \qquad \text{(II-32)}$$

where (II-32) indicates dependence on θ', the angle between $\vec{k}_5$ and $\vec{\rho}$, as well as the arguments of f_{NL}. Further, $\theta' = \theta - \theta_R$ where θ_R is the recoil angle as measured from the z-axis.

Non-symmetric effects can be treated by making a plane wave expansion of $e^{i\vec{k}_5 \cdot \vec{\rho}}$

$$e^{i\vec{k}_5 \cdot \vec{\rho}} = 4\pi \sum_{\ell=0}^{\infty} \sum_{m=-\ell}^{\ell} i^{\ell}\, Y_{\ell}^{*m}(\theta_R, \phi_R)\, Y_{\ell}^{m}(\theta, \phi) j_{\ell}(k_5\rho) \qquad \text{(II-33)}$$

and substituting into (II-32). Using the notation that $f_{NL}(\rho, \theta, \phi)$ $= Y_L^M(\theta, \phi) f_{NL}(\rho)$ and the orthonormality of the spherical harmonics leads to

$$\phi_{NL}(\vec{k}_5) = 4\pi \sum_{\ell m} i^{\ell} (-1)^m Y_{\ell}^{m}(\theta_R, \phi_R) \delta_{\ell L} \delta_{-mM} \int_{\rho=0}^{\infty} j_{\ell}(k_5 \rho) f_{NL}(\rho) \rho^2 d\rho \tag{II-34}$$

Equation (II-34) indicates that for the non-symmetric case in which $L > 0$ the substates of L do contribute to $\phi_{NL}(\vec{k}_5)$. This result is contrasted with the discussion of the symmetric case following equation (II-31). To make predictions for energy or momentum correlations for $L \neq 0$ states it is necessary to include the $M \neq 0$ substates in the calculation. This result is discussed in the literature [Jac 71].

If the plane waves implicit in (II-31) are replaced by distorted waves, the Distorted Wave Impulse Approximation (DWIA) is obtained. The DWIA model is discussed for $(\alpha, 2\alpha)$ reactions [Jac 65a] and more completely for (p, 2p) reactions [Jac 67, Lim 66, Lim 64, Lim 64a]. The PWIA model would weigh the total nuclear volume equally, and would predict no absorption or refraction effects. Optical model wave functions predict that two particle coincidence events from a three body final state should be more strongly localized in the nuclear surface than a corresponding two body experiment [Lim 62, McC 62]. Thus the PWIA, which predicts no surface localization at all, is unrealistic. Insertion of radial cut offs in plane wave calculations has often improved agreement with experiment: this was the case for the ^{6}Li$(\alpha, 2\alpha)$ reaction analyzed with a cut off PWIA [Wat 71]. The DWIA model should provide for surface localization effects. However, this model still assumes the

impulse approximation: i.e., the free α-α collision is described by the asymptotic kinematics and does not take into account the particle dynamics near or in the nucleus.

The work of Lim and McCarthy is directed at a (p, 2p) reaction model which specifically takes the core presence into account in an explicit three body theory. Their reaction theory is called the Distorted Wave T-Matrix Approximation (DWTA). The presence of the core requires that the motion of incident and scattered particles be treated by distorted waves rather than plane waves. In this case Eq. (II-13) does not separate as shown in Eq. (II-28), but the interaction (V' of Eq. II-13) is still given by an on-shell model for the T-matrix [Lim 64a]. Physically, this means that the (p, p) collision that occurs within the nucleus is not characterized by the asymptotic kinematical variables as assumed in the PWIA and the DWIA. Furthermore, since a third body is present, the (p, p) collision does not have to conserve momentum and energy. This is an off-energy shell effect, and the work of Lim and McCarthy indicated that lower energy (p, 2p) experiments could be sensitive to these effects. Some success was found in fitting the $^{12}C(p, 2p)$ reaction at E_p = 50 MeV [Pugh 67]. The DWIA is obtained from the DWTA by taking a delta function interaction and multiplying the resultant quantity by the free (p-p) scattering [Lim 64a]. An $(\alpha, 2\alpha)$ code similar to the DWTA is not available, hence $(\alpha, 2\alpha)$ analyses have been restricted to various forms of the impulse approximation.

The following section describes a theoretical treatment in which the plane waves of (II-31) are replaced by a parametrization of the optical model (distorted wave) wave functions.

F. Phenomenological Distorted Wave Impulse Approximation

Equation (II-31) can be extended to the DWIA by replacing the product of three plane waves implicit in $e^{i\vec{k}_5\cdot\vec{\rho}}$ by the product of three distorted waves:

$$\phi_{NL}(\vec{\xi})=\int d\vec{\rho}\ \chi^{(-)^*}(\vec{k}_3,\vec{\rho})\,\chi^{(-)^*}(\vec{k}_4,\vec{\rho})\chi^{(+)}(\vec{k}_1,\vec{\rho})f_{NL}(\vec{\rho})\ . \qquad \text{(II-35)}$$

It has been suggested that distorted waves could be parametrized by an analytically more simple function than partial wave expansion [McC 61]. The parametrization is based on analogies between nuclear scattering and classical optics as well as intuition concerning the absorption of beam particles by nuclear scattering centers [Eisb 59, McC 59, McC 59a, Amos 66]. The McCarthy, Pursey, and Kromminga form for the parametrization is

$$\chi^{(+)}(\vec{k},\vec{r}) = e^{i(\beta+i\gamma')\vec{k}\cdot\vec{r}}\,[1 + a\,e^{i\phi}\delta(\hat{k}R-\vec{r})] \qquad \text{(II-36)}$$

[McC 68]. This expression is a sum of two terms, the first being related to the scattering wave at the nuclear surface, and the second accounting for focus effects.

The parameters β and γ specify the surface term. The parameter β is related to the real part of the optical model potential, and is always > 1 if V is attractive ($V < 0$). Further, β may be defined in terms of local and asymptotic wave numbers:

$$k_\ell = \beta k_a \qquad \text{(II-37)}$$

where

$$k_\ell = \text{local wave no.} = \frac{2\mu}{\hbar^2}(E-V_\ell)$$

$$k_a = \text{asymptotic wave no.} = \frac{2\mu}{\hbar^2} E$$

The asymptotic energy is E and the real part of the optical model potential is V_ℓ. Using relations in (II-37) β is found to equal:

$$\beta = \left(\frac{E - V_\ell}{E} \right)^{1/2} \qquad \text{(II-38)}$$

Amos [Amos 66] gives a picture of an asymptotic wave encountering an attractive potential with the resultant increase of wave number. The parameter γ is a damping factor which accounts for absorption. An expression for γ has been given in the (p,2p) literature [Deu 68]:

$$\gamma = R_S \left\{ \left(\frac{\mu}{2\hbar^2} \right) \frac{W^2}{E - V_\ell} \right\}^{1/2} \qquad \text{(II-39)}$$

where W is the imaginary part of the optical model potential.

The focus term is specified by three parameters - a the strength parameter and R and ϕ which are the focus position and the phase difference between this position and the nuclear surface. McCarthy and Pursey [McC 61] argued that the focusing is weak for (α, α') scattering, but is strong for nucleon scattering [Krom 62]. The focus term has accordingly been neglected in the present treatment of the $(\alpha, 2\alpha)$ reaction. The full parametrization has been used in theoretical treatments of the (p,2p) reaction [Deu 68, Chat 72].

Assuming that $a = 0$, an incident distorted wave becomes

$$\chi_i^{(+)}(\vec{k}_i, \vec{r}) = N_i \, e^{i(\beta_i + i\gamma_i / k_i R_S)\vec{k}_i \cdot \vec{r}} \qquad \text{(II-40)}$$

where $\vec{k}_i$ is the asymptotic wave number and $\gamma_i / k_i R_S$ replaces γ_i' for the normalization of $\chi_i^{(+)}$. The normalization N_i is determined from the condition that $|\chi_i^+|^2 = 1$ at the nuclear surface, R_S. With this condition

$$N_i = e^{-\gamma_i} \qquad \text{(II-41)}$$

is found. Similarly an exit distorted wave is:

$$\chi_f^{*(-)} = N_f \, e^{-i(\beta_f + i\gamma_f/k_f R_S)\vec{k}_f \cdot \vec{r}} \qquad \text{(II-42)}$$

where $\vec{k}_f$ is the asymptotic wave number in the exit channel. The normalization parameter is determined as in the incident channel, and is found to be:

$$N_f = e^{-\gamma_f} . \qquad \text{(II-43)}$$

In applying these wave functions to the $(\alpha, 2\alpha)$ reaction description the following parameter equalities are defined:

$$\begin{aligned} &\beta_i = \beta_1 \text{ and } \gamma_i = \gamma_1; \ \alpha_i = \alpha_1 = \beta_1 + i\gamma_1 \\ &\beta_f = \beta_3 = \beta_4 \text{ and } \gamma_f = \gamma_3 = \gamma_4; \\ &\alpha_f = \alpha_3 = \alpha_4 = \beta_3 + i\gamma_3 = \beta_4 + i\gamma_4 . \end{aligned} \qquad \text{(II-44)}$$

In principle there should be six parameters to treat the scattering waves; however, since the experiments emphasize the symmetric coplanar geometry the final state parameters are set equal. Hence four parameters are sufficient to characterize the scattering waves.

Substituting the parametrized distorted waves into (II-35), the result for the momentum space wave function is:

$$\phi_{NL}(\vec{\xi}) = N_i N_f^2 \int e^{i\vec{\xi}\cdot\vec{\rho}} f_{NL}(\vec{\rho}) \, d\vec{\rho} \qquad \text{(II-45)}$$

where

$$\vec{\xi} = \alpha_i \vec{k}_1 - \alpha_f(\vec{k}_3 + \vec{k}_4)$$

Expression (II-45) differs from the PWIA (II-31) in that $\vec{\xi}$ equals $\vec{k}_5$ which equals the recoil momentum in that theory. If $\beta_i = \beta_f = 1.0$ and $\gamma_i = \gamma_f = 0$ are inserted in the parametrized DWIA, the PWIA is found. Now the angle θ is defined by (in the symmetric case):

$$\vec{\xi} \cdot \vec{p} = |\vec{\xi}| \; |\vec{\rho}| \cos(\theta), \qquad \text{(II-46)}$$

since $\vec{\xi}$ is collinear with the incident beam direction, and the integration of (II-45) is slightly more complicated than the plane wave theory. Details of the evaluation are given in Appendix II.

G. Bound State Radial Wave Function

Before (II-45) can be integrated, the radial wave function ($R_{NL}(\rho)$) appearing in $f_{NL}(\vec{\rho})$ must be specified. The $R_{NL}(\rho)$ are calculated in a finite well assuming an S = 0, T = 0 particle. [code DWUCK, P. D. Kunz, private communication]. The procedure adjusts the well depth binding the four particle cluster until the correct asymptotic behavior - which is due to the separation energy - is matched. The quantum numbers N (number of radial nodes) and L (orbital angular momentum) must be specified for calculation of $R_{NL}(\rho)$. This is done by considering the conservation of energy within the harmonic oscillator shell model [Den 66, Bed 72]:

$$\sum_{i=1}^{A} (2n_i + \ell_i) = 2N + L + \sum_{f=1}^{A-4} (2n_f + \ell_f) \qquad \text{(II-47)}$$

and with the condition

$$\vec{J}_i = \vec{L} + \vec{J}_f = 0$$

it is always possible to find N and L. Harmonic oscillator radial wave functions have also been used in analysis [McC 68]. The radial wave functions are normalized so that

$$\int_0^\infty |R_{NL}(\rho)|^2 \, d\rho = 1.0 \qquad \text{(II-48)}$$

Integral (II-45) has been solved by finding analytic expressions for L = 0

orbital angular momenta for the angular coordinates. Then the $R_{NL}(\rho)$ is read into the program externally, and a numerical integration is performed over the radial coordinate. Equation (II-47) does not contain the internal quantum numbers n and l of the bound cluster, since the cluster is assumed to exist in the lowest oscillator state.

H. Off-shell Effects in Quasi-Free Scattering

1. Definitions and current status of "off the shell" scattering.

Equation (II-30) explicitly introduces the free scattering into the impulse approximation transition matrix. The procedure for inserting this information in a proper way is a subject of current research. One problem is that if an alpha particle is available within the nucleus for an α-α collision, that alpha particle is not on the energy shell due to its core binding energy. This is seen from the definition of the T-matrix in terms of the S-matrix [Tay 72]:

$$\langle p' | S | p \rangle = \delta_3(\vec{p}' - \vec{p}) - 2\pi i \delta(E_{p'} - E_p)\, T(\vec{p}' \leftarrow \vec{p}). \qquad \text{(II-49)}$$

Thus the on-shell T-matrix, $T(\vec{p}' \leftarrow \vec{p})$ is defined only for $E'_p = E_p$, and it is not justified in principle to use the on shell T-matrix, or equivalently the free α-α scattering. However, inherent in the impulse approximation is that the off-shell effects are negligible.

The study of off-shell effects in three body reactions with a massive residual nucleus is in a very early stage of development. In this paragraph, an "off-shell" effect means that, for example, the p-p collision in a (p,2p) reaction in the presence of a third body is not the same as the free "on-shell" p-p interaction. To extract off-shell information from such a three-body process, a good dynamical theory must exist.

The DWTA of Lim and McCarthy [Lim 64, Lim 66] described briefly in Sec. III-E provides a (p, 2p) theory within the distorted wave framework. They have not included off-shell effects in the (p-p) interaction, but they have shown that at higher incident proton energies (155 MeV) the DWIA and DWTA make the same theoretical predictions, and that they deviate as the incident proton energy is decreased. Unfortunately, as pointed out in Sec. III-E such a code is not available for the $(\alpha, 2\alpha)$ reaction, and $(\alpha, 2\alpha)$ analyses have been restricted to PWIA and DWIA.

Upon making the impulse approximation, ambiguity arises concerning the choice of free α-α scattering cross section. This ambiguity concerns the postulated α-α collision kinematics, since the collision may actually occur at two different α-α center of mass energies - depending on whether the relative energy is calculated in the initial (T_i) or final (T_f) channel. This is due to the bound alpha's momentum. Since the free α-α cross section varies dramatically with energy and angle, the choice of relative energy in the initial or final α-α subsystem may have large effects on the choice of the free α-α cross section interpolated from α-α scattering data. This problem is often referred to as an "off-shell" effect in the $(\alpha, 2\alpha)$ literature, and its nature should be distinguished from the off-shell discussion of the previous paragraph. This ambiguity brought about by the kinematics is discussed in the remainder of this section.

This cross section ambiguity has received considerable attention in the recent literature. Balashov and Meboniya [Bal 68] have made symmetric $(\alpha, 2\alpha)$ calculations on ^{6}Li, ^{7}Li, ^{9}Be, ^{12}C and ^{16}O target nuclei. They have shown that at E_α = 25 MeV the final state prescription

(T_f) for α-α interpolation is preferred. Their calculations have been compared to the $(\alpha, 2\alpha)$ data of V. K. Dolinov, et al. [Dol 69] taken on the ^{6}Li, ^{7}Li, ^{9}Be, and ^{12}C nuclei at E_α = 25 MeV.

A French group studied the ^{6}Li$(\alpha, 2\alpha)$d [Gail 70] reaction at E_α = 42.8 MeV. At this energy a sharp resonance (at 19.8 MeV in the α-α c.m. system) in the α-α free cross section is identified with a sharp structure in the $(\alpha, 2\alpha)$ angular correlation. The PWIA theory utilized in their analysis gave the correct result only when the T_f prescription was used. Their measurements were extended to the ^{9}Be and ^{16}O targets [Gui 71] and again interpretation of their data favored the T_f prescription.

Finally a systematic study of the ^{6}Li$(\alpha, 2\alpha)$ reaction at several incident energies (E_α = 50.4, 59.0, 60.5, 70.3, and 79.6 MeV) was performed [Pugh 69, Wat 71]. In this work the "off the energy shell" $\sigma_{\alpha\alpha}(T, \theta)$ was extracted from their data using the PWIA. The T_f prescription for extracting $\sigma_{\alpha\alpha}(T, \theta)$ gave the best agreement with the free α-α scattering data.

Balashov and Meboniya [Bal 68] suggested that the "method is formally unapplicable in the low energy range." However, they further suggest that the agreement found with the T_f method may not necessarily be accidental but that perhaps the quasi-elastic mechanism in this case is close to an α-pickup reaction which would lead to the intermediate ^{8}Be nucleus and a strong final state interaction. Meboniya [Meb 69] provides theoretical support for the T_f prescription. A possible physical reason suggested for the validity of the T_f prescription is that the incident particle must release the bound particle before a free α-α collision could occur.

2. Derivation and discussion of T_i and T_f prescriptions

The free α-α differential cross section, $\sigma_{\alpha\alpha}(T, \theta)$ is a function of center of mass (c.m.) energy T and c.m. angle θ. Since $\sigma_{\alpha\alpha}(T, \theta)$ varies rapidly as a function of these variables, it is necessary to interpolate a value of $\sigma_{\alpha\alpha}(T, \theta)$ among the available free α-α data. The interpolation is on T - calculated either from the T_i or T_f prescriptions - and on θ. The $\sigma_{\alpha\alpha}(T, \theta)$ are taken from the literature [Nils 56, Bred 59, Conz 60, Tom 63, Darr 65]. Figure II-5 shows most of the $\sigma_{\alpha\alpha}(T, \theta)$ used in the present calculation, and Appendix III gives an explicit summary of the $\sigma_{\alpha\alpha}(T, \theta)$ cross sections.

The non-relativistic kinematics for finding T_i and T_f as well as θ necessary for interpolating in $\sigma_{\alpha\alpha}(T, \theta)$ are now derived. The relative momentum between particle i and j with masses m_i and m_j is:

$$\vec{p}_{ij} = \frac{1}{m_i + m_j} (m_j \vec{p}_i - m_i \vec{p}_j) \qquad \text{(II-50)}$$

For the relative α-α momentum in the incident channel $m_i = m_j = m$ and $p_i = p_1$ = incident beam momentum. The impulse approximation requires that the momentum of the bound alpha equal $-\vec{p}_5$. Thus $\vec{p}_j$ equals $-p_5$ and the relative α-α momentum in the incident channel is

$$\vec{p}_{inc} = \tfrac{1}{2} (\vec{p}_1 + \vec{p}_5) \, . \qquad \text{(II-51)}$$

The non-relativistic c.m. incident energy is then

$$T_i = \frac{|\vec{p}_{inc} \cdot \vec{p}_{inc}|}{2\mu_{\alpha\alpha}} \qquad \text{(II-52)}$$

where

$$\mu_{\alpha\alpha} = \frac{m_\alpha}{2}$$

The final state relative α-α momentum is

$$\vec{p}_{out} = \tfrac{1}{2} (\vec{p}_3 - \vec{p}_4) \qquad \text{(II-53)}$$

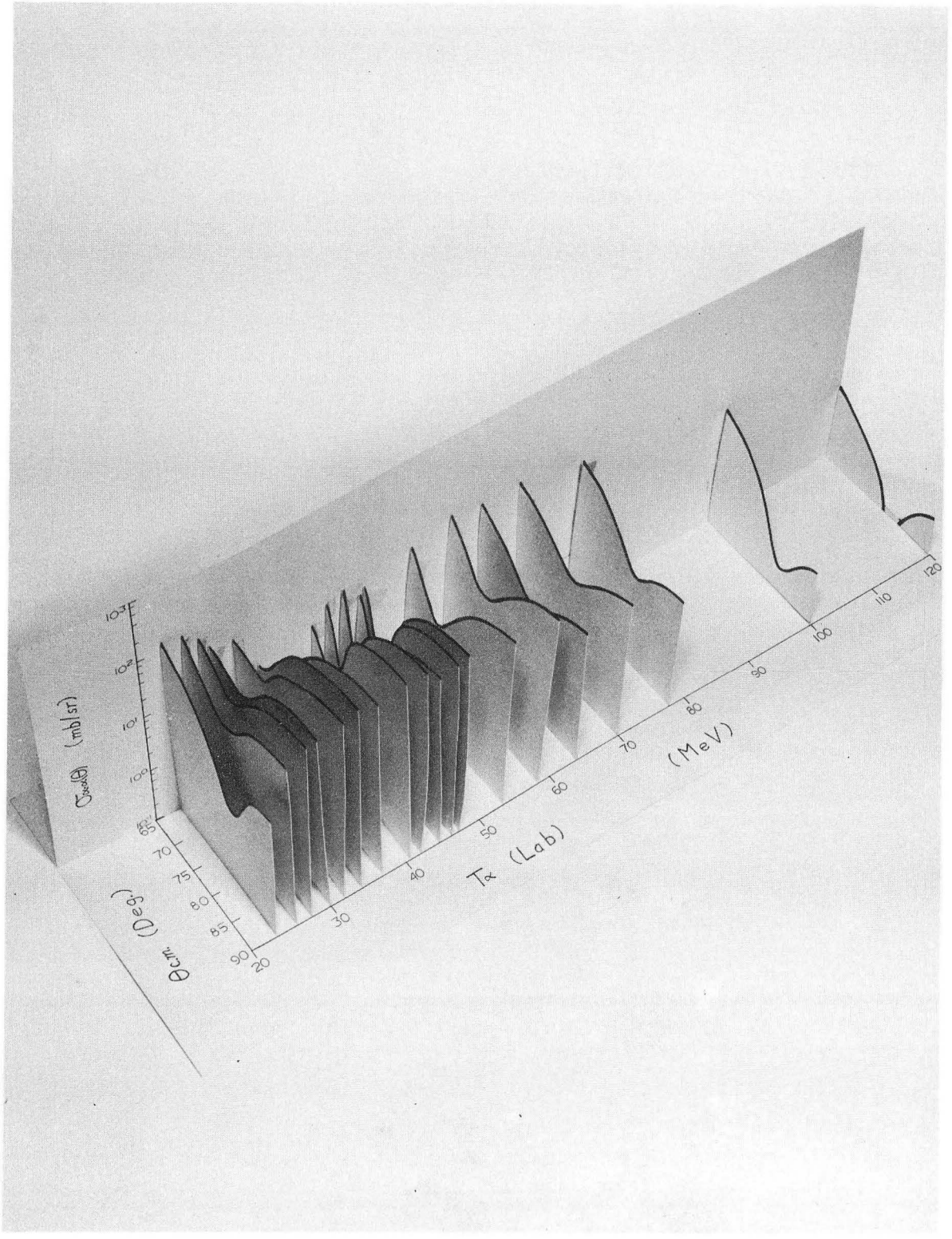

XBB 727-3659

Fig. II-5. Three dimensional plot for most of the free α-α scattering data used in the impulse approximation calculation.

where $\vec{p}_i = \vec{p}_3$ and $\vec{p}_j = \vec{p}_4$ in Eq. (II-48).
Similarly the non-relativistic c.m. final energy is

$$T_f = \frac{|\vec{p}_{out} \cdot \vec{p}_{out}|}{2\mu_{\alpha\alpha}} \qquad \text{(II-54)}$$

The c.m. scattering angle is the angle between $\vec{p}_{inc}$ and $\vec{p}_{out}$. By making x-y projections of the vectors $\vec{p}_{inc}$ and $\vec{p}_{out}$ the following angular relations are found:

$$\theta_{inc} = \text{arc tan} \left[\frac{(p_4 - p_3)\sin\theta}{p_1 - (p_3 + p_4)\cos\theta} \right] \qquad \text{(II-55)}$$

and

$$\theta_{out} = \text{arc tan} \left[\frac{(p_3 + p_4)\sin\theta}{(p_3 - p_4)\cos\theta} \right] \qquad \text{(II-56)}$$

and

$$\theta_{c.m.} = \theta_{out} - \theta_{inc} \qquad \text{(II-57)}$$

All the kinematical relations given in this section were compared with relativistic expressions, and only slight differences were found in results appropriate to the 90 MeV $(\alpha, 2\alpha)$ experiment.

Some interpolation examples using the T_i and T_f prescriptions will be given in the discussion. The $\sigma_{\alpha\alpha}(T, \theta)$ interpolations for the energy correlations do not vary nearly as much as the interpolated $\sigma_{\alpha\alpha}(T, \theta)$ for the angular correlations. The reason is that T_i, T_f, and θ attain a larger range of values in the angular correlation, and therefore the $\sigma_{\alpha\alpha}(T, \theta)$ are varying more rapidly. This leads to the conclusion [Gui 71] that the angular correlation is a more sensitive test of these off shell effects than the energy correlation.

III. Equipment and Analysis

A. Cyclotron, Beam Optics, and Scattering Chamber

1. Cyclotron and choice of beam energy

The experiments were performed with a 90 MeV alpha beam generated by the 88-inch cyclotron. In the theory section it was seen that competition between sequential and direct reaction mechanisms may cause analysis difficulties. However, one may hope that sequential reactions having large ground state α-decay widths are largely limited to those kinematic regions where reasonably sharp energy levels in the intermediate nucleus exist. However, the quasi-elastic or direct knock-out mechanism is characterized by approximately equal energy sharing in the two emitted alpha particles. Thus the two mechanisms can be separated in the T_3-T_4 energy plane by increasing the incident beam energy. Since moderately sharp levels up to 20 MeV excitation in light nuclei are observed, and realizing that α-separation energies are about 10 MeV in light nuclei, an incident energy equal to 90 MeV was adequate to effect separation of quasi-elastic and sequential events.

It may seem advantageous to use a still higher energy beam. This was not pursued for several reasons. First, the simplest quasi-elastic theory would predict the $(\alpha, 2\alpha)$ cross section to fall as the incident energy increases. Since the cross sections were expected to be small, it seemed unwise to follow a course which might result in yet smaller cross sections. Moreover, operation of the cyclotron at the required beam intensity is easier and more stable at 90 MeV than at higher energies. Furthermore, available and reliable 3mm lithium drifted Si detectors were sufficient to stop elastically scattered particles at

E_α = 90 MeV. The cyclotron and beam transport system used in these experiments is summarized in Fig. III-1.

2. Beam optics

After extraction, the beam was defined radially by a 1" collimator, and the diverging beam was immediately focussed to a one inch square with a quadruple doublet. (The optics system is given in Fig. III-1.) The beam was then transmitted to the high resolution beam line [Hin 69] via a 20° bend in the switching magnet. A second quadruple doublet provided a radial focus at the source slit of the magnetic beam analyzing system. Two 110° flat field, edge focusing bending magnets composed the beam analysis system. The first magnet (M41) provided an energy dispersed image to the second slits, which then permitted a selected energy to pass. The second magnet (M42) then acted as a clean-up magnet, eliminating the slit scattered particles. With the source and image slits at 0.020 in., the beam resolution was 0.02% of the beam energy. To increase beam transmission efficiency the slits were opened to 0.080" for the $(\alpha, 2\alpha)$ experiments. This configuration yielded a beam resolution of 72 keV with beam intensities that ranged from 100-500 nA in the 36" scattering chamber. The magnetic analysis system also provided an absolute beam energy from a calibration obtained by scattering molecular hydrogen ion beams on ^{12}C, observing the T = 3/2, 14.232 MeV resonance in ^{13}N [Bach 71]. This calibration yielded energies of 90.33, 89.54, and 90.09 MeV energies for the experiments reported here. Provided the analyzing magnets were stable, the experiment should be free of beam energy changes. The magnetic fields were continually monitored by an NMR probe, and no shifts in the NMR

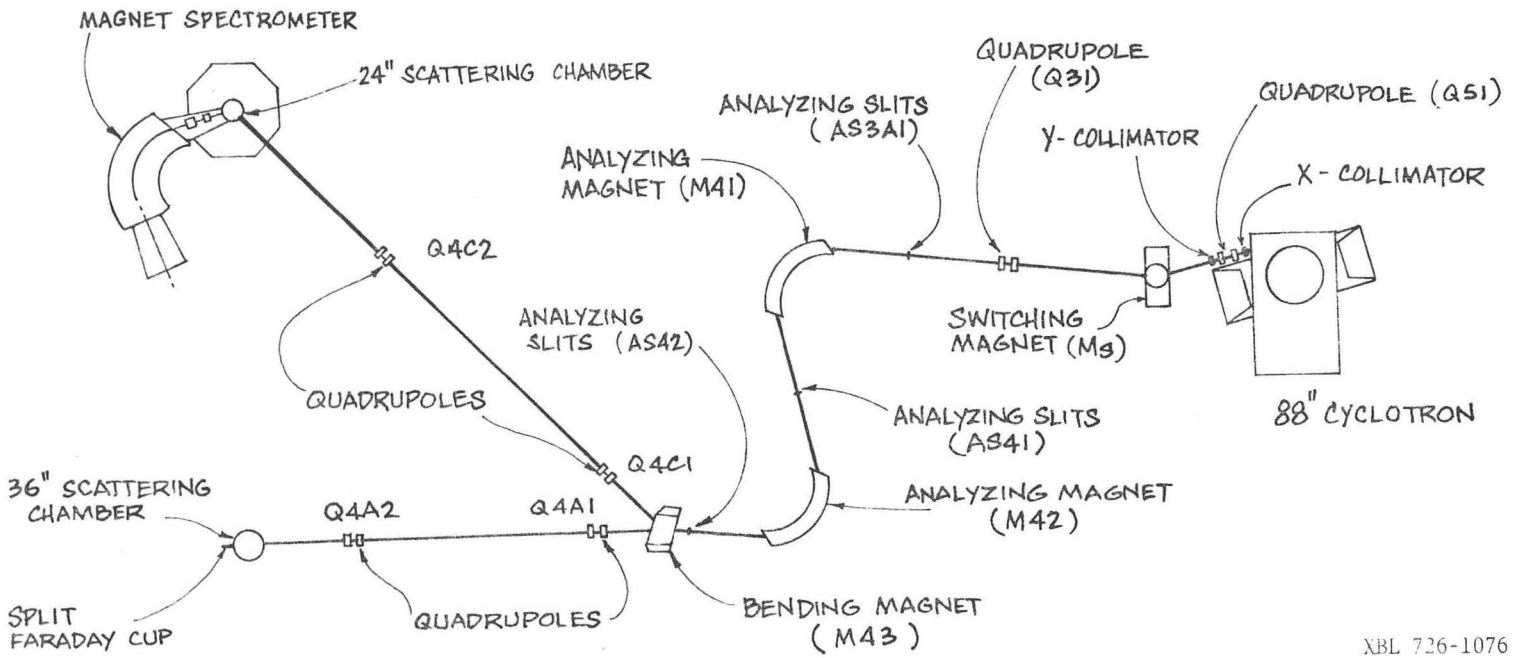

Fig. III-1. Cyclotron and beam transport system to cave 4A 36 in. scattering chamber.

were observed during data taking runs. The beam was finally switched to Cave 4A with the M43 switching magnet.

Two solutions [Meri 70] have been calculated for beam transmission from M42 to the 36 in. scattering chamber. One was a strongly converging beam with a radial magnification of 0.5. This solution gave a very good radial focus (< 1 mm) but apparently allowed part of the beam to strike the beam pipe as very asymmetric counting rates were observed. The second solution has a radial magnification of 2.0, and provided a more parallel beam transport to the target. The convergence angle at the target was 0.5° with this solution, and a beam spot of approximately 2 mm $\times$ 4 mm was typically obtained. No asymmetric counting problems were encountered with this solution.

3. Scattering chamber

The experiment was done in the 36" scattering chamber (Fig. III-2). The scattering chamber was equipped with a remotely controlled rotating table which provided one independent θ motion. In order to measure a symmetric coplanar angular correlation a second independent θ-motion counter mount was installed in the beam - table counter plane. The angular positioning of each counter could be reproduced to an accuracy of $\pm 0.2°$. The total angular range available from the second detector was approximately 100°. A remotely controlled target ladder was also available, and is visible in Fig. III-2 holding the Al_2O_3 scintillator which was used for visually focussing the beam at the target position. The counter mounts accommodated Si(P) transmission and Si(Li) stopping detectors, and these were cooled to -24°C by thermoelectric devices. Table III-1 summarizes the geometries used in these experiments; set

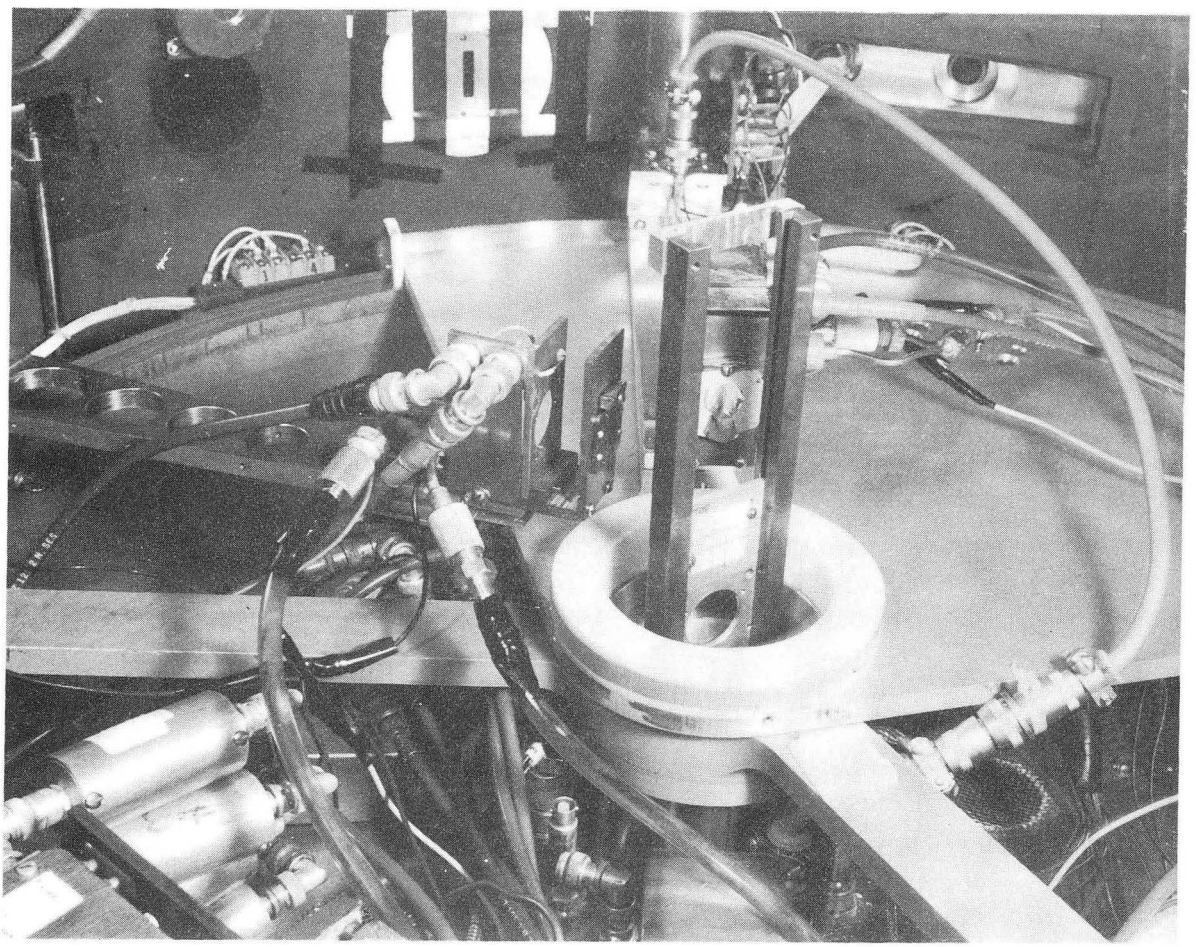

XBB 726-3288

Fig. III-2. Scattering chamber partially assembled for $(\alpha, 2\alpha)$ experiment.

Table III-1. Geometries for coincidence detectors

Set	CTR	Solid angle (msr)	Radii (in.)	Angular radial acceptance (°)	Angular vertical acceptance (°)
A	1	4.70	1.69	2.11	±3.73
	2	4.60	1.66	1.96	±3.73
B	1	1.40	3.09	1.15	±2.09
	2	1.46	2.94	1.09	±2.09

A was used for most measurements, while set B was used for small scattering angle work in the ^{16}O, ^{12}C $(\alpha, 2\alpha)$ reactions.

Accurate beam centering on the target is crucial in experiments with large solid angles and counters at small radii. Counters, targets, and a split Faraday cup were carefully aligned with a transit before each experiment. The coincidence detectors also act as a beam centering monitor, i.e., since they are symmetric in angle and have virtually the same solid angles and angular acceptances, the two count rates should be nearly equal. This criterion was used as a check in ensuring that the beam was centered. If the beam were one beam width off center (~ 2.0 mm), an error of approximately two degrees in scattering angle for one detector would be introduced. Figure III-3 illustrates the problem. For a constant error in beam centering (ΔS) it is seen that the error was a function of the scattering angle θ. The angle θ' is the actual angle of scattering with the displacement ΔS. In the notation of Fig. III-3

$$\theta = \arctan\left(\frac{S}{\ell}\right) \quad \text{and} \quad \theta' = \arctan\left(\frac{S + \Delta S}{\ell}\right) \qquad \text{(III-1)}$$

and the per cent error is given by

$$\% \text{ error} = \left[\frac{\theta' - \theta}{\theta}\right] \times 100 \qquad \text{(III-2)}$$

and grows as θ becomes smaller. For two detectors the errors add, so sizeable angular errors can occur with relatively small beam-detector misalignments.

It was found that the split Faraday cup was extremely sensitive to beam position shifts on target. The Faraday cup rarely indicated position shifts, and beam-detector alignment was well controlled and monitored.

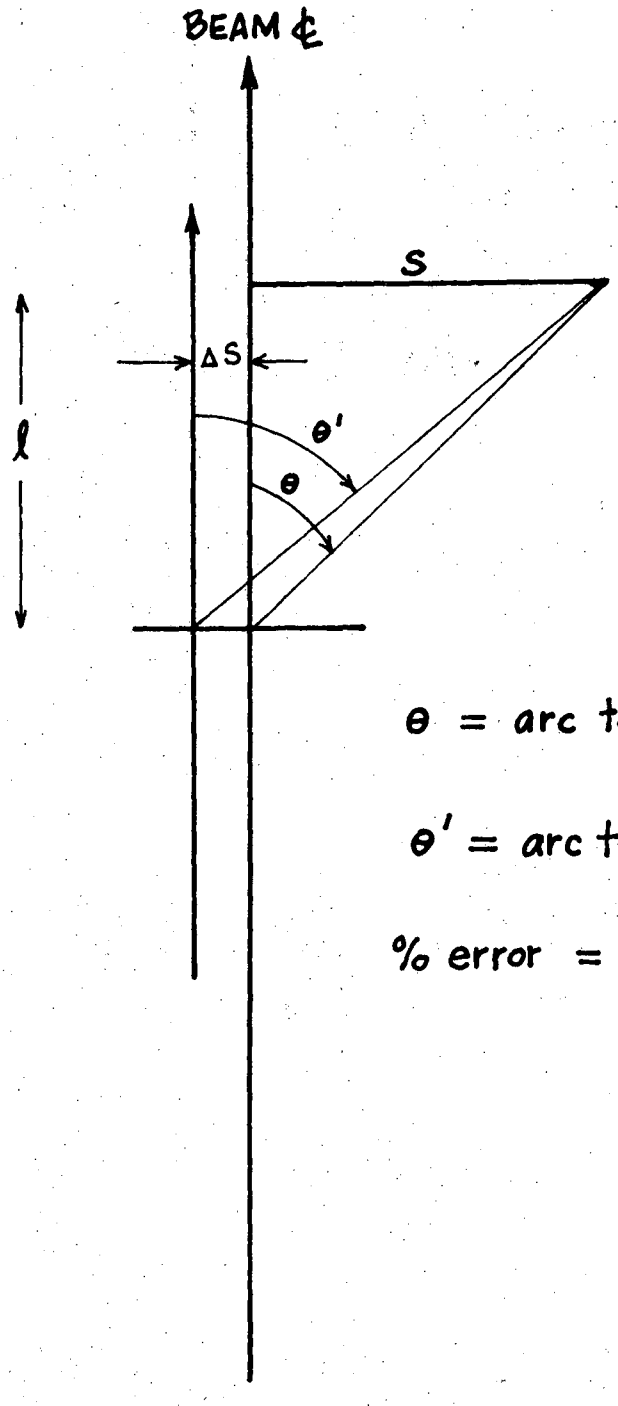

$$\theta = \arctan\left(\frac{S}{\ell}\right)$$

$$\theta' = \arctan\left(\frac{S+\Delta S}{\ell}\right)$$

$$\%\ \text{error} = \frac{|\theta' - \theta|}{\theta} \times 100$$

XBL 7210-5827

Fig. III-3. Figure exhibiting beam centering sensitivities in the $(\alpha, 2\alpha)$ experiment.

The influence of finite beam spot size on scattering angle uncertainty is discussed in a later section.

B. Detectors, Electronics, and On-line Computer

1. Detectors

Scattered particle energies were measured with a Si ΔE-E telescope. The transmission detectors were 250 μm phosphorous-diffused Si detectors; these operated at 200 v bias. For calibration purposes it was necessary to stop elastically scattered beam particles, so 3 mm lithium drifted Si detectors were chosen as the stopping counters: they operated at 400 v bias. All counters used in these experiments were prepared by the LBL detector lab. The detectors were cooled to -24°C, and at this temperature the detectors exhibited very little leakage current. The properties of solid state detectors for use in nuclear physics have been reviewed [Gou 66, TMC 65]. Thin Al foils (1.5 mg/cm^2) were used for electron suppression; one of these suppressors can be seen in place in Fig. III-2.

2. Electronics

A detailed block diagram of the electronics used in this experiment is given in Fig. III-4. The electronics system was composed of a fast coincidence part with inherent time resolution considerably less than the cyclotron period which was approximately 100 ns, and a slow part for handling analog signals and particle discrimination. Electronics for only one slow counter system is illustrated. Both the slow and fast logic employed is similar to that used by J. Moss [Moss 69] in a (p, p'γ) experiment. The maximum singles counting rate in these experiments was limited to 15,000 cps.

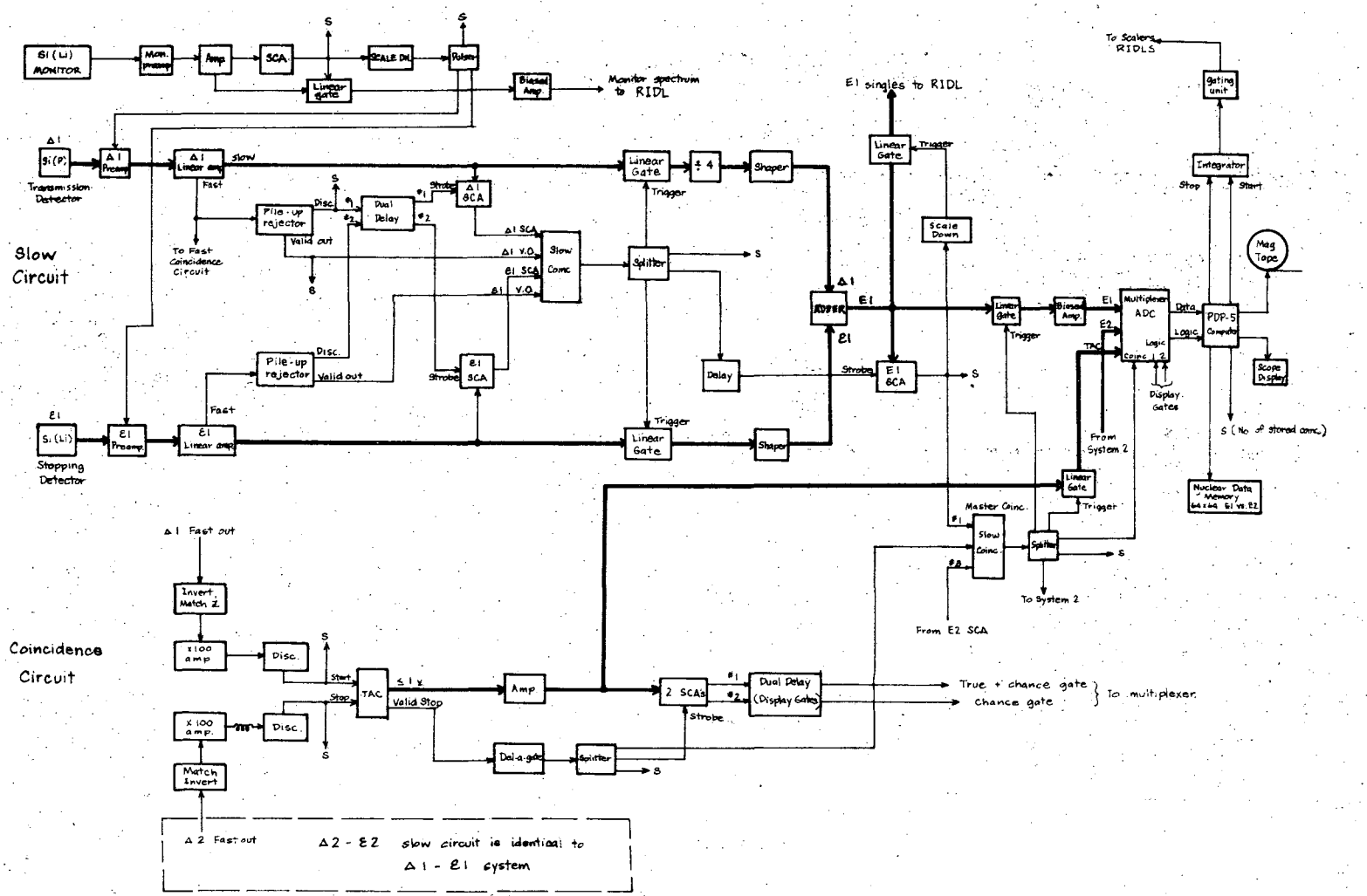

XBL 726-1069

Fig. III-4. Electronics block diagram for coincidence experiment.

a. Slow electronics

Signals from the solid state detectors were fed into charge sensitive preamplifiers which were located in the scattering chamber. The preamps were water cooled to maintain temperature stability. To discriminate against pileup at high count rates, a high rate linear amplifying system was used [Gou 67]. The linear amplifiers were fed by the preamp signals from the scatter chamber. An integrating time of 3 μs was used for the analog output, while a fast linear output was provided by a differentiated signal. The latter signal was used in the fast circuit, as well as strobing the pileup rejector (PUR). The PUR had a 5 μs inspect time, during which period a second pulse following the first was rejected while the first pulse was processed. If two pulses came within a 2 μs period, both were rejected. Treating this 7 μs as a dead time it is seen that each counting system would contribute about 10% dead time at 15,000 cps. (Dead time = $(1 - e^{-R\tau})$ where R equals the count rate and τ the resolving time.)

Each slow counting system was logically independent until the main coincidence. The ΔE-E counting system was run in a discriminating manner; i.e., logic was performed on the ΔE signal to permit only Z = 2 particles to pass the first slow coincidence. This method is possible for two reasons: first, at the energies of interest the energy loss by Z= 1 and Z= 2 particles in a 250 μm ΔE detector differ by at least a factor of two; and second, the $(\alpha, \alpha\ ^3\mathrm{He})$ competing reaction has a much more negative Q-value than the $(\alpha, 2\alpha)$ reaction for all targets studied.

Figure III-5 presents ΔE spectra with different levels of logic in the slow coincidence. (These spectra were taken out of the first linear gate in a slow counting system.) Note that the top system with all coincidences out has events down to zero energy. The large bump in channel 20 was interpreted as low energy protons. A small peak at channel 72 was assumed to be the elastic α-group; pulser calibration indicates this was the correct assignment. The middle spectrum shows dramatic improvement with the inclusion of the PUR in the slow coincidence. The peak-to-background improved from about 4/3 to 4/1. Also the PUR discriminator has eliminated all pulses less than channel 16. The bottom spectrum shows results in the running configuration with both the SCA and PUR in the first slow coincidence. The elastic α scattering peak is apparent in the bottom two figures.

Further logic was accomplished by putting a 3 MeV lower SCA and PUR requirement on the stopping detector. Another lower discriminator of about 20 MeV on the summed (ΔE + E) energy signal was used to eliminate unnecessary count rate. The slow coincidence output from the E_{tot} SCA's provided the input to the main gate from the slow counting systems. The third input was the valid output from the time-to-amplitude converter (TAC) in the fast electronics. If all requirements were met, the main gate sent a logic signal to the coincidence input of the multiplexer - ADC [Rob 68], and the computer was interrupted.

b. Fast electronics

In the ideal coincidence experiment, from the chance problem point of view, there would be one beam particle per electronic resolving time. Then the measurement of two particles in coincidence would be an

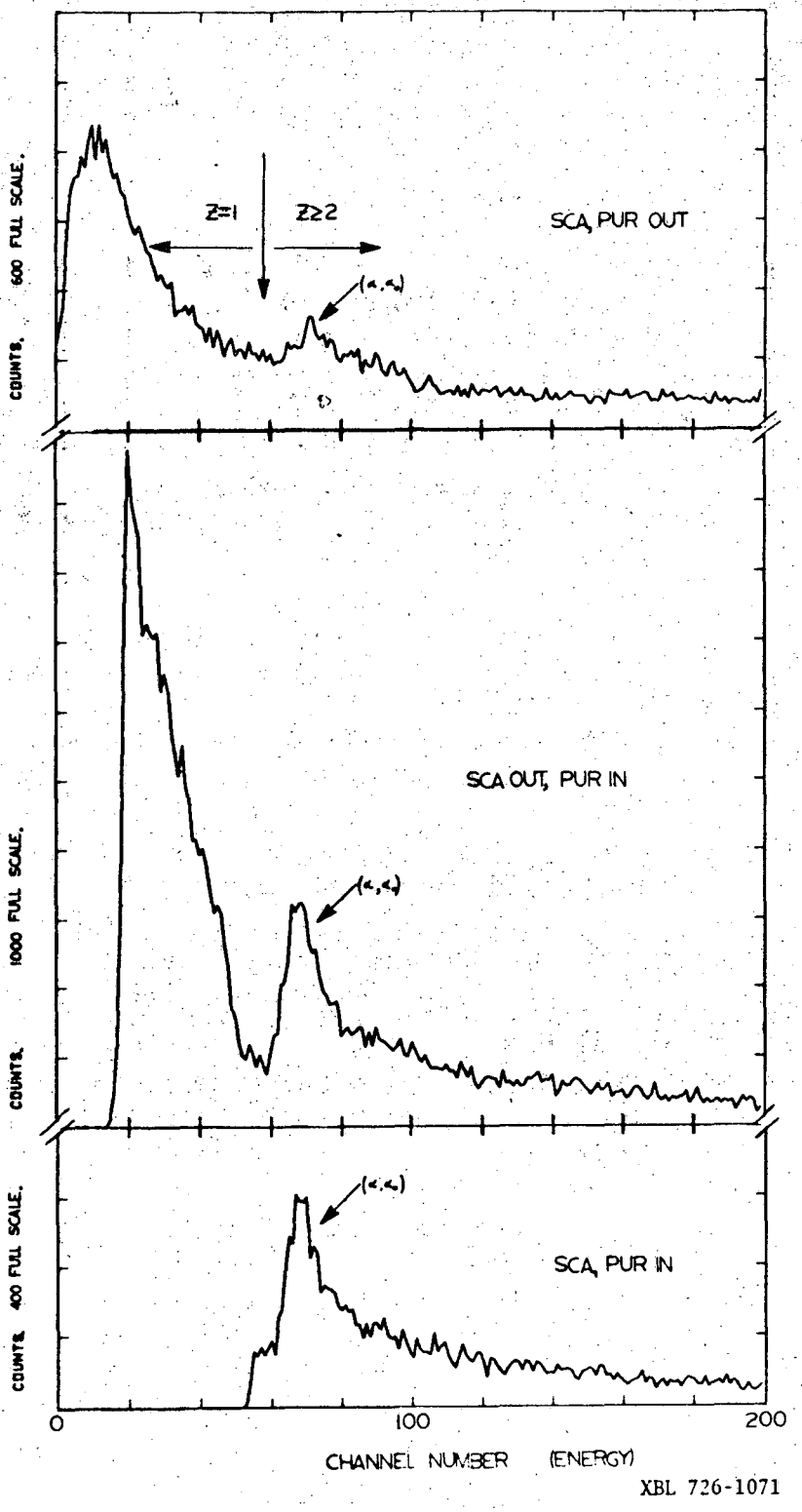

Fig. III-5. Transmission detector spectra with different logic requirements. The top figure has no gate requirements; the middle figure is with the pileup rejector (PUR) gate; and the bottom figure has a PUR and single channel analyzer gate.

unambiguous true event. This experimental situation was impractical; however, it does point out the necessity of maintaining good time resolution. In a cyclotron experiment, the inherent time resolutions of fast electronics permits the ready separation of reaction particles coming from different beam bursts. The 90 MeV α-beam at the 88-in. cyclotron is in resonance at approximately 10.5 MHz: this implies approximately one beam burst/100 ns. The fast plus slow coincidence system gave a time resolution of 8-9 ns, so events from different beam bursts were readily resolved.

One experiment revealed a true + chance time peak that had a sharper peak superimposed on a broader peak, the broad peak being characteristic of the adjacent chance peaks. The chance peaks had a FWHM equal to 7.0 ns; and the true peak FWHM equalled 6.0 ns. The latter was obtained by subtracting a chance peak from the true + chance peak, and then extracting the FWHM. The true peak FWHM should be independent of beam burst width; thus 6 ns reflects electronic and detector contributions to the time resolution. The time of flight difference for the most and least energetic alpha particles was 0.5 ns, so time of flight was not a large factor. Assuming that the only other contributor to chance peak time resolution was the beam pulse duration, and making the further assumption that the widths can be added in quadrature, a beam pulse width of 3.6 ns was derived. Since the velocity of a 90 MeV alpha particle is 0.21c, the beam pulse length was approximately 23 cm.

The bottom section of Fig. III-4 summarizes the fast components. The fast output pulses from the ΔE linear amplifiers were of positive polarity with 125Ω impedance. These signals were inverted and matched

to 50Ω, the input requirements of the EG&G dual updating discriminator. To minimize the fast rise time variations, the signals were fed into a ×100 1 ns rise time DC amplifier. A delay line of approximately 175 ns was used to delay CTR 2 with respect to CTR 1. The discriminator setup is described in the following paragraph. The negative polarity fast discriminator output then fed a TAC, which made a slow signal proportional to the time correlation of the detected particles. If two signals met the timing requirement imposed by the TAC, a valid output was obtained. This signal was the third coincidence input of the main gate.

Experimental beam time required to setup a coincidence experiment with a TAC is minimal. To set the discriminator levels rapidly, a scaled down RF signal was used as a TAC stop signal. In this fashion, no true particle coincidence was actually required, and any scattered particle which met all requirements (except coincidence with another particle) gave a TAC signal. Time resolution as a function of discriminator level or other parameters was thus rapidly acquired. Figure III-6 provides TAC spectra with a 300 ns scan time obtained in run setup. The top TAC spectrum was gated only by the fast valid output; the resolution was 23.8 ns. The bottom spectrum shows the effects of the slow logic requirements as well as the fast (i.e. only $Z = 2$ particles are recorded). The slow requirements eliminated background between the peaks, and improved the resolution by almost a factor of three. These spectra were obtained in one or two minutes running time.

After both counting systems had been individually adjusted, CTR 1 provided the start signal and CTR 2 the TAC stop. Figure III-7

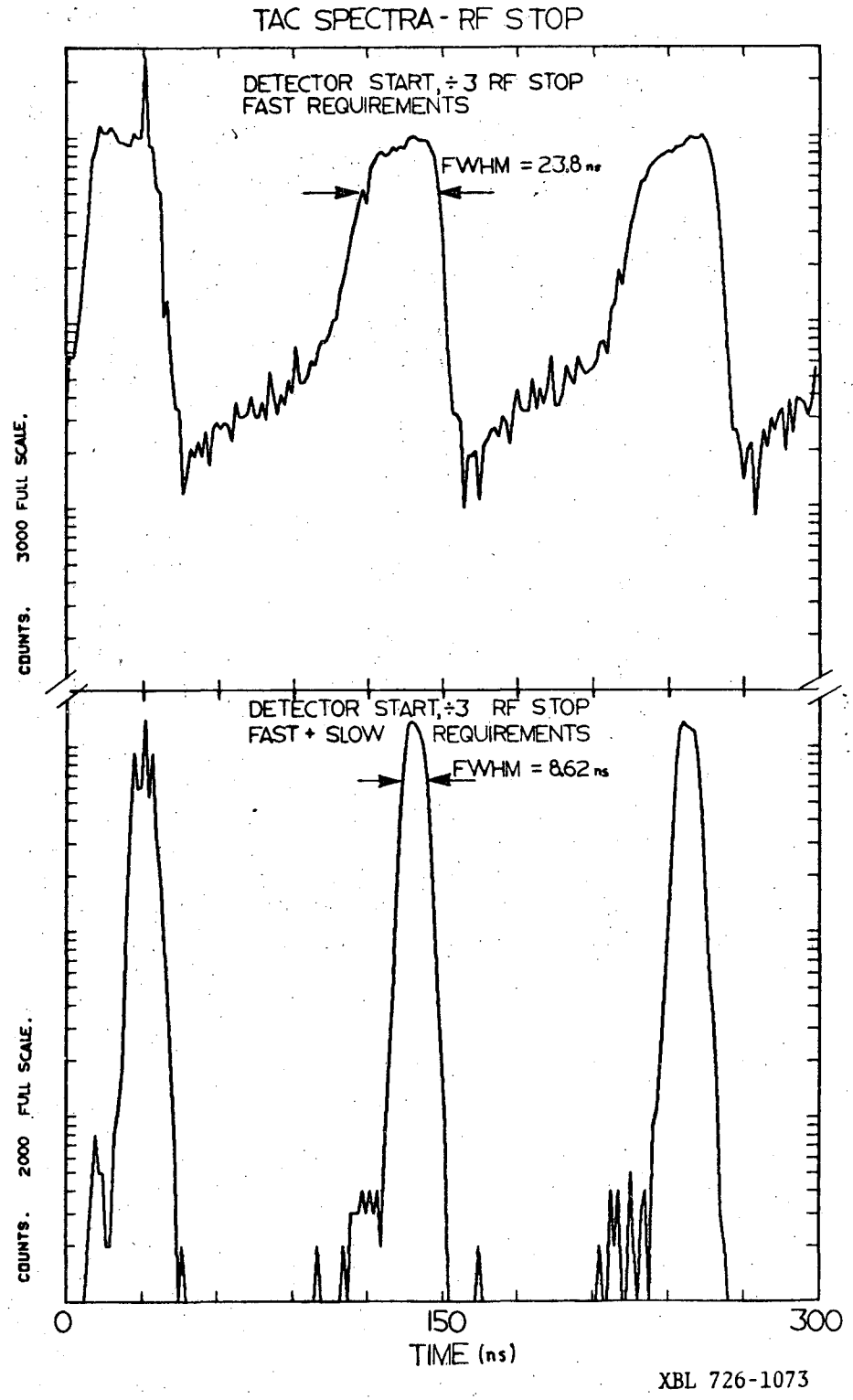

Fig. III-6. TAC spectra with cyclotron RF stop. The top spectrum has only a fast requirement, while the bottom spectrum has fast plus slow logic requirements.

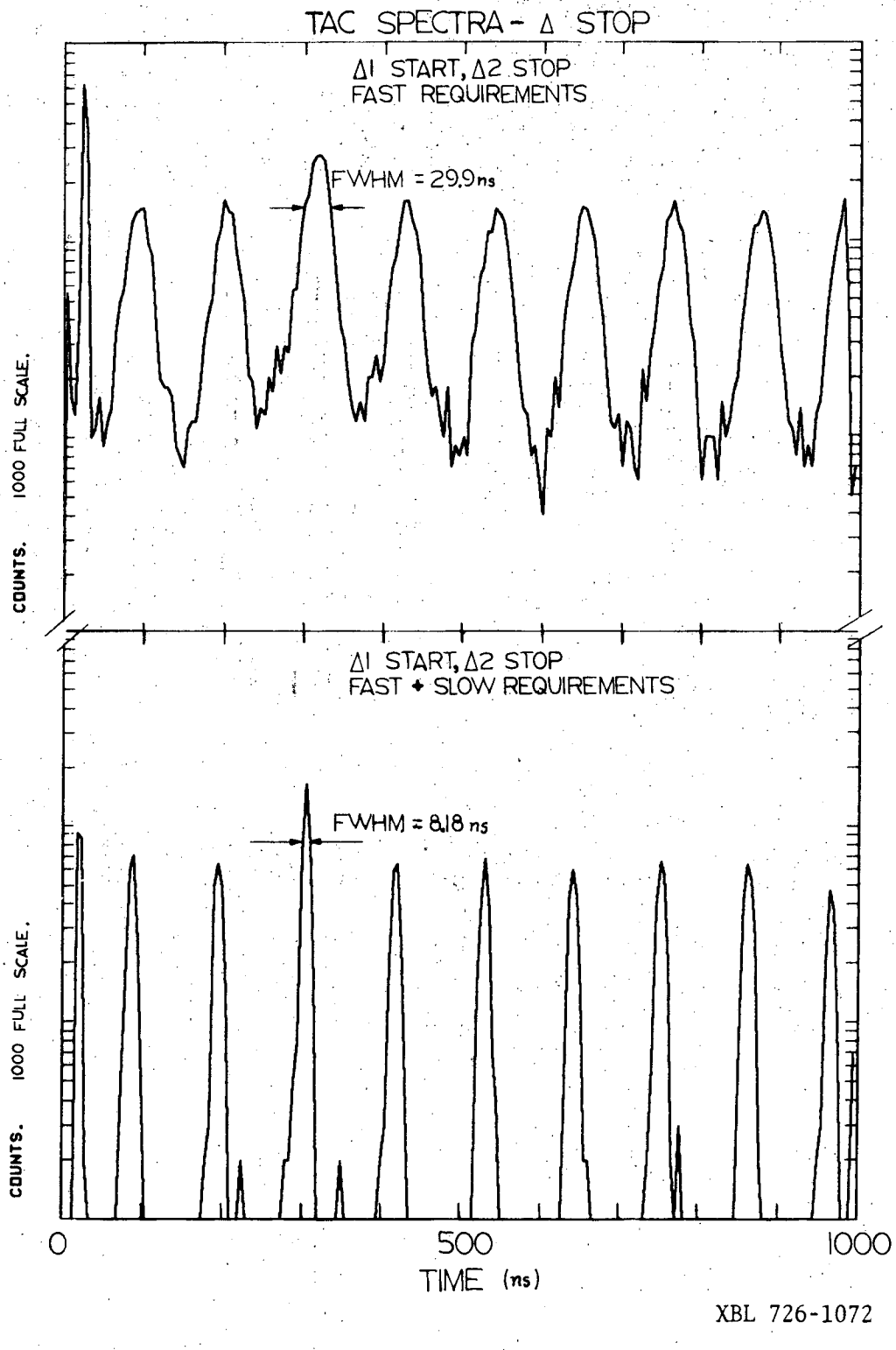

Fig. III-7. TAC spectra with counter one start and counter two stop. The logic requirements are as given in Fig. III-6.

illustrates TAC spectra obtained in this way. The scan time was 1 μs; so nine peaks corresponding to nine beam bursts with different time relations were obtained. Time-to-amplitude spectra with fast and fast + slow requirements are given, as in Fig. III-6. Again it was seen that the slow requirements caused a considerable resolution improvement as well as background reduction. Thirty minutes were required to accumulate the bottom spectrum in Fig. III-7, so the value in time saving by using an RF scaledown pulse as TAC stop signal for setup purposes is apparent.

3. On-line computer

Figure III-4 shows three pieces of analog data and three pieces of logic data input to the multiplexer - ADC. The analog data were the two energy signals of the scattered particles and the third was the TAC signal. These data were digitized and eventually written on magnetic tape. One logic signal was the main coincidence output. The remaining two logic signals were SCA outputs set on the true + chance and chance peak in the TAC spectrum. These latter signals were for display logic only, and did not affect or enter into the storing process of the three parameter data.

The computer outputs information to four devices. First a background display subprogram continually (except when interrupted) monitored the development of five spectra which were stored in display buffer areas. Second, the computer dumped the data buffer to magnetic tape when this buffer was full. Third, the number of coincident events stored was sent to a scaler and the beam integrator was gated by the computer. Fourth, a 64×64 energy array gated by the true + chance

peak was sent to the memory of a 4096 channel device. This last monitor was extremely useful for monitoring the progress of the experiment, as well as giving an approximate idea of the statistics in a kinematic band.

A flow diagram [Dec 68] of the PDP-5 on line program is given in Fig. III-8. The heavy arrows indicate the direction of digitized information flow. The parenthetical numbers given in this path provide the number of PDP-5 instructions contained in the given subroutine. The total number is 159, and if the average cycle time of a PDP-5 instruction was assumed to be 12 μs, the computer took about 1.9 ms to digest one event. This rather long dead time was not a problem because the number of main gates was usually 5 or 10 $(sec)^{-1}$. For only the light target nuclei did the computer dead time become greater than 1%.

Several facts made the use of an on-line computer essential or at least highly desirable. Approximately 200-300 keV energy resolution was obtainable, and it was necessary to store information from 20 MeV to 90 MeV singles energy; thus, for one detector at least a 1000 channel memory would be required. Since there are two counters and it was of primary interest to maintain a knowledge of correlations in the coincident events, a minimum storage space of 1000×1000 or 10^6 memory locations was required. This far exceeds the largest available analyzers. Because the data was stored event-by-event, information concerning the actual time of data taking was obtained. This was useful since the data tape can be corrected or edited for gain shifts or other experimental problems after completion of the experiment. Other reasons included the flexibility of storing true + chance and chance information simultaneously, and also tagging the energy information with other logic.

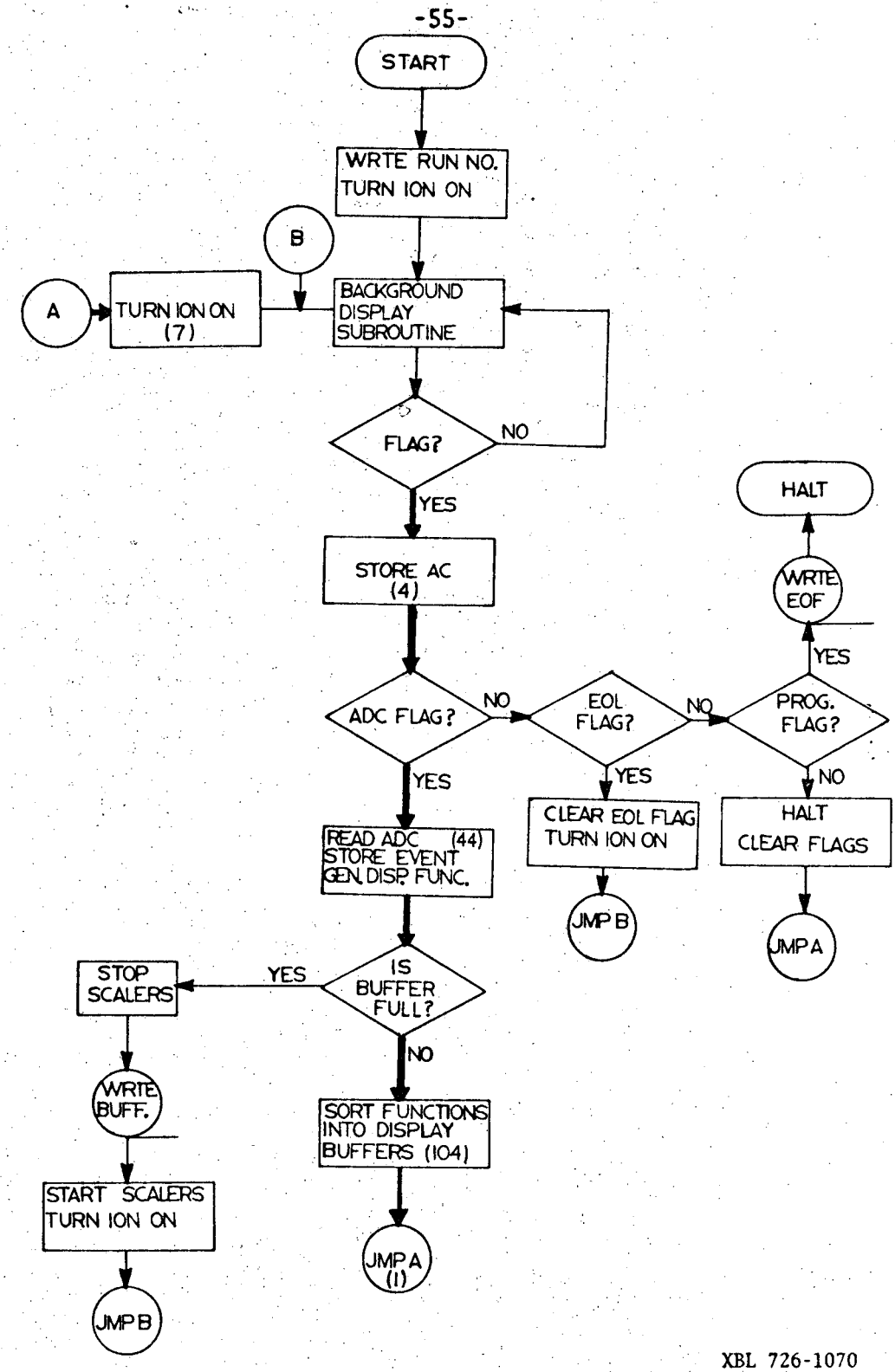

Fig. III-8. Flow diagram for on-line PDP-5 computer program.

C. Targets

A summary of targets is given in Table III-2. Most of the targets were prepared by evaporation of isotopic material using an electron gun. The exceptions were ^{12}C which was prepared from a suspension of ^{12}C in an organic solution, and the ^{16}O target which was obtained by passing oxygen slowly over a thin Ni foil placed in a muffle furnace at a temperature of 700°-800°C. All targets except ^{30}Si were circular, 3/4 in. diameter; ^{30}Si was oval shaped approximately $\frac{1}{2}$" by 3/4". They were mounted on aluminum frames machined to fit the 36" scattering chamber target ladder.

It was necessary to determine target thicknesses accurately since absolute experimental cross section directly reflected this error. Whenever possible two techniques were utilized to find the target thickness. First, the energy loss of 8.78 MeV α's in the target material was measured; and second, 1 cm^2 of target material was weighed on a micro-gram balance. The two techniques did yield consistent results, and the target thickness errors listed in Table III-2 were estimated on the results of the two techniques. The Ca targets were handled in an Ar atmosphere, and they appeared metallic after bombardment. Pressures in the 36 in. scatter chamber were 10^{-5} - 10^{-6} Torr. Table III-2 lists the targets, their isotopic purity, the methods of determining target thicknesses, and finally the derived target thickness. If two techniques were not used in a determination, an error of 15% in the one value was assigned. This seemed reasonable based on the experience gained in measuring other targets by dual techniques.

Table III-2. Summary of target information for $(\alpha, 2\alpha)$ experiments.

Date	Target	Isotopic Purity	Method	Thickness (mg/cm^2)
4/72	NiO	Natural	1. Complete oxidation of Ni foil 2. Weight of $1 cm^2$	0.172±0.014
4/72	^{44}Ca	98.5%	1. Weight of $1 cm^2$ 2. Energy loss	0.420±0.020
4/72	^{28}Si	Natural	1. Weight of $1 cm^2$ 2. Energy loss	0.692±0.020
4/72	^{24}Mg	> 99% ^{24}Mg	1. Weight of $1 cm^2$ 2. Energy loss	1.075±0.040
4/72	^{26}Mg	> 99% ^{26}Mg	1. Weight of $1 cm^2$ 2. Energy loss	0.435±0.020
8/72	^{12}C	Natural	1. Weight of $1 cm^2$ 2. Energy loss	0.379±0.010
8/72	^{66}Zn	^{66}Zn - 97.8% ^{64}Zn - 1.2%	1. Weight of $1 cm^2$ 2. Energy loss	0.586±0.060
8/72	^{40}Ca	Natural	1. Weight of $1 cm^2$	0.457±0.090
8/72	NiO	Natural	1. Weight of $1 cm^2$	0.255±0.050
8/72	^{30}Si	^{30}Si - 89% ^{28}Si - 10% ^{29}Si - 1%	1. Weight of $1 cm^2$	0.076±0.015
1/73	^{12}C	Natural	1. Weight of $1 cm^2$	0.415±0.062
1/73	NiO	Natural	1. Weight of $1 cm^2$	0.242±0.036

D. Factors Affecting Energy and Recoil Momentum Resolution

1. Energy resolution

Energy resolution factors in a complete three body experiment are similar to the two body case, with a few exceptions. The most striking difference is that $d(T_3 + T_4)/d\theta$ derived from the three-body kinematics is smaller than the $dT/d\theta$ in the two body case. If this were not true, it would be very difficult to do a good resolution three body experiment. The three body $d(T_3 + T_4)/d\theta$ is a strong function of target mass and scattering angle, and in the case of the quasi-elastic angle (no recoil energy) $d(T_3 + T_4)/d\theta = 0$ for point detectors. A plot of summed kinetic energies vs. θ is given in Fig. III-9. The quantity $d(T_3 + T_4)/d\theta$ is derived from such a plot. Angles typically studied are indicated; the vertical lines show the range of scattering angle due to finite angular detector acceptances.

A rather large loss of $(\alpha, 2\alpha)$ energy resolution at $E_\alpha = 90$ MeV can come from the target if its thickness is not optimized. If an $(\alpha, 2\alpha)$ event occurred on the target's back edge, the energy loss is that characterized by a single 90 MeV α particle passing through the target. This energy loss is given by

$$\Delta E_1 = t\left(\frac{dE}{dx}\right)_{90\ \text{MeV}} \qquad \text{(III-3)}$$

However, if the reaction occurred on the front face, the energy loss is characterized by two alphas having $E_\alpha \approx 40$ MeV. In addition, the 40 MeV particles penetrate more target material since the scattering angle was always unequal to zero. In this case

$$\Delta E_2 = 2\left(\frac{t}{\cos\theta}\right)\left(\frac{dE}{dx}\right)_{40\ \text{MeV}}. \qquad \text{(III-4)}$$

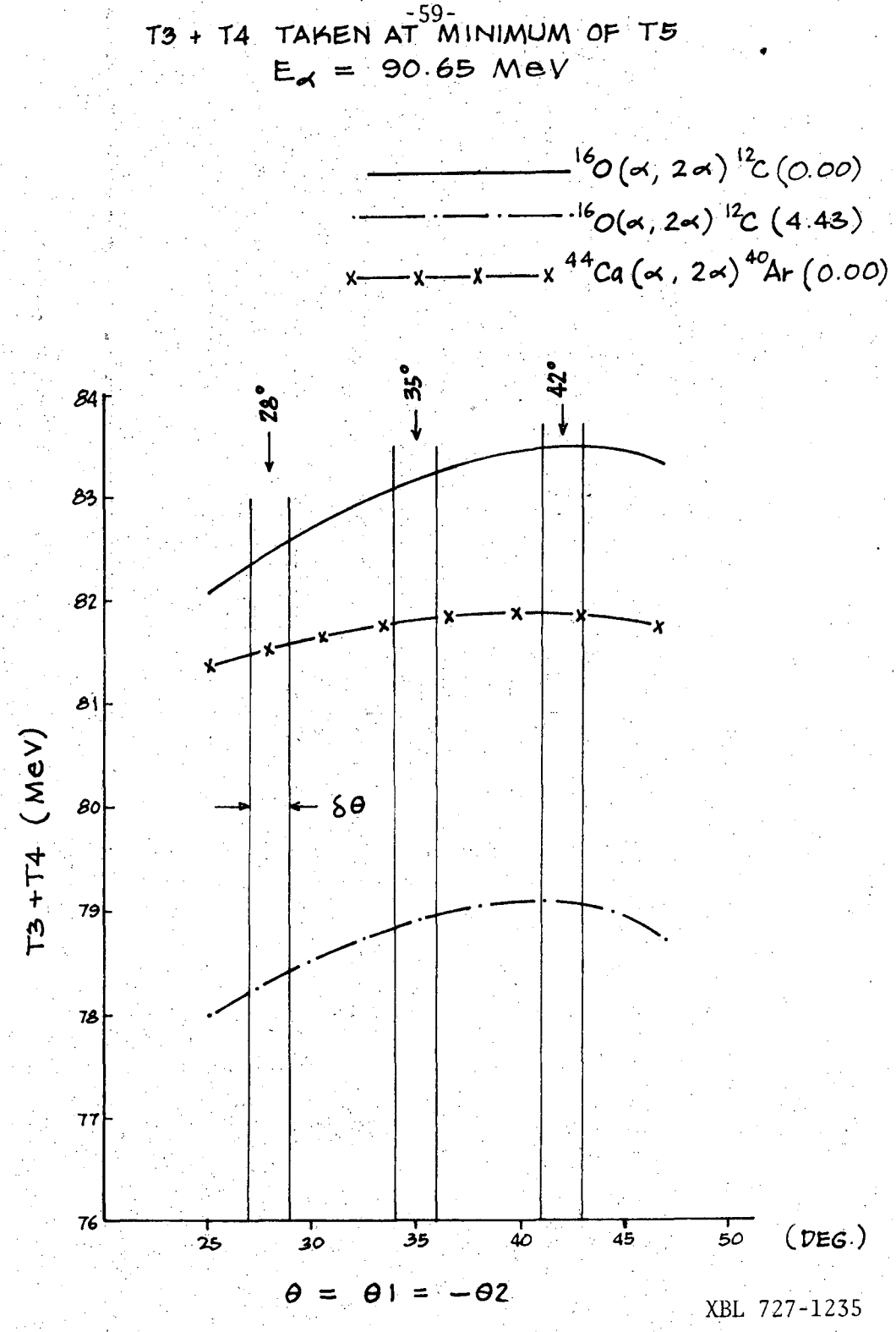

Fig. III-9. Kinematic plot of summed energy versus correlation angle.

The possible energy difference at these extremes is then,

$$\Delta E = \Delta E_2 - \Delta E_1 = t \left[\frac{2}{\cos\theta} \left(\frac{dE}{dx}\right)_{40\ MeV} - \left(\frac{dE}{dx}\right)_{90\ MeV} \right] \quad \text{(III-5)}$$

and contributes to the energy resolution. Figure III-10 summarizes this situation. For lighter targets a thickness of 500 $\mu gm/cm^2$ seemed prudent. For heavier targets the thicknesses could be increased in proportion to A_t/Z_t without changing the energy loss.

Figure III-11 provides a summary of factors contributing to the energy resolution for the symmetric $^{26}Mg(\alpha, 2\alpha)$ case. The finite geometry curve is the kinematical contribution to energy resolution arising from the finite acceptances. These are treated in detail in the next section. This contribution was a strong function of angle, and is seen to have a non-zero minimum at the quasi-elastic angle (41°). It would be zero at this angle for point apertures. The contribution from target thickness increases with angle. The remaining contributions were not functions of angle and were familiar from two body experiments. The straggling contribution was dominated by the Al e^- suppressors, which were 1.5 mg/cm^2 thick.

The total predicted energy resolution was obtained by adding the components in quadrature, and is given by a solid line in Fig. III-11. The experimental results leading to the ^{22}Ne (g. s.) are given as squares in the figure. The prediction qualitatively fits the experimental shape, although there is a disagreement of approximately 20 keV in the normalization, and the 41° point is unexpectedly high. This may be due to comparatively poor statistics in the 41° data. The normalization problem may be due to the folding procedure, an underestimate of effects outlined in Fig. III-11, or the neglect of non-coplanar factors.

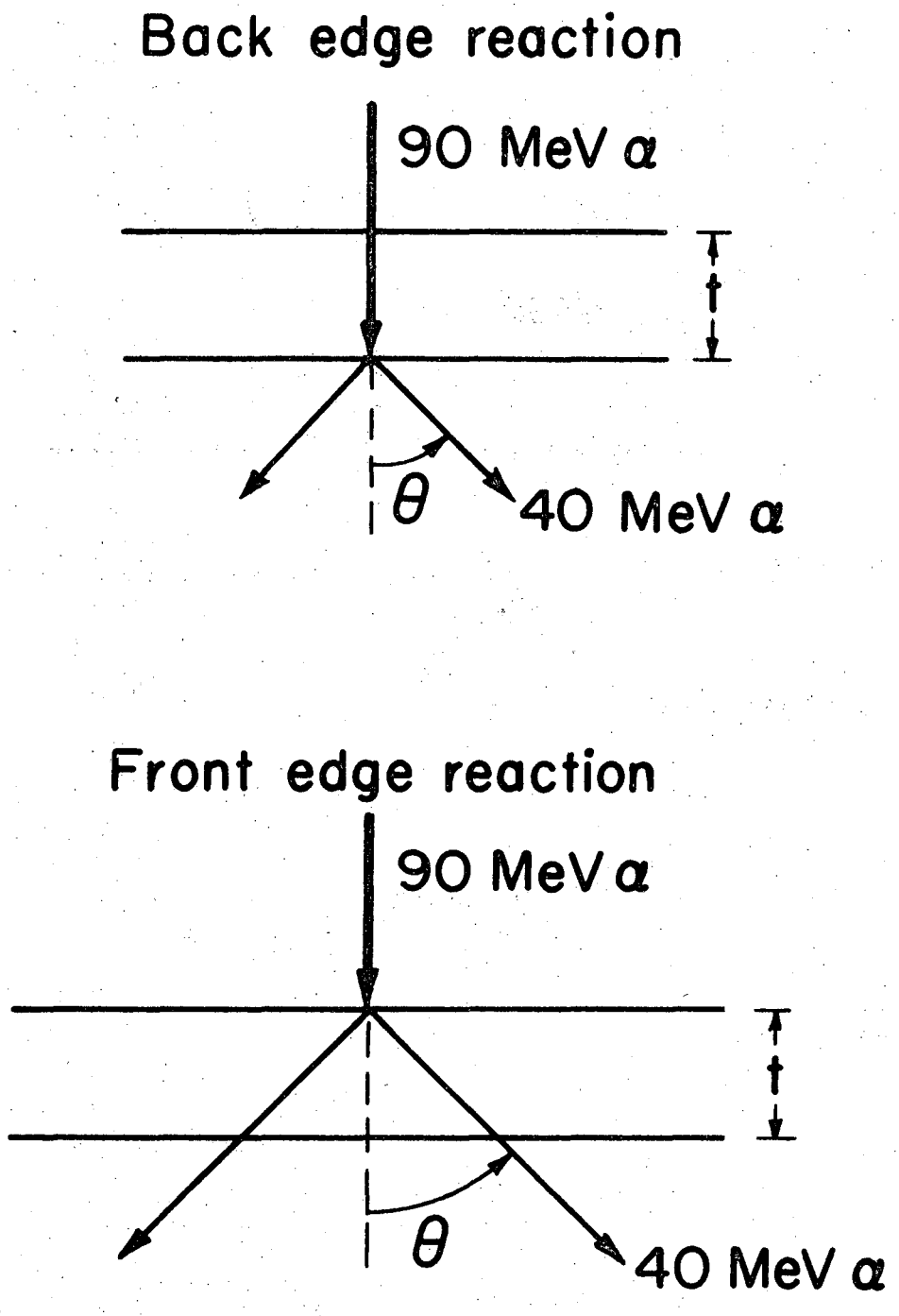

Fig. III-10. Target resolution effects in the $(\alpha, 2\alpha)$ reaction.

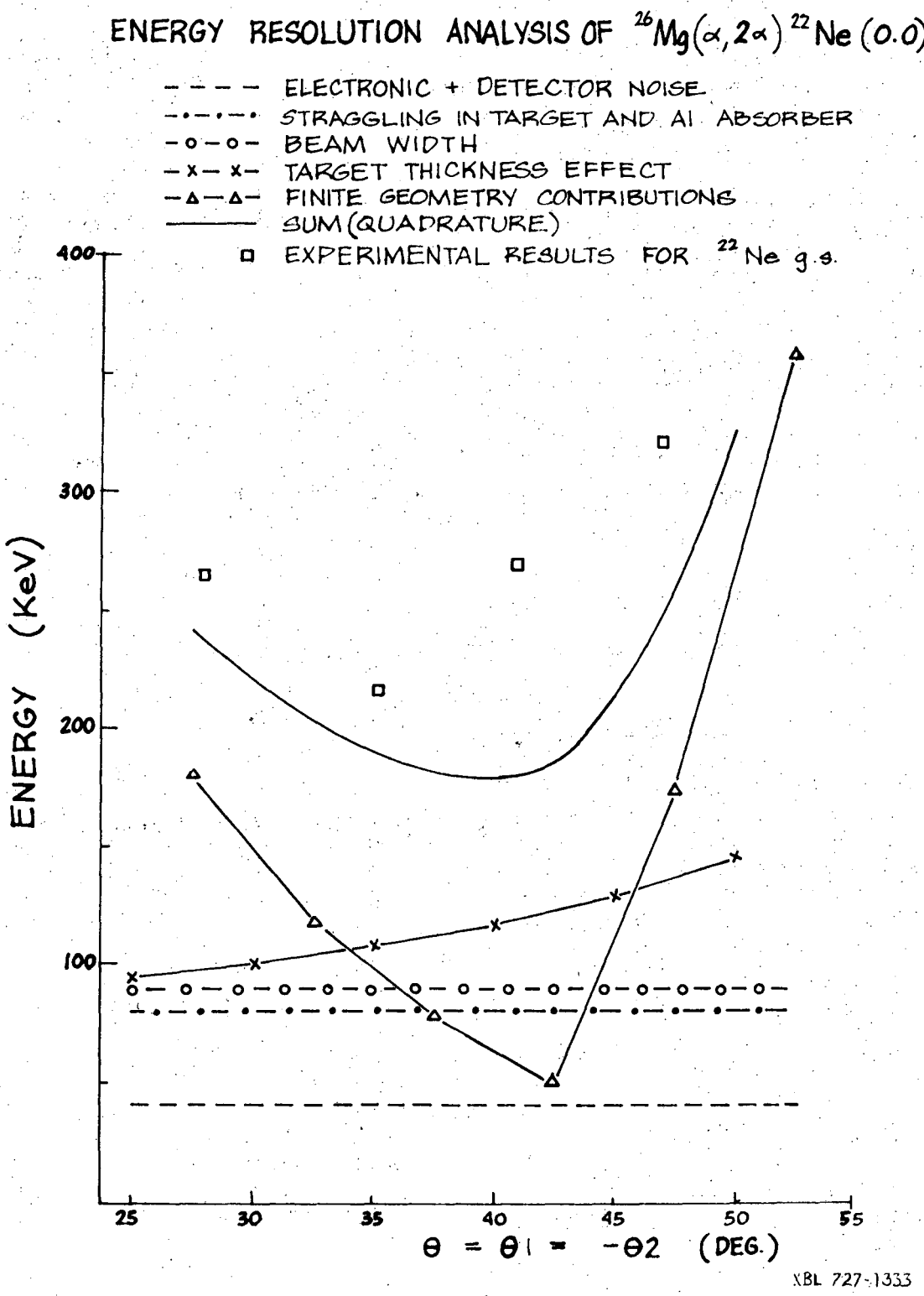

Fig. III-11. Analysis of energy resolution in the $^{26}Mg(\alpha, 2\alpha)^{22}Ne(0.0)$ reaction.

2. Recoil Momentum Resolution

The large angular uncertainties resulted in the acceptance of a recoil momentum range at a given angular setting. It has been pointed out that [Gott 70] these uncertainties also cause a shift away from the nominal recoil momentum, particularly near the quasi-elastic angle. Table III-3 summarizes the angular uncertainty origins. These three contributions were folded by use of the convolution integral [Moss 66]:

$$\rho(t) = \int_{-\infty}^{+\infty} \theta(x)\, X\,(t-x)\, dx \qquad \text{(III-6)}$$

The resultant peak is approximately Gaussian in shape and has a FWHM of 2.80°. Given this angular uncertainty, the error in the recoil momentum may be obtained from three body kinematics by solving the kinematic equations for q (recoil momentum) at the limits of the angular acceptances.

Figure III-12 gives the results of the angular convolution. The t-axis is proportional to angle uncertainty, and the distributions X(t-x) correspond to the 2.0° uncertainties. The function $\theta(x)$ is the 0.5° error due to beam convergence. The $\rho(t)$ is the intermediate convolution of $\theta(x)$ and X(t-x), while f(t) is the final result. All functions have been normalized to unity. It is worthwhile to do this careful analysis in order to derive the error due to finite geometries in the variable q. This is necessary since the triple differential cross section is often plotted versus this variable (momentum correlation), and also this analysis permits the averaging of theoretically derived quantities over the radial angular acceptances. These procedures are followed in the $(\alpha, 2\alpha)$ data analysis.

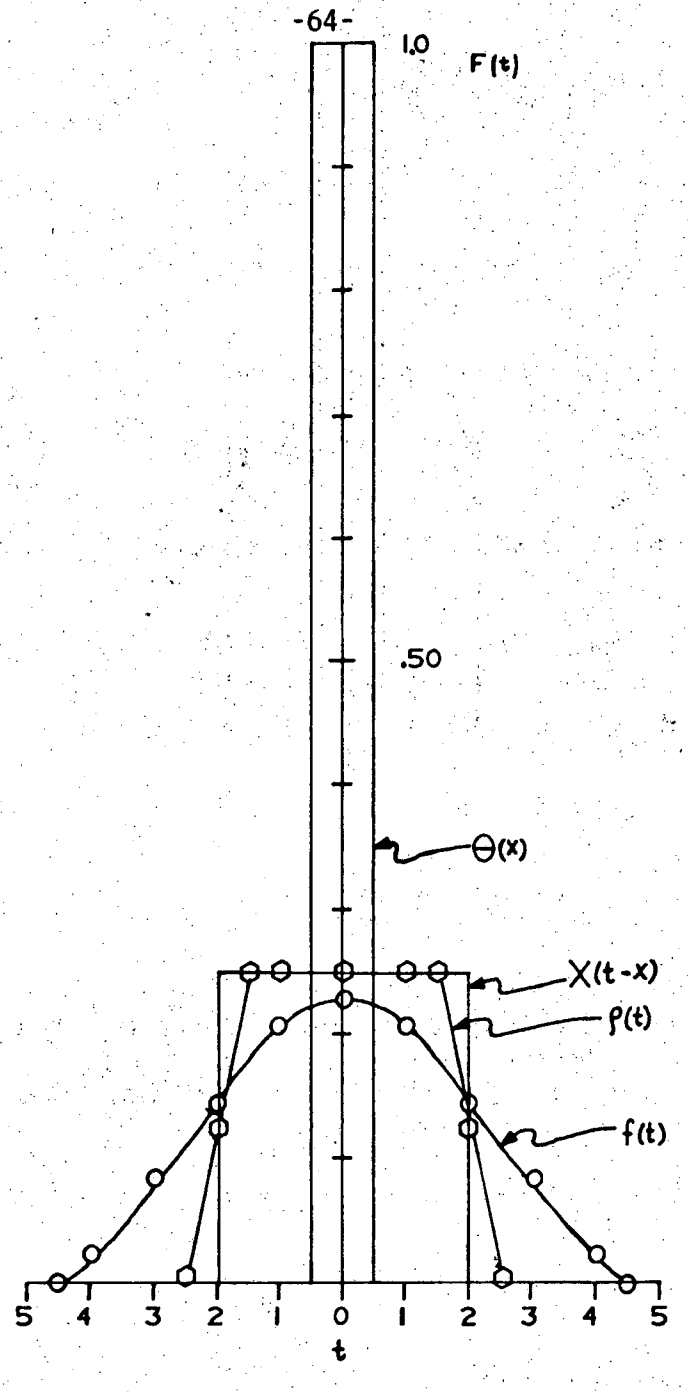

Fig. III-12. Folding procedure for determining total radial angular uncertainty in the $(\alpha, 2\alpha)$ experiment.

Table III-3. Origins of radial angular uncertainties.

Origin	Angular Uncertainty	Distribution
Detector angular acceptance	2.0	Rectangular
Finite beam spot	2.0	Rectangular
Beam convergence at target	0.5	Rectangular

The finite detector size also introduces non-coplanar effects in recoil momentum resolution. Nuclear structure information is obtainable from the non-coplanar (p, 2p) reaction [Jac 67a], and these ideas have been extended to examination of non-coplanar effects in coplanar quasi-elastic scattering [Elt 67]. The most significant non-coplanar influence occurred near $q = 0$ for $L \neq 0$ transitions in the angular correlations. The PWIA predicts a strong minimum in such a case, and experiments have always shown a less pronounced minimum. Inclusion of distortion effects tends to fill in the minimum, and Elton and Jackson [Elt 67] have shown that non-coplanar effects in DWIA calculations also raise the minimum towards experimental agreement. Non-coplanar effects have not been included in the $(\alpha, 2\alpha)$ theoretical calculations since these were done only for $L = 0$ transfers. The $L = 2$ $(\alpha, 2\alpha)$ data have shown very little indication of minima at $q = 0.00$ in the angular correlation, and this suggests that distortions and/or non-coplanar effects were dominant. Much more experimental investigation in coplanar and non-coplanar configurations is needed to unravel these problems.

E. Data and Error Analysis

1. Singles data

The acquisition of singles data allowed energy calibration as well as providing a check on the chance background observed in the true + chance coincidence array. Figure III-13 shows $^{12}C(\alpha, \alpha')$ spectra taken in one experiment. Calibration of these spectra based on the known ^{12}C states establishes the T_3 scale in the $T_3 + T_4$ vs. T_3 coincidence plot. Several targets were used in acquiring singles data, thus leading to a better determination in the T_3 calibration. The singles data

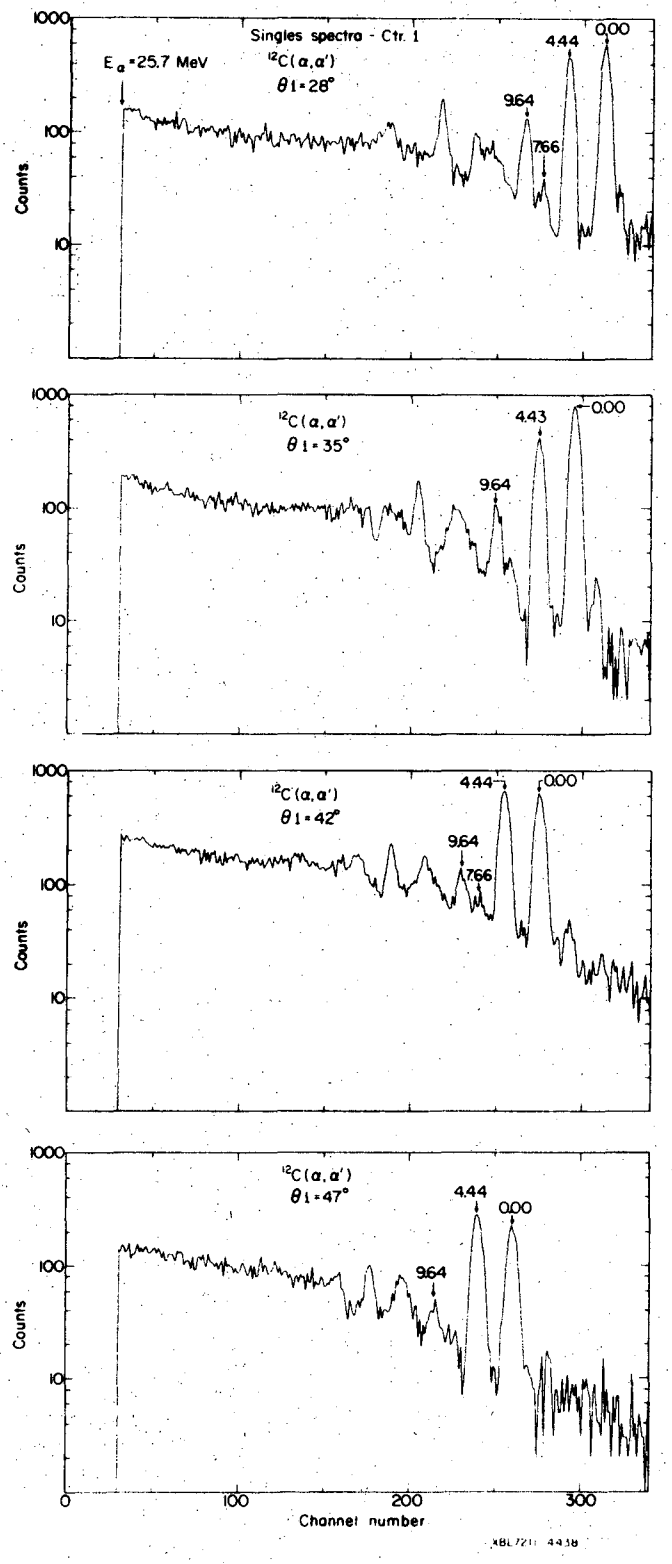

Fig. III-13. Singles spectra obtained from the ^{12}C target.

indicated that the lower energy cut off error in T_3 was approximately ± 1.50 MeV. This interpretation was consistent with pulser calibrations as well as with extrapolations in the $T_3 + T_4$ spectra. The T_3 calibration is found in Appendixes IV and V, where the coincidence data are summarized.

2. Coincidence data analysis

Every stored event was characterized by three parameters: two energy signals (T_3 and T_4) and the TAC signal. This information was written in binary mode by the PDP-5 on IBM magnetic tape. After completion of the experiment, these tapes were analyzed on a CDC 6600 computer. The first level of analysis was to use the program TAC, which reconstructs TAC spectra from the data tapes. Plots and print-out of these spectra enabled extraction of logical gates which characterized the true + chance and chance peaks. This information was then supplied to the program TWODI, which then scanned the data tapes, storing those energy events which satisfied the TAC logic in appropriate buffer areas. The analysis program was flexible in that only the kinematic regions which were appropriate for the reaction Q-values were printed and plotted. This truncation was appropriate because only a small part of the complete untruncated energy array (2048 × 2048) contains the true coincidence data.

Figures II-2 and III-14 give examples of two dimensional energy arrays. TWODI forms the sum $T_3 + T_4$ and plots this vs. T_3 so the data appears as kinematic bands, similar to the bottom of Fig. II-2, in the computer print out. The curvature of the kinematic lines was due to the recoil energy. This feature is seen in the $^{44}Ca(\alpha, 2\alpha)^{40}Ar$ Dalitz

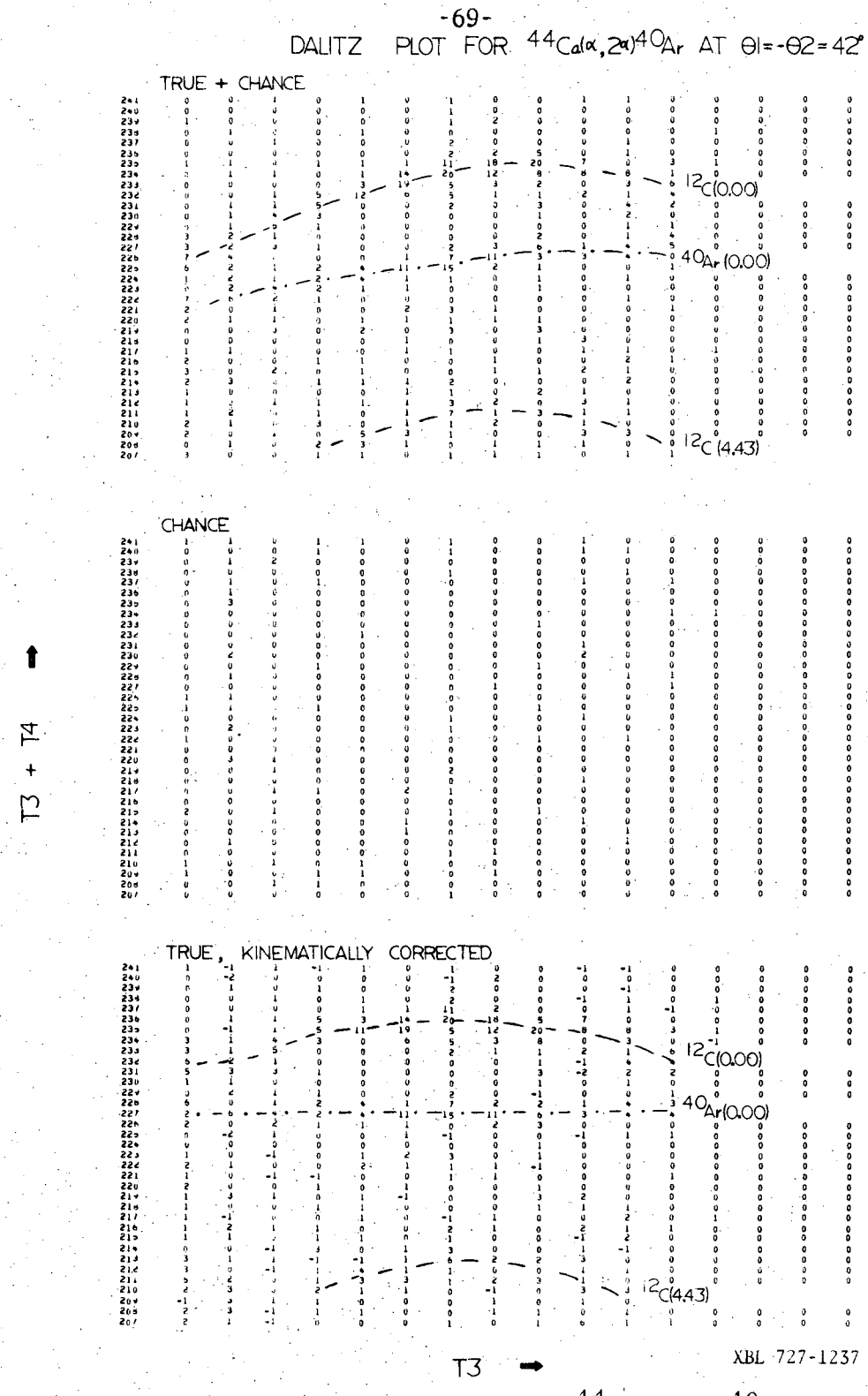

Fig. III-14. Dalitz plot for the $^{44}Ca(\alpha, 2\alpha)^{40}Ar$ reaction.

plot [Will 71] given in Fig. III-14. The dashed lines intend to guide the eye through the channels containing the maximum counts corresponding to the ^{40}Ar(g. s.), and the reactions on the ^{16}O impurities leading to the ^{12}C(0.0) and ^{12}C(4.44) states. The top part of the figure is the data gated by the true + chance peak, and the middle print out is the same kinematic region but it was gated by a chance TAC peak. Finally the bottom portion is the true array which corresponded to the true + chance array corrected for the chance array and for the kinematic bend due to the recoiling nucleus.

A further function of TWODI was to form $T_3 + T_4$ projections. Figures II-2, III-14, and III-15 indicate that a kinematic correction was necessary to realize the best resolution in a $T_3 + T_4$ projection. An example of the improvement is given in Fig. III-15. The top figure is the projection without kinematic correction, and the bottom figure is the same spectrum with the correction. The correction yielded a factor of two improvement in resolution for the ^{40}Ar(0.0) case, and was optimized for the ^{44}Ca($\alpha, 2\alpha$) reaction. Hence, a similar improvement was not obtained for the ^{16}O($\alpha, 2\alpha$) impurity reaction. A primary purpose for making this corrected projection was to identify weakly excited states; an example is provided by the 5.75 MeV level in ^{40}Ar.

3. Energy calibration of projected spectra

The $T_3 + T_4$ projections previously described provided the means for extracting excitation energies in the residual nuclei. The calibration was done internally, since the ground and first excited states in the residual nuclei were unambiguous. Also, ^{16}O and ^{12}C contaminants usually contributed peaks for energy calibration. The method was to

T3 + T4 PROJECTIONS

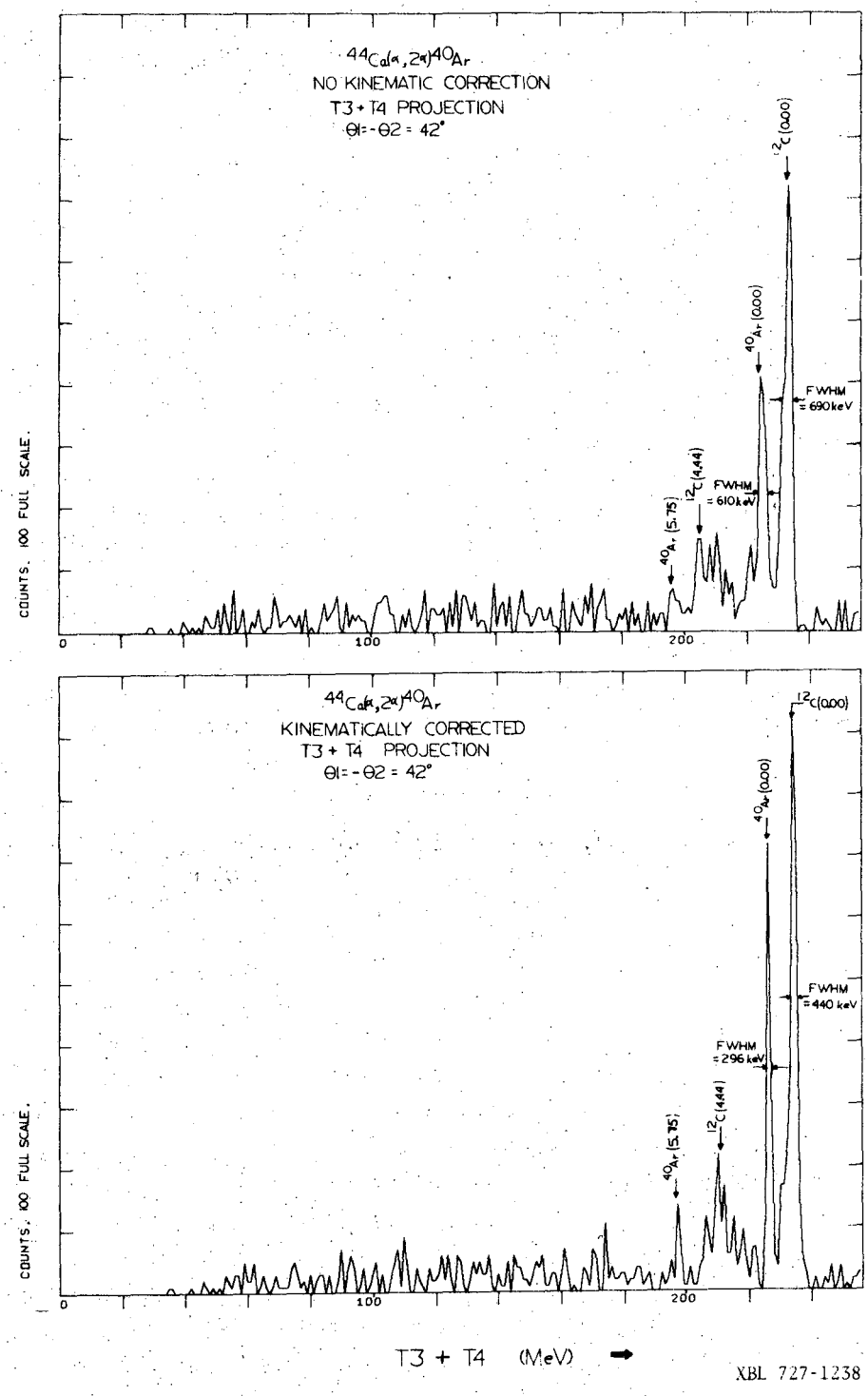

Fig. III-15. Example of kinematically corrected $T_3 + T_4$ projection.

make the kinematic correction previously described at the point $T_3 = T_4$, and then project onto the $T_3 + T_4$ axis. Then centroids were extracted from these data, and used in a linear least squares fitting program (MADAM) which established an energy calibration for the $T_3 + T_4$ axis. The program also returned excitation energies when the channel number of an unknown peak was read into the program. The "reverse" kinematics for this case is given in Appendix I.C. With few exceptions the fitting was done over a small excitation region, and in no case could evidence for non-linearities be found. Known levels populated in the $(\alpha, 2\alpha)$ reaction were usually extracted with an error of $\pm$ 50 keV or less, although a larger error was usually assigned for the weak excited states.

4. Extraction of triple differential cross section

The most detailed experimental information obtained from these experiments was the triple differential cross section. This cross section is unique to kinematically complete three body reactions, and provides stringent tests for nuclear theory. The triple differential cross section ($d^3\sigma/d\Omega_1 d\Omega_2 dT_3$ or $\sigma^3(\theta)$) in units of [mb/(sr)^2-MeV)] was extracted from the data by the formula

$$\frac{d^3\sigma}{d\Omega_1 d\Omega_2 dT_3} = \frac{0.265 * N_{CTS} * A * Z * \cos(\theta)}{T * C * \Delta\Omega_1 * \Delta\Omega_2 * \Delta T_3} \qquad \text{(III-7)}$$

where

N_{CTS} = no. of counts within the bin width ΔT_3

A = molecular weight of target

Z = beam charge

θ = angle between target perpendicular and beam direction

T = target thickness (mg/cm^2)

C = integrated beam current (μC)

$\Delta\Omega_1$ = CTR 1 solid angle (msr)

$\Delta\Omega_2$ = CTR 2 solid angle (msr)

ΔT_3 = T_3 step size (MeV)

The ΔT_3 bin size was typically 3 MeV. Due to large solid angles the $\sigma^3(\theta)$ are experimentally integrated over a non-infinitesmal volume of phase space. This effect was discussed in the literature [Gott 70], and the approach adopted here was to average theory over the same experimentally integrated region, since it is difficult to correct III-7 for finite solid angle effects.

5. Chance analysis and true-to-chance ratio

a. Chance analysis

This section summarizes chance evaluation for the case of random coincidence using a cyclotron beam. The discussion is similar to earlier work [Moss 69].

The correction for chance events in the true + chance array was not necessarily a straightforward subtraction procedure, i.e. true = true + chance - chance. This procedure is only valid if the number of particles in each beam burst remains constant. To see this, consider the following definitions and developments:

τ_c = period of pulsed beam

C = average singles counting rate

C_i = count rate from $i^{\underline{th}}$ beam pulse

C_{ii} = chance coincidence count rate from prompt beam burst

C_{cii} = averaged chance coincidence rate arising from prompt beam burst

N = total number of counts

N_i = singles counts from $i^{\underline{th}}$ beam burst

N_{ii} = number of chance events in prompt beam burst

N_{cii} = averaged number of chance coincidence counts from the $i^{\underline{th}}$ burst

C_{cij} = averaged chance coincidence rate arising from delayed beam bursts

T = length of experiment in seconds

The average singles count rate is

$$C = \frac{1}{T} \sum_{i=1}^{T/\tau_c} N_i = \frac{N}{T} \qquad \text{(III-8)}$$

The total number of counts N, and total charge Q, are related to an average number of counts $\bar{N}$ and average charge $\bar{Q}$:

$$N = \frac{\bar{N}T}{\tau_c} \quad \text{and} \quad Q = \frac{\bar{Q}T}{\tau_c} \qquad \text{(III-9)}$$

Further, the singles counts in the $i^{\underline{th}}$ beam burst for detector 1 is:

$$(N_i)_1 = \frac{N_1 Q_i}{Q} = \frac{\bar{N}_1}{\bar{Q}} Q_i \qquad \text{(III-10)}$$

which has the corresponding count rate

$$(C_i)_1 = (N_i)_1/\tau_c \qquad \text{(III-11)}$$

Also, the chance coincidence count rate coming from a prompt beam burst is

$$C_{ii} = \tau_c (C_i)_1 (C_i)_2 = \frac{(N_i)_1 (N_i)_2}{\tau_c} \qquad \text{(III-12)}$$

where $2\tau_R$ (twice the resolving time) is taken to be the cyclotron period τ_c. This substitution is valid in the present case since $2\tau_R \approx 16$ ns while $\tau_c \approx 100$ ns. The number of chance events in a prompt beam burst is

$$N_{ii} = \tau_c C_{ii} = \tau_c^2 (N_i)_1 (N_i)_2 / \tau_c^2 \qquad \text{(III-13)}$$

and the total number of chances N_c is

$$N_c = \frac{N_{ii} T}{\tau_c} = \frac{T}{\tau_c} \sum_{i=1}^{T/\tau_c} (N_i)_1 (N_i)_2 \qquad \text{(III-14)}$$

Using Eq. (III-10) in (III-14) the number of chance counts from the $i^{\underline{th}}$ beam burst is

$$N_{cii} = \frac{T}{\tau_c} \bar{N}_1 \bar{N}_2 \sum_{i=1}^{T/\tau_c} \frac{Q_i^2}{(\bar{Q})^2} \qquad \text{(III-15)}$$

and substituting for $\bar{N}_1$ and $\bar{N}_2$ from (III-9) into (III-15):

$$N_{cii} = \frac{\tau_c}{T} N_1 N_2 \sum_{i=1}^{T/\tau_c} Q_i^2/(\bar{Q})^2 \qquad \text{(III-16)}$$

Equation (III-16) can be put in terms of count rate from (III-8):

$$C_{cii} = \tau_c C_1 C_2 \sum_{i=1}^{T/\tau_c} Q_i^2/(\bar{Q})^2 \qquad \text{(III-17)}$$

where C_{cii} is the averaged chance coincidence rate arising from a prompt beam burst. A chance event resulting from a delayed beam burst is described by a similar equation:

$$C_{cij} = \tau_c C_1 C_2 \sum_{i=1}^{T/\tau_c} Q_i * Q_j/(\bar{Q})^2 \qquad \text{(III-18)}$$

where Q_j is the charge in the delayed beam burst. Two vectors of arbitrary dimension obey the following inequality

$$\vec{p} \cdot \vec{p} + \vec{q} \cdot \vec{q} = p^2 + q^2 \geq 2 \vec{p} \cdot \vec{q} \qquad \text{(III-19)}$$

Applying (III-19) to sums occurring in Eqs. (III-17) and (III-18)

$$\sum_{i=1}^{T/\tau_c} Q_i^2 + \sum_{j=1}^{T/\tau_c} Q_j^2 \geq 2 \sum_{ij}^{T/\tau_c} Q_i Q_j \qquad \text{(III-20)}$$

or

$$\sum_{i=1}^{T/\tau_c} Q_i^2 \geq \sum_{ij}^{T/\tau_c} Q_i Q_j$$

Thus one obtains the result:

$$C_{cii} \geq C_{cij} \qquad \text{(III-21)}$$

This analysis shows that a correction should be made to the chance array before subtracting the chance information from the true + chance array. This correction factor was found in the $(p, p'\gamma)$ work [Moss 69] by comparing the γ's in coincidence with elastically scattered protons in both the true + chance and chance arrays. The derived correction factor was 1.08. In the $(\alpha, 2\alpha)$ case this correction factor was found by comparing the summation of chance events composed of scattered α-particles whose summed energies were greater than the $(\alpha, 2\alpha)$ threshold. This comparison was made between the true + chance and chance arrays as in the $(p, p'\gamma)$ experiment. Statistics usually amounted to at least several hundred events; and an averaged correction factor of 1.14 was found. Since the chance background in the 4/72 and 8/72 experiments was small (cf Fig. III-14) this correction was not included in that analysis. However, it was used in the analysis of the 1/73 experiment and was found to affect the extracted cross section by approximately 10% in some cases.

b. True-to-chance ratio

The true coincidence count rate is given by Eq. (III-7):

$$N_{COINC} = K * \sigma^3(\theta) * T * I * \Delta\Omega_1 * \Delta\Omega_2 * \Delta T_3 \qquad \text{(III-15)}$$

where $I = C/t$ = averaged beam current, K is a constant, and the other quantities were given previously. The chance coincidence rate is given approximately by

$$N_C = 2\tau_R N_1 * N_2 \qquad \text{(III-16)}$$

where the singles counting rates N_1 and N_2 are given by

$$N_i = K_i * \sigma(\theta) * T * I * \Delta\Omega_i$$

and K_i is a constant. The quantity τ_R is the fast coincidence resolving time. Then the true-to-chance ratio (R) is

$$R = \frac{N_{COINC}}{N_C} \alpha \frac{1}{\tau_R * T * I} \qquad \text{(III-17)}$$

In this coincidence experiment, $\sigma^3(\theta)$ is expected to be small, thus Eq. (III-15) shows that the reduction of the product (T * I) should not be the first or best method to increase R. The solid angles $\Delta\Omega_1$ and $\Delta\Omega_2$ must first be made as large as feasible, taking into account the desired resolution in energy and recoil momentum. Then, if necessary, reductions in (T * I) should be investigated as a means for obtaining a more favorable R.

Because of the relationship between solid angles and true-to-chance ratios, the choice of counter radius maintaining a constant solid angle is not straightforward. This is because radial angular resolution can be improved by moving the collimators closer to the target and cutting down the radial width to maintain a constant solid angle. The angular

resolution will always improve since $d\Omega \alpha \frac{1}{r^2}$ and $d\theta \alpha \frac{1}{r}$. However, the vertical angular opening will increase, and non-coplanar effects will become more important. Thus a balance must be found between the radial and vertical angular apertures.

A macro-structure with an approximate 8 ms period was observed in the earliest data accumulation experiment. The structure was beam off 40% of the time and on 60%. From Eq. (III-17) for R this macro-structure is seen to adversely affect the true-to-chance ratio, since the structure is equivalent to an instantaneous increase of I, the beam current. To compensate the macro-structure, it was necessary to limit the average singles count rate in the (4/72) experiment to 10,000 $(sec)^{-1}$ or less, which was equivalent to about 15,000 $(sec)^{-1}$ instantaneously. The problem was eventually traced to regulator instabilities, which caused the deflector to switch the beam on and off with 120 $(sec)^{-1}$ frequency.

Table III-4 summarizes information pertaining to the ratio R. The first three columns give the experiment date, target, and symmetric scattering angles. The fourth column refers to the experimental geometry used, and they are summarized in Table III-1. The singles count rate and the ratio R derived by summing the ground state transition kinematic regions for the true + chance and chance arrays are given in the last two columns. Often, the singles count rate was limited by available beam intensity and target thickness; this is most noticeable for the 8/72 ^{30}Si data.

Table III-4. True-to-chance ratio data for the $(\alpha, 2\alpha)$ experiments.

Date	Target	Angle (sym.)	Geometry	Singles count rate $(sec)^{-1}$	R
4/72	^{28}Si	35°	A	8,000	20
4/72	^{16}O	35°	A	8,000	41
4/72	^{26}Mg	35°	A	6,500	26
4/72	^{24}Mg	35°	A	6,000	50
8/72	^{12}C	35°	A	14,000	103
8/72	^{30}Si	35°	A	2,600	36
8/72	^{66}Zn	35°	A	8,500	38
8/72	^{40}Ca	32°	A	14,000	24
1/73	^{16}O	28°	B	8,000	6
1/73	^{12}C	28°	B	14,000	6

Note that 8/72 data were generally taken at a higher singles counting rate, yet the ratio R was equal or better than in the experiment of 4/72. This reflects the beam macro-structure problem which had been resolved in the 8/72 experiment. Also, R was lower by more than an order of magnitude for the ^{12}C 1/73 experiment as compared to the 8/72 run, because the product of solid angles between the 1/73 and 8/72 experiments differed by more than a factor of ten.

6. Monitor counter and dead time correction

A further and very important correction that must be applied to the raw data was a factor which corrected for electronic and computer dead time. A dead time correction factor was obtained by triggering a pulser system from the monitor counter. Signals simulating two coincident α particles were fed into the preamplifiers. Then, by comparing the number of triggers with the number of pulse generator events eventually written on magnetic tape, an overall dead time correction factor was found. Reasonable assumptions concerning the dead time arising from the pileup rejectors and the TAC unit gave agreement within a few per cent of the experimentally extracted dead time. Due to the slow coincidence counting rates ($\sim 1 \rightarrow 10$ $(sec)^{-1}$) the computer accounted for only a small part of the dead time. Further, the monitor counter was also used to detect any change in effective target thickness from run to run: no significant changes were observed. Finally, the monitor pulse was always arranged to fall within the chance gate which was being monitored by the computer. This provided a convenient method for detecting gain shifts.

7. Data reproducibility

Several sources of systematic error were possible. In Fig. III-16 data for the $^{12}C(\alpha, 2\alpha)^{8}Be(0.0)$ reaction taken nine months apart are given. Different detectors and targets were used. The same scattering chamber, solid angles, and counting electronics were used. The open circles correspond to data of 11/71 and the closed circles to the data of 8/72. No normalization was used between the two experiments, and in cases where data were taken at the same angle, the data were in agreement within the statistics.

However, the experiment of 1/73 which had rather different solid angles and angular acceptances (cf. Table III-1) did not normalize to the earlier experiments within the 12% statistical errors. On the basis of the required normalization it was estimated that the absolute cross section scale error was 40%.

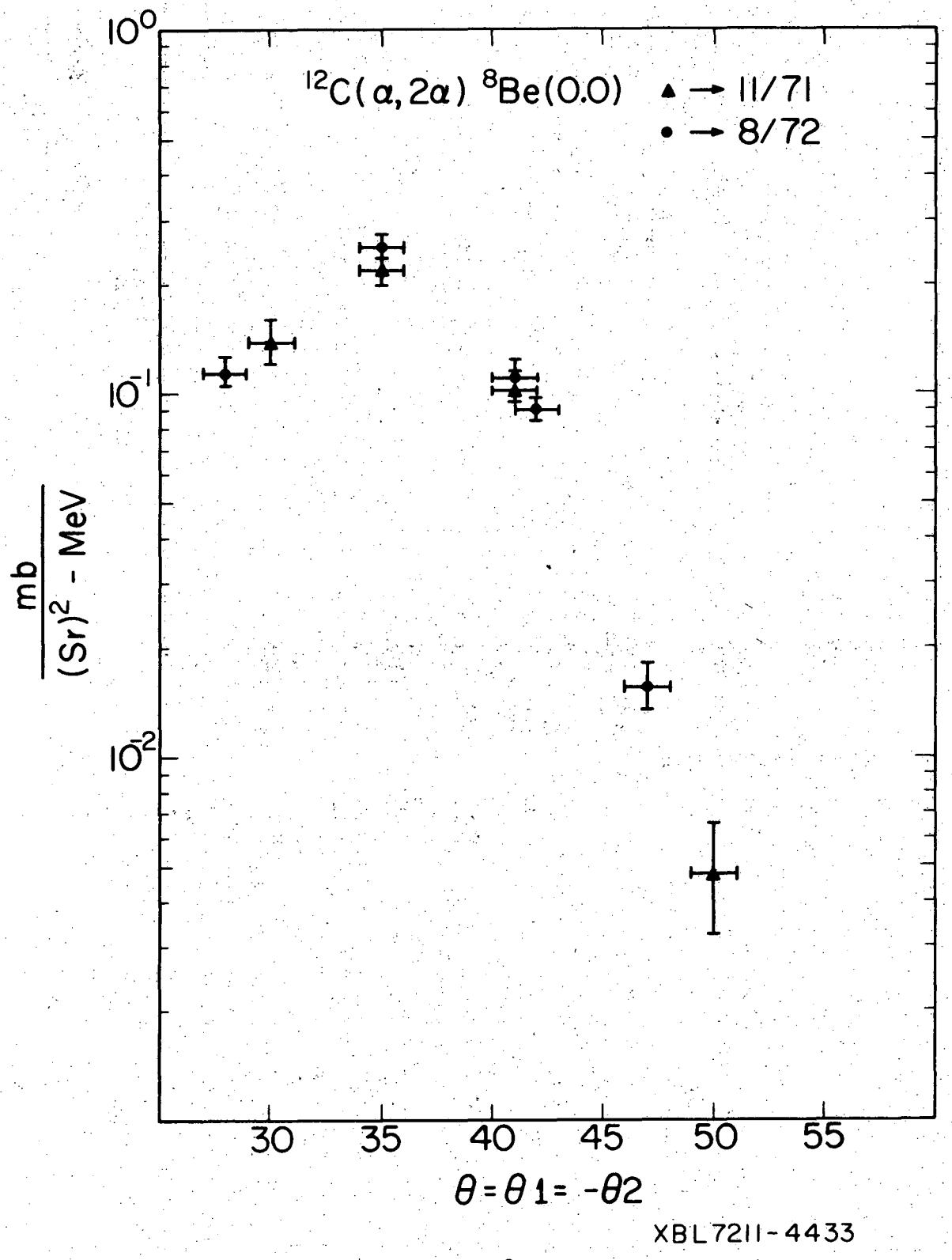

Fig. III-16. The $^{12}C(\alpha, 2\alpha)^{8}Be(0.0)$ angular correlation taken on two separate dates.

IV. Experimental Results

A. Projected ($T_3 + T_4$) Spectra and Observed Energy Levels

1. $^{12}C(\alpha, 2\alpha)^{8}Be$ and $^{16}O(\alpha, 2\alpha)^{12}C$ reactions

The $T_3 + T_4$ projections of the ^{12}C and ^{16}O $(\alpha, 2\alpha)$ reactions are given in Figs. IV-1 and IV-2. These projections have been corrected for the curvature in the $T_3 + T_4$ vs. T_3 energy plane as described in Sec. III -E. The $(\alpha, \alpha\ ^{3}He)$ thresholds are indicated in the figures, and they lie well below the summed energies corresponding to $(\alpha, 2\alpha)$ events leaving the residual nuclei in the ground and low excited states. There is no evidence for $(\alpha, \alpha\ ^{3}He)$ events coming from the ^{12}C and ^{16}O targets. The background counts occurring from the highest to lowest channels are due at least in part to chance events; these spectra have been chance corrected and if negative counts were plotted, the baseline (zero counts) would be enveloped with "noise" due to the chance correction procedure. There may be four-body breakup background in the $^{12}C(\alpha, 2\alpha)^{8}Be$ spectrum, since the $^{12}C(\alpha, 3\alpha)\alpha$ reaction has a Q-value of -7.26 MeV. This latter reaction has a Q-value of about -14 MeV for the ^{16}O target.

Table IV-1 summarizes the states observed in the ^{8}Be and ^{12}C residual nuclei. The second column gives the excitation energies used in fitting a linear least squares line through the data. Since only two levels were consistently observed in these nuclei, no prediction for the error in the excitation energies–hence the fitting procedure–was possible. However, the linear fit to the ^{12}C and ^{8}Be data were consistent with slopes obtained at different angles and different nuclei.

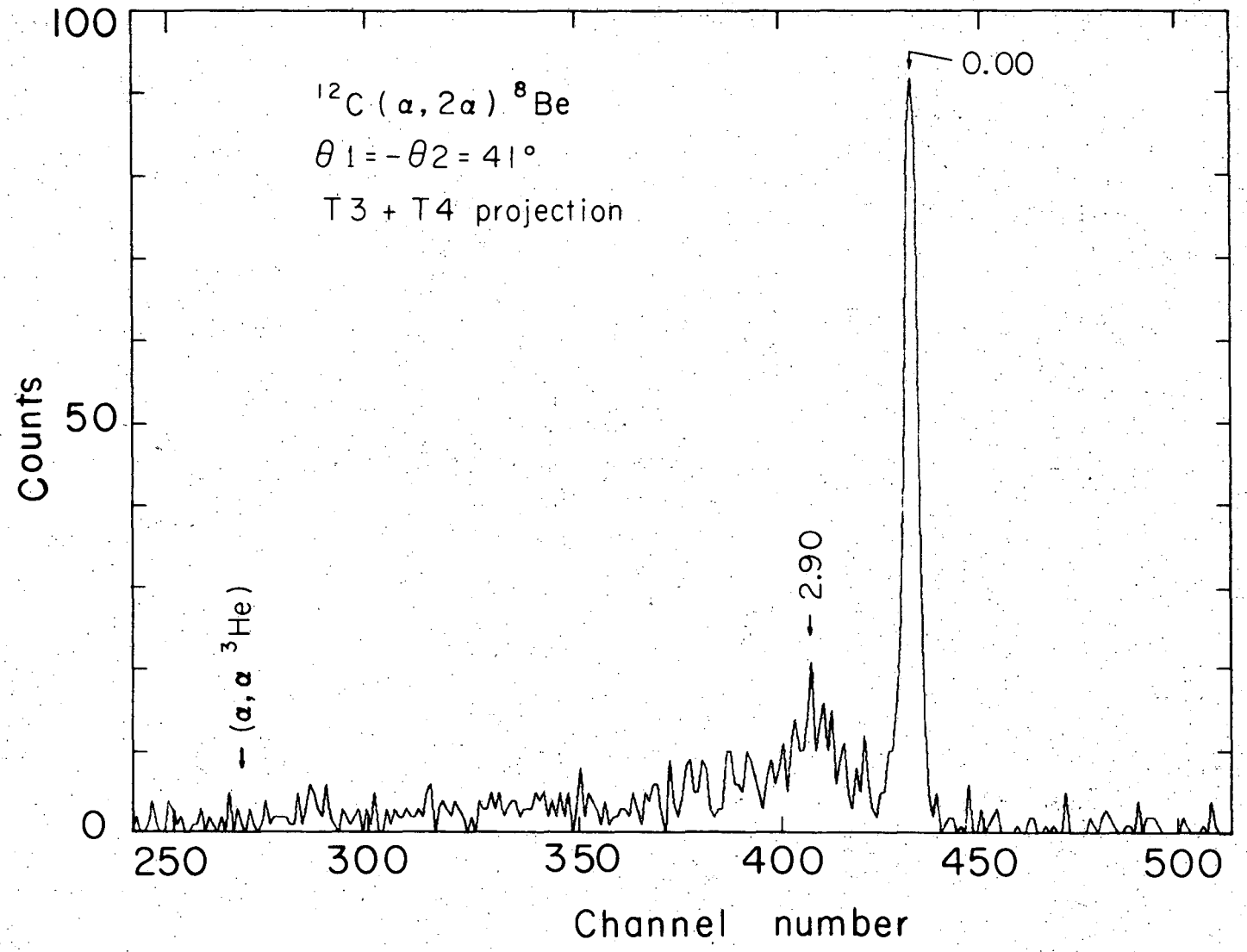

Fig. IV-1. The $^{12}C(\alpha, 2\alpha)^{8}Be$ $T_3 + T_4$ projected spectra.

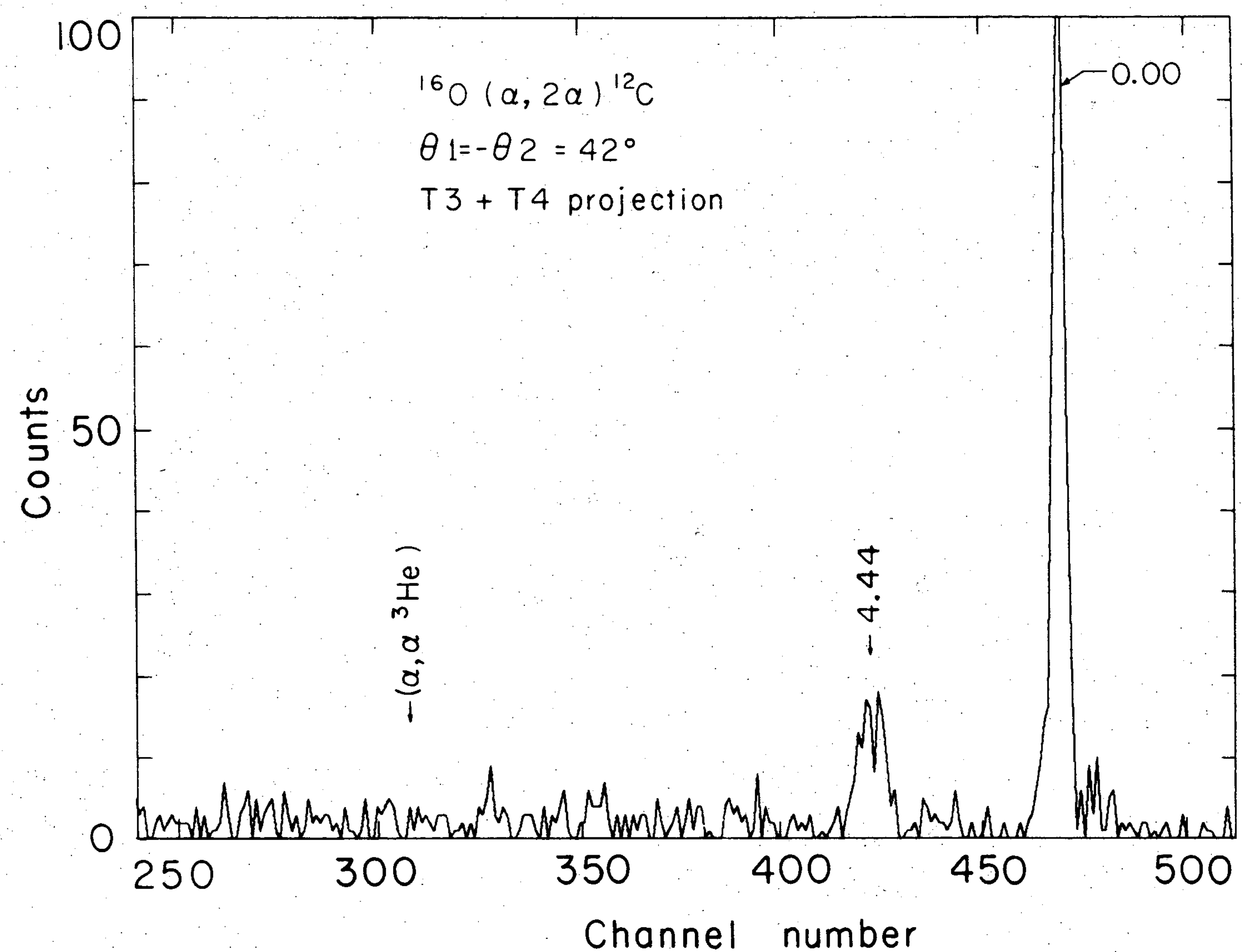

XBL 729-4023

Fig. IV-2. The $^{16}O(\alpha, 2\alpha)^{12}C$ $T_3 + T_4$ projected spectra.

Table IV-1. Summary of observed levels and intensities with E_x and J^π from the literature for the ^8Be and ^{12}C nuclei.

Nucleus	E_{exp} (MeV)	E_{lit} (MeV)	J^π	θ	Integral $(mb/(sr)^2)$	Error $(mb/(sr)^2)$
^8Be	0.00	0.00[a]	0^+	35°	4.89	.34
	2.90	2.90	2^+		2.54	.25
^{12}C	0.00	0.00[b]	0^+	35°	3.41	.35
	4.44	4.439	2^+		.88	.17
	7.65	7.653	0^+		---	---

[a] T. Lauritson and F. Ajzenberg-Selove, Nucl. Phys. 78, 1 (1966).

[b] F. Ajzenberg-Selove and T. Lauritson, Nucl. Phys. A114, 1 (1968).

The third and fourth columns give the excitation energies and J^{π} values from the literature; the ^{8}Be data is taken from [Lau 66] and the ^{12}C data from [Ajz 68]. The sixth and seventh columns present the integrated energy correlations and the associated error at the symmetric angle listed in the fifth column. The intent is to give an indication of the relative excitation strengths in the residual nuclei. Errors listed in the seventh column represent the difference between trapezoidal integration based on the data points and the integration based on the limits of the statistical error bars. This analysis indicates that the first excited state transitions in the ^{8}Be and ^{12}C residual nuclei are not as strong as the ground state transitions. This is particularly pronounced for the ^{12}C residual nucleus.

2. ^{24,26}Mg(α, 2α)^{20,22}Ne and ^{28,30}Si(α, 2α)^{24,26}Mg

The $T_3 + T_4$ chance and kinematically corrected spectra from the ^{24,26}Mg(α, 2α)^{20,22}Ne and the ^{28,30}Si(α, 2α)^{24,26}Mg reactions are given in Figs. IV-3 to IV-6. The ^{16}O and ^{12}C target contaminants are apparent in all spectra except possibly the ^{28}Si target. The (α, α ^{3}He) thresholds are also indicated, and only in the ^{26}Mg and ^{28}Si targets are there indications that this reactions occurs. The most remarkable feature of these spectra is the predominance of the ground state transitions.

Table IV-2 summarizes the observed states in the ^{20}Ne and ^{22}Ne residual nuclei. The ^{20}Ne excitation energies and J^{π} values are taken from [Ajz 72], and the corresponding ^{22}Ne information is taken from the ^{18}O(^{7}Li, t)^{22}Ne[Scho 72] and the ^{21}Ne(d, p)^{22}Ne[Neo 72] reactions.

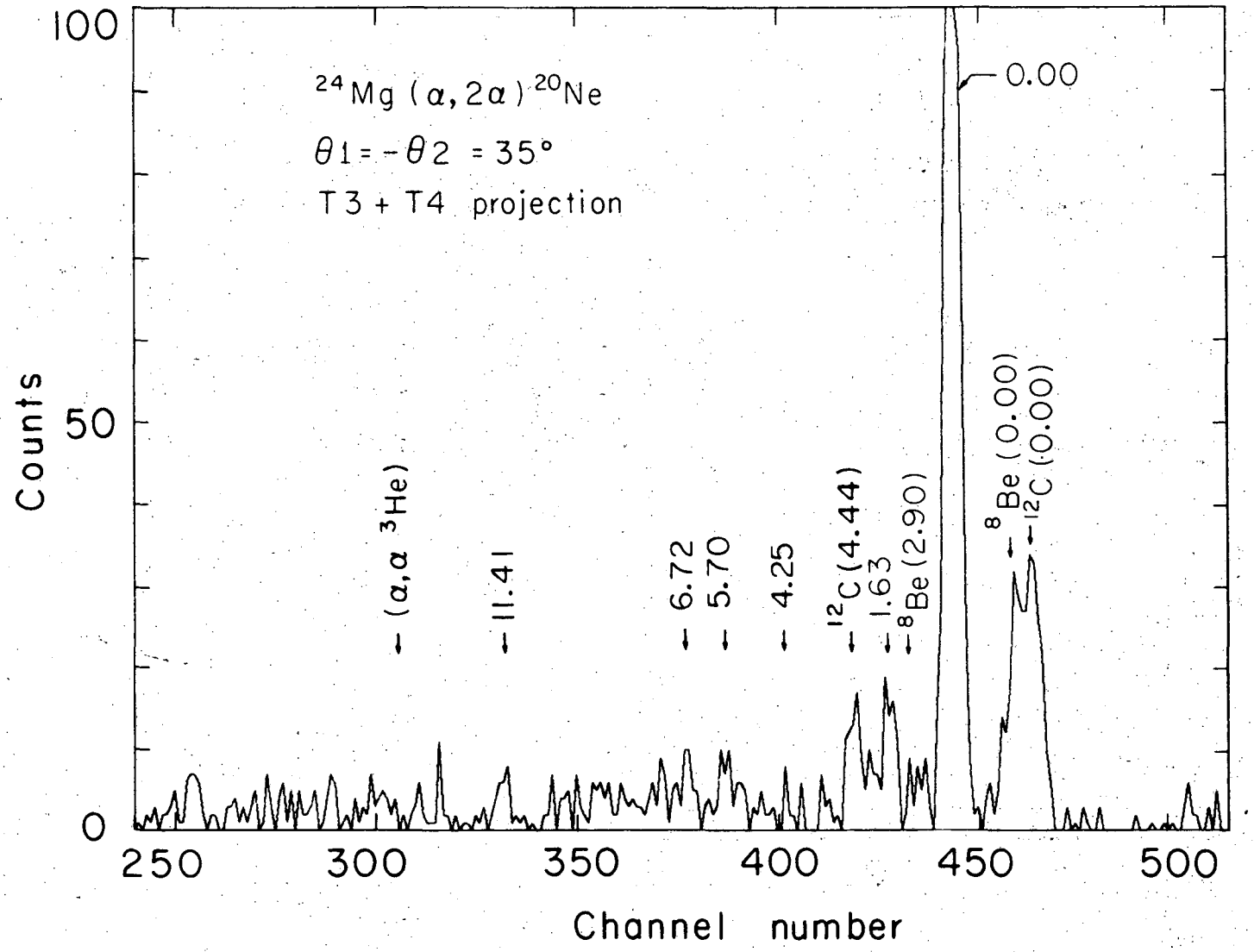

XBL729-4024

Fig. IV-3. The ^{24}Mg(α, 2α)^{20}Ne $T_3 + T_4$ projected spectra.

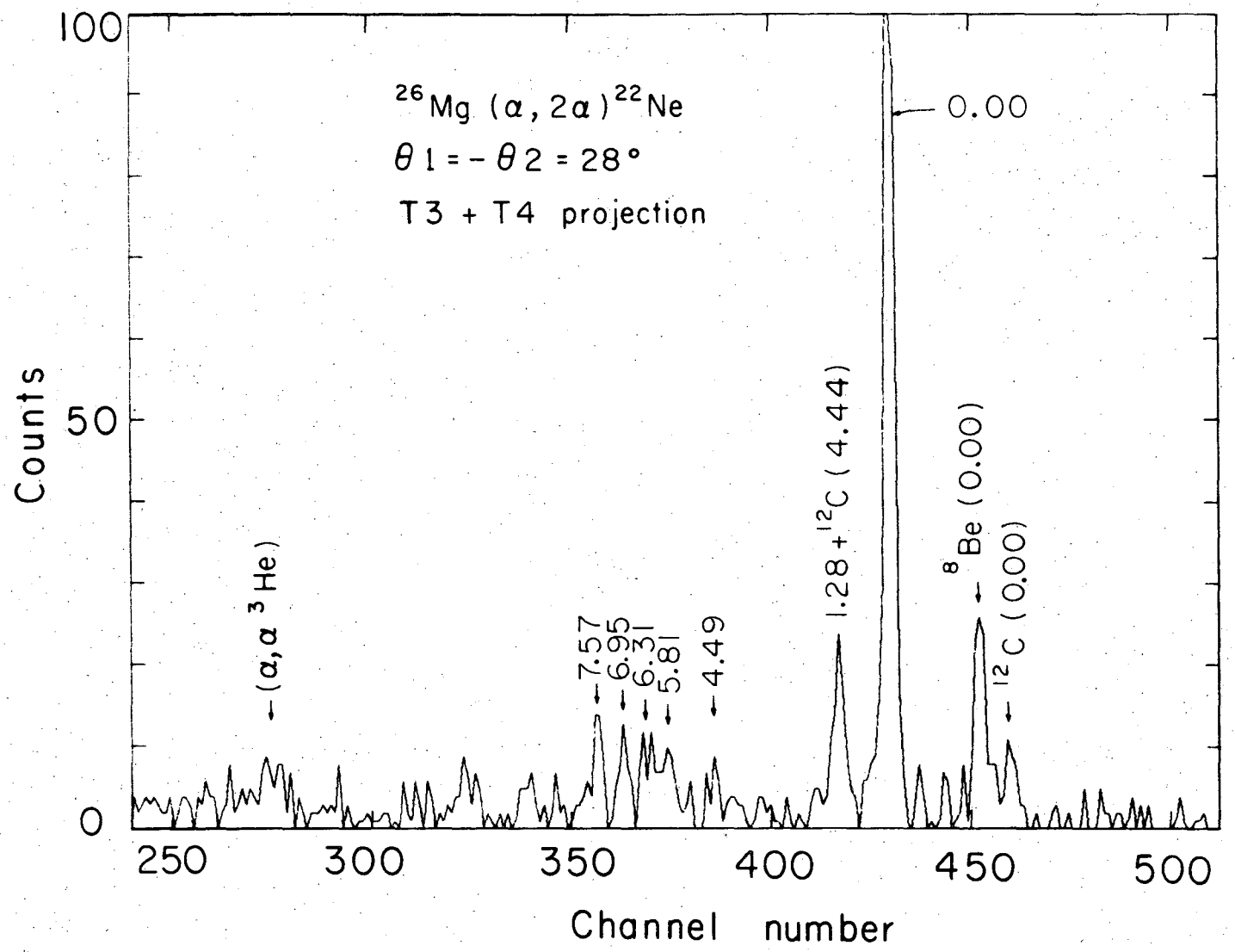

XBL729-4025

Fig. IV-4. The ^{26}Mg(a, 2a)^{22}Ne $T_3 + T_4$ projected spectra.

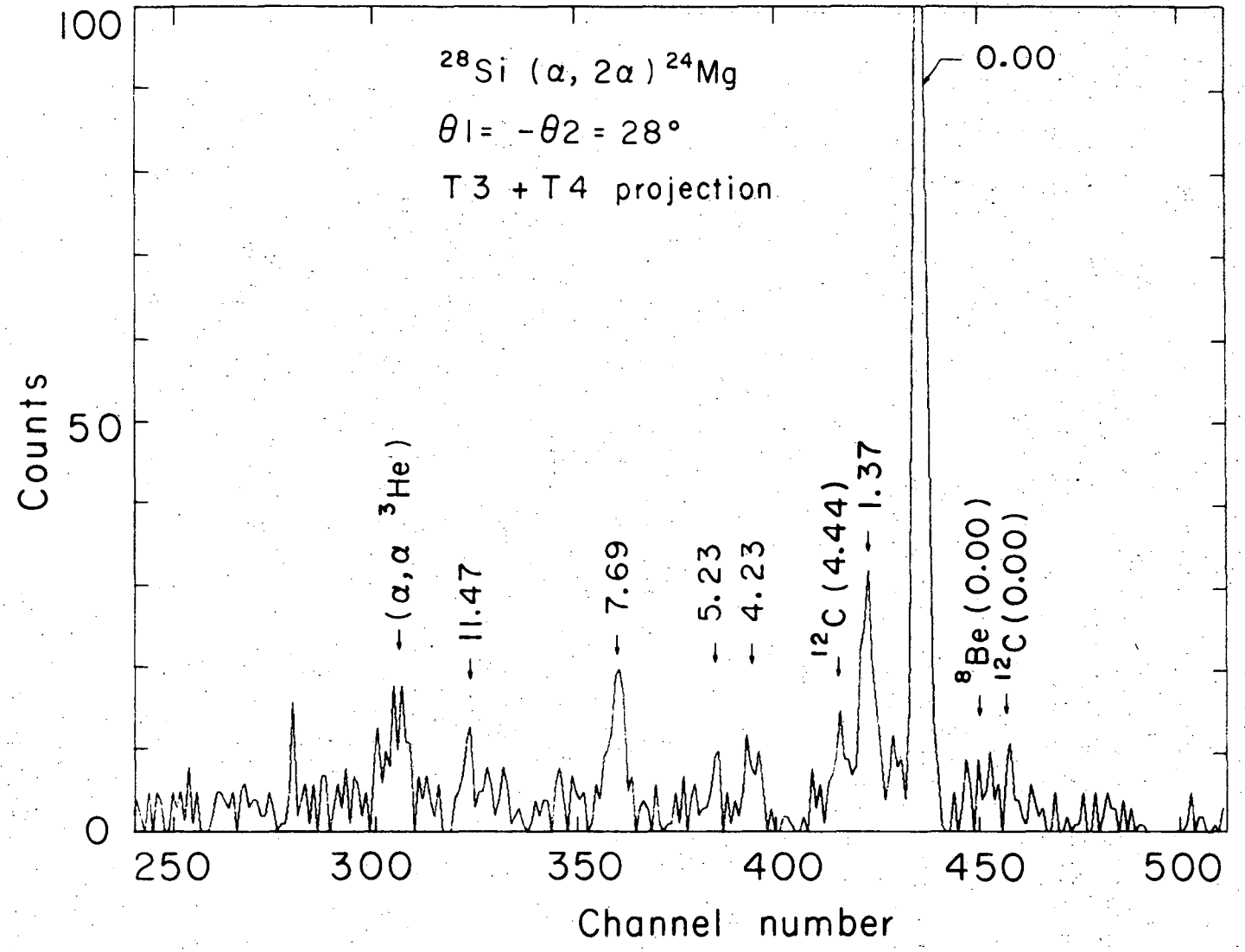

XBL729 - 4026

Fig. IV-5. The ^{28}Si(α, 2α)^{24}Mg $T_3 + T_4$ projected spectra.

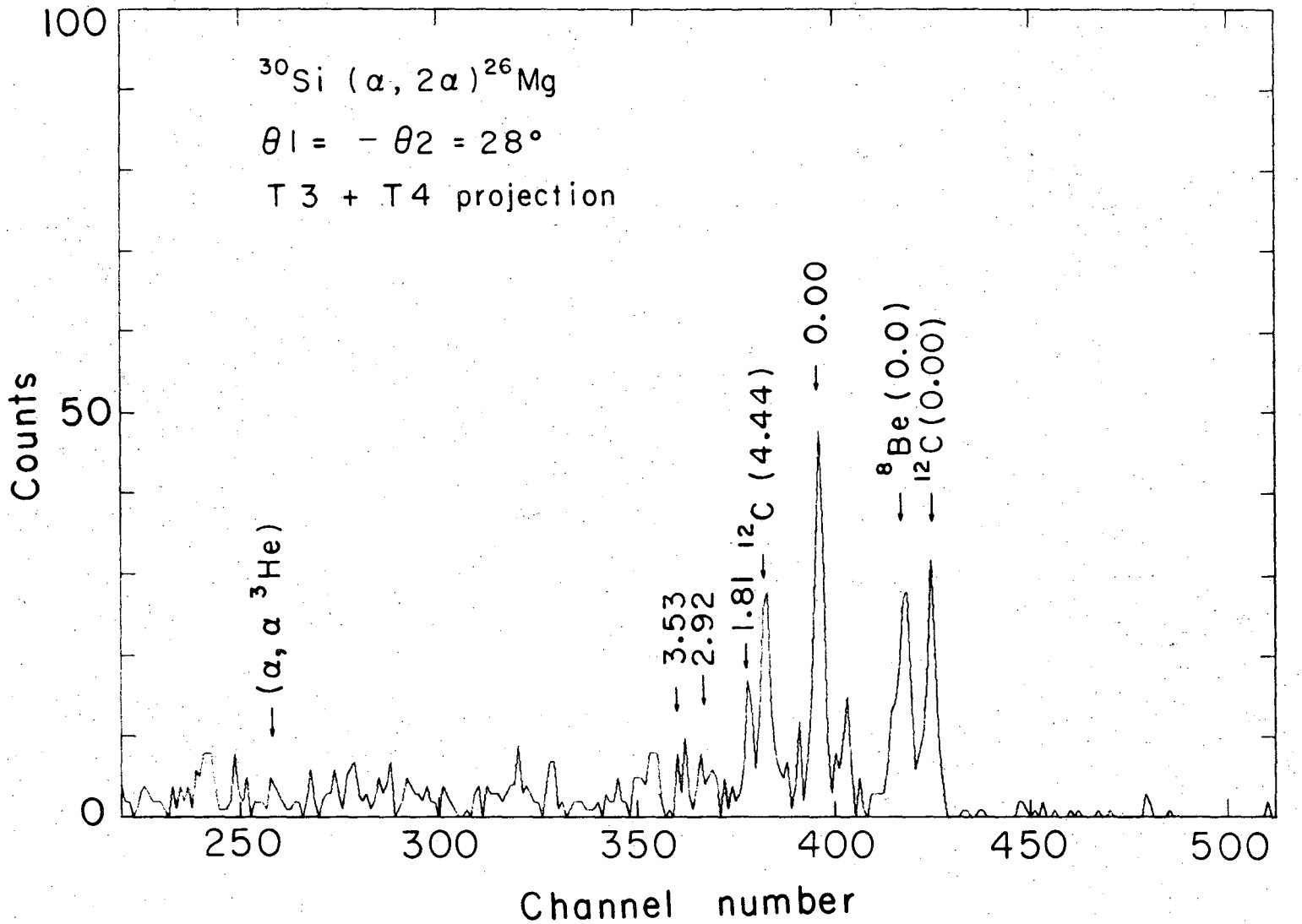

XBL729 − 4027

Fig. IV-6. The ^{30}Si(a, 2a)^{26} Mg T_3 + T_4 projected spectra.

Table IV-2. Summary of observed levels and intensities with E_x and J^π from the literature for the ^{20}Ne and ^{22}Ne nuclei.

Nucleus	E_{exp} (MeV)	Error (keV)	E_{lit} (MeV)	J^π	θ	Integral (mb/(sr)^2)	Error (mb/(sr)^2)
^{20}Ne	0.00	±20	0.00[a]	0^+	35°	1.31	.15
	1.63	±35	1.63	2^+		.108	.042
	4.25	±60	4.25	4^+		.018	.019
	5.70	±60	5.62, 5.79	$3^-, 1^-$		.063	.031
	6.72	±50	6.72	0^+		.065	.028
	11.41	±50	Many levels			.039	.022
^{22}Ne	0.00	±50	0.00[b]	0^+	35°	1.03	.12
	1.28	±60	1.28	2^+		.16	.05
	4.49	±80	4.46	2^+		.025	.018
	5.81	±60	5.93	-		.018	.014
	6.31	±80	6.34	6^+		.052	.024
	6.95	±150	6.90	0^+		.030	.016
	7.57	±60	7.49, 7.64	$1^-, 2^+$		.059	.026

[a] F. Ajzenberg-Selove, Nucl. Phys. A190, 1 (1972).

[b] W. Scholz, P. Neogy, K. Bethge, and R. Middleton, Phys. Rev. (C) 6, 893 (1972); P. Neogy, R. Middleton, and W. Scholz, Phys. Rev. (C) 6, 885 (1972).

Data taken at all angles were used to extract an averaged experimental excitation energy; the errors were determined by comparing the averaged experimental energy for levels with energies known from the literature. These estimated errors were usually greater than the sample standard deviation derived from the averaged energies.

The experimental resolution and statistics were not adequate to discern whether the weak excitation in the ^{20}Ne 5.7 MeV region was due to the 5.62 MeV (3^-) or 5.79 (1^-) states. The weak excitations observed in ^{22}Ne at $E_x > 4.49$ MeV seemed to correlate with levels observed in the $^{18}O(^7Li, t)^{22}Ne$ reaction [Scho 72]. The final two columns in Table IV-2 indicate the ground state transitions are dominant, with the first excited $J^\pi = 2^+$ states having significantly less strength and being more characteristic of the higher weakly excited states.

Table IV-3 summarizes the levels observed in the ^{24}Mg and ^{26}Mg residual nuclei. The excitation energies and J^π assignments are taken from [End 67]. The experimental errors were determined as in the ^{20}Ne and ^{22}Ne nuclei. The weak excitation in the ^{24}Mg 4 MeV region could not be unambiguously assigned to the 4.12 MeV (4^+) or 4.23 MeV (2^+) levels. The calibration did seem to favor the 4.23 MeV state, however. The 5.23 MeV 3^+ level in ^{24}Mg is the only evidence of unnatural parity state population in the present (α, 2α) survey. The ^{26}Mg statistics were comparatively poor due to the target thinness, and Fig. IV-6 indicates considerable ^{16}O and ^{12}C target contamination. The final two columns of Table IV-3 have the same systematics as the ^{20}Ne and ^{22}Ne nuclei: a dominant ground state transition with comparatively

Table IV-3. Summary of observed levels and intensities with E_x and J^π from the literature for the ^{24}Mg and ^{26}Mg nuclei.

Nucleus	E_{exp} (MeV)	Error (keV)	E_{lit} (MeV)	J^π	θ	Integral (mb/(sr)^2)	Error (mb/(sr)^2)
^{24}Mg	0.00	±20	0.00[a]	0^+	35°	.84	.11
	1.37	±40	1.369	2^+		.156	.047
	4.23	±30	4.123 4.23	$4^+, 2^+$		---	---
	5.23	±70	5.228	3^+		.033	.020
	7.69	±50	Several levels			.040	.023
	11.47	±50	Many levels			.045	.021
^{26}Mg	0.00	±50	0.00[a]	0^+	35°	.61	.16
	1.81	±50	1.809	2^+		.12	.07
	2.92	±100	2.938	2^+		---	---
	3.53	±100	3.585	0^+		---	---

[a]P. M. Endt and C. Van Der Leun, Nucl. Phys. A105, 1 (1967).

weak transitions to the excited states. A previous study of the $^{28}Si(\alpha, 2\alpha)^{24}Mg$ reaction [Pli 69] at E_α = 104 MeV suggested that the 1.37 MeV and 4.23 MeV states were populated more strongly than the ^{24}Mg ground state. The result at E_α = 90 MeV is contrary to this conclusion. Furthermore, the $^{28}Si(\alpha, 2\alpha)^{24}Mg$ reaction was studied at E_α = 70 MeV [Kene 73], and the ^{24}Mg ground state was also dominant at this energy.

3. $^{40,44}Ca(\alpha, 2\alpha)^{36,40}Ar$ and $^{66}Zn(\alpha, 2\alpha)^{62}Ni$

Figures IV-7 to IV-9 give the projected and corrected $T_3 + T_4$ spectra for the $^{40,44}Ca(\alpha, 2\alpha)^{36,40}Ar$ and $^{66}Zn(\alpha, 2\alpha)^{62}Ni$ reactions. The Ca targets have a large oxygen impurity as anticipated. The correlation angles studied in the Ca targets were chosen to ensure minimal data analysis problems in removing contaminant ^{12}C bands. The projected ^{36}Ar spectrum has considerable structure above the (α, α ^3He) threshold.

Table IV-4 summarizes the residual levels observed in these nuclei. The ^{36}Ar and ^{40}Ar data are taken from [End 67] and the ^{62}Ni information from [Led 67]. The ^{36}Ar nucleus is an exception to the systematic observation that the ground state transitions to the residual nuclei predominate in the (α, 2α) reaction. The 1.97 MeV and the 4.37 MeV integrated cross sections given in Table IV-4 nearly equal the ^{36}Ar (0.00) value. The ^{40}Ar and ^{62}Ni nuclei follow the previous excitation strength systematics, as Table IV-4 indicates.

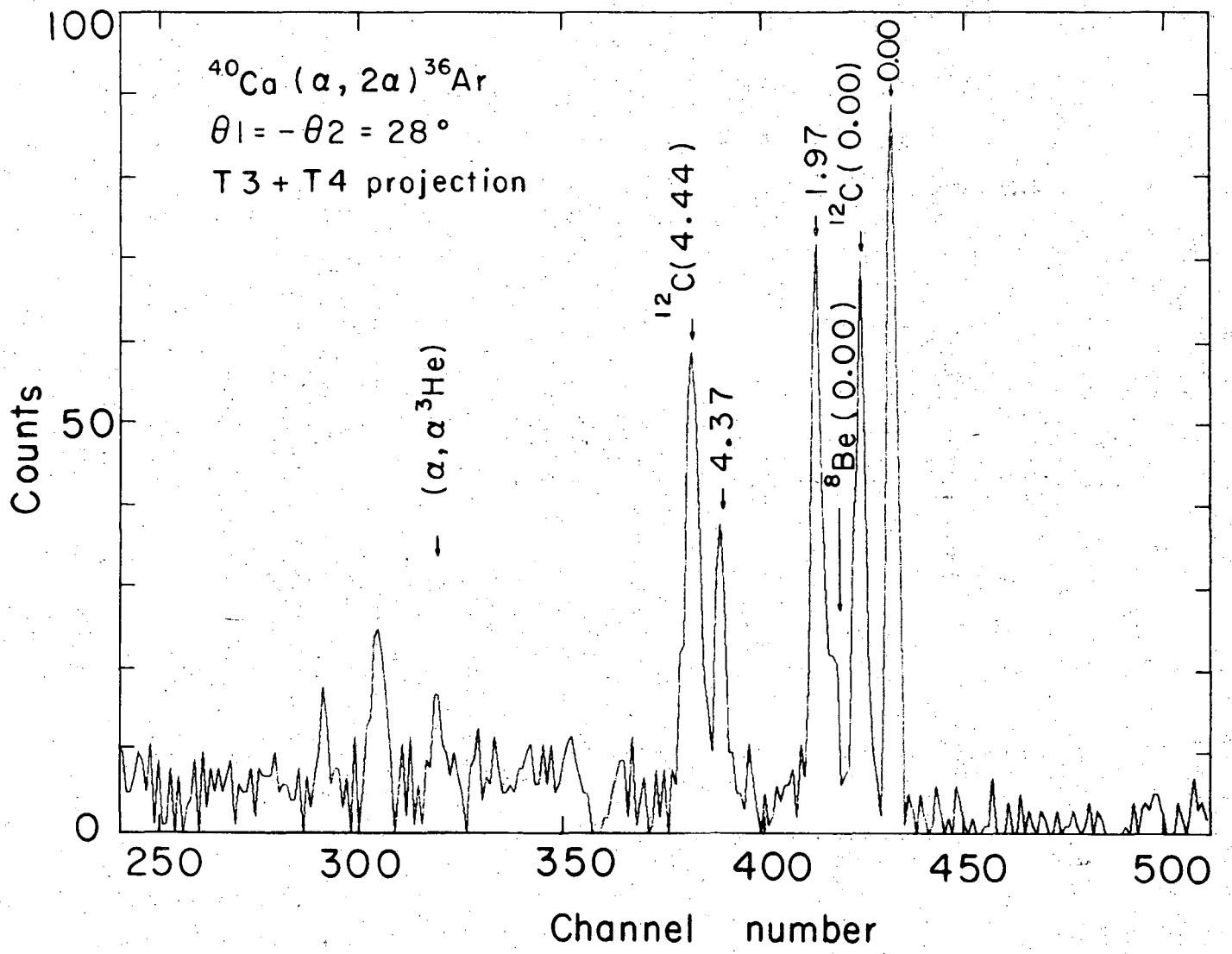

XBL729-4028

Fig. IV-7. The ^{40}Ca(α, 2α)^{36}Ar T3 + T4 projected spectra.

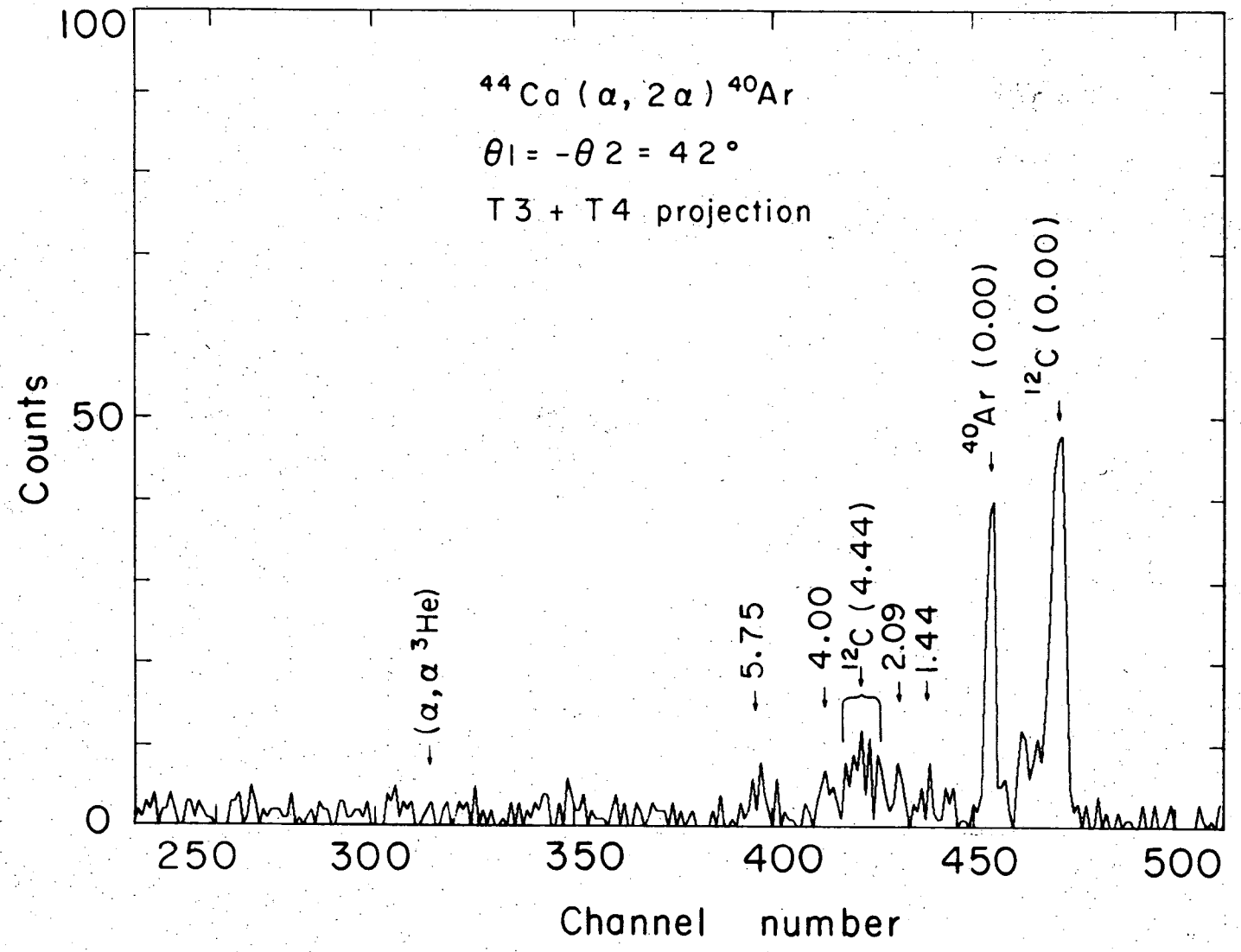

XBL729 - 4029

Fig. IV-8. The ^{44}Ca(α, 2α)^{40}Ar $T_3 + T_4$ projected spectra.

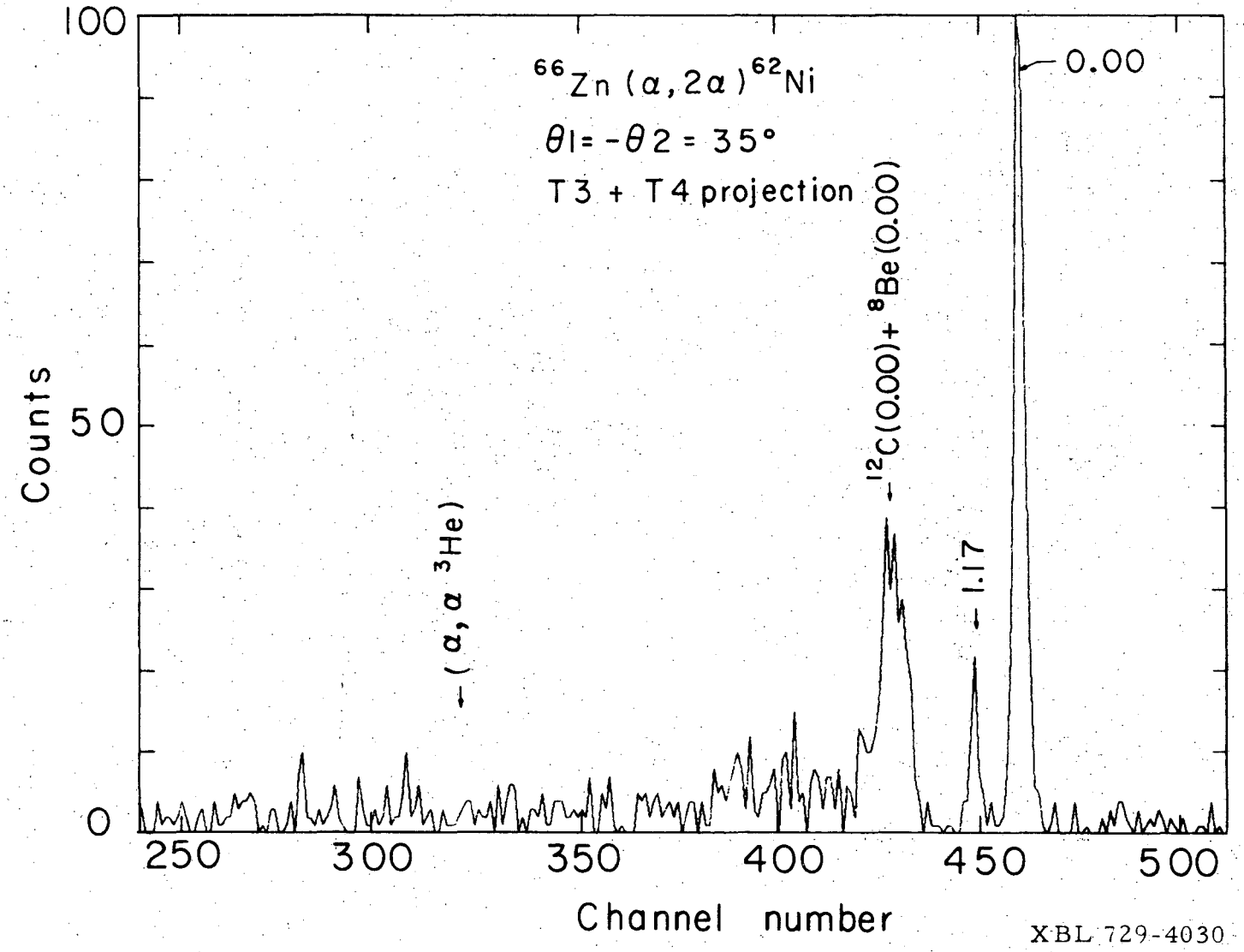

Fig. IV-9. The ^{66}Zn(a, 2a)^{62}Ni $T_3 + T_4$ projected spectra.

Table IV-4. Summary of observed levels and intensities with E_x and J^π from the literature for the ^{36}Ar, ^{40}Ar, and ^{62}Ni nuclei.

Nucleus	E_{exp} (MeV)	Error (keV)	E_{lit} (MeV)	J^π	θ	Integral (mb/(sr)^2)	Error (mb/(sr)^2)
^{36}Ar	0.00	±40	0.00[a]	0^+	32°	.50	.089
	1.97	±30	1.970	2^+		.30	.070
	4.37	±100	Several levels			.10	.039
^{40}Ar	0.00	±80	0.00[a]	0^+	28°	.58	.12
	1.44	±50	1.460	2^+		.027	.032
	2.09	±90	2.125	0^+		.052	.034
	4.00	±40	Several levels			.080	.044
	5.75	±70				.026	.025
^{62}Ni	0.00	±30	0.00[b]	0^+	35°	.42	.071
	1.17	±40	1.172	2^+		.062	.026
	2.36	±100	2.303, 2.34	$2^+, 4^+$		---	---

[a] P. M. Endt and C. Van Der Leun, Nucl. Phys. A105, 1 (1967).

[b] C. M. Lederer, J. M. Hollander, and I. Perlman, Table of Isotopes, 6th edition, (1967).

B. Energy, Momentum, and Angular Correlations

1. Energy correlations

Energy correlations are projections of kinematical bands onto the T_3 axis where $\sigma^3(\theta)$ is calculated according to Eq. (III-7). Energy correlation examples are given for the $^{16}O(\alpha, 2\alpha)^{12}C(0.0)$ reaction (Fig. IV-10) and the $^{24}Mg(\alpha, 2\alpha)^{20}Ne(0.0)$ case (Fig. IV-11).

An energy correlation was extracted and plotted for each target, angular setting, and excited state observed with significant statistics. The $\sigma^3(\theta)$ have been corrected for chance events by subtraction of a chance array from the true + chance array. This procedure and justification is outlined in Sec. III. Furthermore, if a contaminant ^{8}Be or ^{12}C band were degenerate in energy with a level of interest, care was taken to remove the contaminant events from the T_3 energy bins. The most notable example of this procedure is the $^{40}Ca(\alpha, 2\alpha)^{36}Ar(0.0)$ reaction at the symmetric quasi-elastic angle (42°). In this case the $^{16}O(\alpha, 2\alpha)^{12}C(0.0)$ transition falls on top of the residual $^{36}Ar(0.0)$. For this transition, an ^{16}O target was studied in the same experiment and the results were used to correct the impurity in the $^{36}Ar(0.0)$ data. A summary of the symmetric $\sigma^3(\theta)$ for the ground and first excited states extracted in these experiments is given in Appendix IV. The excited state statistics are poor, particularly for those levels greater than the first excited states. The errors in Appendix IV and Figs. IV-10 and IV-11 are statistical. The normalization of the 1/73 experiment indicated a 40% uncertainty in the absolute scale; the relative uncertainties between targets are determined by the precision of the

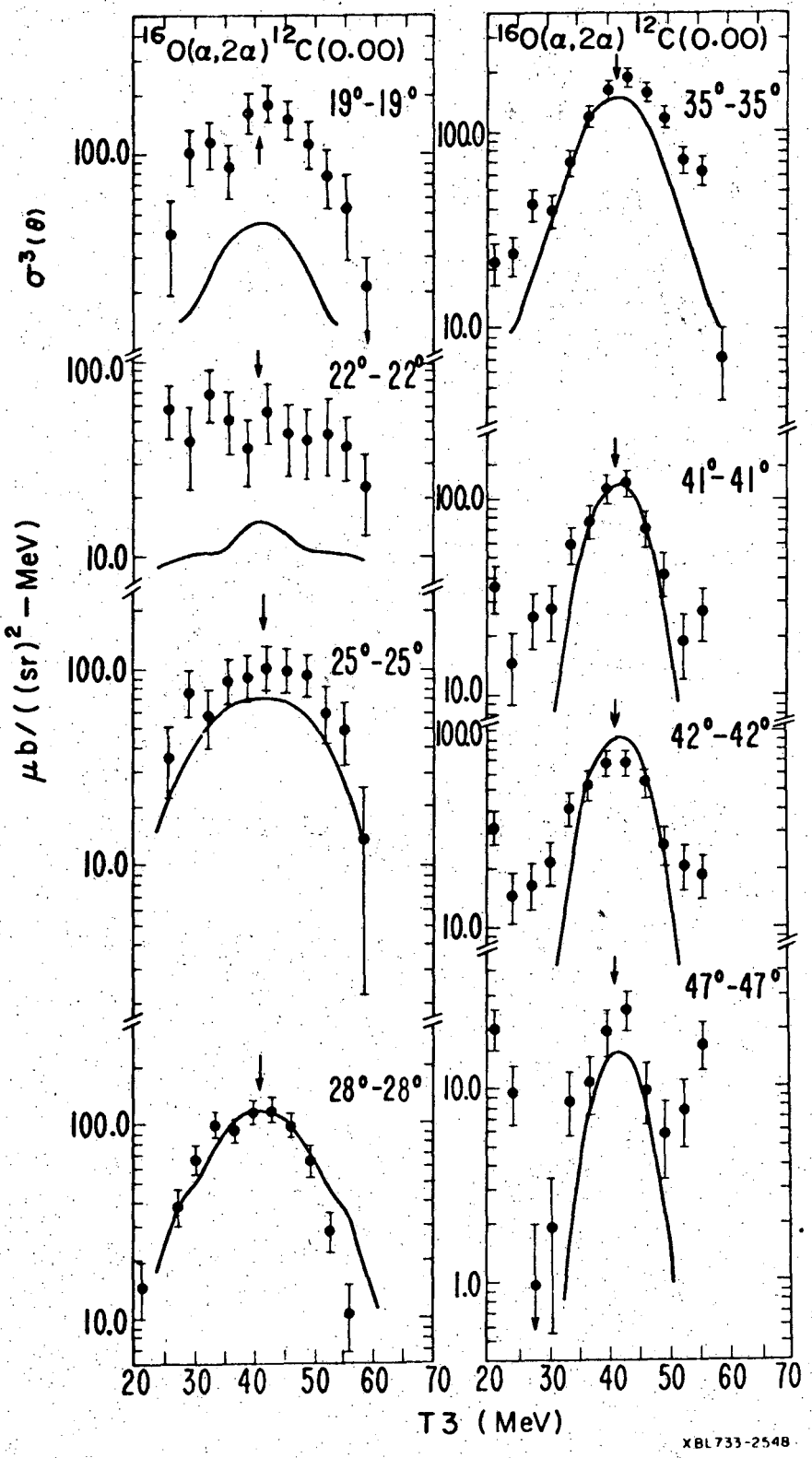

Fig. IV-10. Energy correlations for the $^{16}O(\alpha, 2\alpha)^{12}C(0.0)$ transition.

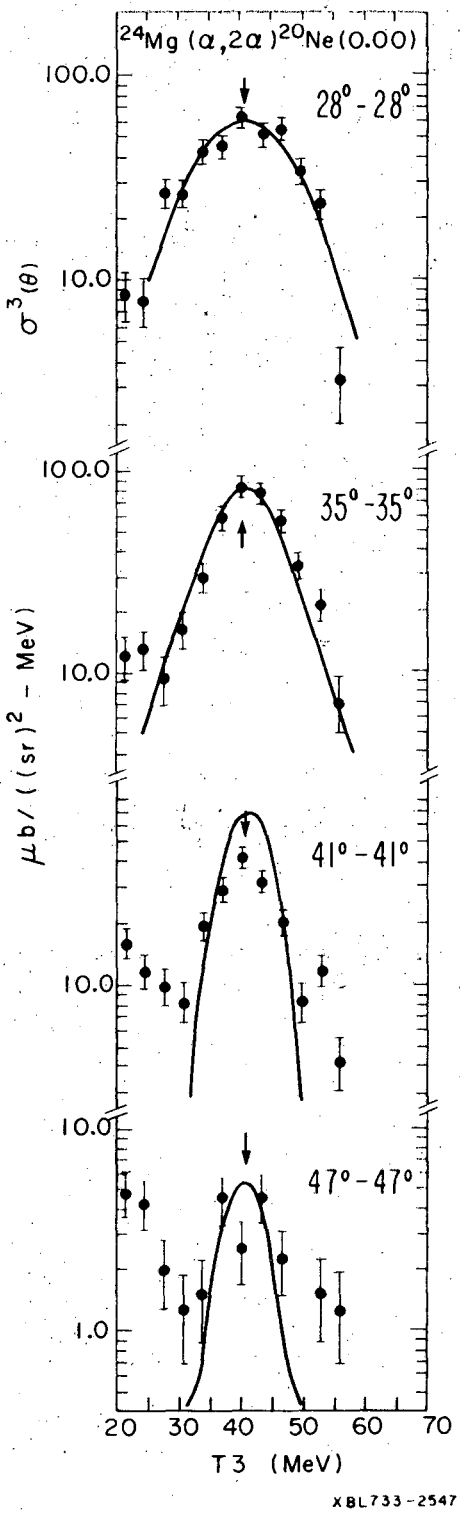

Fig. IV-11. Energy correlation for the ^{24}Mg(α, 2α)^{20}Ne(0.0) transition.

target thickness measurements (cf. Table III-2).

There are several systematic features which characterize the energy correlations. First, the maximum in the correlations comes at equal energy sharing in the two outgoing α-particles. An arrow in Figs. IV-10 and IV-11 marks the point where $T_3 = T_4$. Secondly, the cross section is characterized by a broad, smooth bump which is a signature of a quasi-elastic knock-out mechanism [Holm 69]. Sequential processes would be characterized by much sharper structure on the T_3 axis or broad structure at high excitation in the singles data. A third general feature is that the correlation structure broadens as the symmetric correlation angle moves forward from the quasi-elastic angle. This angle is 42° for the ^{16}O and 41° for the ^{24}Mg target. A fourth observation is that under the condition that $T_3 = T_4$ a peak in $\sigma^3(\theta)$ occurs at the 35° symmetric angle point. It is emphasized that these features are characteristic of the nine ground state to ground state transitions studied, and a (α, 2α) reaction theory should confront these points. The solid curves are theoretical parametrized DWIA predictions that will be discussed in Sec. V.

2. Momentum correlations

If the $\sigma^3(\theta)$ are plotted vs. the recoil nucleus momentum, the momentum correlation is obtained. Figures IV-12 to IV-14 present the momentum correlations found in the $^{12}C(\alpha, 2\alpha)^8Be$ (0.00), the $^{16}O(\alpha, 2\alpha)^{12}C(0.00)$, and the $^{44}Ca(\alpha, 2\alpha)^{40}Ar(0.00)$ reactions. The errors in $\sigma^3(\theta)$ are statistical; the errors in q were determined by the finite aperture calculations described in Sec. III-D. The $\sigma^3(\theta)$ is also plotted versus the averaged q, as discussed in an earlier section.

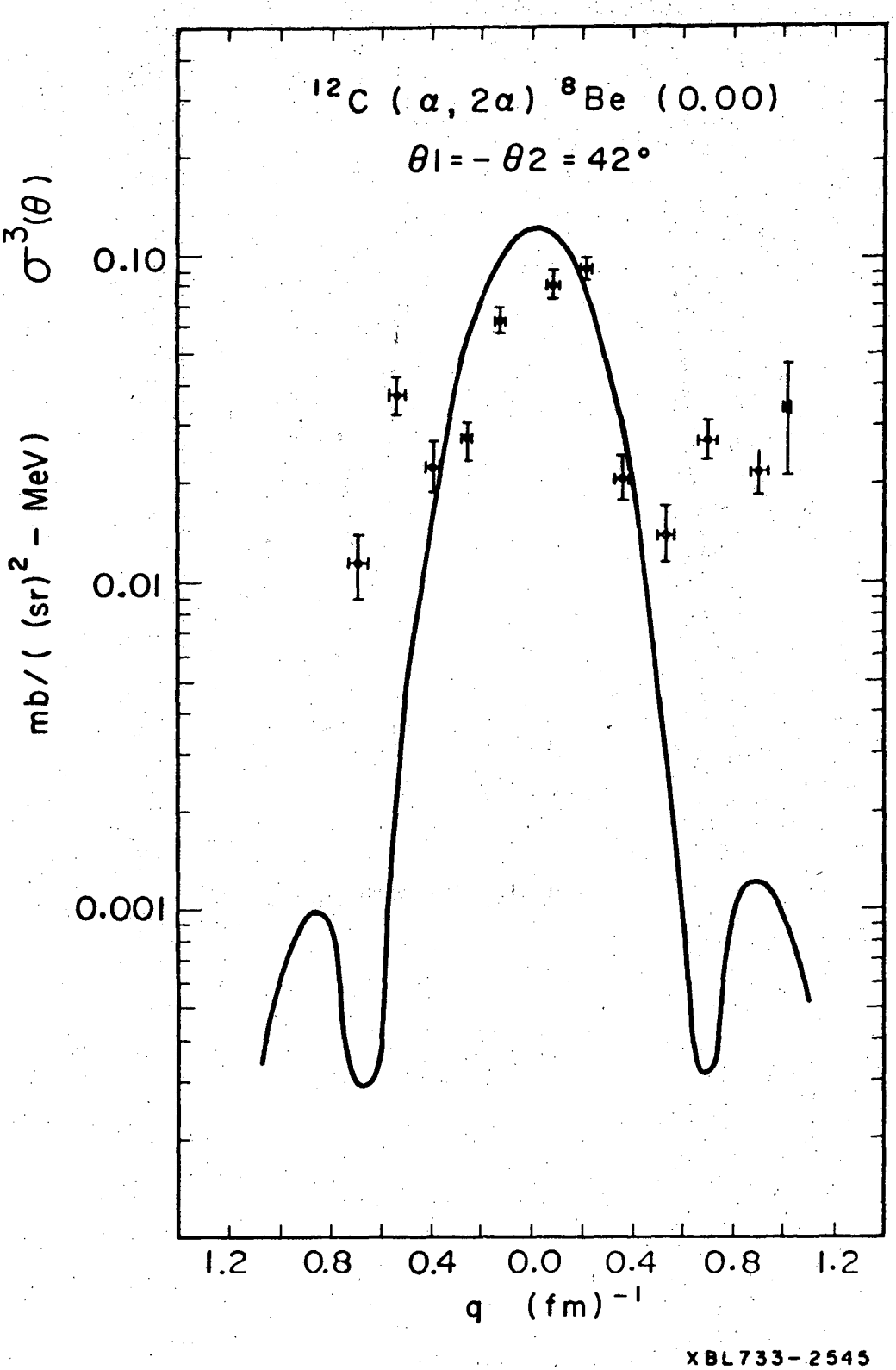

Fig. IV-12. Momentum correlation for the $^{12}C(a,2a)^{8}Be(0.0)$ transition.

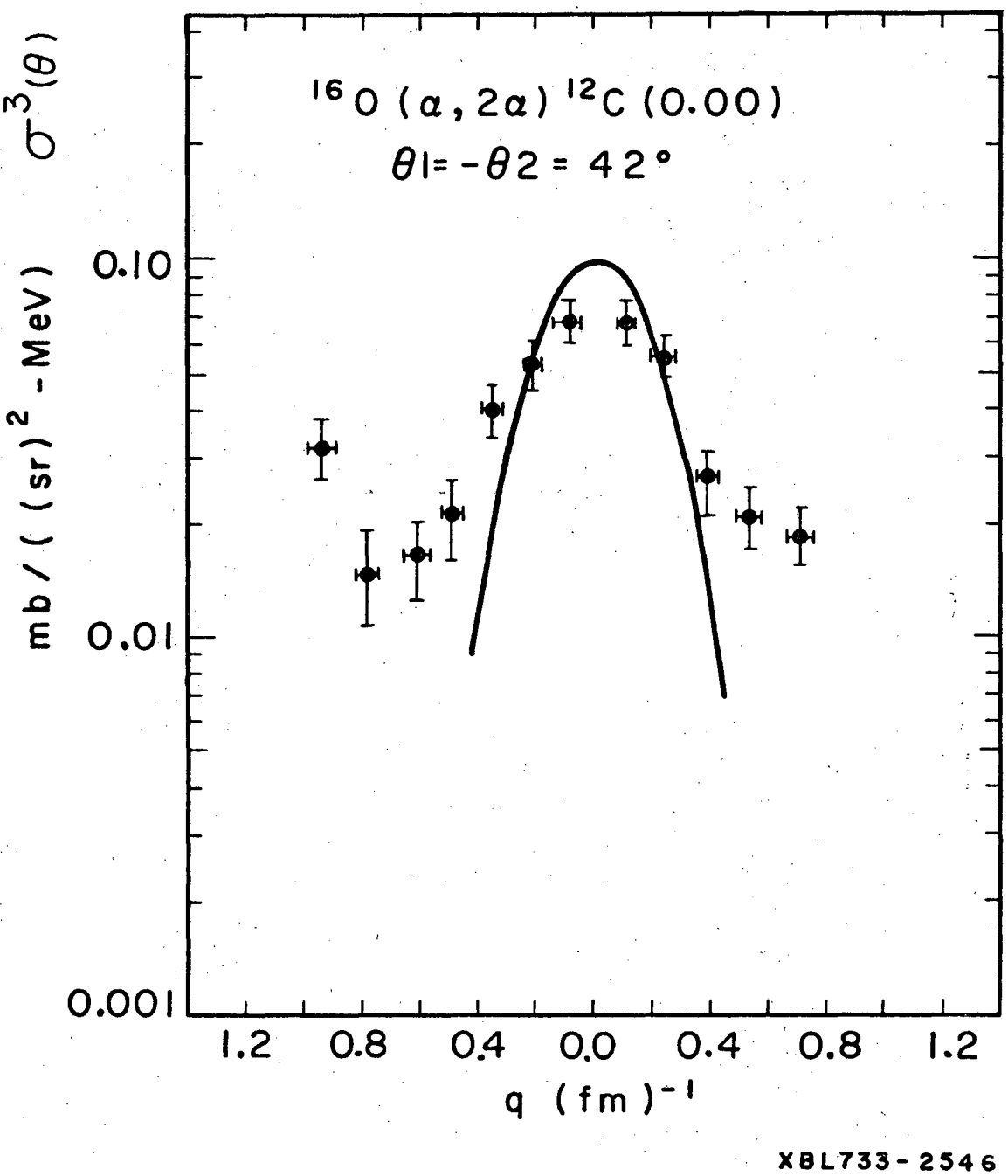

Fig. IV-13. Momentum correlation for the $^{16}O(\alpha, 2\alpha)^{12}C(0.0)$ transition.

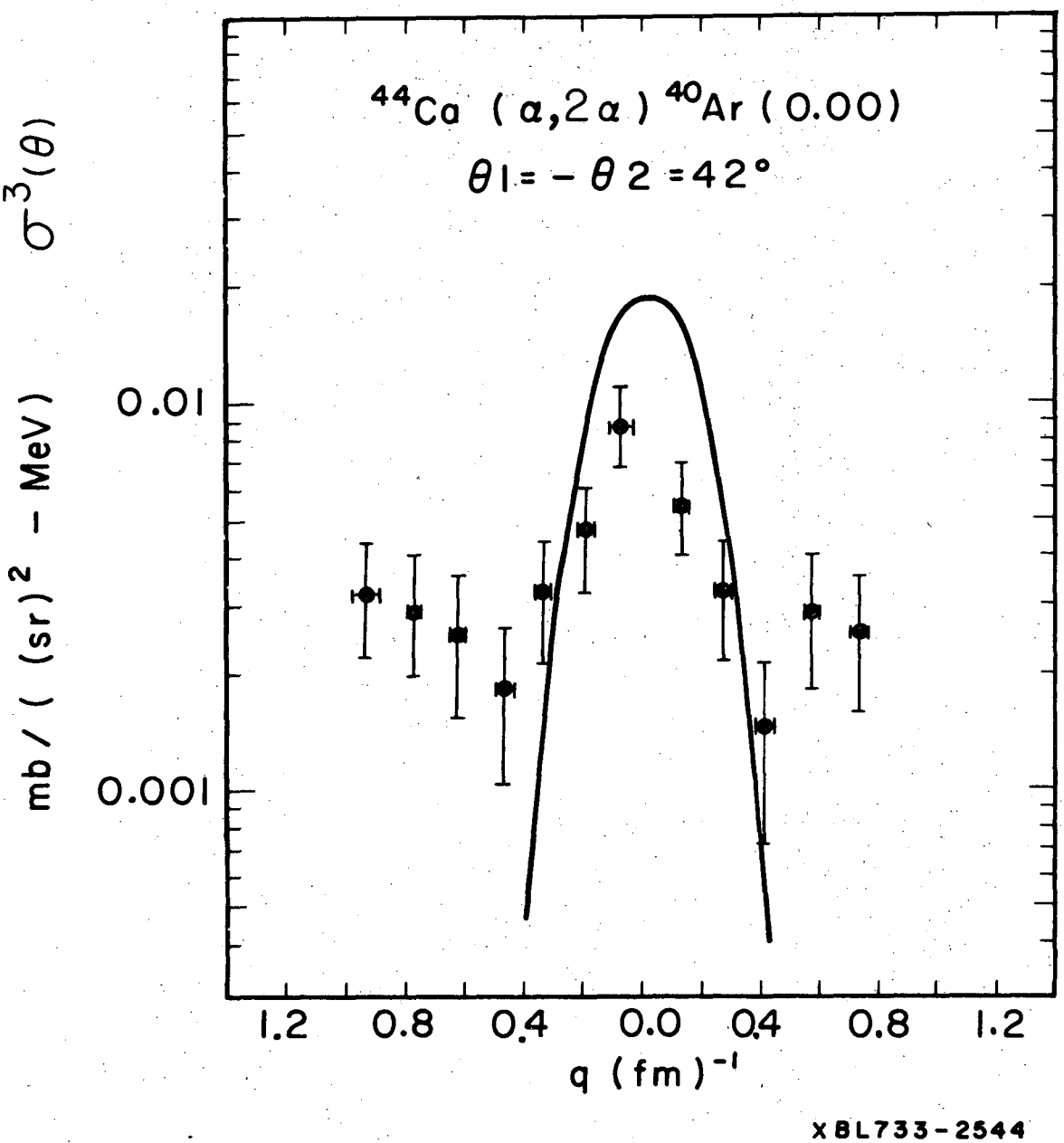

Fig. IV-14. Momentum correlation for the $^{44}Ca(\alpha, 2\alpha)^{40}Ar(0.0)$ transition.

The symmetric quasi-elastic angle for the three examples given is 42°. The correlations peak at q = 0 and are approximately symmetric about this point. The abscissa ranges generally from 1 $(fm)^{-1}$ to 0.0 $(fm)^{-1}$ and then back to 1 $(fm)^{-1}$. This corresponds to $T_3 < T_4$, $T_3 = T_4$, and $T_3 > T_4$, respectively, in the kinetic energies of the two detected alpha particles. The momentum correlations have a lower non-zero limit in the range of q away from the quasi-elastic angle, as indicated in Fig. II-3.

Within the PWIA the momentum correlations are closely connected to the momentum distribution of the bound alpha particle. Analysis of the momentum correlations in this framework is given in the discussion. The solid curves in Figs. IV-12 to IV-14 are calculations based on the parametrized DWIA.

3. Angular correlations

a. Symmetric angular correlations

The symmetric angular correlation is defined by the requirements that $\theta 1 = \theta 2$ and that $T_3 = T_4$. Since a rather large ΔT_3 bin width of approximately 3 MeV was necessary to obtain good statistics within the bin, there is an uncertainty in the $\sigma^3(\theta)$ value at the $T_3 = T_4$ point. The symmetric $\sigma^3(\theta)$ were extracted from energy correlations by reading an average value of $\sigma^3(\theta)$ at the $T_3 = T_4$ point on the energy correlation plots. The associated error in $\sigma^3(\theta)$ was estimated by comparisons with the neighboring statistical error bars. This procedure was checked by taking two data points occurring at the $T_3 = T_4$ point in the energy correlations, and then calculating $\sigma^3(\theta)$ and the statistical error.

This was done for two complete angular correlations, and the two methods yielded agreement in magnitude, but the statistical error associated with the second method was approximately 25% less than the estimated error from the first procedure. Since the averaging procedure was typically done over two data points, the uncertainty in the statement that $T_3 = T_4$ is $|T_3 - T_4| \leq 3$ MeV. There is an uncertainty in the scattering angle due to the large counter collimators. The set A geometry in Table III-1 was used for all measurements at symmetric angle 28° and greater; the set B was used in the ^{12}C and ^{16}O work at angles $< 28°$. The $\sigma^3(\theta)$ at forward angles in the ^{8}Be and ^{12}C residual nuclei are seen to have less angular error due to use of the set B collimators.

The ground state to ground state angular correlations for all targets are given in Figs. IV-15 to IV-20. Figures IV-15 and IV-16 are the angular correlations for the $^{12}C(\alpha, 2\alpha)^{8}Be(0.0)$ and the $^{16}O(\alpha, 2\alpha)$ $^{12}C(0.0)$ reactions. These targets were studied in the symmetric angular range from 19° to 47°. The ^{16}O target data reveal a minimum at 22°, a maximum at 35°, and then a rapid decrease at larger angles. The ^{12}C target shows the latter two features, but a minimum at 22° is not defined since the 19° datum point was not taken.

The remaining nuclei were studied at three or four symmeteic angles in the 28° to 47° range, and the angular correlations are summarized in Figs. IV-17 for the $^{24,26}Mg(\alpha, 2\alpha)^{20,22}Ne(0.00)$, IV-18 for the $^{28,30}Si(\alpha, 2\alpha)^{24,26}Mg(0.00)$, IV-19 for the $^{40,44}Ca(\alpha, 2\alpha)^{36,40}Ar$ (0.00), and IV-20 for the $^{66}Zn(\alpha, 2\alpha)^{62}Ni(0.00)$. These correlations demonstrate the same features as the ^{12}C and $^{16}O(\alpha, 2\alpha)$ data: a maximum at approximately 35°, and a rapid fall at larger angles. The

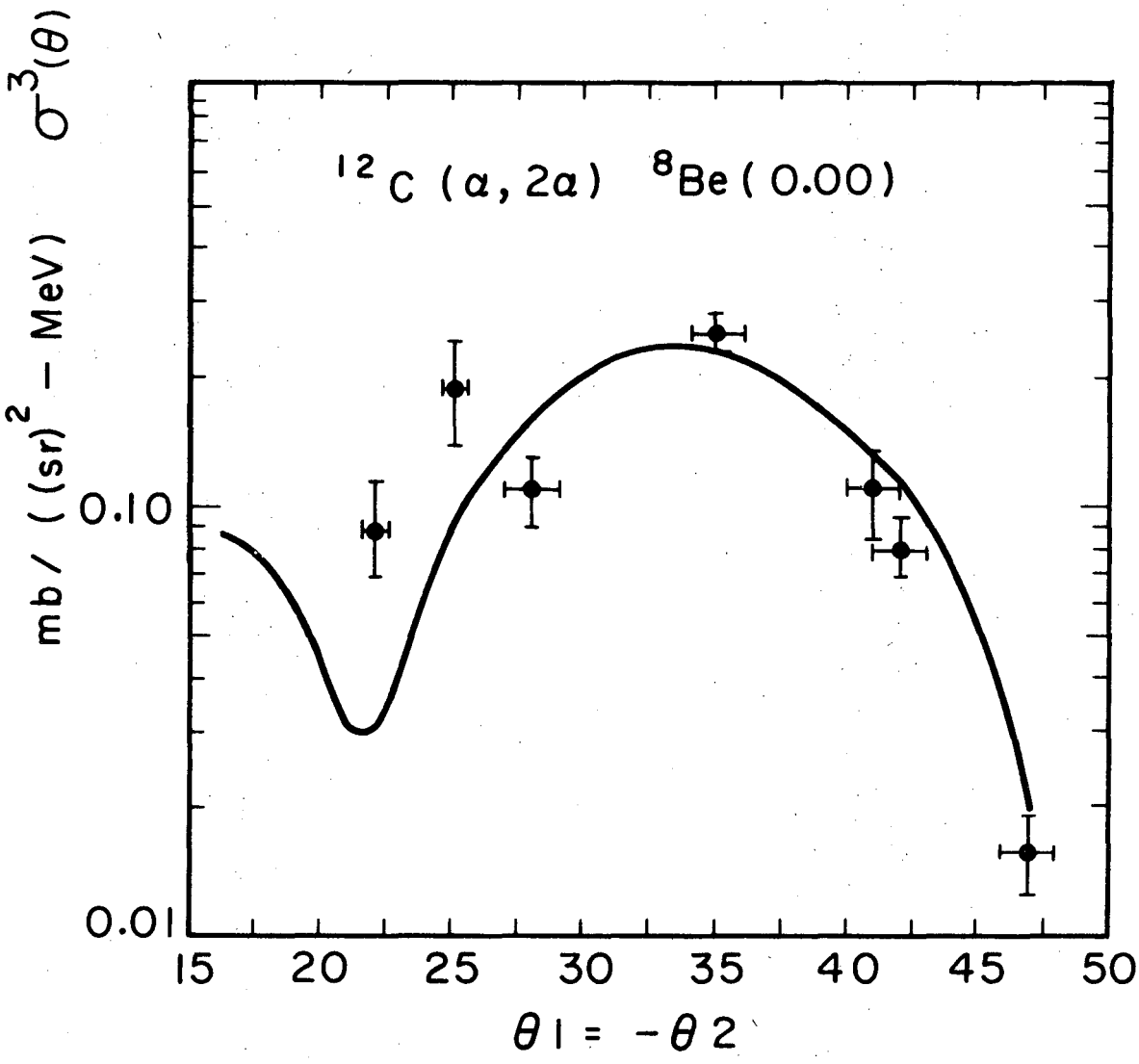

XBL733-2554

Fig. IV-15. Symmetric angular correlation for the $^{12}C(\alpha,2\alpha)^{8}Be$ (0.0) reaction.

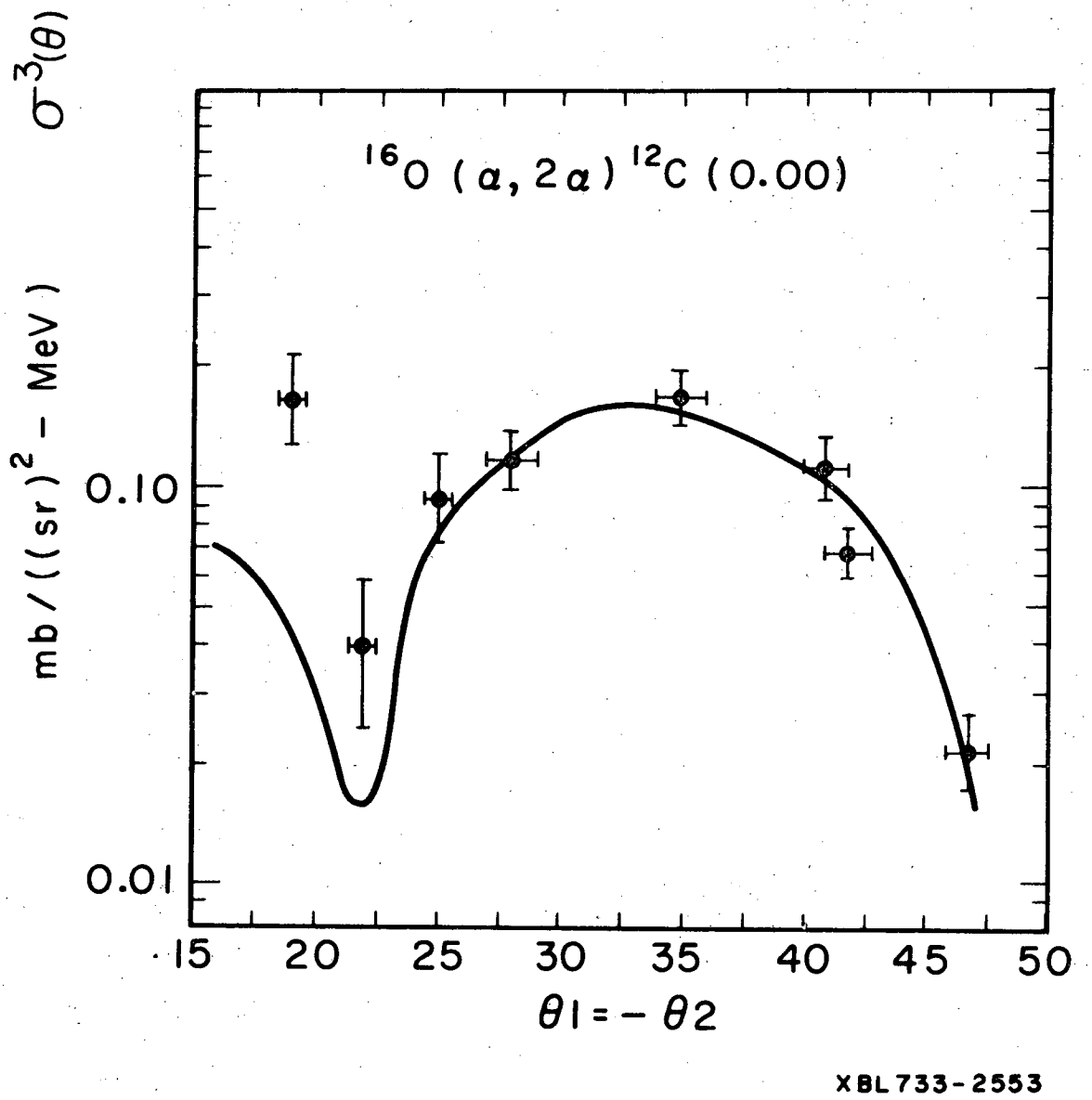

XBL733-2553

Fig. IV-16. Symmetric angular correlation for the $^{16}O(\alpha, 2\alpha)$ $^{12}C(0.0)$ reaction.

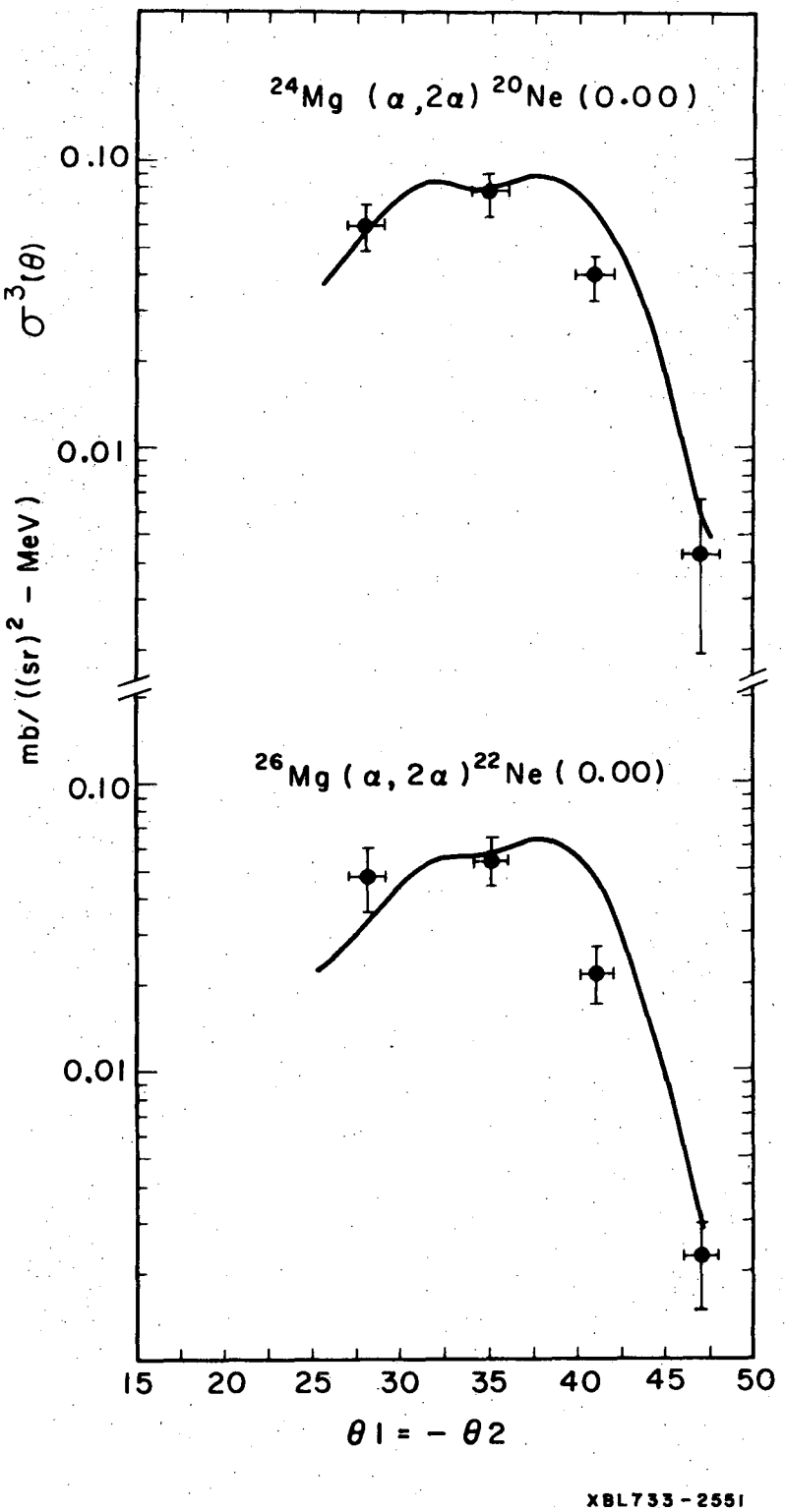

Fig. IV-17. Symmetric angular correlation for the ^{24,26}Mg(α, 2α)^{20,22}Ne(0.0) reactions.

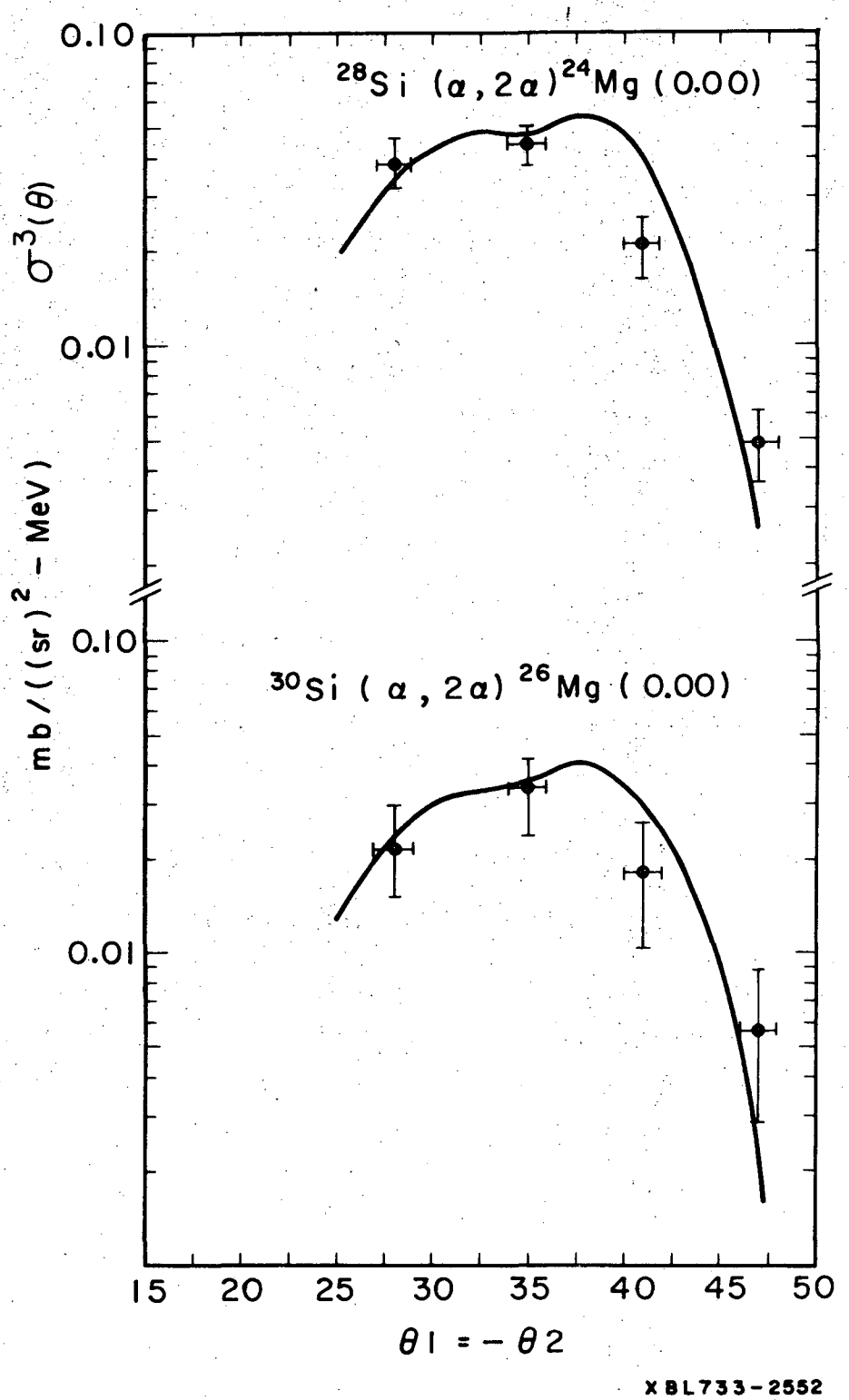

Fig. IV-18. Symmetric angular correlations for the $^{28,30}Si(\alpha, 2\alpha)^{24,26}Mg(0.0)$ reactions.

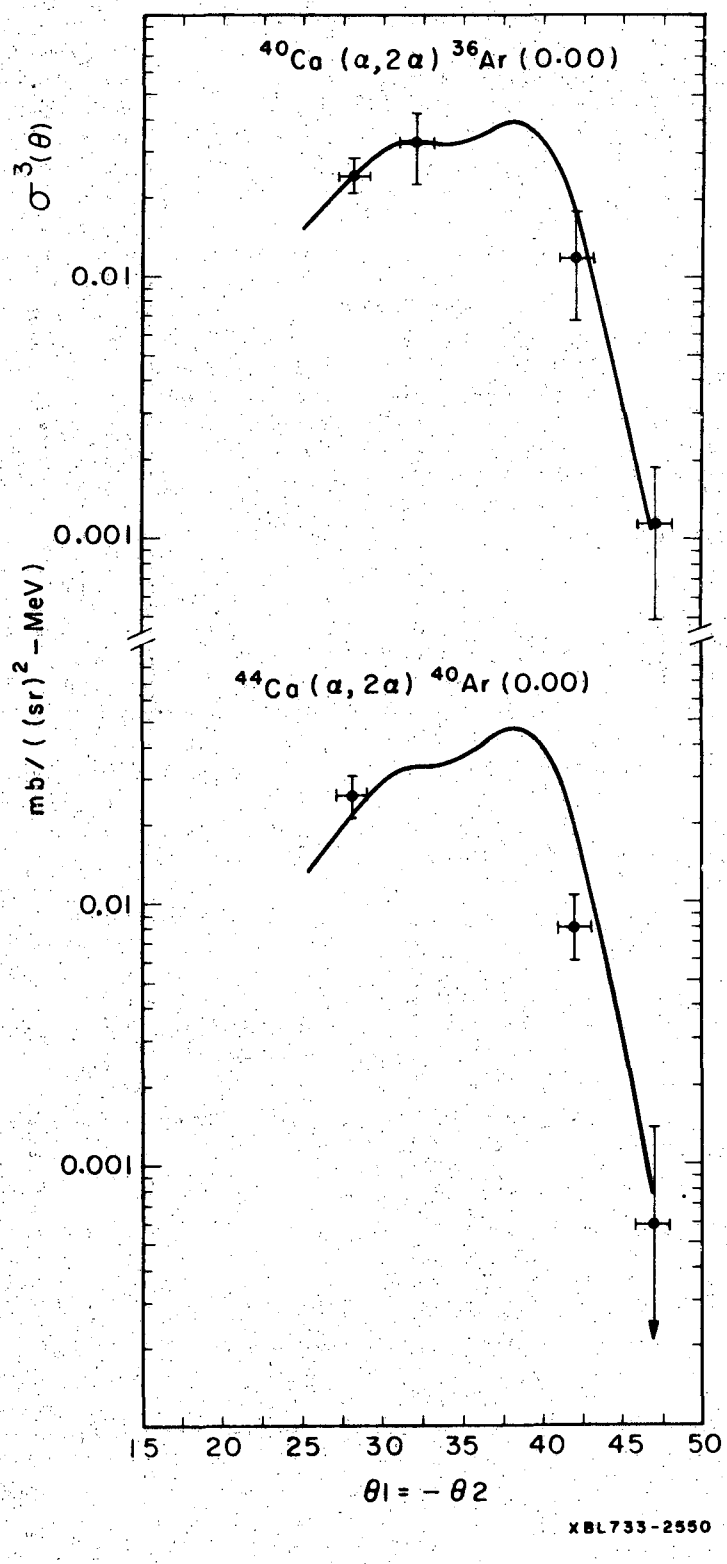

Fig. IV-19. Symmetric angular correlations for the ^{40,44}Ca(α, 2α)^{36,40}Ar(0.0) reactions.

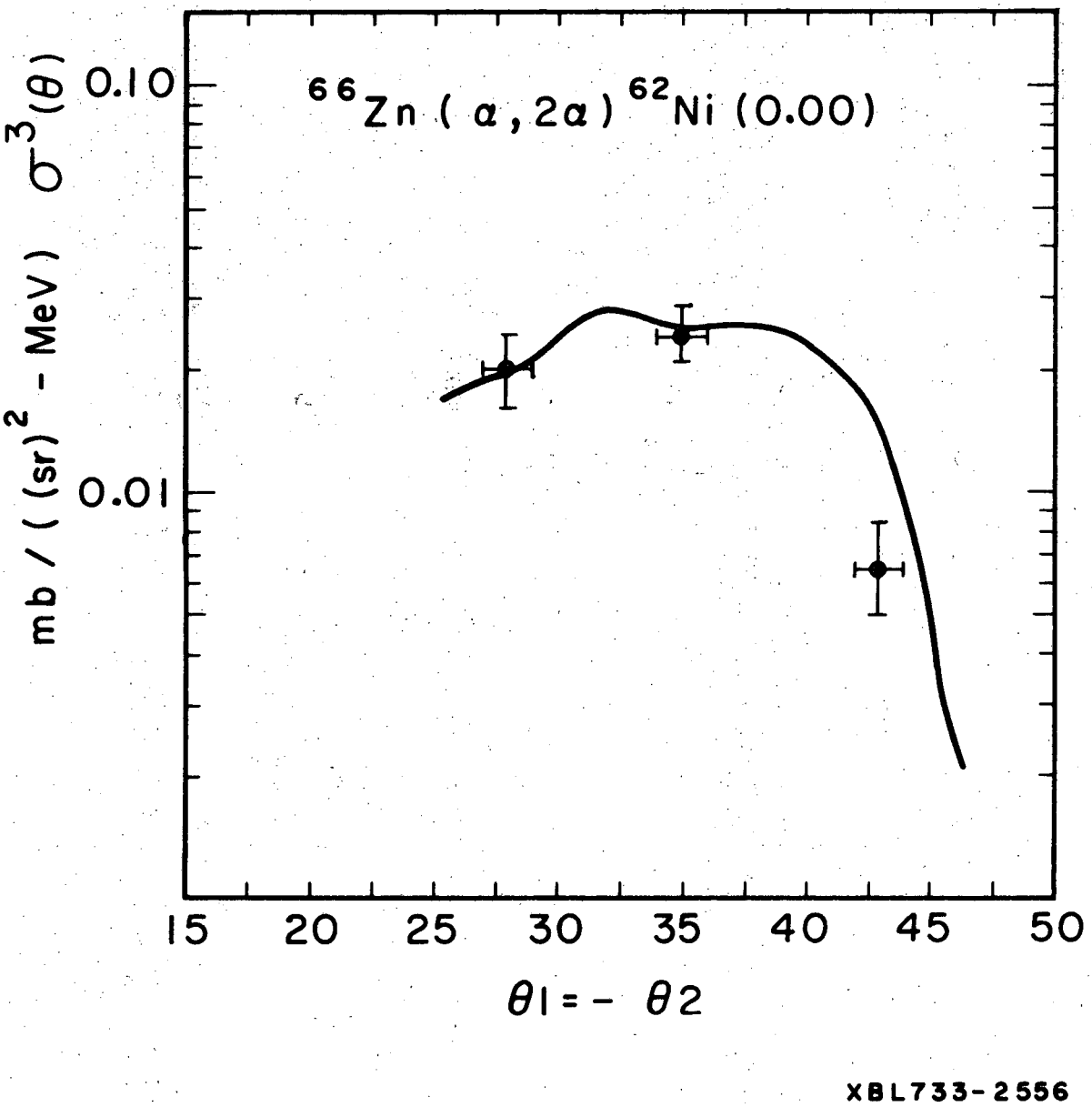

Fig. IV-20. Symmetric angular correlation for the ^{66}Zn(α, 2α)^{62}Ni(0.0) reaction.

peak cross section at the 35° point decreases steadily from ^{12}C to ^{30}Si. Beyond ^{30}Si this peak cross section remains relatively constant. Again the solid curves are parametrized DWIA calculations.

Angular correlations for transitions to the 2^+, 4.44 MeV state in ^{12}C and the 2^+, 1.97 MeV level in ^{36}Ar are given in Fig. 21. A dip in cross section at 22° is present in the $^{12}C(4.44)$ data; a similar structure was also observed in ^{12}C ground state transition (cf. Fig. IV-16). The $^{12}C(4.44)$ angular correlation then decreases monotonically with angle from the maximum at 25°. The 1.97 MeV angular correlation in ^{36}Ar does not decrease as rapidly with angle as the $^{12}C(4.44)$, and in fact the 1.97 MeV correlation from ^{36}Ar is more characteristic of the other 2^+ angular correlations. The PWIA for $L \neq 0$ transitions would predict a sharp minimum at the quasi-elastic angle. This feature is not observed in the angular correlations of Fig. IV-21.

b. Asymmetric angular correlations

The $^{12}C(\alpha, 2\alpha)^8Be$ and $^{16}O(\alpha, 2\alpha)^{12}C$ reactions were studied in an angle-asymmetric configuration. Counter 1 was fixed at 42°, while the second counter traversed the angular range from $\theta 2 = -25°$ to -47°. The asymmetric energy correlations are summarized in Appendix V. An asymmetric angular correlation was defined by extracting $\sigma^3(\theta)$ at the T_3 value where the residual recoil momentum would be constrained to lie along the beam axis. This condition occurred at a minimum in the recoil momentum-at least for the asymmetric angular range studied here. The asymmetric data were extracted in the same manner as that outlined for the symmetric angular correlation.

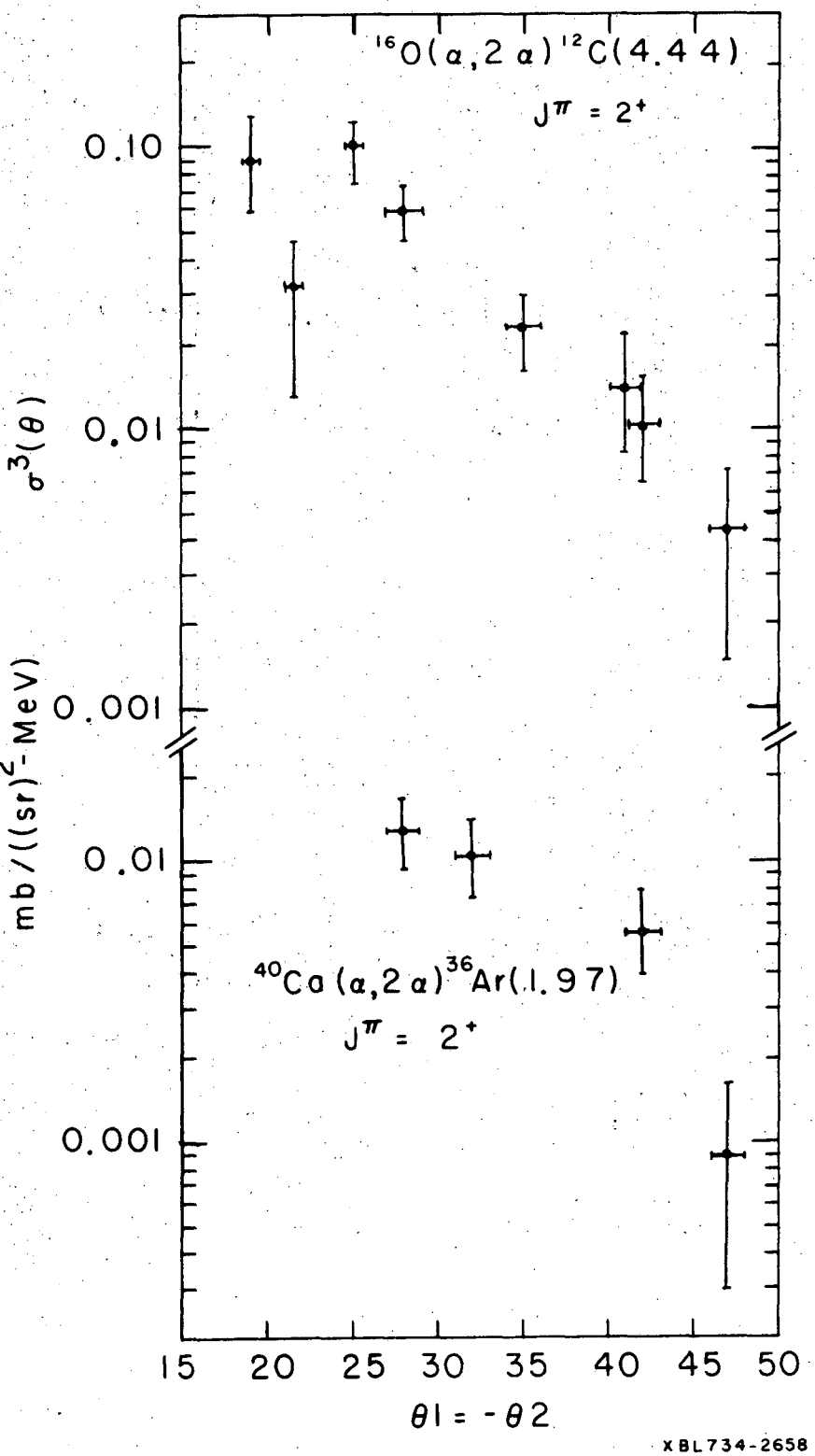

Fig. IV-21. Symmetric angular correlations for the $^{16}O(\alpha, 2\alpha)^{12}C(4.44)$, $J^\pi = 2^+$; and the $^{40}Ca(\alpha, 2\alpha)^{36}Ar(1.97)$, $J^\pi = 2^+$ reactions.

Figures IV-22 and IV-23 present the $^{12}C(\alpha, 2\alpha)^{8}Be(0.0)$ and the $^{16}O(\alpha, 2\alpha)^{12}C(0.0)$ asymmetric angular correlations. By comparison with the symmetric angular correlations (Figs. IV-15 and IV-16) the asymmetric correlations are flatter in the 28° - 42° range, and both correlations fall off rapidly at 47°. Unfortunately it was not possible to extract $\sigma^{3}(25°)$, since this angle for the second alpha particle corresponded to a kinetic energy T_3 of the first alpha which fell below the T_3 experimental cut off. As in previous figures, the solid curves are theoretical calculations which are discussed in the following section.

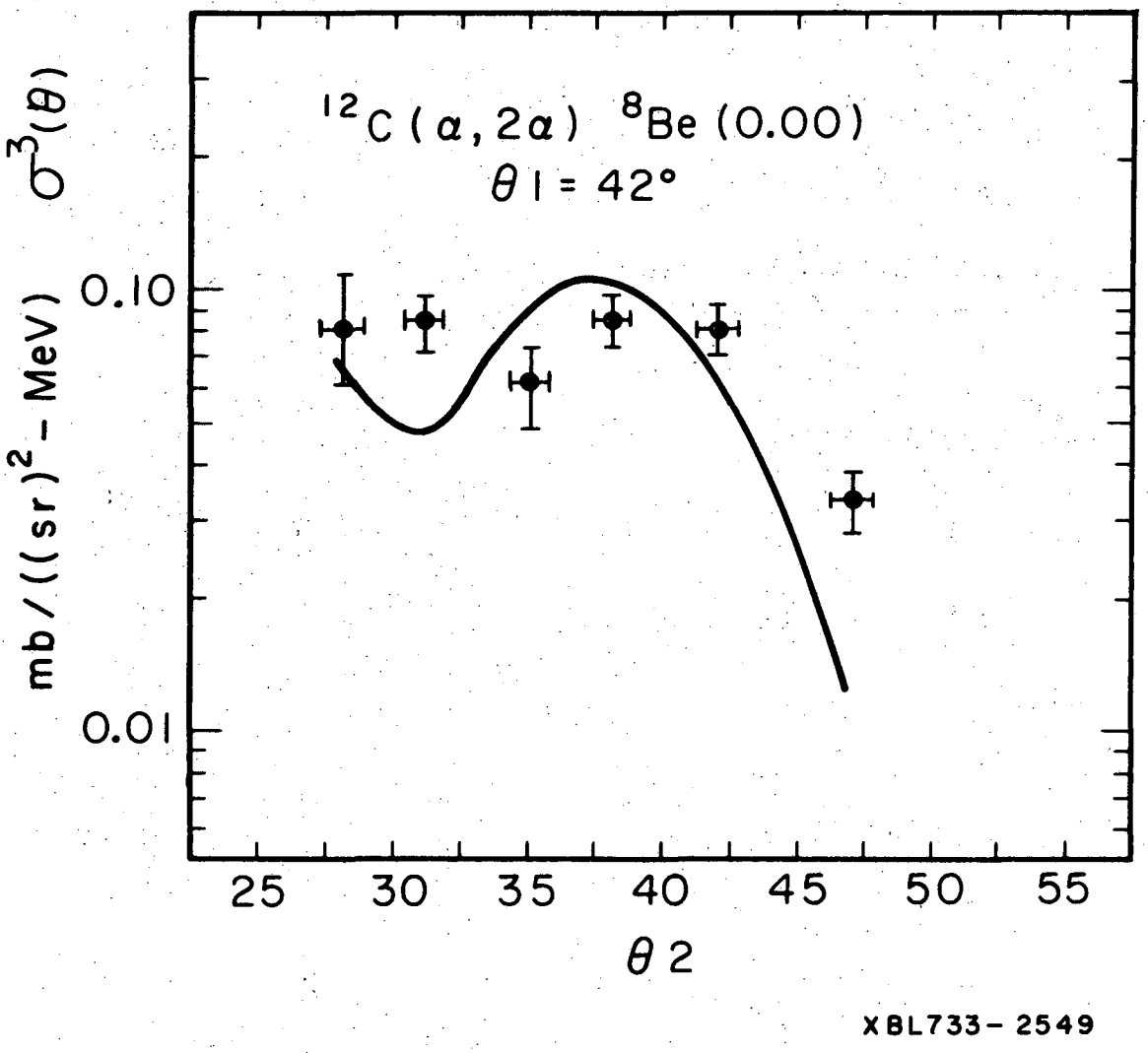

Fig. IV-22. Asymmetric angular correlation for the $^{12}C(\alpha, 2\alpha)^{8}Be(0.0)$ reaction.

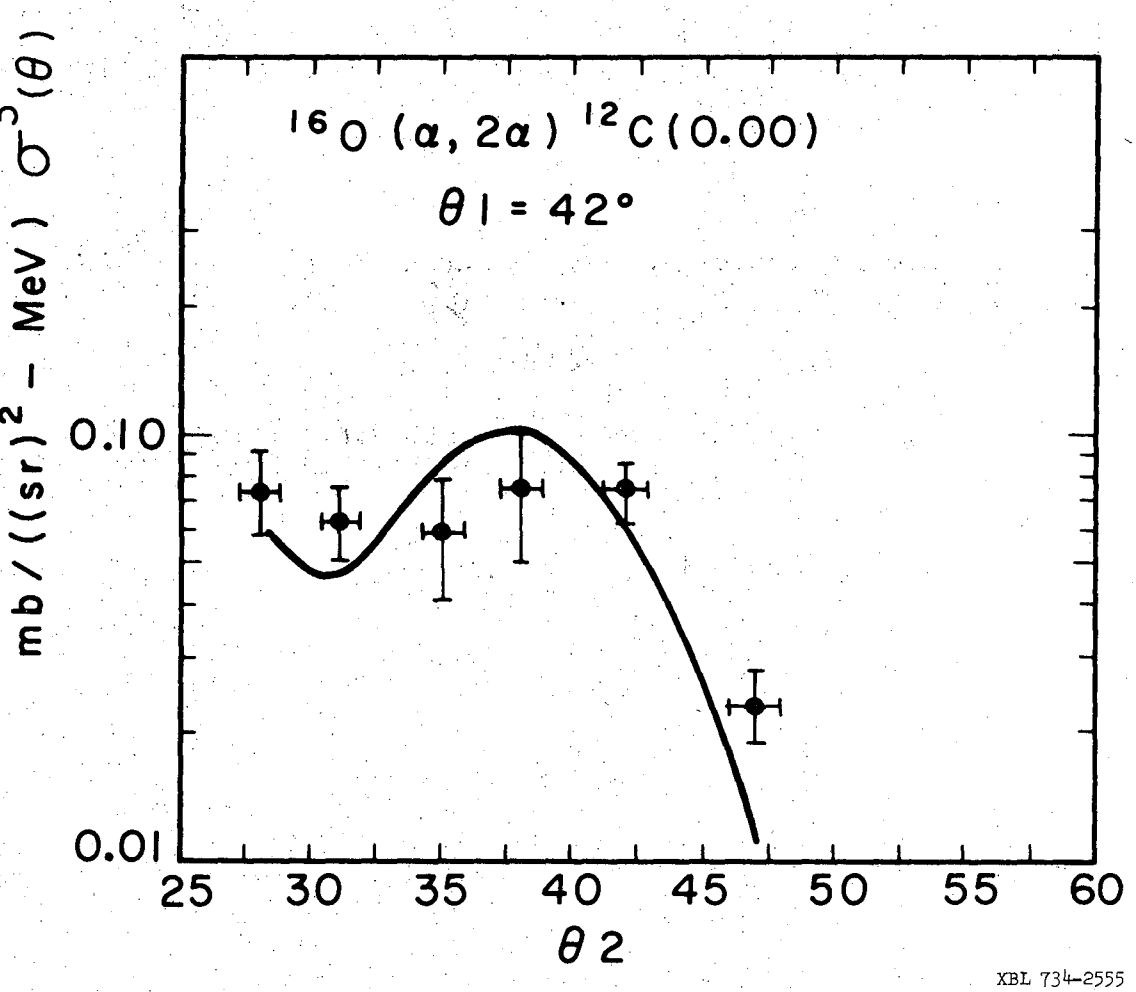

Fig. IV-23. Asymmetric angular correlation for the $^{16}O(\alpha, 2\alpha)^{12}C(0.0)$ reaction.

V. Discussion

A. Phenomenological DWIA

1. Finite detector size effects

The large solid angles used in these experiments result in a significant experimental integration of the triple differential cross section. These finite geometry effects are treated by averaging any theoretically derived quantity which is compard with experiment over the limits of the radial angular acceptances, these limits being set by the nominal and extremum angles. The nominal angle is the scattering angle which would be defined by point detectors; the extremum angles are the largest and smallest scattering angles permitted by the finite collimator widths. The total angular acceptance was about 2° per detector for most measurements. For example, the DWIA calculations based on the Sec. II discussion are carried out independently at the nominal and extremum angles and subsequently averaged. Each prediction is the result of three calculations averaged over the finite angles.

An example of averaging the theoretically predicted angular correlation cross section over the finite angles is given in Fig. V-1. The solid curve is the averaged result while the broken lines represent the nominal angle and angular extrema contributions. In these plots, the angular correlation is more complicated than the momentum or energy correlations because values of the extracted $\sigma_{aa}(T, \theta)$ vary rapidly as the symmetric angles varies. The minimum at 22° in the nominal angle prediction is much less pronounced in the averaged result.

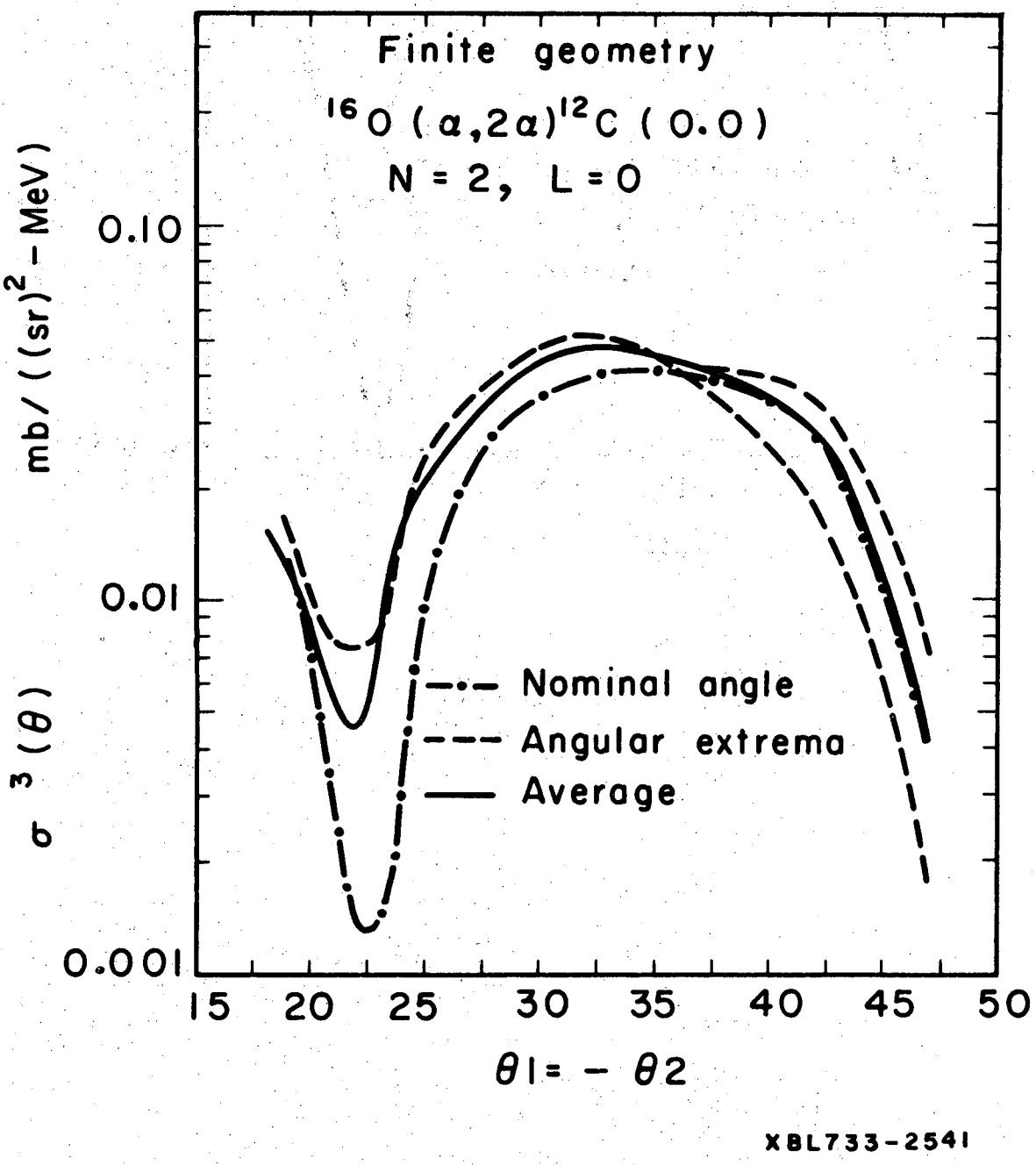

Fig. V-1. Average of theoretical angular correlation over the nominal and extremum angles. The distortion parameters are those given in Table V-1.

Finite aperture effects are also illustrated by the distribution of values attained by the recoil momentum, the distribution width being proportional to the angular acceptances. This effect is most important at the quasi-elastic angle, where the introduced uncertainties systematically combine to move the recoil momentum away from the nominal value. Both theoretical and experimental momentum distributions are plotted versus the recoil momentum averaged over the nominal and extremum angles.

All subsequent theoretically derived quantities, whether in the DWIA or PWIA framework, have been averaged in this manner. Figure V-1 is the angular correlation result given by the T_f prescription; the next section deals with experimental evidence which favors the T_f method for interpolating $\sigma_{\alpha\alpha}(T, \theta)$.

2. T_i and T_f prescription

The T_i and T_f prescription ambiguity for extracting $\sigma_{\alpha\alpha}(T, \theta)$ was introduced in Sec. II.H., and recent $(\alpha, 2\alpha)$ experiments were seen to favor the T_f method. A simple statement of the triple differential cross section in the present DWIA is

$$\sigma^3(\theta) = (KF)\ \sigma_{\alpha\alpha}(T, \theta)\ |\phi_{NL}(\vec{\xi})|^2. \qquad (V\text{-}1)$$

The equation has a simple form, and suggests that if the experimental $\sigma^3(\theta)$ reveals significant shape dependencies, it might be possible to relate these variations with one of the three factors in (V-1).

a. Symmetric data.

The experimental symmetric angular correlation for the $^{16}O(\alpha, 2\alpha)^{12}C(0.0)$ reaction is given in Fig. IV-6. Note that a minimum

occurs at the 22° point. It is now shown that this minimum can be accounted for within the framework of Eq. V-1 only if the T_f method for finding $\sigma_{\alpha\alpha}(T, \theta)$ is used. Figure V-2 gives the free α-α cross sections interpolated according to the T_i and T_f prescriptions for the $^{16}O(\alpha, 2\alpha)^{12}C(0.0)$ reaction. Finite geometry effects are included, and the T_f method predicts a minimum at 22° whereas the T_i prescription results in a flat curve in this angular range. Further, the kinematic factors are slowly varying in this kinematic region. Finally Fig. V-3 plots theoretical predictions for $|\phi_{20}(\vec{\xi})|^2$ using three distortion parameter sets. For parameters appropriate to the PWIA ($\beta_i = \beta_f = 1.0$ and $\gamma_i = \gamma_f = 0.0$) a minimum at 27° occurs. However, as the distortion parameters leave this limit, the $|\phi_{20}(\vec{\xi})|^2$ assumes a more smooth behavior, and no evidence for a minimum due to $|\phi_{20}(\vec{\xi})|^2$ at 22° is seen in any case. Thus the forward angles in the $^{16}O(\alpha, 2\alpha)^{12}C(0.0)$ angular correlation indicate the T_f prescription if favored. Also, the $^{16}O(\alpha, 2\alpha)^{12}C(4.44)$ angular correlation in Fig. IV-21 has a minimum at 22°. This structure may be due to the α-α scattering from the T_f prescription, but since a prediction for $|\phi_{12}(\vec{\xi})|^2$ is not available, the argument is not as complete as for the ground state transition.

b. Asymmetric data

A further experiment involving asymmetric geometries was pursued to help clarify the T_i and T_f ambiguity. The asymmetric angular correlation is described in Sec. IV.B. and data for the $^{16}O(\alpha,2\alpha)^{12}C(0.0)$ and $^{12}C(\alpha,2\alpha)^{8}Be(0.0)$ asymmetric angular correlations are given in Figs. IV-22 and IV-23. The asymmetric angles yield values for T_i, T_f, and θ different from those obtained in the symmetric case, and this

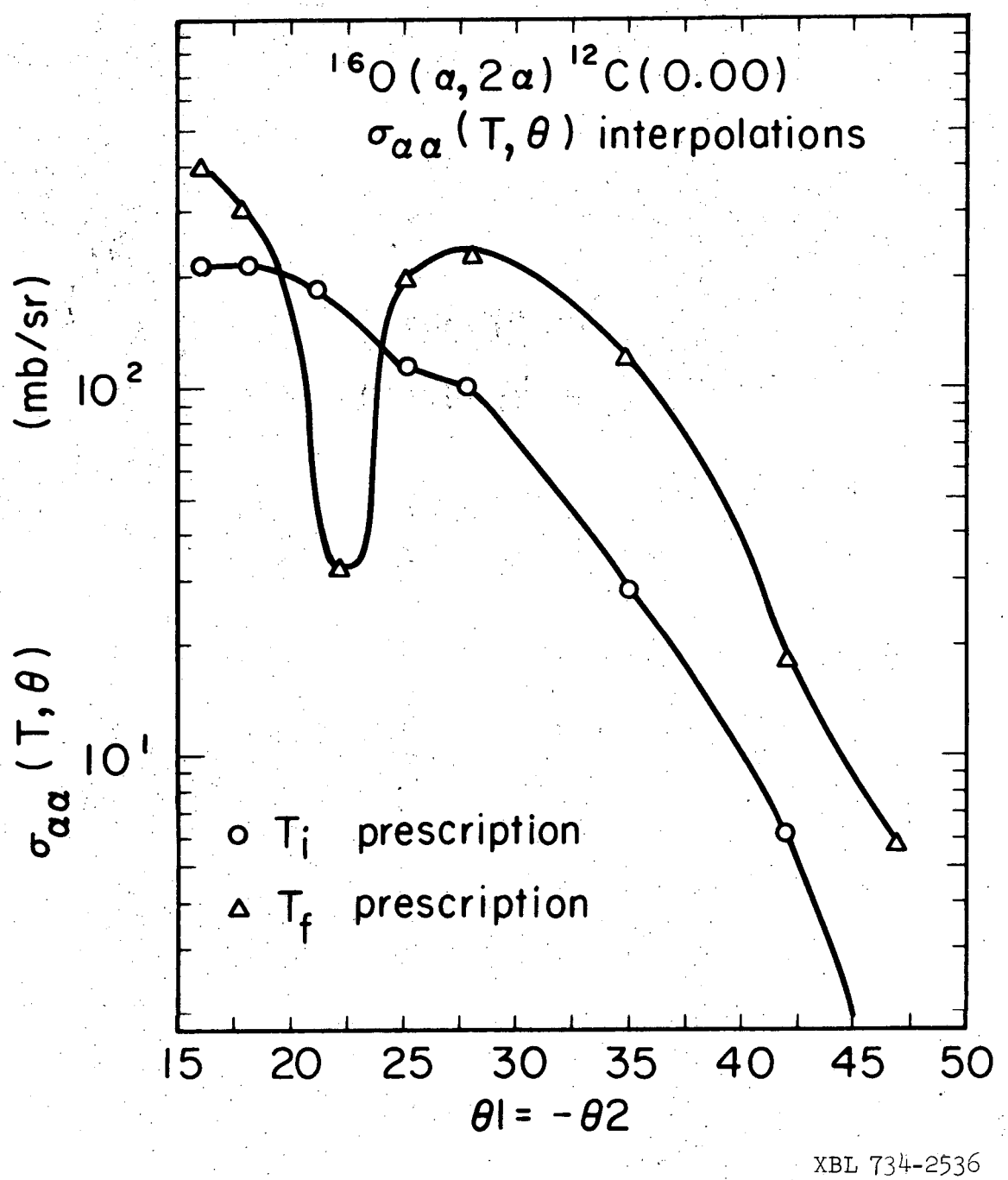

Fig. V-2. Free alpha-alpha scattering cross sections interpolated on the basis of the T_i and T_f prescriptions appropriate for the symmetric $^{16}O(\alpha, 2\alpha)^{12}C(0.0)$ angular correlation at E_α = 90 MeV.

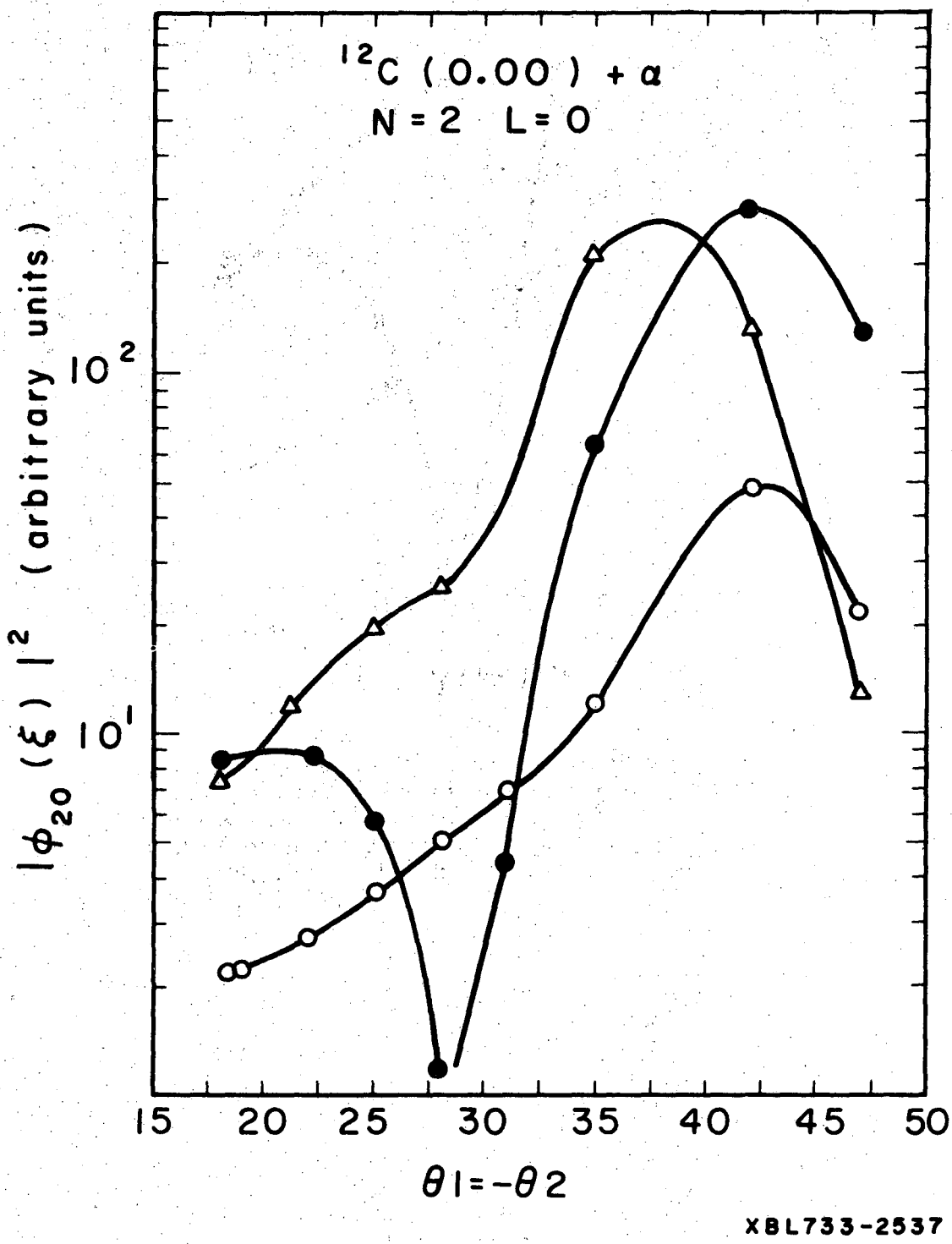

Fig. V-3. Plots of the distorted momentum distribution versus the symmetric correlation angle as a function of distortion parameters. The closed circles have $\beta_i = \beta_f = 1.0$ and $\gamma_i = \gamma_f = 0.0$; the open circles have $\beta_i = 1.30$, $\beta_f = 1.32$, $\gamma_i = .98$, and $\gamma_f = 1.28$; and finally the open triangles have $\beta_i = 1.70$, $\beta_f = 1.60$, $\gamma_i = .17$, and $\gamma_f = .55$.

experiment thus provides an independent test for the T_i or T_f method. Figure V-4 shows the free α-α cross sections - appropriate for the asymmetric $^{16}O(\alpha, 2\alpha)^{12}C(0.0)$ angular correlation - interpolated on the basis of the T_i and T_f procedures. The T_f method predicts a rather flat correlation at forward angles while the T_i prescription indicates a rapid decrease in the 28° to 35° angular region. The $|\phi_{20}(\vec{\xi})|^2$ for a range of distortion parameters is comparatively flat, particularly at the forward angles. Figures IV-22 and IV-23 revealed a flat structure at the forward angles, and thus the triple differential cross section is again most consistent with the T_f prescription.

The results of these analyses show that the free α-α cross section interpolated according to the T_f method accounts for several features in the symmetric and asymmetric angular correlations. In particular, the minimum at 22° in the $^{16}O(\alpha, 2\alpha)^{12}C(0.0)$ angular correlation as well as the decrease in $\sigma^3(\theta)$ of the symmetric and asymmetric angular correlations at large angles is accounted for. It was also seen that the forward angle structure of the asymmetric angular correlation was reproduced by the T_f method. Further, this analysis shows that the impulse approximation as represented in Eq. V-1 appears to have some validity if the T_f prescription is utilized. All subsequent calculations using the impulse approximation, unless noted otherwise, have used the T_f method for finding $\sigma_{\alpha\alpha}(T, \theta)$. The next two sections deal with the distortions of incident and scattered particles and the bound state properties of the distorted momentum distribution.

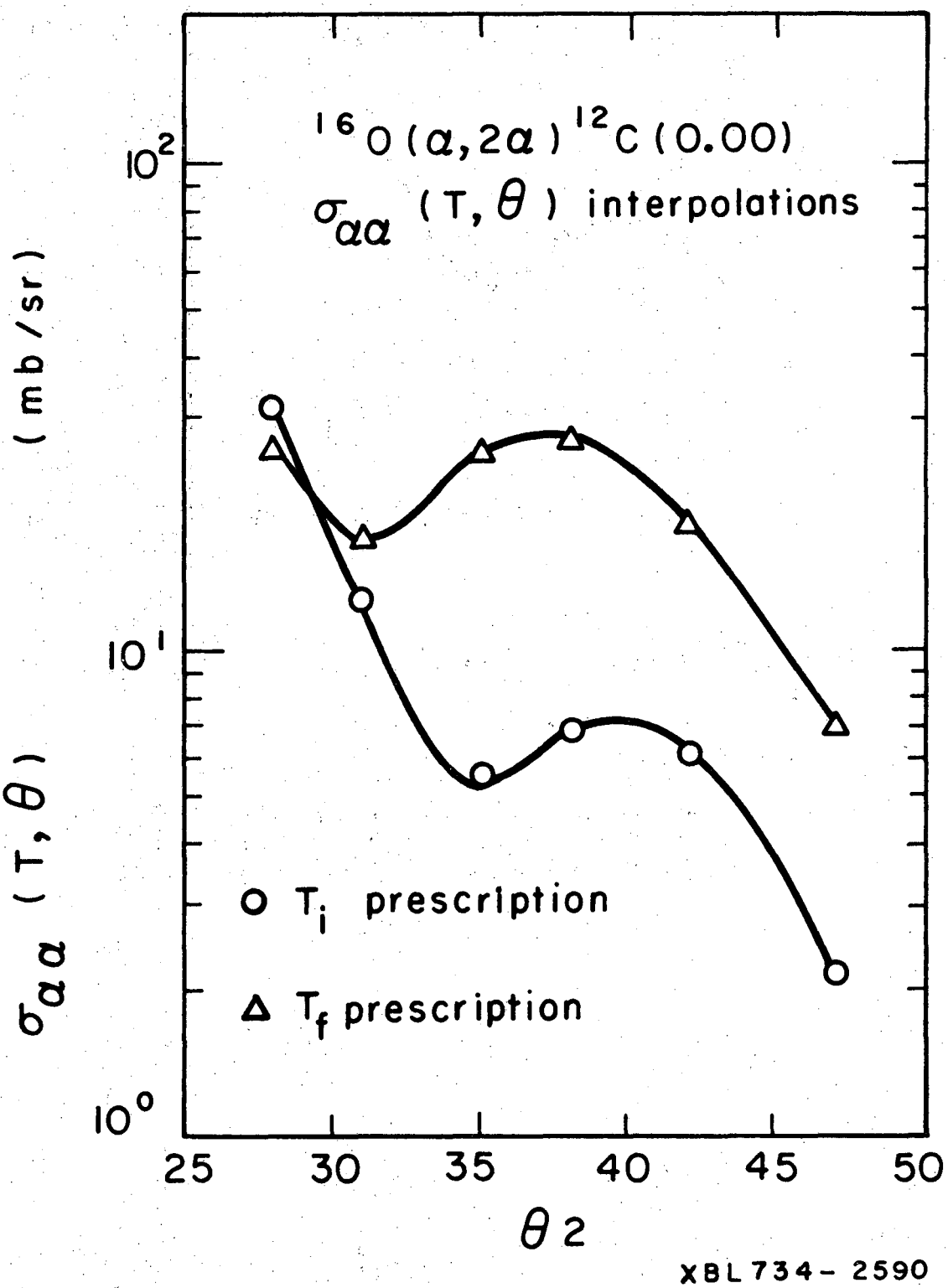

Fig. V-4. Free alpha-alpha scattering cross sections interpolated for the T_i and T_f prescription appropriate for the asymmetric $^{16}O(\alpha, 2\alpha)^{12}C(0.0)$ reaction at E_α = 90 MeV.

3. Parametrization of McCarthy-Pursey wave functions

Section II-F provided development of a phenomenological DWIA in terms of four parameters, two characterizing the incident wave (β_i and γ_i) and two characterizing the final scattered waves (β_f and γ_f). The purpose of this section is to provide a summary of parameter variation influences on theoretical predictions for the various experimentally observed correlations. It is a general result of this model that the distortion parameters have a strong effect on both the magnitude and shape of the correlations. However, the correlations are in general less sensitive to the bound state parameters.

First consider the angular correlations for the $^{16}O(\alpha, 2\alpha)^{12}C(0.0)$ reaction. Figure V-5 shows the shape and magnitude variation as β_f changes while other parameters were constant. As β_f progresses from values less than β_i to values greater than β_i, the angular correlation curve is seen to get progressively flatter. Also, for $\beta_f < \beta_i$ the peak in the angular correlation moves slowly to smaller angles and increases rapidly in magnitude. The same behavior was discovered when β_i varied from values less than β_f to values greater than β_f, while β_f, γ_i, and γ_f were constant. Best agreement with the symmetric angular correlation was obtained when $\beta_i \approx \beta_f$.

Figure V-6 shows the variation of angular correlation with the γ_f parameter, while β_i, β_f, and γ_i are constant. As γ_f goes from values less than γ_i to values greater than γ_i, a minimum at 35° disappears and the cross section for $\theta > 35°$ decreases. There is also a small decrease in absolute magnitude at the forward correlation angles as γ_f becomes larger. If the γ_i parameter is varied so that it increases with values always less than γ_f, while β_i, β_f, γ_f are constant, then the angular correlation curve drops monotonically. For example, with the values $\beta_i = 1.30$, $\beta_f = 1.32$, and $\gamma_f = 1.28$, the γ_i could be varied from .50 to 1.00 without appreciably changing the angular correlation shape, although the magnitude was displaced nearly an order of magnitude. For $\gamma_i = .35$ the minimum at 22° became too deep, and for values $\gamma_i > 1.00$ the non-physical structures outlined in Fig. V-6 became evident. Setting $\gamma_i = \gamma_f = 0.0$, the predicted magnitude increased by a factor of

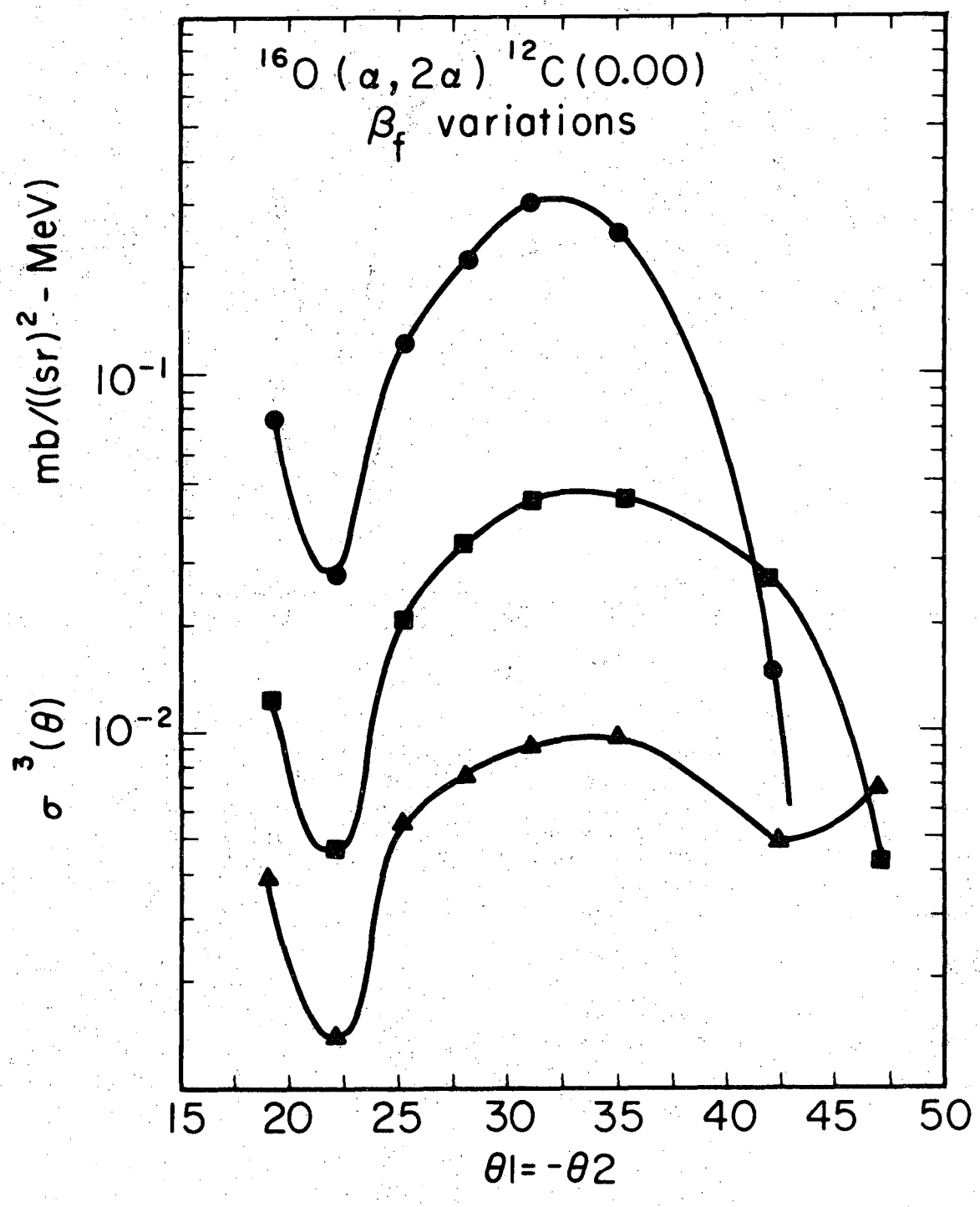

XBL733-2540

Fig. V-5. Variation of β_f, a test for magnitude and shape dependence of the $^{16}O(\alpha, 2\alpha)^{12}C(0.0)$ reaction. The circles have $\beta_f = 1.20$; the squares have $\beta_f = 1.32$; and the triangles have $\beta_f = 1.44$. The remaining distortion parameters are $\beta_i = 1.30$, $\gamma_i = .98$, and $\gamma_f = 1.28$, and were held constant.

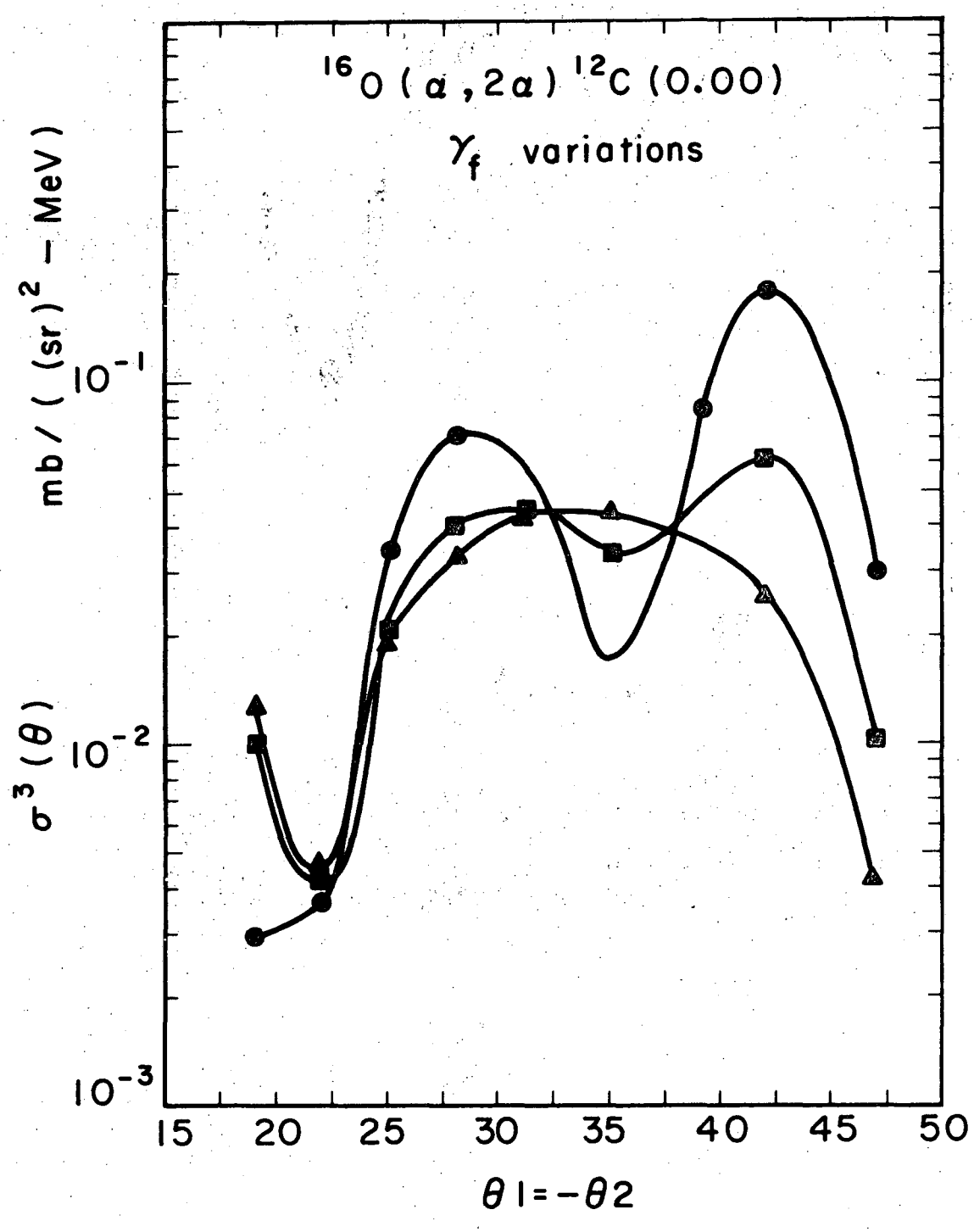

XBL733-2539

Fig. V-6. Variation of γ_f, a test for magnitude and shape dependence of the $^{16}O(\alpha, 2\alpha)^{12}C(0.0)$ reaction. The circles have $\gamma_f = .60$; the squares have $\gamma_f = .90$; and the triangles have $\gamma_f = 1.28$. The remaining distortion parameters are constant and their values are $\beta_i = 1.30$, $\beta_f = 1.32$, and $\gamma_i = .98$.

seventy-five, but the shape remained similar to the $\gamma_f = 0.60$ curve in Fig. V-6.

The momentum correlation predictions were most sensitive to variations in β_i and β_f. Taking $\gamma_i = .98$ and $\gamma_f = 1.28$ and decreasing the couple (β_i, β_f) from (1.60, 1.56) to (1.10, 1.08) the momentum correlation broadened about .1 $(fm)^{-1}$, the difference taken at the FWHM of the two curves. The prediction corresponding to (1.10, 1.08) was about 4% greater in magnitude than the (1.60, 1.56) prediction. The γ_f variation outlined in Fig. V-6 had very little effect on the momentum correlation shape, although the curves did drop regularly in magnitude as γ_f increased. This analysis was made over the range $|\vec{q}| < .5\ (fm)^{-1}$. For $|\vec{q}| > .5\ (fm)^{-1}$ the theoretical prediction fails to fit the data magnitude.

One set of distortion parameters was found which gave good fits to the angular correlations for targets from ^{12}C to ^{30}Si. These are given in columns 2-5 of Table V-1. A slight adjustment in the β_f parameter was necessary to maintin comparable shape fits for the Ca and Zn targets and this value is given in the table. The γ_i and γ_f parameters were chosen to give a total normalization of $\sigma^3_{exp}(\theta)/\sigma^3_{theory}(\theta) = 3.0$ for the ^{12}C target. This was a rather arbitrary procedure, as only the magnitude and not the shape was changed when γ_i was varied with $\gamma_i < \gamma_f$, as previously discussed. A much smaller normalization of approximately .005 would have been obtained from the PWIA.

Columns 6-9 of Table V-1 give theoretical predictions for the β, γ parameters based on α-nucleus optical model potentials and relations II-38 and II-39. The theoretical β_i and γ_i for ^{24}Mg, ^{26}Mg, and ^{28}Si targets are calculated from the shallow optical model parameters given

Table V-1. Theoretical and fit distortion parameters for the symmetric angular correlations.

	Fit Parameters				Derived Parameters			
Target	β_i	γ_i	β_f	γ_f	β_i	γ_i	β_f	γ_f
^{12}C	1.30	.98	1.32	1.28				
^{16}O	1.30	.98	1.32	1.28				
^{24}Mg	1.30	.98	1.32	1.28	1.46	1.16	1.72	.822
^{26}Mg	1.30	.98	1.32	1.28	1.38	2.18		
^{28}Si	1.30	.98	1.32	1.28	1.42	2.08	1.57	.929
^{30}Si	1.30	.98	1.32	1.28				
^{40}Ca	1.30	.98	1.28	1.28	1.45	1.25	1.62	1.28
^{44}Ca	1.30	.98	1.28	1.28			1.65	1.53
^{66}Zn	1.30	.98	1.28	1.28				

by Rebel [Reb 72] in the analysis of 104 MeV α scattering. The shallow well of Hauser [Hau 72] also taken with E_α = 104 MeV was used for the theoretical ^{40}Ca initial state distortion parameters.

The ^{24}Mg and ^{28}Si final state distortion parameters were calculated from an optical model analysis of 28 MeV alpha scattering [Sat 65]. The ^{40}Ca and ^{44}Ca final state parameters were taken from an analysis of α -Ca elastic scattering at E_α = 31 MeV [Lipp 67]. A comparison of the fit and predicted distortion parameters shows that the fit parameters are generally smaller than the derived quantities. This result is similar to (p, 2p) work using the complete McCarthy-Pursey wave functions [Deu 68, McC 68].

It is interesting to examine the theoretical distorted momentum distribution of Eq. II-45 plotted as a function of T_3. Such a plot for the ^{16}O(α, 2α)^{12}C(0.0) reaction at the symmetric angles of 28°, 35°, and 42° is given by the solid lines in Fig. V-7. The distortion parameters are those which gave a best fit to the angular correlation data. The $|\phi_{20}(\vec{\xi})|^2$ reveals a strong peaking tendency at the quasi-elastic angle for the $0^+ \rightarrow 0^+$ transitions. A similar plot of interpolated α-α cross sections over the same T_3 and angle range also yields an inverted parabolic shape, which is much more slowly varying with angle. Contrary to the $|\phi_{20}(\vec{\xi})|^2$ behavior, however, the angular variation of $\sigma_{\alpha\alpha}(T, \theta)$ flattens as it approaches the quasi-elastic angle. The net result is that calculations based on $|\phi_{20}(\vec{\xi})|^2$ predict a narrowing of the energy correlation as the quasi-elastic angle is approached from smaller symmetric angles. The symmetric angle energy correlations from the ^{16}O(α, 2α)^{12}C(0.0) and the ^{24}Mg(α, 2α)^{20}Ne(0.0) data given in Figs.

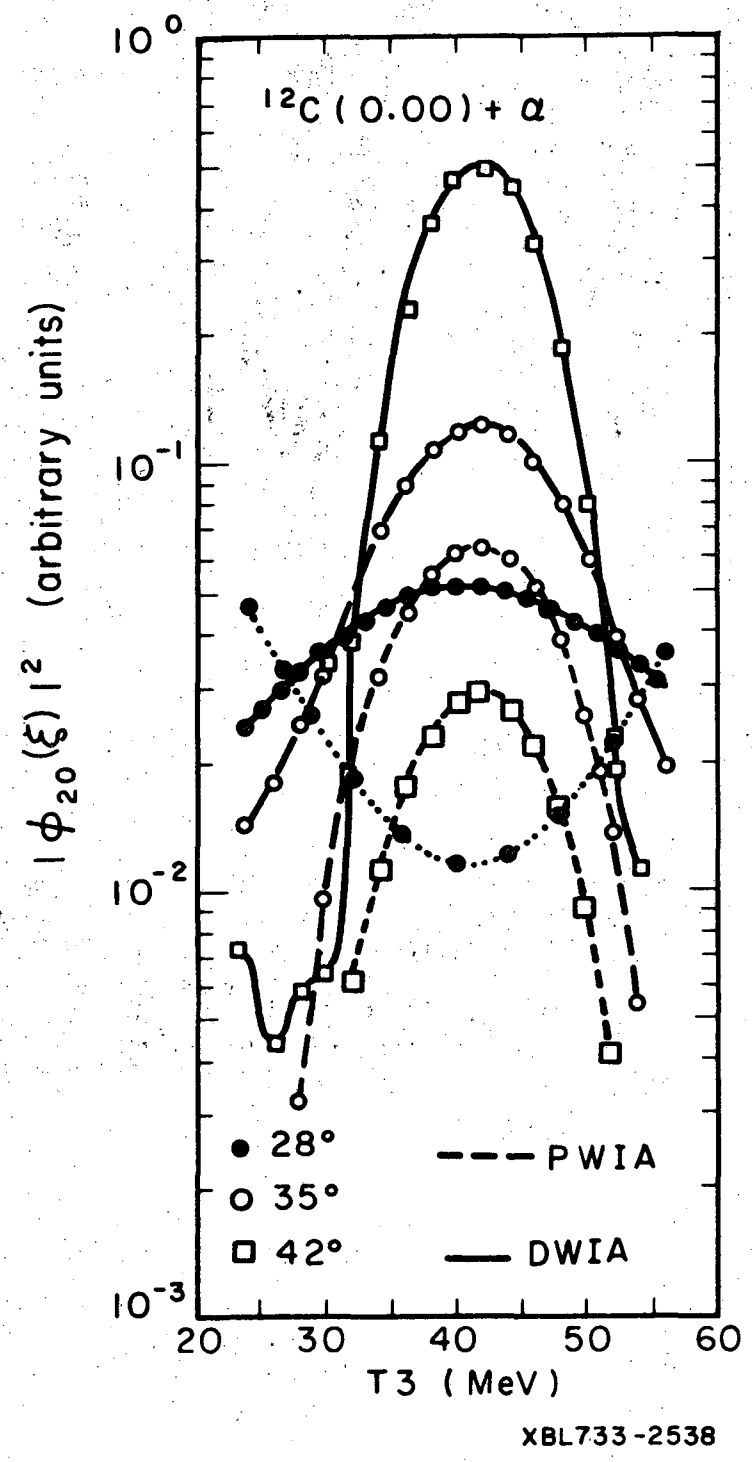

Fig. V-7. Plot of the theoretical momentum distribution for the $^{12}C(0.0)+\alpha$ state versus T_3. The DWIA with distortion parameters from Table V-1 and PWIA ($\beta_i = \beta_f = 1.0$ and $\gamma_i = \gamma_f = 0.0$) are compared as a function of angle.

IV-10 and IV-11 revealed this identical behavior: a narrowing of the energy correlation as a symmetric quasi-elastic angle is approached. The dashed lines in Fig. V-7 give the PWIA prediction for $|\phi_{20}(\vec{\xi})|^2$ and the 28° PWIA result is seen to be very different from the 28° DWIA prediction which does fit the data (cf. solid lines in Fig. IV-10). The conclusion is that the distorted momentum distribution does account for the systematic energy correlation behavior, and that the PWIA counterpart would fail in describing the systematics. Thus, as in the preceding section concerning the interpolation method for free α-α cross sections, the simple statement of the DWIA in Eq. (V-1) has permitted the identification of significant experimental observations with specific terms in this equation.

Thus the DWIA has been shown to have at least three significant advances over the PWIA: first, the predicted cross section is much smaller than the PWIA; second, it has accounted for the narrowing of the energy correlation as the quasi-elastic angle is approached; and third, by varying the distortion parameters, reasonably good shape fits have been obtained for the various correlations. The successes of the last two sections give confidence in using V-1 for further data analysis.

4. Radial wave function

The bound state radial wave function was introduced in Sec. II.G., and is part of the $|\phi_{NL}(\vec{\xi})|^2$ calculation. A summary of parameters and investigations used to determine the $R_{NL}(\rho)$ is given here.

One may question the uniqueness of Eq. (II-47) in determining N, the number of radial nodes in $R_{NL}(\rho)$. An alternative proposal

The harmonic oscillator radial wave functions were also investigated as a possibility for calculating the theoretical momentum distribution. The radial harmonic oscillator wave function given in Fig. V-8 has oscillator constant equal to .75, and it is seen to approach zero more rapidly than the finite well wave function at the largest radii. Predictions based on a harmonic oscillator wave function for the $^{16}O(\alpha, 2\alpha)^{12}C(0.0)$ momentum correlation are nearly identical in shape with the finite well wave function for $q \leq .5(fm)^{-1}$, although the harmonics oscillator predicted an absolute magnitude 20% lower.

Angular correlations calculated with harmonic oscillator and finite well wave functions are given in Fig. V-9. The oscillator prediction is similar to the finite well angular correlation, but it peaks at a slightly more forward angle and the cross section falls off faster at large angles. At the angular correlation peak the harmonic oscillator yielded approximately 50% more cross section than the finite well radial wave function. The oscillator parameter used in Fig. V-9 was .75: this value was derived by fitting to the $^{16}O(\alpha, 2\alpha)^{12}C(0.0)$ data. The distortion parameters are constant in Fig. V-9, and are those which gave a best fit to the data using the finite well wave function. Subsequent calculations revealed that changing the distortion parameters for the harmonic oscillator radial wave function made the shape predictions poorer. As the finite well wave function fit to the $^{16}O(\alpha, 2\alpha)^{12}C(0.0)$ angular correlation (Fig. IV-16) is quite good, this analysis suggests a preference for finite well wave functions.

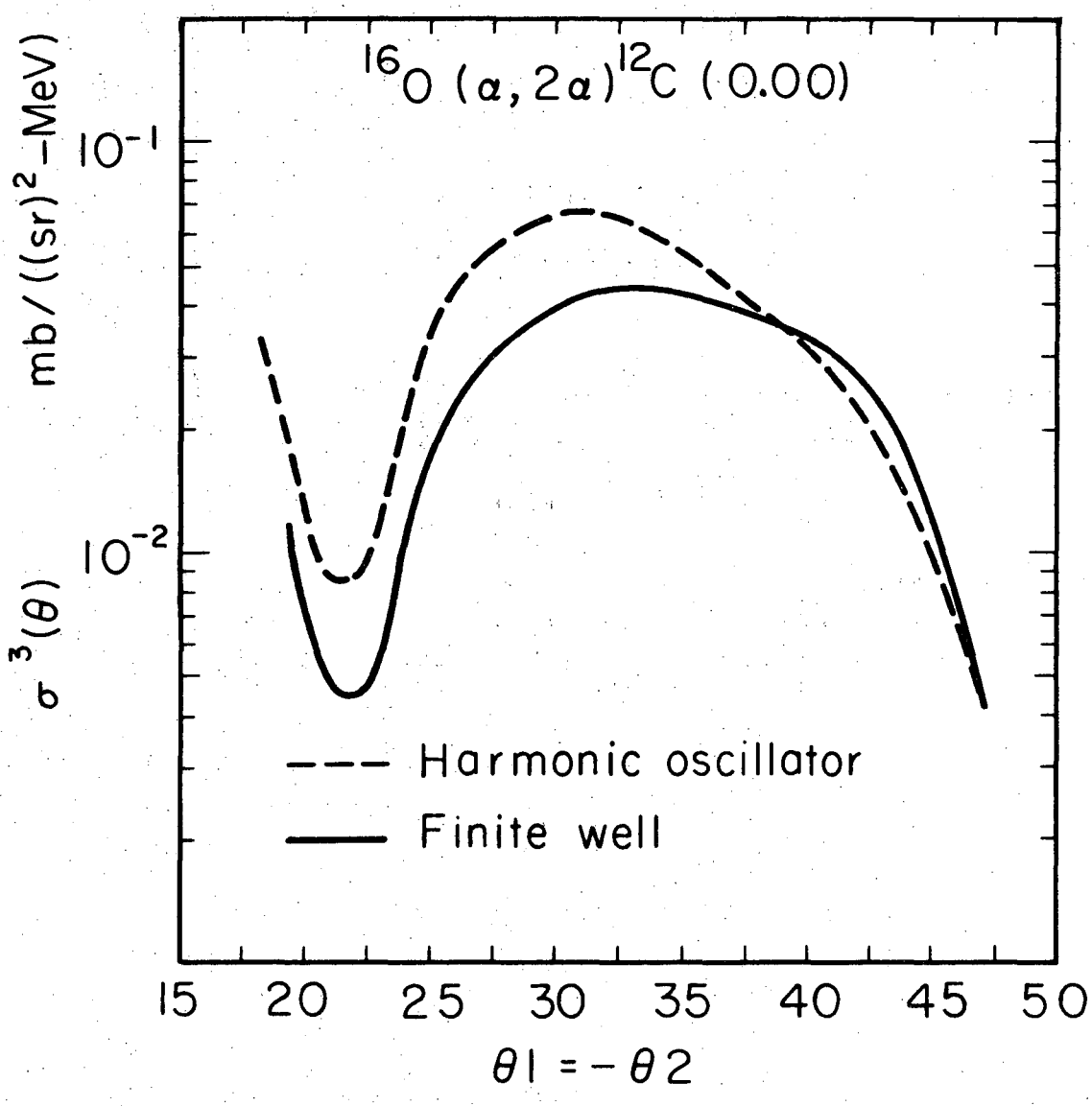

XBL733-2542

Fig. V-9. Result for the $^{16}O(\alpha, 2\alpha)^{12}C(0.0)$ angular correlation using finite well and harmonic oscillator wave functions. The distortion parameters are given in Table V-1.

The most obvious conclusion of the bound state wave function analysis is that the predicted cross section is not very sensitive to the bound state features of the calculation. A large change in the angular correlation is found when N = 0 finite well wave functions replaced $N \neq 0$ wave functions, and it was discovered that the fit to angular correlation shapes with N = 0 wave functions are inferior. Good shape fits could not be recovered by varying the distorted wave parameters.

All future calculations, unless noted, have used finite well radial wave functions using Eq. (11-47) for the nodal determination. Table V-2 summarizes the targets, bound state parameters, alpha separation energies, number of radial nodes based on L = 0, and the derived binding potential. These potentials are in reasonable accord with optical model parameters derived from alpha-nucleus scattering over a broad energy range [Reb 72, Sat 65, Bar 71, McF 66]. The Coulomb radius used in these calculations is $R_c = 1.44\ A^{1/3}$.

5. Target mass (A) dependence and surface localization in DWIA

a. A dependence of DWIA

In order to investigate the DWIA A dependence, a series of calculations for the ^{16}O, ^{28}Si, ^{40}Ca, and ^{66}Zn targets were carried out. Finite well wave functions with the nodal prescription of Eq. (II-47) are used; the alpha separation energies for determining the bound state wave function and reaction Q-values which determine the $\sigma_{aa}(T, \theta)$ are taken to be constants equal to +5.0 MeV and -5.0 MeV, respectively. Also, the distortion parameters are constant. The angular correlation results for this set of conditions are given in Fig. V-10. It is seen

Table V-2. Bound state parameters for the finite well calculations.

Target	r_0 (fm)	a_0 (fm)	Sep. energy (MeV)	N	V (MeV)
^{12}C	1.30	.73	7.369	2	68.8
^{16}O	1.30	.73	7.161	2	60.9
^{24}Mg	1.30	.73	9.316	4	109.5
^{26}Mg	1.30	.73	10.614	4	106.9
^{28}Si	1.30	.73	9.981	4	104.1
^{30}Si	1.30	.73	10.650	4	100.9
^{40}Ca	1.30	.73	7.041	4	87.5
^{44}Ca	1.30	.73	8.846	5	109.4
^{66}Zn	1.35	.73	4.558	6	109.2

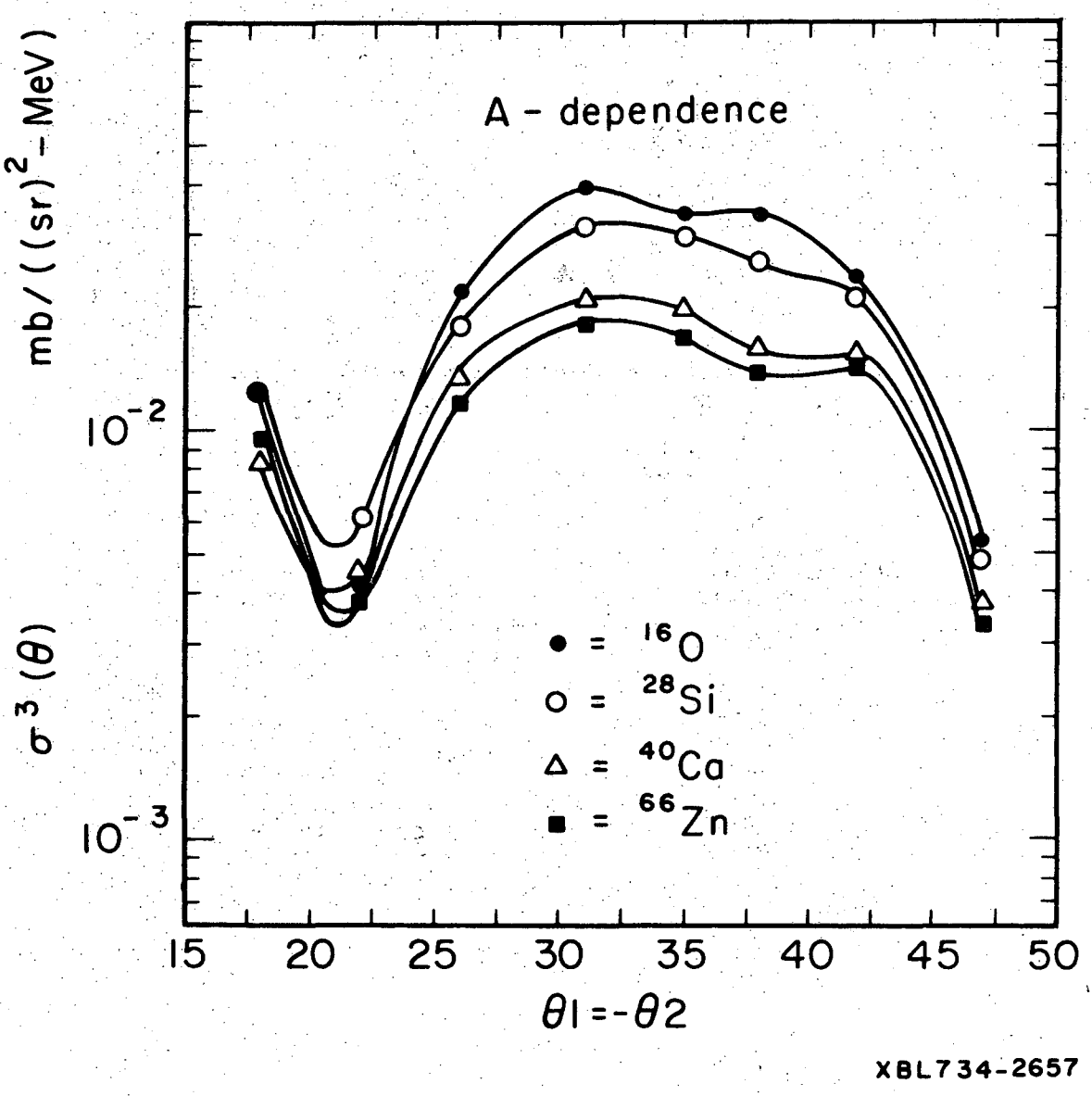

Fig. V-10. Target mass dependence given by the theoretical prediction for the angular correlation. The distortion parameters are constant, and they equal the ^{16}O values given in Table V-1.

that the curves are similar in shape and that they decrease regularly with increasing A. All the curves have a maximum at 31° symmetric angle.

The A dependence of a nuclear reaction cross section depends on whether the reaction occurs throughout the nuclear volume, on the surface, or perhaps only on a ring about the nucleus. If these three possibilities are normalized to the nuclear mass A, then the following A dependencies occur:

$$\text{Volume:} \quad f_V = (r_0 A^{1/3})^3/(r_0 A^{1/3})^3 = 1 \tag{V-2}$$

$$\text{Surface:} \quad f_S = 4\pi(r_0 A^{1/3})^2/\frac{4}{3}\pi(r_0 A^{1/3})^3 \propto \frac{1}{A^{1/3}} \tag{V-3}$$

$$\text{Ring:} \quad f_R = 2\pi(r_0 A^{1/3})/\frac{4}{3}\pi(r_0 A^{1/3})^3 \propto \frac{1}{A^{2/3}} \tag{V-4}$$

i.e., no A dependence of cross section for a volume reactions, as $A^{-1/3}$ for surface reaction, and as $A^{-2/3}$ for a reaction that occurs on a ring. Assuming the form

$$\sigma^3(\theta) = cA^x \tag{V-5}$$

one can derive the A dependence, the value of x, from the results of Fig. V-10. Taking $\sigma^3(\theta)$ at the 31° maximum and plotting the four points available from Fig. V-10 a value of x from the linear equation

$$\ell n\, \sigma^3_{max}\,(31°) = \ell n\, c + x\, \ell n\, A \tag{V-6}$$

equal to -.56 is found. This result is intermediate between the surface and ring model, and is consistent with the surface localization predicted by Lim and McCarthy [Lim 62, McC 62].

Further A dependence calculations were carried out with N = 0, L = 0 wave functions. They gave no A-dependence at the angular correlation peak. This suggests that the localization is due to bound state properties rather than the reaction theory effects. This interpretation (bound state properties) of surface localization has been given to (p, 2p) reaction calculations involving the p-orbital [Lim 64]. However, there are several indications that this is not the case in the (α, 2α) reaction. First, the previous section showed that the N = 0 case did not provide as good a fit to the angular correlation as the N = 2 wave function. Second, since the ^{62}Ni(0.0) +α relative wave function has N = 6 and the corresponding ^{12}C(0.0) + α wave function has N = 2, one would expect the ^{66}Zn wave function to weigh the nuclear surface more strongly than the ^{16}O wave function on the basis of bound state radial wave function arguments. This is true since the N = 6 wave function has larger pieces of wave function at greater radii than the N = 2 relative motion wave function. However, Fig. V-10 shows that the opposite behavior is observed: the predicted cross section decreases with A. Thus the N = 0 wave functions seem to give an anomalous result. Perhaps this should not be too surprising since these wave functions did not fit the angular correlations. Hence, it is concluded that the DWIA predicts a decrease in $\sigma^3(\theta)$ as A increases, and the decrease is most nearly characteristic of a reaction taking place on a ring. The next section shows still further that the (α, 2α) reaction is occurring on the nuclear surface.

b. Surface localization investigations with radial cut offs

If the reaction is localized in the nuclear surface-as the previous discussion suggests-one might expect to be able to set the interior

contribution of the DWIA matrix element to zero without changing the predictions. A series of DWIA calculations with a cut off in the radial integrals for the $^{16}O(a, 2a)^{12}C(0.0)$ angular correlation is given in Fig. V-11. Wave functions with N = 2 were used and distortion parameters were constant. The cut offs used in Fig. V-11 are indicated by arrows in Fig. V-8. For cut offs up to 2.50 fm there are small changes in shape but very little change in magnitude. Furthermore, a cut off at 3.10 fm is still very similar to the cut off at 2.50 fm in both magnitude and shape. However, at a cut off radius of 3.80 fm a factor of two decrease in cross section occurs. One may conclude then that the significant contributions to the cross section occur at radii greater than 3.1 fm. The radius calculated from $R = r_0 A^{1/3}$ for ^{16}O with $r_0 = 1.30$ fm is 3.28 fm, which corresponds to the half density point in a Woods-Saxon form. This same result was obtained for ^{28}Si and ^{66}Zn cut off calculations, and the conclusion is that the nuclear interior has only minor effects in determining $\sigma^3(\theta)$. This conclusion supports the A-dependence calculations of the previous section.

Another test for localization can be made by going to the plane wave limit, and again examining the cut off effects in the radial integrals. Such a calculation is given for the $^{16}O(a, 2a)^{12}C(0.0)$ angular correlation in Fig. V-12. The result is that the theoretical PWIA predictions are influenced to a larger extent than the DWIA by insertion of cut offs. That is, the PWIA cross section changes more rapidly no matter what cut off enters the calculation. This is a reasonable result since the plane waves are not localized and thus are sensitive to the whole nuclear volume; this again favors the localization of the DWIA to the nuclear surface.

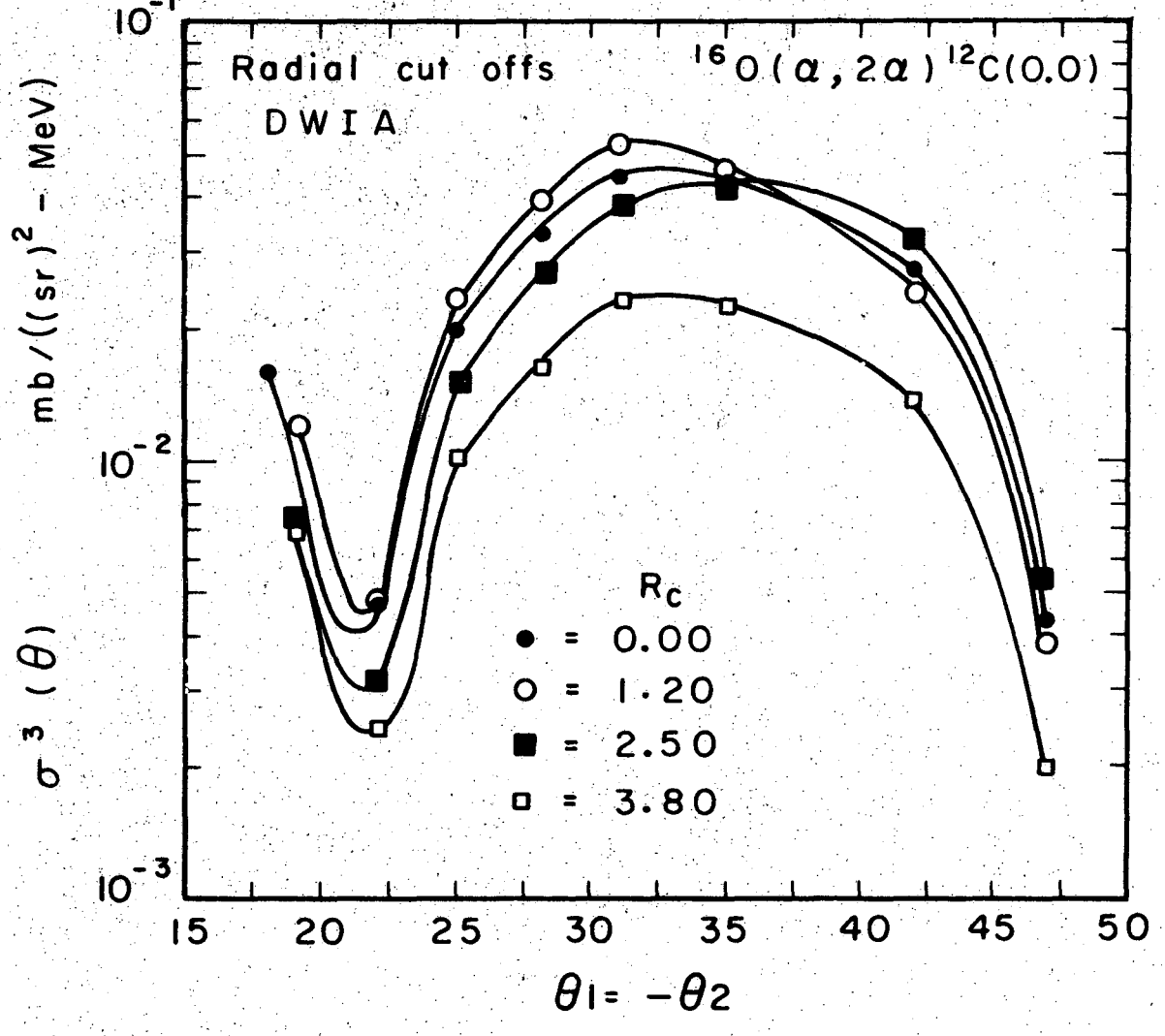

XBL734-2656

Fig. V-11. Effects of radial cut offs in the theoretical angular correlation predictions for the $^{16}O(\alpha, 2\alpha)^{12}C$ reaction. The ^{16}O distortion parameters from Table V-1 were used.

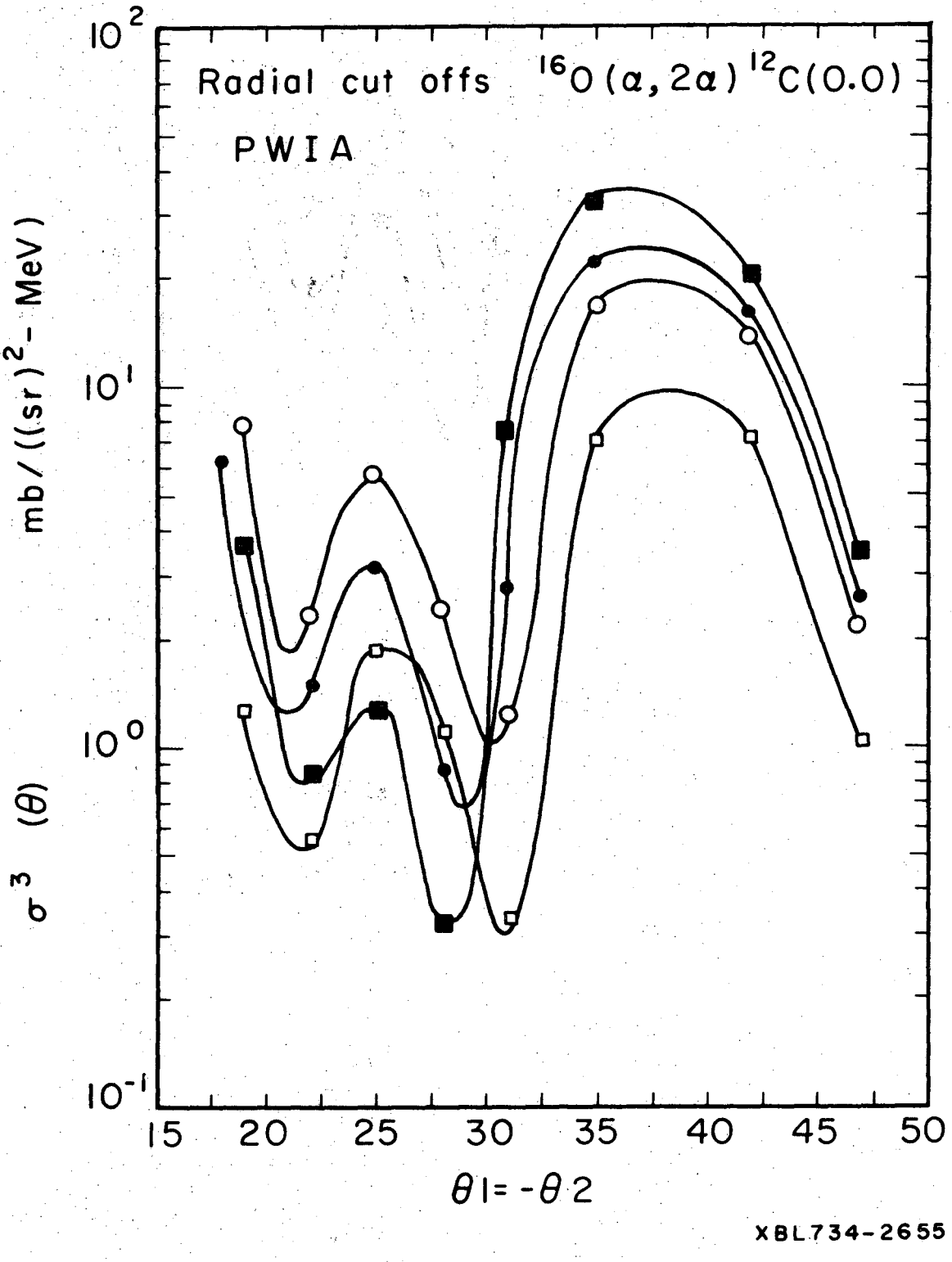

Fig. V-12. Effects of radial cut offs in the PWIA predictions for the $^{16}O(\alpha, 2\alpha)^{12}C(0.0)$ angular correlation. The same bound state was used in Fig. V-12 as in Fig. V-11. The notation for cut off radii is the same as in Fig. V-11.

6. DWIA predictions for experimental correlations

This section summarizes the DWIA fits to the various experimental correlations. Summarizing the previous five sections, the theoretical curves contain the following assumptions, approximations, and assertions:

(1) the theoretical calculations are averaged over the nominal and extreme angles of the detecting system;

(2) the T_f prescription for finding $\sigma_{a\alpha}(T, \theta)$ is used;

(3) the fit parameters of Table V-1 are used in the phenomenological distorted waves, and a combination of γ_i and γ_f parameters were found which gave $\sigma^3_{exp}(\theta)/\sigma^3_{theory}(\theta) = 3.0$ for the ^{12}C target;

(4) finite well wave functions are used with the bound state parameters given in Table V-2; implicit in this procedure is that the bound alpha is in the lowest oscillator state;

(5) experience with the phenomenological DWIA–because it accounted for many aspects of the data–gives confidence in extracting relative spectroscopic factors.

a. Angular correlations

(i) Symmetric

The fits to the ground state to ground state angular correlations are given in Figs. IV-15 to IV-20 for all the targets studied. The distortion parameters were not changed from ^{12}C to ^{30}Si since the shape fits seemed to be acceptable without any adjustment over these masses. A small adjustment was made in β_f for the Ca and Zn targets to maintain good shape fits. A summary of the distortion parameters is given

in Table V-1, and the corresponding bound state parameters are given in Table V-2. The Coulomb radius parameter was 1.44 fm.

Equation (II-29) and Eq. (1) of Appendix II show that a spectroscopic factor measuring the amount of alpha clustering can be defined by:

$$S_\alpha = \sigma^3_{exp}(\theta) / \sigma^3_{theory}(\theta) \qquad (V\text{-}6)$$

where

$$\sigma^3_{theory}(\theta) = (KF)\, \sigma_{\alpha\alpha}(T, \theta) \int_{-\infty}^{+\infty} e^{i\vec{\xi}\cdot\vec{\rho}}\, R_{NO}(\rho)/\sqrt{4\pi}\ d\vec{\rho}\,. \qquad (V\text{-}7)$$

It has been mentioned that a rather arbitrary variation of the γ_i parameter yielded $S_\alpha = 3.00$ for ^{12}C. Angular correlation calculations for all nuclei were done using parameters of Tables V-1 and V-2, and the extracted S_α are given in column II of Table V-3. The errors indicate the limits at which the normalization is judged to worsen the shape fit. Due to the somewhat arbitrary and empirical approach to the determination of distortion parameters, the S_α should be considered as relative quantities.

(ii) Asymmetric

The fits to the asymmetric angular correlations are given in Figs. IV-22 and IV-23 for the $^{12}C(\alpha, 2\alpha)^8Be(0.0)$ and the $^{16}O(\alpha, 2\alpha)^{12}C(0.0)$ reactions. It was necessary to change the symmetric distortion parameters to obtain the fits in these figures; β_f was reduced and γ_i parameter was adjusted to give $S_\alpha = 3.0$ for the ^{12}C target. No further adjustments were made to extract S_α for the ^{16}O target. The values of the parameters are given in Table V-4. That small changes in the distortion

Table V-3. Summary of spectroscopic information from (α, 2α) and (^{3}He, ^{7}Be) ground state transitions.

Target	Symmetric S_α	Asymmetric S_α	(^{3}He, ^{7}Be)[a] Relative	S_α[a, b] Theory
^{12}C	3.00± .50	3.00± .50	.3	.674
^{16}O	3.50± .50	4.20± .60	1	.295
^{24}Mg	1.60± .20			
^{26}Mg	1.00± .20			
^{28}Si	1.00± .20		.3	.0044
^{30}Si	.70± .20			
^{40}Ca	.75± .10		.2	.0043
^{44}Ca	.58± .10			
^{66}Zn	.90± .10			

[a] C. Detraz, H. H. Duhm, and H. Hafner, Nucl. Phys. A147, 488 (1970).

[b] I. Rotter, Nucl. Phys. A135, 378 (1969).

Table V-4. Fit distortion parameters for the asymmetric angular correlations.

Target	β_i	β_f	γ_i	γ_f
^{12}C	1.30	1.26	1.18	1.28
^{16}O	1.30	1.26	1.18	1.28

parameters from the symmetric data are needed to obtain a fit is not surprising, since the symmetric angular correlation has considerably different kinematical conditions. The results of the asymmetric analysis are given in Table V-3. A value of S_α equal to $4.2 \pm .06$ is obtained for ^{16}O; and this value is greater than that given by the symmetric data, but is still within the errors.

b. Energy and momentum correlations

(i) Energy correlations

The $^{16}O(\alpha, 2\alpha)^{12}C(0.0)$ and the $^{24}Mg(\alpha, 2\alpha)^{20}Ne(0.0)$ energy correlations are given in Figs. IV-10 and IV-11. The solid curves are the DWIA predictions, and the arrows indicate the T_3 value where $T_3 = T_4$. The theory correctly predicts the energy correlation broadening as the angular separation is symmetrically reduced from the quasi-elastic angle. This effect was discussed in V.A-4., where it was related to the distorted momentum distribution. The normalizations used in the angular correlations are also used for the energy and momentum correlations. Consequently, the energy correlation predictions do not always exactly normalize to the data (cf. the forward angle $^{16}O(\alpha, 2\alpha)^{12}C(0.0)$ data, and the 41° point in $^{24}Mg(\alpha, 2\alpha)^{20}Ne$). The center of

mass energy of the α-α system extracted according to the T_f prescription at the 22°-22° point in the $^{16}O(\alpha, 2\alpha)^{12}C(0.0)$ reaction is about 11 MeV. This is the energy of the broad 4^+ resonance in ^8Be, and resonant behavior may be expected at this angle. Indeed, the experimental energy correlation cross section is about a factor two less than the adjoining energy correlations, and is not characteristic of the other energy correlation shapes. Except for normalization, the DWIA energy correlation at this angle does fit the data.

(ii) Momentum correlations

Momentum correlations for the ground state transitions from ^{12}C, ^{16}O, and ^{44}Ca targets are given in Figs. IV-12 to IV-14. The solid curves are DWIA predictions with normalizations taken from the angular correlation data. Figure IV-12 for the ^{12}C target shows secondary maxima at about .9 $(fm)^{-1}$; these do not match the observed data by an order of magnitude for these recoil momenta. It appears that the present approximation theory fails to describe the data for $q > .5\ (fm)^{-1}$.

c. Experimental distorted momentum distribution

Equation V-1 shows that an experimental distorted momentum distribution can be extracted from the experimental $\sigma^3(\theta)$ through the equation:

$$|\phi_{NL}(\vec{\xi})|^2 = \sigma^3_{exp}(\theta)/((KF)^* \sigma_{\alpha\alpha}(T, \theta)). \qquad (V\text{-}8)$$

A similar quantity is defined within the PWIA framework [Riou 65], where $\vec{\xi}$ is replaced by the recoil momentum $\vec{q}$. The discussion of Appendix II has shown that the $|\vec{\xi}|$ is a complex quantity, and thus a three dimensional plot is necessary to show the dependence of $|\phi_{NL}(\vec{\xi})|^2$

on $|\vec{\xi}|$. Before such a plot can be made, the $|\vec{\xi}|$ must be determined which requires that the DWIA theory must be fitted to the data. Figure V-13 shows a plot of $|\phi_{NL}(\vec{\xi})|^2$ extracted from (V-7) with the $|\vec{\xi}|$ determined from the scattering parameters of TableV-1. The ordinate is the $\mathrm{Im}(|\vec{\xi}|)$ and the abscissa is the $\mathrm{Re}(|\vec{\xi}|)$. The magnitudes of the $|\phi_{NL}(\vec{\xi})|^2$ are given by the circles in the figures. The largest circle corresponds to $|\phi_{NL}(\vec{\xi})|^2$ magnitudes of .9 $(\mathrm{fm})^3$ or greater; the progressively smaller circles correspond to $|\phi_{NL}(\vec{\xi})|^2$ magnitudes decreasing by .10 $(\mathrm{fm})^3$ step size. The $\mathrm{Re}(|\vec{\xi}|)$ parallels the values of $|\vec{q}|$ from the PWIA, but $\mathrm{Im}|\vec{\xi}|)$ has no meaning within the PWIA. It is noted that the momentum distributions fall into bands characterized by the symmetric scattering angles; these angles are marked on the graph. A general feature is that the $|\phi_{NL}(\vec{\xi})|^2$ become larger as the $\mathrm{Re}(|\vec{\xi}|)$ goes to a minimum; this is the behavior that would be expected for a $0^+ \rightarrow 0^+$ transition within the PWIA. Another general rule seems to be that the $\mathrm{Im}(|\vec{\xi}|)$ and $\mathrm{Re}(|\vec{\xi}|)$ are inversely related. This relation was also noted in the $^{12}C(a, 2a)^8Be(0.0)$ momentum distributions: it is not well understood.

Figure V-14 gives a plot of the theoretically predicted momentum distribution in the $|\vec{\xi}|$ plane. The predictions fall in the same bands as those of Fig. V-13, as they must, since the band locus is determined only by the "distorted" kinematics. The values of the theoretical $|\phi_{NL}(\vec{\xi})|^2$ are plotted in the same way as Fig. V-13, and with the inclusion of $S_a = 3.5$, the same systematics in the magnitudes of $|\phi_{NL}(\vec{\xi})|^2$ are observed. That is, $|\phi_{NL}(\vec{\xi})|^2$ increase as the $\mathrm{Re}(|\vec{\xi}|)$ becomes smaller and the $\mathrm{Im}(|\vec{\xi}|)$ gets larger. Comparison of Figs. V-13 and V-14 shows that the DWIA describes quite well the magnitudes of the

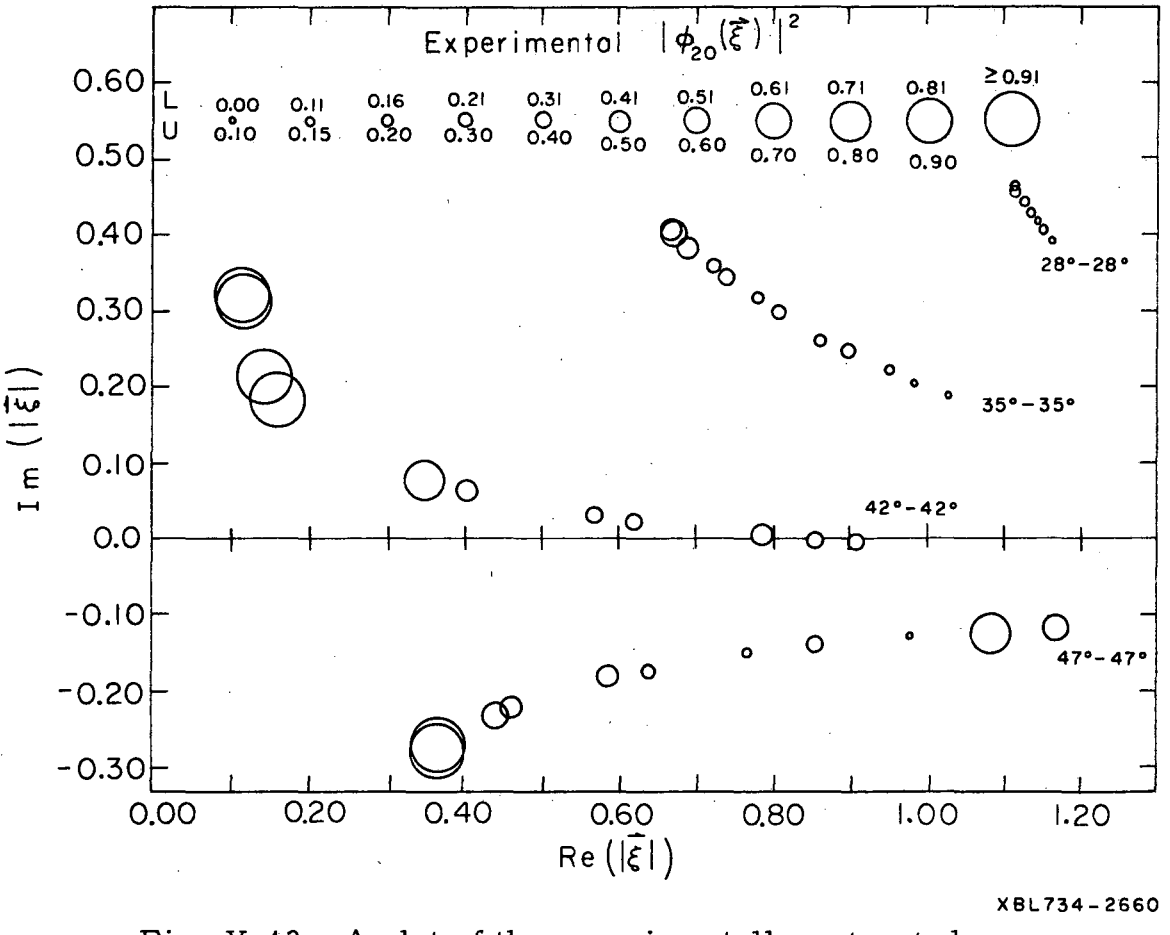

Fig. V-13. A plot of the experimentally extracted $^{16}O \rightarrow {}^{12}C(0.0) + \alpha$ momentum distribution in the $|\vec{\xi}|$ plane. The distortion parameters used in this plot are from Table V-1.

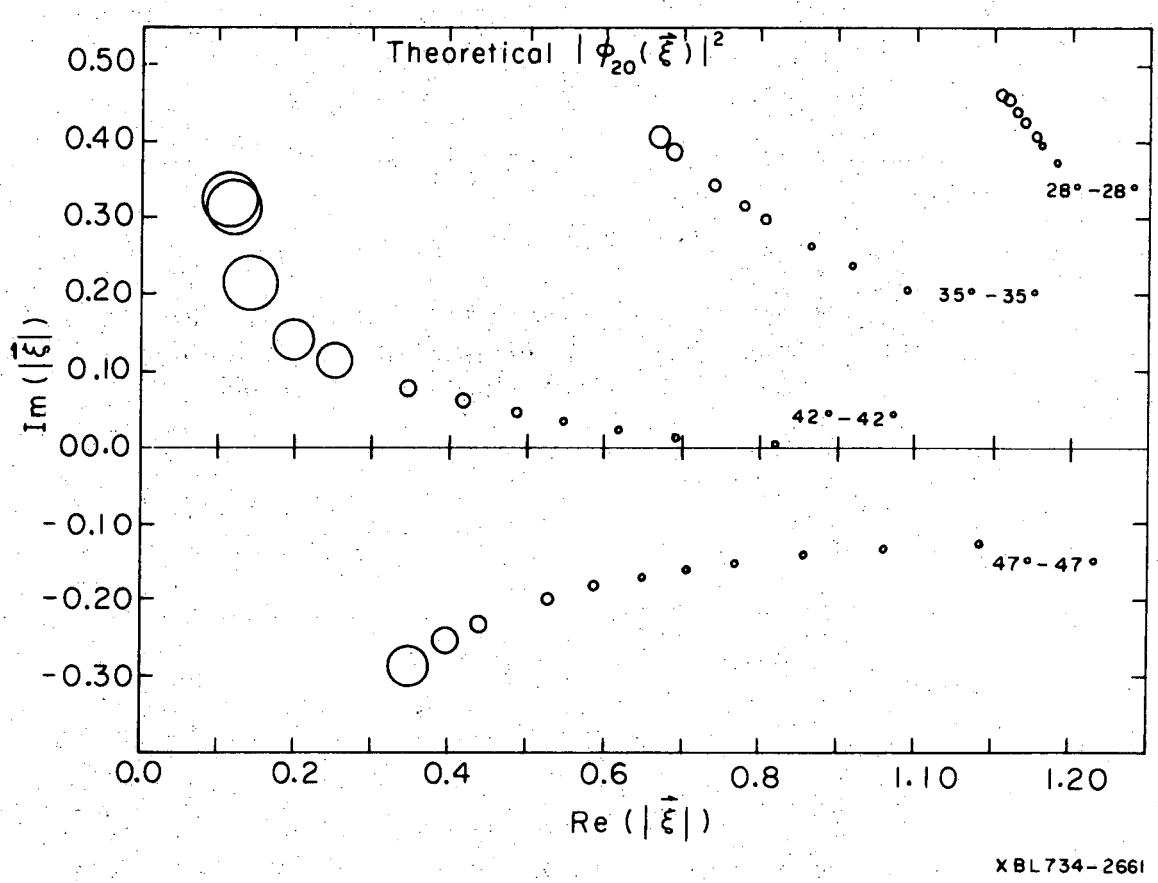

XBL734-2661

Fig. V-14. A plot of the theoretical $^{16}O \rightarrow {}^{12}C(0.0) + 2$ distorted momentum distribution in the $|\vec{\xi}|$ plane. The distortion parameters are from Table V-1.

distorted momentum distributions.

It should be emphasized than an experimental plot like V-13 for the $^{16}O(\alpha, 2\alpha)^{12}C(0.0)$ transition summarizes all the experimental data for the ground state transition. For instance, the angular correlations are related to the value of $|\phi_{NL}(\vec{\xi})|^2$ at the minimum of $Re(|\vec{\xi}|)$ as a function of angle. Also, the momentum and energy correlations as usually defined are related to any one of the bands in Fig. V-13 versus recoil momentum and T_3, respectively.

d. Discussion

The main thrust of Sec. V.A. has been to discuss and justify a comparatively simple $(\alpha, 2\alpha)$ reaction model. The quantity S_α, which is proportional to the number of alpha clusters in the target nucleus has been defined in the previous sections, and the results derived by comparing the DWIA with symmetric and asymmetric angular correlations are given in Table V-3. Column four summarizes the relative spectroscopic factors derived from a DWBA analysis of the (^{3}He, ^{7}Be) reaction at $E_{^3He}$ = 30 MeV[Det 70]. The DWBA cross section decreased by two to three orders of magnitude from ^{12}C to ^{40}Ca. Since the (^{3}He, ^{7}Be) experimental cross sections decreased at a similar rate, the authors concluded that the alpha clustering probability remained constant within one order of magnitude. The A dependence in the (^{3}He, ^{7}Be) DWBA calculation is at least 50 times more pronounced than the $(\alpha, 2\alpha)$ A dependence, as shown in Fig. V-10. Despite these very different A dependencies, the relative values of S_α extracted from the $(\alpha, 2\alpha)$ and (^{3}He, ^{7}Be) reactions compare quite favorably. The one exception is that the (^{3}He, ^{7}Be) finds a relatively smaller S_α than the $(\alpha, 2\alpha)$ for the ^{12}C

target.

The (^{3}He, ^{7}Be) authors [Det 70] reported shell model spectroscopic factors calculated by H. Yoshida from a formalism outlined by I. Rotter [Rot 69]. The results of that calculation are given in column five of Table V-3. Detraz and co-workers concluded that the shell model wave functions used in calculation of S_α were inadequate, and more α-structure correlations must be present in the wave function to account for the data. The (α, 2α) reaction at E_α = 90 MeV makes a similar conclusion.

Recent work by Rotter [Rot 73] suggests that sums over intermediate states may have very important influences on spectroscopic factors derived from heavy-ion transfer and/or knock-out reactions. The intermediate states are those states which are allowed to have nonzero n, l values where n and l are the internal quantum numbers of the transferred group of nucleons. The assumption used in the (α, 2α) work is that $n = l = 0$, and that all the oscillator energy quanta have gone into the center of mass quantities, N and L (cf. Table V-2). Model calculations taking these intermediate states properly into account should be interesting, as two independent experiments and analyses are in agreement that the shell model predictions for S_α cannot account for systematic alpha transfers.

B. PWIA Interpretations

1. Validity and application of the PWIA

If $\vec{\xi}$ of equation (V-1) is replaced by the recoil momentum $\vec{q}$, the PWIA is obtained:

$$\sigma^3(\theta) = (KF)\, \sigma_{\alpha\alpha}(T, \theta) |\phi_{NL}(\vec{q})|^2 \qquad (V-9)$$

where the first two terms of (V-9) are kinematics factors and the free alpha-alpha scattering cross section, and they are identical to Eq. (V-1). A considerable number of high energy ($E_p > 150$ MeV) (p, 2p), and (p, pα) experiments [Jam 63, Gott 70, Riou 65] have been analyzed within this framework. Distortions are predicted to invalidate (V-9) [McC 62, Lim 62], and in particular the interpretation of $|\phi_{NL}(\vec{q})|^2$ as a "billiard ball" momentum distribution of the knocked-out particle within the nucleus seems unlikely [McC 62]. Nevertheless, there have been few alternatives to classify and understand three body final state reaction data. The previous sections have shown the use of a comparatively simple DWIA analysis of the ground state transitions, and the PWIA analysis is done for the present (α, 2α) data for two reasons: first, to extract information concerning the first excited 2^+ states; and second, to make comparisons with (p, 2p) and (p, pα) experiments analyzed within PWIA.

If Eq. (V-9) is valid, then an equation for $|\phi_{NL}(\vec{q})|^2$ analogous to Eq. (V-8) for $|\phi_{NL}(\vec{\xi})|^2$ must hold, and the $|\phi_{NL}(\vec{q})|^2$ extracted in such a manner must be constant for equal $\vec{q}$'s extracted at different angle sets. A plot of $|\phi(q)|^2$ vs. q is given in Fig. V-15 and is analogous to Fig. V-13 where $|\phi(\vec{\xi})|^2$ was plotted vs. $|\vec{\xi}|$. Data taken at 25°, 28°, 35°,

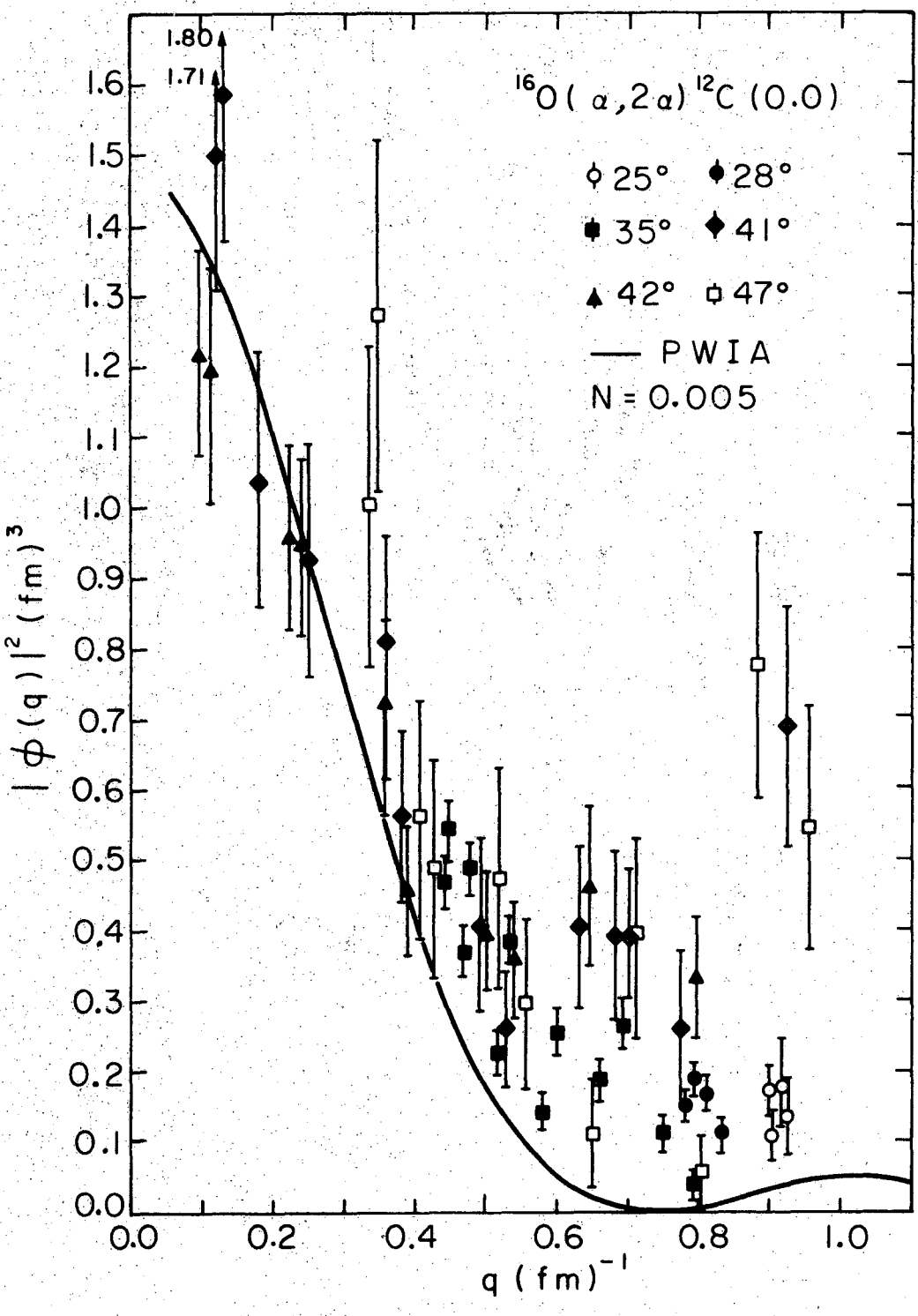

XBL734-2659

Fig. V-15. Plots the experimentally extracted momentum distribution versus the recoil momentum. The momentum distributions are also given as a function of symmetric angle.

41°, 42°, and 47° symmetric angle from the $^{16}O(a, 2a)^{12}C(0.0)$ transition are plotted, and the agreement of the $|\phi_{NL}(\vec{q})|^2$ taken at different angles is quite good. Plots for several other nuclei were prepared, and similar–although generally poorer–results were found. The solid curve in Fig. V-15 is a PWIA prediction with normalization equal to .005.

Two pieces of information can be obtained from the experimentally extracted $|\phi(\vec{q})|^2$. First, an effective number of alpha clusters is obtained from the integration of $|\phi(\vec{q})|^2$ extracted at the quasi-elastic angle over all values of q [Gott 70, Kann 68]:

$$N_a = 4\pi \int_0^{+\infty} |\phi(\vec{q})|^2 \, q^2 \, dq . \qquad \text{(V-10)}$$

Values of N_a extracted from the (a, 2a) experiment are listed in column three of Table V-5; these integrals were taken over $q \leq .60$ (fm)$^{-1}$. This limit on q was set since Fig. IV-12 has shown that the DWIA fails to fit the $^{12}C(a, 2a)^{8}Be(0.0)$ momentum correlation magnitude for $|\vec{q}| > .50$ (fm). A reasonable interpretation is that the cross section in this kinematic region may be due to competing reactions, and thus should not be included in the integration of (V-10) for N_a. The associated error in the fourth column was arrived at by comparing the integration through the error bar extremes with N_a.

Table V-6 compares the N_a calculated from V-10 with the S_a extracted from the DWIA calculations. The N_a data are normalized to S_a at the ^{24}Mg target. The N_a values are in good relative agreement with the DWIA results, and this gives confidence that the N_a extracted for the excited 2^+ states listed in Table V-5 are also good relatively. The

Table V-5. Summary of information derived from PWIA analysis of the (α, 2α) data.

Residual Nucleus	E_x (MeV)	N_α	Error	Gaussian FWHM $(fm)^{-1}$	Error $(fm)^{-1}$	(p, pα) Branching ratio	Error	Theory S_α[c]	S_α[d]	S_α[e]	S_α[f]
^{8}Be	0.0	.99	±.13	.46	±.06	1.0[a]		.674	.759	.675	.557
	2.90	.94	±.11			.6	±.10			.844	.713
^{12}C	0.0	.99	±.18	.72	±.07	1.0[b]		.295	.333	.296	.235
	4.44	.24	±.08			.40	±.15		1.667	1.481	1.301
^{20}Ne	0.0	.36	±.06	.58	±.06						
	1.63	.13	±.04								
^{22}Ne	0.0	.18	±.03	.52	±.06						
	1.28	.044	±.016								
^{24}Mg	0.0	.18	±.04	.58	±.06			.0044			
	1.37	.064	±.020								
^{26}Mg	0.0	.13	±.04	.58	±.14						
	1.81	.042	±.022								
^{36}Ar	0.0	.13	±.03	.58	±.14			.0043	.0087		
	1.97	.075	±.025								
^{40}Ar	0.0	.082	±.030	.46	±.06						
^{62}Ni	0.0	.20	±.06	.46	±.06						
	1.17	.034	±.018								

[a] B. Gottschalk and S. L. Kannenberg, Phys. Rev. (C) 2, 24 (1970).

[b] S. L. Kannenberg, Ph.D. Thesis, 1968 (unpublished).

[c] C. Detraz, H. H. Duhm, and H. Hafner, Nucl. Phys. A147, 488 (1970).

[d] H. H. Gutbrod, H. Yoshida, and R. Bock, Nucl. Phys. A165, 240 (1971); H. H. Gutbrod, H. Yoshida, and R. Bock, Nuclear Reactions Induced by Heavy Ions, edited by R. Bock and W. R. Hering (North Holland, 1970).

[e] P. Beregi, et al., Nucl. Phys. 66, 513 (1965).

[f] D. Kurath, preprint (1973).

Table V-6. Normalization of N_a (g.s.) derived from PWIA to S_a (g.s.) derived from DWIA.

Target	S_a DWIA	N_a [a] PWIA
^{12}C	3.00± .50	4.40± .58
^{16}O	3.50± .50	4.42± .81
^{24}Mg	1.60± .20	1.60± .25
^{26}Mg	1.00± .20	.80± .15
^{28}Si	1.00± .20	.78± .17
^{30}Si	.70± .20	.56± .19
^{40}Ca	.75± .10	.58± .15
^{44}Ca	.58± .10	.36± .13
^{66}Zn	.90± .10	.88± .28

[a] Normalized to S_a (DWIA) at ^{24}Mg.

integrations for the excited state N_α values were also limited by $|\vec{q}| \leq 0.60$ (fm)$^{-1}$. The 2^+ states are more weakly excited than the ground states. It is therefore possible that competing reactions contribute relatively more to the 2^+ cross sections than to the g.s. cross sections. Thus the N_α values for the 2^+ states given in Table V-5 may be upper limits.

The second derivable quantity is the $|\phi(\vec{q})|^2$ width. This is discussed for (p, 2p) by Riou [Riou 65]. The method employed here is to fit a gaussian to the momentum distribution and then quote the full width at half maximum (FWHM) of the fit gaussian. These results from the (α, 2α) experiment are listed in column five and the error in column six. The error is determined by noting the gaussian widths which give a worse fit to the momentum distribution, and then comparing this value with the best fit. The most striking feature of this analysis is the constancy of the widths as a function of nuclear mass; an exception is the ^{12}C residual nucleus in which case the momentum distribution width is considerably larger than for the other nuclei. Figure V-16 shows a plot of the momentum correlation with the fit gaussian for the ^{16}O(α, 2α)^{12}C(0.0) case.

2. Discussion of PWIA results

a. Effective number of alpha clusters

Figure V-17 shows the results for the N_α PWIA analysis for the ground and lowest excited (2^+) levels. There is seen to be a strong decrease in N_α from the ^{12}C target to the ^{30}Si target, while N_α is then relatively constant to ^{66}Zn. This is the same result as obtained for the ground state transitions in the DWIA analysis.

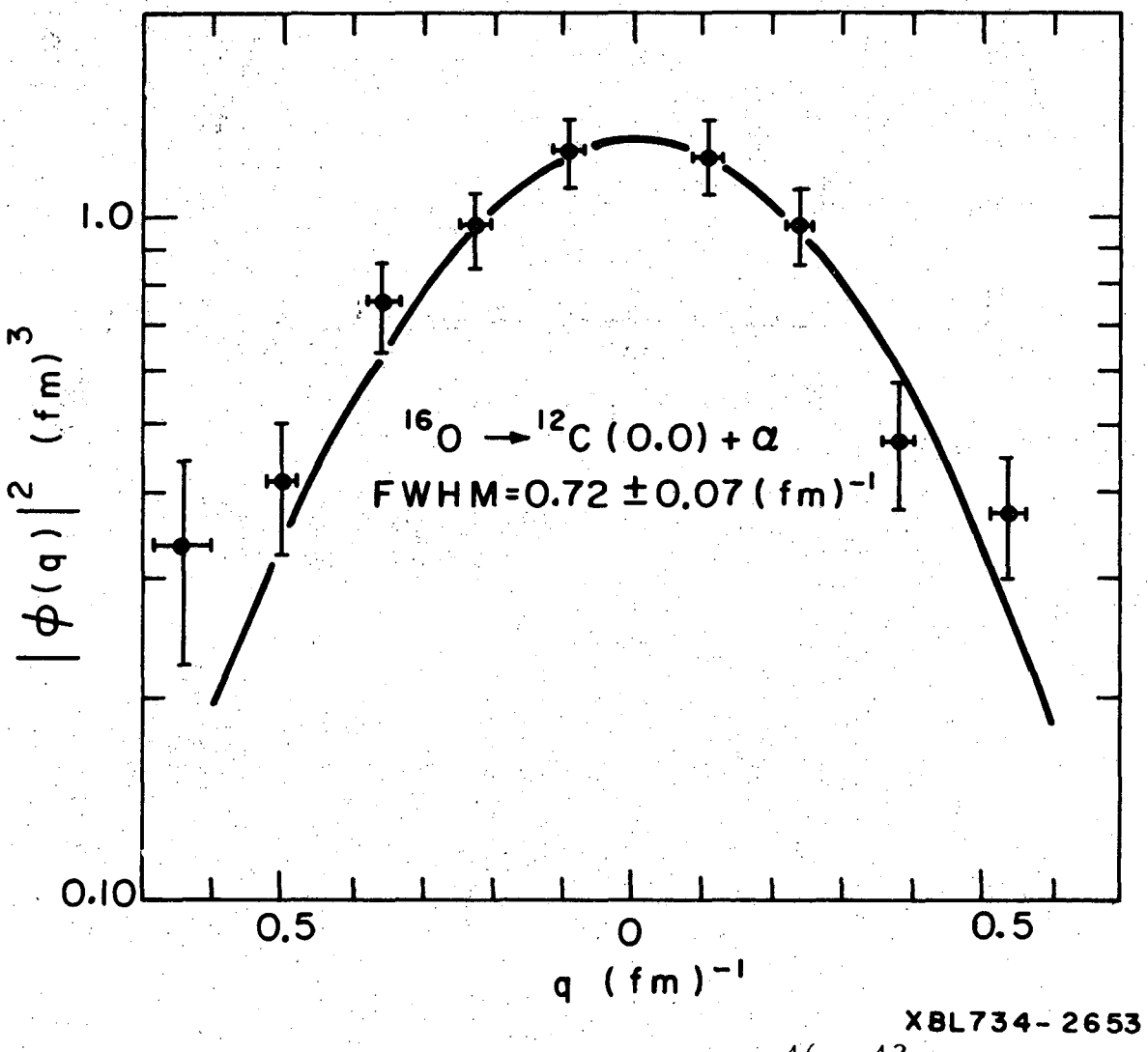

Fig. V-16. The experimentally extracted $^{16}O \rightarrow ^{12}C(0.0) + \alpha$ momentum distribution plotted versus q. The solid line is the fit gaussian.

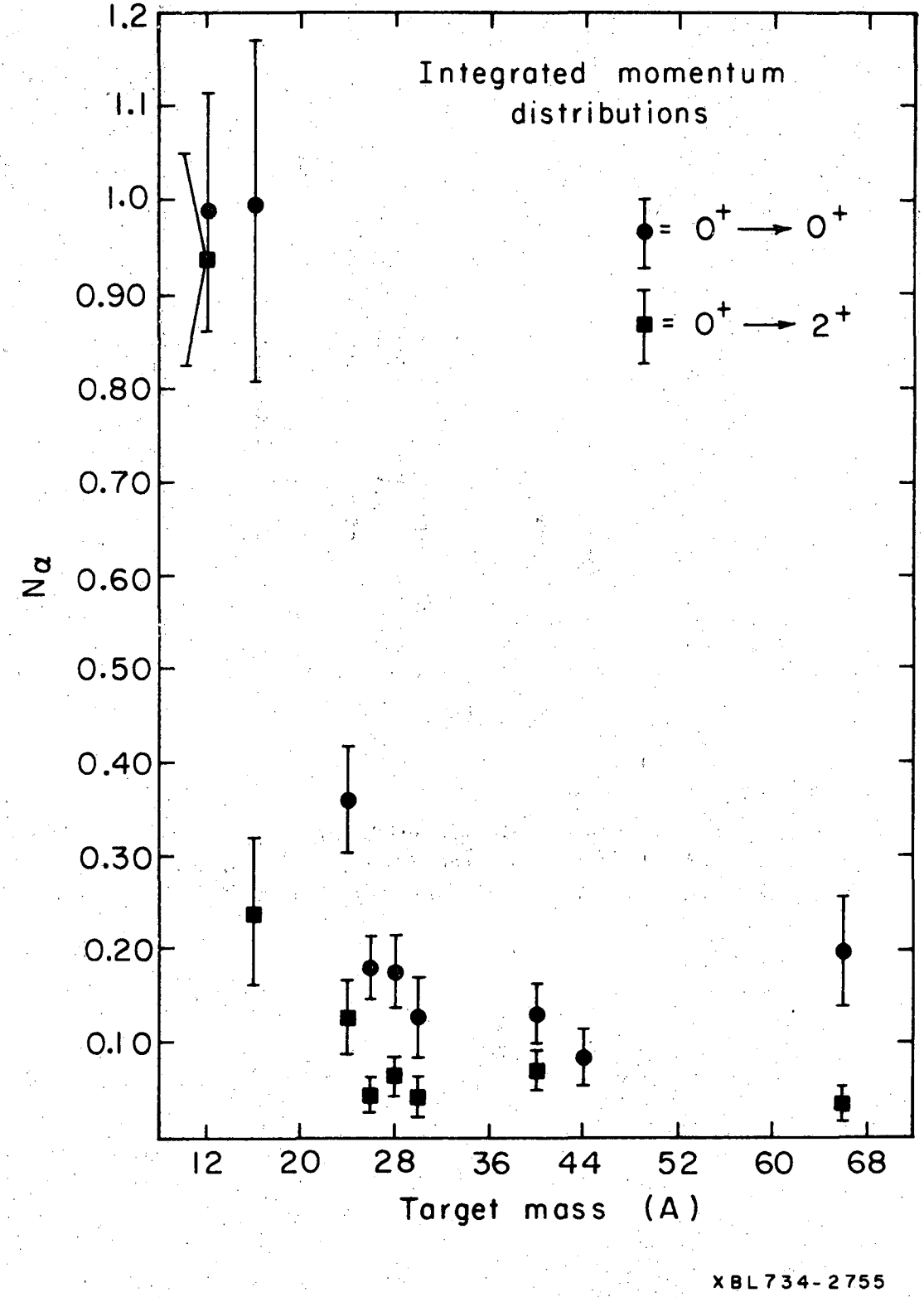

Fig. V-17. Plot of the N_α for the ground and first excited states in the residual nuclei. The N_α was calculated with Eq. V-10, but with an upper limit on q.

The ^{12}C and ^{16}O nuclei have been studied experimentally and theoretically in terms of cluster structure. Table V-5 lists branching ratios derived from the $^{12}C(p, p\alpha)$ and $^{16}O(p, p\alpha)$ experiments at $E_p = 160$ MeV, and these reactions are seen to follow the same systematics as the N_α derived from the $(\alpha, 2\alpha)$ experiment. The (^3He, ^7Be) and (d, ^6Li) α pickup reactions [Gut 71, McG 71, Det 70] have given evidence for excitation of $^8Be(2.90)$ state greater than or equal to $^8Be(0.0)$, and they have also shown that the $^{12}C(4.44)$ is three or four times more strongly populated than the $^{12}C(0.0)$. This latter result is quite unlike the alpha knock-out experiments, which have indicated that $^{12}C(0.0)$ is more strongly populated than the $^{12}C(4.44)$ (approximately a factor of 4 in the $(\alpha, 2\alpha)$ and 2-1/2 in the $(p, p\alpha)$. Numerous calculations [Det 70, Gut 71, Ber 65, Kur 73] (cf. last four columns of Table V-5) have predicted that the dominant parent of ^{16}O in an α-cluster model is the $\{^{12}C(4.44) + \alpha\}$ rather than the $\{^{12}C(0.0) + \alpha\}$ configuration.

The first two columns of the theoretical predictions are alpha cluster spectroscopic factors calculated from simple shell model wave functions [Det 70, Gut 71] based on a procedure given by Rotter [Rot 69]. The third column summarizes LS coupling shell model predictions [Ber 65], and the fourth column gives spectroscopic factors calculated from intermediate coupling wave functions [Kur 73]. The conclusion from this latter work is that good agreement with Rotter [Rot 68] is obtained, as is seen in Table V-5. Thus several calculations predict a strong component of the $\{^{12}C(4.44) + \alpha\}$ configuration in the ^{16}O ground state in agreement with the α pickup reactions. The population of final states in ^{12}C from the $^{16}O(\alpha, 2\alpha)$ and $(p, p\alpha)$ reactions, therefore, is not

consistent either with the (d, ^{6}Li) and (^{3}He, ^{7}Be) results or with several shell model calculations for alpha spectroscopic factors. This same ^{16}O(α, 2α) result at E_α = 70 MeV has been obtained by Kenefick [Kene 73]. This difference in the two and three body final state results is interesting since the ^{16}O structure must be constant, and thus the (α, 2α) and α pickup reactions are apparently not equivalent probes for finding four particle clusters in nuclei. There seems to be no simple explanation for this result, and a theoretical investigation of the reaction mechanisms involved may be very enlightening.

The relative N_α from Table V-5 and Fig. V-17 can give some information concerning alpha clustering in the N = Z and N = Z + n nuclei; where n = neutron number > 0. Enhanced elastic alpha scattering [Oes 72] at $\theta_{lab} > 90°$ has been systematically studied for several nuclei in the sd shell. Earlier work postulated enhanced alpha clustering [Sch 70] to account for the enhanced back angle alpha scattering of ^{40}Ca over ^{44}Ca [Gau 69]. Systematics from the (α, 2α) reaction are found by summing the N_α for the transitions to the 0^+ and 2^+ states for the entries in Table V-5. It is seen that the ^{24}Mg target is enhanced by a factor of about two as compared to the ^{26}Mg target, and that the ^{28}Si target is slightly enhanced as compared to the ^{30}Si target. Finally, the ^{40}Ca target is enhanced by more than a factor of 2 when compared with the ^{44}Ca target. These systematics are in fair agreement with the (α, α_0) scattering [Oes 72] if the enhanced elastic scattering is to be taken as indicative of enhanced alpha clustering. The exception to the (α, α_0) expectation is the ^{24,26}Mg(α, 2α) reaction pair. Since the excess neutrons are not occupying a shell higher than the N = Z core, the (α, α_0)

systematics would predict (again if enhanced back angle (α, α_0) scattering is sensitive to alpha clustering) constant alpha clustering in ^{24}Mg and ^{26}Mg. This result is not consistent with the $(\alpha, 2\alpha)$ results. Indeed, the ^{24}Mg summed N_α is enhanced over ^{26}Mg to about the same extent as the ^{40}Ca summed N_α is over ^{44}Ca. Since the $^{24}Mg(\alpha, \alpha_0)$ and $^{26}Mg(\alpha, \alpha_0)$ were not actually studied in the elastic α-scattering [Oes 72], it would seem worthwhile to study these targets to see if the (α, α_0) systematics fail in this case. The $^{28,30}Si$ $(\alpha, 2\alpha)$ and $^{40,44}Ca(\alpha, 2\alpha)$ qualitatively follow the (α, α_0) systematics.

The $(\alpha, 2\alpha)$ data provide additional information which should be included in discussing the study of alpha structures from (α, α_0) scattering. That is, the $(\alpha, 2\alpha)$ yields the relative enhancement of alpha clustering, and it would be interesting to see if this relative enhancement is sufficient to account for the back angle elastic scattering differences. For instance, Table V-5 shows that the four neutrons outside the ^{40}Ca core do not destroy the alpha structure of ^{44}Ca, but rather reduce it by a factor of two. The question might be proposed: can a reduction of N_α by two in ^{44}Ca account for the observed (α, α_0) effects in these nuclei?

b. Momentum distribution widths

The momentum distribution extracted from

$$\left|\phi(\vec{q})\right|^2 = \sigma^3_{exp}(\theta)/(\sigma_{\alpha\alpha}(T, \theta)\ (KF)) \qquad (V\text{-}11)$$

for the $^{16}O(\alpha, 2\alpha)^{12}C(0.0)$ experiment is given in Fig. V-16. The solid curve in this figure is a fit from a gaussian wave function (infinite harmonic oscillator) in q-space:

$$\psi(q) = \exp\left[-\frac{1}{2}\left(\frac{q}{q_a}\right)^2\right] = \exp\left[-\frac{1}{2}(a\,q)^2\right] \qquad \text{(V-12)}$$

where $\ell = 0$ has been taken [Riou 65],

$$q_a = 1/a \qquad \text{(V-13)}$$

and the units of q are $(\text{fm})^{-1}$. The $\psi(q)$ is not normalized. The Fourier transform of (V-12) is

$$\psi(r) = \exp\left[-\frac{1}{2}\left(\frac{r}{a}\right)^2\right]. \qquad \text{(V-14)}$$

The FWHM values of the gaussian fits to the ground state momentum distributions are given in column five of Table V-5.

The half-widths at $\frac{1}{e}$ of (p, 2p) momentum distribution have been summarized for target nuclei up to ^{12}C[Riou 65]. By assuming that the (p, 2p) momentum distributions are gaussian in shape, the FWHM of the gaussian corresponding to the half-width at $\frac{1}{e}$ can be calculated from

$$q_{FWHM} = 1.665\,(q_{\frac{1}{e}}), \qquad \text{(V-15)}$$

where $(q_{\frac{1}{e}})$ is defined as the half-width of a gaussian at $\frac{1}{e}$ of its peak height. Converting the (p, 2p) momentum distribution width values from [Riou 65] to gaussian FWHM values (as quoted in Table V-5 for the (α, 2α) work), values of 1.05 $(\text{fm})^{-1}$ and 1.26 $(\text{fm})^{-1}$ are found for the ^{10}B and ^{12}C nuclei, respectively.

By comparing momentum distribution widths extracted from the (p, 2p) and (α, 2α) experiments, some interesting comparisons can be made concerning the motion of a bound proton and a bound alpha. First, a relation between the average proton and alpha momenta will be found.

The oscillator parameters a_p and a_α of Eq. (V-12) are found by substituting $(q_{FWHM})_p = 1.10\ (fm)^{-1}$ and $(q_{FWHM})_\alpha = .55\ (fm)^{-1}$ in (V-12) where $\psi(q) = 0.50$. The values

$$a_p = 1.07\ fm, \qquad a = 2.14\ fm \tag{V-16}$$

are found. The expectation value of q, $\langle q \rangle$, is easily found by using the wave function (V-12) in calculating $\langle q \rangle$:

$$\langle q \rangle = \int_0^\infty |\psi(q)|^2\, q\, dq \Big/ \int_0^\infty |\psi(q)|^2\, dq = \frac{1}{\sqrt{\pi}\, a} . \tag{V-17}$$

Therefore, the average values of the proton and alpha momenta are

$$\langle q \rangle_p = .527\ (fm)^{-1}$$

and (V-18)

$$\langle q \rangle_\alpha = .264\ (fm)^{-1}$$

and it is found that

$$\langle q \rangle_p = 2 \langle q \rangle_\alpha . \tag{V-19}$$

Thus by comparing the momentum distribution widths obtained from the (p, 2p) and (α, 2α) reactions within the PWIA framework, the average value of the proton momentum is seen to be twice the average alpha momentum. Given the average momenta of Eq. (V-18) the velocities corresponding to these averages can be calculated from the relation.

$$\langle \beta \rangle = \frac{v}{c} = \frac{\langle cp \rangle}{mc^2} \tag{V-20}$$

and the results are:

$$\langle \beta \rangle_p = .11 \quad = \text{average proton velocity} \tag{V-21}$$

and

$$\langle \beta \rangle_\alpha = .014 \quad = \text{average alpha velocity.}$$

A second point is made by comparing Eqs. (V-12) and (V-14). Since $a_\alpha > a_p$ the alpha momentum space wave function is more peaked about $q = 0$ than the proton momentum space wave function. However, the opposite is true for the coordinate space wave functions: since $a_\alpha > a_p$ the alpha coordinate space wave function is more diffuse than the proton coordinate space wave function. Carrying out the analysis of V-17 in coordinate space the expectation of r, $\langle r \rangle$, is found

$$\langle r \rangle = \frac{\int_0^\infty |\psi(r)|^2 \, r \, dr}{\int_0^\infty |\psi(r)|^2 \, dr} = \frac{a}{\sqrt{\pi}} \tag{V-22}$$

from which

$$\begin{aligned} \langle r \rangle_p &= .604 \text{ fm} \\ \langle r \rangle_\alpha &= 1.21 \text{ fm.} \end{aligned} \tag{V-23}$$

The picture from this analysis is that bound alpha particles move much slower and at a greater radius on the average than a proton within the nucleus.

VI. Summary

A systematic study of the (α, 2α) reaction at E_α = 90 MeV has been completed. This is the first instance of systematic work directed towards using a three body final state reaction for spectroscopic purposes in mass regions outside of the OsOp shell. "Spectroscopic purposes" means that sufficient energy resolution has been achieved to identify discrete low-lying states, if they are populated in the (α, 2α) reaction. The introduction to this work pointed out that alpha clustering and the role of the alpha particle in nuclear structure has long been a topic of interest in nuclear physics. One reason for the recent increased interest in alpha clustering and clustering in general is that the shell model description of correlated or multi-particle, multi-hole states is complicated [Bri 66]. Nucleon clustering provides a physical picture of correlations, and it also provides a different framework for understanding nuclear properties. The introduction also mentioned several experimental techniques for gaining further information about four particle correlations, and historically it is time to investigate knock-out coincidence experiments as another source of spectroscopic information.

The third section of this work relates the coincidence technique for obtaining the (α, 2α) data. Surprising differences between various aspects of two and three body final states were discussed, and these differences were generally related to the dissimilar kinematics. Probably the simplest way to remember these kinematic effects is that the

recoil energy in these three body final state experiments is generally much less than the corresponding two body experiment. This section also discussed a correction for the kinematic band present in the Dalitz plot in order to realize the best resolution in the $T_3 + T_4$ projections. This correction was made off line and is possible because data are taken event by event. This procedure permitted identification of several weakly excited states which might have otherwise gone unnoticed.

Experimental results were summarized in Section IV. Several interesting systematics of the (α, 2α) reaction were pointed out. These include a strong preference for ground state to ground state transitions, a characteristic angular correlation pattern for these transitions, and a systematic broadening of the energy correlation as the symmetric angle moved away from the quasi-elastic angle to more forward symmetric angles.

The final part discussed the experimental results in terms of a phenomenological DWIA and PWIA theory. The DWIA theory was constructed for $0^+ \rightarrow 0^+$ transitions, and was seen to do a remarkably good job in describing many features of the three body experiment. In order to find the best fits it was necessary to vary the distortion parameters; however, upon finding a good fit to the $^{16}O(\alpha, 2\alpha)^{12}C(0.0)$ data the parameters were nearly constant for the remaining nuclei. The final fit parameters of the McCarthy-Pursey wave functions were consistent with the choice of (p, 2p) parameters using similar wave functions. An absolute normalization to ^{12}C was found such that $S_\alpha = 3.0$,

and spectroscopic factors were extracted for the remaining nuclei based on this normalization. These agreed rather well in a relative sense with the S_α extracted from a DWBA analysis of the (^{3}He, ^{7}Be) reaction. Different results in the ^{16}O(^{3}He, ^{7}Be)^{12}C and the ^{16}O(α, 2α) ^{12}C final state population have been discussed. The alpha pickups excited the ^{12}C(4.44) quite strongly compared to the ground state while the opposite behavior was observed in the (α, 2α) reaction. The PWIA theory was used to describe the relative population of the ground and first excited 2^+ states, and to extract certain average properties connected to the momentum distribution. The PWIA seemed to give spectroscopic information that agreed with the DWIA in a relative sense, although it was seen that the DWIA accounted for several experimental features in which the PWIA failed. The problem of detecting alpha particle enhancements by (α, α_0) scattering has been discussed with the (α, 2α) PWIA analysis, and certain questions have been proposed for the (α, α_0) scattering.

Appendix I.A.

A derivation leading to relativistic expressions for various kinematical quantities pertinent to three-body final state is given here. The notation is that of Fig. II-1.

The four vector

$$P = \underline{p}_1 + \underline{p}_2 = \underline{p}_3 + \underline{p}_4 + \underline{p}_5 \tag{1}$$

can be decomposed into

(1) total energy conservation

$$E = E_1 + E_2 = E_3 + E_4 + E_5 \tag{2}$$

and

(2) three momentum conservation

$$\vec{p} = \vec{p}_1 + \vec{p}_2 = \vec{p}_3 + \vec{p}_4 + \vec{p}_5 \tag{3}$$

where

$$E_i^2 = (cp_i)^2 + m_i^2 c^4 \text{ and } E_i = T_i + m_i c^2. \tag{4}$$

The general procedure is to reexpress E_5 in Eq. (2) by using the scalar product of Eq. (3). All calculations are carried out in the lab system, so

$$\vec{p}_2 = 0 \quad \text{and} \quad \vec{p}_1 = \vec{p}.$$

Equation (2) can be rewritten with the help of Eq. (4) as:

$$(E-E_3)^2 - 2(c^2p_4^2 + m_4^2c^4)^{\frac{1}{2}}(E-E_3) + m_4^2c^4 - m_5^2c^4 = c^2p_5^2 \tag{5}$$

The scalar product of (3) leads to

$$c^2p_5^2 = c^2p_1^2 + c^2p_3^2 + c^2p_4^2 - 2cp_1\,cp_3\cos\theta_1 - 2cp_1\,cp_4\cos\theta_2 + 2cp_3cp_4\cos\theta_{12} \tag{6}$$

where $\theta_{12} = \theta_1 - \theta_2$ (θ_2 negative).

Substituting (6) in (5), expanding, and grouping in powers of (cp_4):

$$(cp_4)^2[(E-E_3)^2 - (cp_1\cos\theta_2 - cp_3\cos\theta_{12})^2]$$

$$+ (cp_4)(2A)(cp_3\cos\theta_{12} - cp_1\cos\theta_2) + m_4^2c^4(E-E_3)^2 - A^2 = 0 \qquad (7)$$

where

$$A = (\underline{P}^2 + m_3^2c^4 + m_4^2c^4 - m_5^2c^4)/2 - EE_3 + c^2\vec{p}_1 \cdot \vec{p}_3 .$$

Use of the metric

$$\underline{P}^2 = E^2 - |\vec{P}|^2 = (E_1+E_2)^2 - (c\vec{p}_1)^2$$

$$= 2E_1E_2 + E_2^2 + m_1^2c^4$$

has been made.

By examining Eq. (7) it is noted that a value of cp_4 can be calculated given a value for cp_3. This is done by solving the quadratic equation

$$ax^2 + bx + c = 0$$

where

$$a = (E-E_3)^2 - (cp_1\cos\theta_2 - cp_3\cos\theta_{12})^2$$

$$b = 2A(cp_3\cos\theta_{12} - cp_1\cos\theta_2)$$

and

$$c = m_4^2c^4(E-E_3)^2 - A^2.$$

Thus a formula yielding an expression for the relativistic momentum of particle 4 given the momentum of particle 3 is the general solution of the quadratric equation:

$$cp_4 = \frac{-b \pm \sqrt{b^2 - 4ac}}{2a} .$$

For a real solution to exist, $b^2 - 4ac \geq 0$.

Two solutions exist (the double-value case) when

$$-b - \sqrt{b^2 - 4ac} \geq 0.$$

In all kinematic regions investigated in the present (a, 2a) work, the one solution $(-b + \sqrt{b^2-4ac})$ case prevailed.

Upon solving for cp_4 many other kinematical quantities are readily calculated. Those of interest to this experiment include the kinetic energy of particle 4 (T_4), the summed kinetic energies of particles 3 and 4 ($T_{34} = T_3 + T_4$), the kinetic energy of particle 5 (T_5), and the recoil momentum cp_5. Also calculated is the momentum change suffered by the incident particle. This 3-momentum transfer is given by

$$\vec{cp}_t = \vec{cp}_1 - \vec{cp}_3$$

$$c^2\vec{p}_t \cdot \vec{p}_t = c^2|\vec{p}_t|^2 = (\vec{cp}_1 - \vec{cp}_3) \cdot (\vec{cp}_1 - \vec{cp}_3)$$

$$= c^2|\vec{p}_1|^2 + c^2|\vec{p}_3|^2 - 2.0\, c^2|\vec{p}_1|\,|\vec{p}_3|\cos\theta_1.$$

Summarizing, the complete solution of the three body kinematic problem restricts solutions of T_4 to lie along a curved line as T_3 varies. Examples of kinematic calculations in the T_3 vs. T_4 and T_3 vs. $T_3 + T_4$ plane are given in Fig. II-2.

Appendix I.B.

The derivation of the quasi-elastic angle is given. Since, by definition of the quasi-elastic angle $T_5 = 0$, the problem can be reduced to a two body inelastic problem. The inelasticity is due to the binding energy of the knocked out particle to the core. First, a non-relativistic derivation is given, and a relativistic derivation is indicated.

(1) Non-relativistic

The scattering process for the (a, 2a) case is viewed as an inelastic collision of two alpha particles:

$$a_1 + a_2 + Q \rightarrow a_3 + a_4^*$$

where Q is the binding of (core + a) in the 3-body system. In the lab system

$$\vec{p}_2 = \vec{p}_5 = 0$$

and $$T_2 = 0$$

so the non-relativistic equations for the conservation of momentum and energy are

$$T_1 + Q = T_3 + T_4 \qquad (1)$$

and $$\vec{p}_1 = \vec{p}_3 + \vec{p}_4. \qquad (2)$$

Substituting $T_i = p_i^2/2m_i$ in Eq. (1)

and subsequently replacing $|\vec{p}_1|^2$ with $(\vec{p}_3 + \vec{p}_4)\cdot(\vec{p}_3 + \vec{p}_4)$ from Eq. 2) one obtains

$$2\vec{p}_3 \cdot \vec{p}_4 + 2m_a Q = 0$$

or $$|\vec{p}_3|\ |\vec{p}_4| \cos\theta_{12} = -m_a Q.$$

Substituting the non-relativistic relations for $|\vec{p}_3|$ and $|\vec{p}_4|$ and recognizing $\theta_{\text{quasi-elastic}} = \theta_{Q.E.} = \theta_{12/2}$ for the symmetric angle case, the result is:

$$\cos 2\theta_{Q.E.} = \frac{-Q}{2\sqrt{T_3 T_4}}$$

or taking $T_3 = T_4$

$$\theta_{Q.E.} = \frac{1}{2}\left[\arccos\left(\frac{-Q}{2T_3}\right)\right]. \qquad (3)$$

(2) Relativistic

Total energy conservation is expressed as $E_1 + E_2 + Q = E_3 + E_4$. However, in our (a, 2a) case all rest masses of the particles are identical so this equation immediately goes over to the non-relativistic case of Eq. (1). By finding the scalar product of (2) (which is true relativistically) and eliminating $|\vec{p}_1|^2$ from this equation by use of (1) it is found that

$$2T_3T_4 - 2Q(T_3+T_4) + Q^2 - 2m_a c^2 Q = 2\sqrt{T_3^2 + 2m_a c^2 T_3}\ \sqrt{T_4^2 + 2m_a c^2 T_4}\cos 2\theta_{Q.E.}\,.$$

Taking $T_3 = T_4$ and solving for $\cos 2\theta_{Q.E.}$:

$$\cos(2\theta_{Q.E.}) = (T_3^2 - 2QT_3 + Q^2/2.0 - m_a c^2 Q)/(T_3^2 + 2m_a c^2 T_3). \qquad (4)$$

It should be emphasized that these equations were derived explicitly for the (a, 2a) case where $\theta_{Q.E.} = \theta_{12}/2$. It is interesting to take the non-relativistic limit of (4). In this case $T_3^2 \to 0$, $-2QT_3 \to 0$ and

$Q^2/2.0 \rightarrow 0$. So (4) reduces to

$$\cos(2\theta_{Q.E.}) = \frac{-m_a c^2 Q}{2m_a c^2 T_3} = \frac{-Q}{2T_3}$$

$$\text{or} \quad \theta_{Q.E.} = \frac{1}{2}\left[\arccos\left(\frac{-Q}{2T_3}\right)\right]$$

as in Eq. (3).

Considering the large angular acceptances in the 90 MeV (a, 2a) work, it is inconsequential whether Eq. (3) or (4) is used to calculate $\theta_{Q.E.}$. It should be noted that the quasi-elastic angle in the non-relativistic limit is a function only of the binding energy and T_3 where $T_3 = T_4$.

Appendix I.C.

The non-relativistic derivation for finding the excitation of an unknown peak in $T_3 + T_4$ projected spectrum is given here. The following conditions are built into the derivation: (1) $T_3 = T_4$, (2) Q (g.s.) is known, (3) $m_3 = m_4$, (4) $T_3 + T_4$ is known, and (5) angles are symmetric and equal to θ.

Energy conservation requires

$$T_1 + Q = T_3 + T_4 + T_5 \tag{1}$$

in the lab frame. Using the relation $T_i = p_i^2/2m_i$ and making the identifications

1 → incident α

3, 4 → detected α's

5 → recoiling, undetected nucleus

Eq. (1) becomes

$$p_1^2 + 2m_a Q = 2p_3^2 + u\,p_5^2 \tag{2}$$

where $u = m_a/m_R$.

The quantity p_5^2 can be eliminated from (2) by using the conservation of momentum

$$\vec{p}_5 = \vec{p}_1 - \vec{p}_3 - \vec{p}_4 . \tag{3}$$

By taking the scalar product of (3) it is found

$$p_5^2 = 2p_3^2 (1 + \cos(2\theta)) - 4\cos(\theta)\,|\vec{p}_1|\,|\vec{p}_3| + p_1^2 . \tag{4}$$

By substituting (4) in (2) and also making the substitution

$$Q = Q_{g.s.} - E_x \tag{5}$$

where

$Q < 0$ for endothermic reaction

$Q > 0$ for exothermic reaction

the final expression is obtained

$$E_x = Q_{g.s.} + T_1(1-u)$$

$$+ 4u\sqrt{T_1 T_3}\cos\theta - 2T_3\{1+u(1+\cos(2\theta))\}. \qquad (6)$$

Appendix II.

The intent of this appendix is to outline the evaluation of the distorted momentum distribution, Eq. (II-43), for $0^+ \rightarrow 0^+$ transitions. The integral

$$\phi_{NL}(\vec{\xi}) = N_i N_f^2 \int_{-\infty}^{+\infty} e^{i\vec{\xi}\cdot\vec{\rho}} f_{NL}(\vec{\rho})\, d\vec{\rho} \qquad \text{(II-45)}$$

where

$$\vec{\xi} = a_i \vec{k}_1 - a_f(\vec{k}_3 + \vec{k}_4) \qquad \text{(II-45)}$$

is evaluated in polar coordinates. The N_i and N_f of (II-45) are determined in Eqs. (II-41) to (II-43). The radius of the nuclear surface used in these expressions is given by $R_s = 1.30 * A^{1/3}$ for (II-40) and $R_s = 1.30 * (A-4)^{1/3}$ for (II-42). The $f_{NL}(\vec{\rho})$ (Eq. (II-29) is quite simple for a $0^+ \rightarrow 0^+$ transition:

$$f_{NO}(\vec{\rho}) = S_a^{1/2} \frac{R_{NO}(\rho)}{\sqrt{4\pi}} \qquad (1)$$

and the $R_{NO}(\rho)$ is normalized according to (II-48). Furthermore, since $f_{NO}(\vec{\rho})$ is isotropic no complications exist in the θ integration of (II-45) as outlined in Eqs. (II-32) to (II-34).

The ϕ and θ integrations yield

$$\phi_{NO}(\vec{\xi}) = \frac{N_i N_f^2 2\pi^{1/2} S_a^{1/2}}{|\vec{\xi}|} \int_{\rho=0}^{\infty} R_{NO}(\rho) \sin(|\vec{\xi}|\rho) d\rho \qquad (2)$$

where $$|\vec{\xi}| = |\vec{\xi}\cdot\vec{\xi}|^{1/2} . \qquad (3)$$

Thus the quantity $|\vec{\xi}|$ is complex, and from Eq. (II-44) it is seen the $|\vec{\xi}|$ is a function of the asymptotic momenta and the distortion parameters; explicitly:

$$|\vec{\xi}| = \{(a_1)^2 k_1^2 + (a_3)^2 k_3^2 + (a_4)^2 k_4^4 - 2a_1 a_3 \vec{k}_1 \cdot \vec{k}_3 - 2a_1 a_4 \vec{k}_1 \cdot \vec{k}_4 + 2a_3 a_4 \vec{k}_3 \cdot \vec{k}_4\}^{1/2} \tag{4}$$

$$= (a + ib)^{1/2}.$$

The quantities a and b in (4) are obtained by substituting the β and γ distortion parameters via Eqs. (II-44) into (4), and separating the resultant expression into real and imaginary parts. In the plane wave limit, b = 0 and $\vec{\xi} = \vec{k}_1 - \vec{k}_3 - \vec{k}_4$, a purely real quantity.

The square root of (a + ib) is in general another complex number, i.e.,

$$|\vec{\xi}| = (a+ib)^{1/2} = c + i \frac{b}{|\vec{b}|} d . \tag{5}$$

The sign of b determines the sign of d; d itself is always ≥ 0. The expressions for c and d in terms of a and b are found in [Ahl 66]. The result is that $\mathrm{Im}(|\vec{\xi}|)$ may be and is in many cases negative.

Upon expanding $\sin(|\vec{\xi}|\,\rho) = \sin[(c+id)\rho]$ in terms of trigonometric and hyperbolic functions it is found that

$$\phi_{NO}(\vec{\xi}) = \frac{2\pi^{1/2} N_i N_f^2 S_a^{1/2}}{|\vec{\xi}|} [A0 + i\, B0] \tag{6}$$

where

$$A0 = \int_{\rho=0}^{\infty} R_{NO}(\rho)\,\sin(c\rho)\,\cosh(d\rho)\,d\rho$$

and (7)

$$B0 = \int_{\rho=0}^{\infty} R_{NO}(\rho)\,\cos(c\rho)\,\sinh(d\rho)\,d\rho .$$

The final result needed for evaluation of $|M|^2$ in Eq. (II-26) is:

$$\phi^{*}_{NO}(\vec{\xi})\,\phi_{NO}(\vec{\xi}) = \frac{4\pi N_i^2 N_f^4 S_a}{c^2 + d^2}\left[(A0)^2 + (B0)^2\right] . \tag{8}$$

The quantities $(A0)^2$ and $(B0)^2$ are evaluated by numerical integration of Eq. (7).

Appendix III. This appendix is a listing of the free α-α cross sections used in the impulse approximation theories. The energy given in the tables is the laboratory kinetic energy of the incident alpha particle, and the angles and cross sections are given in the center of mass system. The data are taken from [Nils 56, Bred 59, Conz 60, Tom 63, Darr 65].

ENERGY = 3.840

C.O.M. ANGLE	DIFF. X-SECTION(MB/SR)
55.000	210.00000
60.000	210.00000
65.000	200.00000
70.000	200.00000
75.000	185.00000
80.000	180.00000
85.000	175.00000
90.000	175.00000

ENERGY = 5.260

C.O.M. ANGLE	DIFF. X-SECTION(MB/SR)
55.000	100.00000
60.000	42.00000
65.000	10.00000
70.000	3.20000
75.000	10.10000
80.000	22.00000
85.000	37.00000
90.000	42.00000

ENERGY = 6.470

C.O.M. ANGLE	DIFF. X-SECTION(MB/SR)
55.000	55.00000
60.000	33.00000
65.000	90.00000
70.000	195.00000
75.000	300.00000
80.000	400.00000
85.000	460.00000
90.000	510.00000

ENERGY = 6.960

C.O.M. ANGLE	DIFF. X-SECTION(MB/SR)
55.000	49.00000
60.000	52.00000
65.000	120.00000
70.000	240.00000
75.000	380.00000
80.000	500.00000
85.000	580.00000
90.000	600.00000

ENERGY = 7.470

C.O.M. ANGLE	DIFF. X-SECTION(MB/SR)
55.000	35.00000
60.000	52.00000
65.000	120.00000
70.000	260.00000
75.000	400.00000
80.000	500.00000
85.000	560.00000
90.000	620.00000

ENERGY = 7.880

C.O.M. ANGLE	DIFF. X-SECTION(MB/SR)
55.000	28.00000
60.000	56.00000
65.000	150.00000
70.000	280.00000
75.000	400.00000
80.000	510.00000
85.000	590.00000
90.000	610.00000

ENERGY = 8.870

C.O.M. ANGLE	DIFF. X-SECTION(MB/SR)
55.000	18.00000
60.000	52.00000
65.000	140.00000
70.000	230.00000
75.000	340.00000
80.000	430.00000
85.000	500.00000
90.000	520.00000

ENERGY = 9.880

C.O.M. ANGLE	DIFF. X-SECTION(MB/SR)
55.000	8.50000
60.000	38.00000
65.000	105.00000
70.000	200.00000
75.000	310.00000
80.000	400.00000
85.000	460.00000
90.000	500.00000

ENERGY = 10.880

C.O.M. ANGLE	DIFF. X-SECTION(MB/SR)
55.000	4.50000
60.000	35.00000
65.000	101.00000
70.000	200.00000
75.000	285.00000
80.000	360.00000
85.000	400.00000
90.000	390.00000

ENERGY = 11.880

C.O.M. ANGLE	DIFF. X-SECTION(MB/SR)
55.000	2.30000
60.000	28.00000
65.000	85.00000
70.000	170.00000
75.000	270.00000
80.000	320.00000
85.000	380.00000
90.000	400.00000

ENERGY = 12.300

C.O.M. ANGLE	DIFF. X-SECTION(MB/SR)
55.000	2.42000
60.000	24.40000
65.000	90.40000
70.000	165.00000
75.000	270.00000
80.000	337.00000
85.000	408.00000
90.000	418.00000

ENERGY = 15.200

C.O.M. ANGLE	DIFF. X-SECTION(MB/SR)
55.000	19.40000
60.000	29.90000
65.000	67.80000
70.000	128.00000
75.000	190.00000
80.000	257.00000
85.000	292.00000
90.000	317.00000

ENERGY = 17.800

C.O.M. ANGLE	DIFF. X-SECTION(MB/SR)
55.000	65.10000
60.000	61.90000
65.000	74.90000
70.000	98.50000
75.000	130.00000
80.000	163.00000
85.000	188.00000
90.000	204.00000

ENERGY = 19.100

C.O.M. ANGLE	DIFF. X-SECTION(MB/SR)
55.000	1[illegible]3.00000
60.000	103.00000
65.000	89.20000
70.000	90.10000
75.000	97.20000
80.000	121.00000
85.000	140.00000
90.000	143.00000

ENERGY = 20.400

C.O.M. ANGLE	DIFF. X-SECTION(MB/SR)
55.000	130.50000
60.000	110.00000
65.000	93.20000
70.000	78.50000
75.000	80.40000
80.000	92.00000
85.000	101.00000
90.000	108.00000

ENERGY = 21.800

C.O.M. ANGLE	DIFF. X-SECTION(MB/SR)
55.000	238.00000
60.000	202.00000
65.000	134.00000
70.000	67.30000
75.000	30.70000
80.000	20.50000
90.000	31.60000

ENERGY = 22.250

C.O.M. ANGLE	DIFF. X-SECTION(MB/SR)
54.000	247.00000
59.720	213.00000
64.000	156.00000
70.140	69.40000
76.200	20.20000
80.000	15.00000
85.000	21.10000
90.000	27.10000

ENERGY = 22.900

C.O.M. ANGLE	DIFF. X-SECTION(MB/SR)
54.800	285.70000
60.000	241.80000
65.000	150.20000
70.200	60.30000
76.200	7.20000
82.000	6.30000
86.000	17.20000
90.000	21.10000

ENERGY = 23.100

C.Q.M. ANGLE	DIFF. X-SECTION(MB/SR)
65.000	144.00000
70.000	59.10000
75.000	12.80000
80.000	2.30000
85.000	13.10000
90.000	18.00000

ENERGY = 25.500

C.O.M. ANGLE	DIFF. X-SECTION(MB/SR)
60.000	244.00000
70.000	46.70000
80.000	57.40000
90.000	118.00000

ENERGY = 27.600

C.O.M. ANGLE	DIFF. X-SECTION(MB/SR)
64.000	102.00000
70.000	36.10000
75.000	45.70000
80.000	112.00000
85.000	151.00000
90.000	186.00000

ENERGY = 29.800

C.O.M. ANGLE	DIFF. X-SECTION(MB/SR)
65.000	56.00000
70.000	36.60000
75.000	50.00000
80.000	151.00000
85.000	226.00000
90.000	208.00000

ENERGY = 31.800

C.O.M. ANGLE	DIFF. X-SECTION(MB/SR)
65.000	43.00000
70.000	31.20000
75.000	76.00000
80.000	137.00000
85.000	212.00000
90.000	235.00000

ENERGY = 34.200

C.O.M. ANGLE	DIFF. X-SECTION(MB/SR)
65.000	8.70000
70.000	29.00000
75.000	101.00000
80.000	175.00000
85.000	247.00000
90.000	286.00000

ENERGY = 35.100

C.O.M. ANGLE	DIFF. X-SECTION(MB/SR)
65.000	7.80000
70.000	26.90000
75.000	76.10000
80.000	134.00000
85.000	200.00000
90.000	261.00000

ENERGY = 36.850

C.O.M. ANGLE	DIFF. X-SECTION(MB/SR)
65.700	4.63000
69.700	18.30000
75.700	76.30000
79.700	129.00000
85.700	199.00000
89.700	209.00000
90.000	210.00000

ENERGY = 41.900

C.O.M. ANGLE	DIFF. X-SECTION(MB/SR)
65.000	25.66000
69.200	2.22000
75.800	61.80000
80.200	144.80000
84.400	223.40000
88.400	256.70000
90.000	269.00000

ENERGY = 38.400

C.O.M. ANGLE	DIFF. X-SECTION(MB/SR)
65.000	.86000
70.000	11.60000
75.000	36.40000
80.000	69.10000
85.000	100.00000
90.000	110.00000

ENERGY = 40.770

C.O.M. ANGLE	DIFF. X-SECTION(MB/SR)
65.300	14.00000
69.300	4.39000
75.300	57.60000
79.300	121.00000
85.300	213.00000
89.300	246.00000
90.000	250.00000

ENERGY = 44.410

C.O.M. ANGLE	DIFF. X-SECTION(MB/SR)
64.800	38.80000
70.800	1.79000
74.800	20.50000
78.800	62.30000
86.400	151.20000
88.400	160.00000
90.000	168.00000

ENERGY = 46.120

C.O.M. ANGLE	DIFF. X-SECTION(MB/SR)
65.800	3.50000
69.800	2.07000
75.800	52.90000
79.800	118.00000
84.400	181.70000
88.400	216.20000
90.000	220.00000

ENERGY = 47.100

C.O.M. ANGLE	DIFF. X-SECTION(MB/SR)
65.500	21.40000
69.500	1.65000
75.500	51.20000
79.500	122.90000
85.500	216.70000
89.500	238.90000
90.000	240.00000

ENERGY = 53.400

C.O.M. ANGLE	DIFF. X-SECTION(MB/SR)
65.020	42.93000
70.730	30.45000
74.560	32.05000
80.320	51.57000
86.120	101.30000
89.990	118.30000
90.000	119.00000

ENERGY = 58.490

C.O.M. ANGLE	DIFF. X-SECTION(MB/SR)
64.100	70.41000
69.790	28.20000
75.540	15.54000
79.380	34.02000
85.170	83.16000
89.050	99.59000
90.000	100.00000

ENERGY = 63.910

C.O.M. ANGLE	DIFF. X-SECTION(MB/SR)
64.120	65.34000
70.770	29.39000
74.590	15.33000
78.440	16.40000
84.220	40.55000
88.140	56.64000
90.000	57.00000

ENERGY = 69.910

C.O.M. ANGLE	DIFF. X-SECTION(MB/SR)
64.140	52.93000
70.790	28.71000
74.620	13.69000
80.380	11.43000
84.250	20.07000
89.050	28.21000
90.000	28.50000

ENERGY = 77.550

C.O.M. ANGLE	DIFF. X-SECTION(MB/SR)
64.170	37.97000
70.180	23.90000
74.270	11.69000
80.190	4.81000
84.280	8.07000
90.000	10.60000

ENERGY = 99.600

C.O.M. ANGLE	DIFF. X-SECTION(MB/SR)
64.240	11.63000
70.860	4.95000
75.310	2.33000
79.540	.63200
85.320	.51200
89.200	.95300
90.000	.90000

ENERGY = 119.900

C.O.M. ANGLE	DIFF. X-SECTION(MB/SR)
63.370	2.60800
68.110	1.50700
73.840	.61800
81.530	.05400
85.400	.26700
89.280	.50600
90.000	.51000

Appendix IV. This appendix provides a summary of the symmetric triple differential cross sections for the ground and first excited state transitions given as a function of T_3 (energy correlation). All quantities are given in the laboratory system. The results are arranged by increasing mass, and then by increasing excitation energy within a given mass.

RECOIL MASS = 8 A.M.U.

EXCITATION ENERGY = 0. (MEV)

SYMMETRIC ANGLE = 22 DEG.

T3 (MEV)	SIGMA (MB/((SR)**2*MEV)	STAT. ERROR (MB/((SR)**2*MEV)
25.88	.0486	.0100
29.16	.1288	.0210
32.44	.0985	.0140
35.72	.0972	.0140
39.00	.0863	.0160
42.28	.1045	.0170
45.56	.0972	.0140
48.84	.0985	.0180
52.12	.0887	.0160
55.40	.0754	.0150
58.68	0.	-0.

RECOIL MASS = 8 A.M.U.

EXCITATION ENERGY = 0. (MEV)

SYMMETRIC ANGLE = 25 DEG.

T3 (MEV)	SIGMA (MB/((SR)**2*MEV)	STAT. ERROR (MB/((SR)**2*MEV)
25.88	.0656	.0180
29.16	.1134	.0270
32.44	.0835	.0250
35.72	.1402	.0300
39.00	.1551	.0340
42.28	.2029	.0360
45.56	.1671	.0310
48.84	.1521	.0300
52.12	.1193	.0280
55.40	.0835	.0200
58.68	.0060	.0060

RECOIL MASS = 8 A.M.U.

EXCITATION ENERGY = 0. (MEV)

SYMMETRIC ANGLE = 28 DEG.

T3 (MEV)	SIGMA (MB/((SR)**2*MEV)	STAT. ERROR (MB/((SR)**2*MEV)
25.74	.0174	.0032
29.02	.0300	.0042
32.30	.0779	.0068
35.58	.0857	.0072
38.86	.1103	.0081
42.14	.1121	.0082
45.42	.0935	.0075
48.70	.0671	.0063
51.98	.0479	.0054
55.26	.0300	.0042
58.54	.0090	.0023
61.82	.0006	.0006

RECOIL MASS = 8 A.M.U.

EXCITATION ENERGY = 0. (MEV)

SYMMETRIC ANGLE = 35 DEG.

T3 (MEV)	SIGMA (MB/((SR)**2*MEV)	STAT. ERROR (MB/((SR)**2*MEV)
25.74	.0346	.0051
29.02	.0629	.0069
32.30	.0699	.0073
35.58	.1608	.0110
38.86	.2172	.0128
42.14	.2533	.0138
45.42	.2435	.0135
48.70	.2052	.0124
51.98	.1330	.0100
55.26	.0669	.0071
58.54	.0601	.0067
61.82	.0023	.0013

RECOIL MASS = 8 A.M.U.

EXCITATION ENERGY = 0. (MEV)

SYMMETRIC ANGLE = 41 DEG.

T3 (MEV)	SIGMA (MB/((SR)**2*MEV)	STAT. ERROR (MB/((SR)**2*MEV)
25.74	.0146	.0046
29.02	.0539	.0089
32.30	.0467	.0082
35.58	.0510	.0086
38.86	.1093	.0126
42.14	.0991	.0120
45.42	.1035	.0123
48.70	.0758	.0105
51.98	.0219	.0056
55.26	.0262	.0062
58.54	.0365	.0073
61.82	.0029	.0021

RECOIL MASS = 8 A.M.U.

EXCITATION ENERGY = 0. (MEV)

SYMMETRIC ANGLE = 42 DEG.

T3 (MEV)	SIGMA (MB/((SR)**2*MEV)	STAT. ERROR (MB/((SR)**2*MEV)
25.74	.0116	.0024
29.02	.0378	.0043
32.30	.0223	.0033
35.58	.0276	.0037
38.86	.0626	.0055
42.14	.0810	.0063
45.42	.0907	.0066
48.70	.0209	.0032
51.98	.0141	.0026
55.26	.0276	.0037
58.54	.0223	.0033
61.82	.0034	.0013

RECOIL MASS = 8 A.M.U.

EXCITATION ENERGY = 0. (MEV)

SYMMETRIC ANGLE = 47 DEG.

T3 (MEV)	SIGMA (MB/((SR)**2*MEV)	STAT. ERROR (MB/((SR)**2*MEV)
25.74	.0026	.0008
29.02	.0050	.0011
32.30	.0093	.0016
35.58	.0074	.0014
38.86	.0114	.0017
42.14	.0167	.0021
45.42	.0122	.0018
48.70	.0053	.0012
51.98	.0063	.0013
55.26	.0061	.0013
58.54	.0026	.0008
61.82	.0005	.0004

RECOIL MASS = 8 A.M.U.

EXCITATION ENERGY = 2.90 (MEV)

SYMMETRIC ANGLE = 22 DEG.

T3 (MEV)	SIGMA (MB/((SR)**2*MEV)	STAT. ERROR (MB/((SR)**2*MEV)
25.88	.0620	.0120
29.16	.1058	.0160
32.44	.0851	.0140
35.72	.0948	.0170
39.00	.0717	.0160
42.28	.0778	.0140
45.56	.1009	.0200
48.84	.0754	.0140
52.12	.0571	.0130
55.40	0.	-0.

RECOIL MASS = 8 A.M.U.

EXCITATION ENERGY = 2.90 (MEV)

SYMMETRIC ANGLE = 25 DEG.

T3 (MEV)	SIGMA (MB/((SR)**2*MEV)	STAT. ERROR (MB/((SR)**2*MEV)
25.88	.0507	.0200
29.16	.0955	.0230
32.44	.1104	.0270
35.72	.1044	.0260
39.00	.1581	.0333
42.28	.1163	.0230
45.56	.1253	.0270
48.84	.1253	.0270
52.12	.0985	.0240
55.40	.0448	.0140

RECOIL MASS = 8 A.M.U.

EXCITATION ENERGY = 2.90 (MEV)

SYMMETRIC ANGLE = 28 DEG.

T3 (MEV)	SIGMA (MB/((SR)**2*MEV)	STAT. ERROR (MB/((SR)**2*MEV)
25.74	.0252	.0039
29.02	.0408	.0049
32.30	.0497	.0055
35.58	.0665	.0063
38.86	.0449	.0052
42.14	.0677	.0064
45.42	.0731	.0066
48.70	.0527	.0056
51.98	.0575	.0059
55.26	.0473	.0053
58.54	.0084	.0022

RECOIL MASS = 8 A.M.U.

EXCITATION ENERGY = 2.90 (MEV)

SYMMETRIC ANGLE = 35 DEG.

T3 (MEV)	SIGMA (MB/((SR)**2*MEV)	STAT. ERROR (MB/((SR)**2*MEV)
25.74	.0594	.0067
29.02	.0872	.0081
32.30	.0864	.0081
35.58	.0722	.0074
38.86	.0609	.0068
42.14	.0661	.0071
45.42	.0661	.0071
48.70	.0872	.0081
51.98	.1090	.0091
55.26	.0992	.0086
58.54	.0218	.0040

RECOIL MASS = 8 A.M.U.

EXCITATION ENERGY = 2.90 (MEV)

SYMMETRIC ANGLE = 41 DEG.

T3 (MEV)	SIGMA (MB/((SR)**2*MEV)	STAT. ERROR (MB/((SR)**2*MEV)
25.74	.0175	.0050
29.02	.0365	.0073
32.30	.0394	.0076
35.58	.0437	.0080
38.86	.0423	.0079
42.14	.0306	.0067
45.42	.0219	.0056
48.70	.0408	.0077
51.98	.0467	.0082
55.26	.0219	.0056
58.54	.0131	.0044

RECOIL MASS = 8 A.M.U.

EXCITATION ENERGY = 2.90 (MEV)

SYMMETRIC ANGLE = 42 DEG.

T3 (MEV)	SIGMA (MB/((SR)**2*MEV)	STAT. ERROR (MB/((SR)**2*MEV)
25.74	.0209	.0032
29.02	.0359	.0042
32.30	.0461	.0047
35.58	.0364	.0042
38.86	.0412	.0045
42.14	.0408	.0045
45.42	.0291	.0038
48.70	.0291	.0038
51.98	.0369	.0042
55.26	.0296	.0038
58.54	.0044	.0015

RECOIL MASS = 8 A.M.U.

EXCITATION ENERGY = 2.90 (MEV)

SYMMETRIC ANGLE = 47 DEG.

T3 (MEV)	SIGMA (MB/((SR)**2*MEV)	STAT. ERROR (MB/((SR)**2*MEV)
25.74	.0180	.0022
29.02	.0252	.0026
32.30	.0267	.0027
35.58	.0167	.0021
38.86	.0159	.0020
42.14	.0212	.0024
45.42	.0225	.0024
48.70	.0238	.0025
51.98	.0220	.0024
55.26	.0286	.0028
58.54	.0016	.0007

RECOIL MASS = 12 A.M.U.

EXCITATION ENERGY = 0. (MEV)

SYMMETRIC ANGLE = 19 DEG.

T3 (MEV)	SIGMA (MB/((SR)**2*MEV)	STAT. ERROR (MB/((SR)**2*MEV)
25.88	.0397	.0180
29.16	.1010	.0300
32.44	.1155	.0300
35.72	.0866	.0240
39.00	.1660	.0350
42.28	.1840	.0400
45.56	.1516	.0310
48.84	.1155	.0360
52.12	.0794	.0230
55.40	.0541	.0270
58.68	.0144	.0160
61.96	0.	-0.

RECOIL MASS = 12 A.M.U.

EXCITATION ENERGY = 0. (MEV)

SYMMETRIC ANGLE = 22 DEG.

T3 (MEV)	SIGMA (MB/((SR)**2*MEV)	STAT. ERROR (MB/((SR)**2*MEV)
25.88	.0575	.0170
29.16	.0402	.0180
32.44	.0690	.0180
35.72	.0517	.0180
39.00	.0373	.0150
42.28	.0575	.0200
45.56	.0431	.0170
48.84	.0402	.0150
52.12	.0431	.0160
55.40	.0373	.0130
58.68	.0230	.0110

RECOIL MASS = 12 A.M.U.

EXCITATION ENERGY = 0. (MEV)

SYMMETRIC ANGLE = 25 DEG.

T3 (MEV)	SIGMA (MB/((SR)**2*MEV)	STAT. ERROR (MB/((SR)**2*MEV)
25.88	.0365	.0140
29.16	.0783	.0200
32.44	.0589	.0190
35.72	.0897	.0220
39.00	.0925	.0210
42.28	.1038	.0200
45.56	.1010	.0220
48.84	.0953	.0240
52.12	.0617	.0200
55.40	.0505	.0170
58.68	.0140	.0110

RECOIL MASS = 12 A.M.U.

EXCITATION ENERGY = 0. (MEV)

SYMMETRIC ANGLE = 28 DEG.

T3 (MEV)	SIGMA (MB/((SR)**2*MEV)	STAT. ERROR (MB/((SR)**2*MEV)
21.20	.0151	.0045
24.36	0.	0.
27.53	.0384	.0073
30.69	.0671	.0096
33.85	.1028	.0119
37.02	.0959	.0115
40.18	.1178	.0127
43.34	.1192	.0128
46.50	.1000	.0117
49.67	.0658	.0095
52.83	.0288	.0063
55.99	.0110	.0039
59.16	.0014	.0014

RECOIL MASS = 12 A.M.U.

EXCITATION ENERGY = 0. (MEV)

SYMMETRIC ANGLE = 35 DEG.

T3 (MEV)	SIGMA (MB/((SR)**2*MEV)	STAT. ERROR (MB/((SR)**2*MEV)
21.20	.0219	.0048
24.36	.0240	.0050
27.53	.0428	.0067
30.69	.0396	.0064
33.85	.0699	.0085
37.02	.1210	.0112
40.18	.1628	.0130
43.34	.1889	.0140
46.50	.1596	.0129
49.67	.1189	.0111
52.83	.0720	.0087
55.99	.0636	.0081
59.16	.0073	.0028

RECOIL MASS = 12 A.M.U.

EXCITATION ENERGY = 0. (MEV)

SYMMETRIC ANGLE = 41 DEG.

T3 (MEV)	SIGMA (MB/((SR)**2*MEV)	STAT. ERROR (MB/((SR)**2*MEV)
21.20	.0356	.0086
24.36	.0146	.0055
27.53	.0251	.0073
30.69	.0272	.0075
33.85	.0586	.0111
37.02	.0774	.0127
40.18	.1130	.0154
43.34	.1213	.0159
46.50	.0711	.0122
49.67	.0418	.0094
52.83	.0188	.0063
55.99	.0272	.0075

RECOIL MASS = 12 A.M.U.

EXCITATION ENERGY = 0. (MEV)

SYMMETRIC ANGLE = 42 DEG.

T3 (MEV)	SIGMA (MB/((SR)**2*MEV)	STAT. ERROR (MB/((SR)**2*MEV)
21.20	.0322	.0056
24.36	.0146	.0038
27.53	.0166	.0040
30.69	.0215	.0046
33.85	.0400	.0063
37.02	.0527	.0072
40.18	.0683	.0082
43.34	.0683	.0082
46.50	.0547	.0073
49.67	.0263	.0051
52.83	.0205	.0045
55.99	.0185	.0043

RECOIL MASS = 12 A.M.U.

EXCITATION ENERGY = 0. (MEV)

SYMMETRIC ANGLE = 47 DEG.

T3 (MEV)	SIGMA (MB/((SR)**2*MEV)	STAT. ERROR (MB/((SR)**2*MEV)
21.20	.0205	.0045
24.36	.0097	.0031
27.53	.0010	.0010
30.69	.0020	.0014
33.85	.0088	.0029
37.02	.0107	.0032
40.18	.0195	.0044
43.34	.0253	.0050
46.50	.0097	.0031
49.67	.0058	.0024
52.83	.0078	.0028
55.99	.0166	.0040

RECOIL MASS = 12 A.M.U.

EXCITATION ENERGY = 4.44 (MEV)

SYMMETRIC ANGLE = 19 DEG.

T3 (MEV)	SIGMA (MB/((SR)**2*MEV)	STAT. ERROR (MB/((SR)**2*MEV)
25.88	.0353	.0190
29.16	.0902	.0300
32.44	.0650	.0220
35.72	.1155	.0300
39.00	.0902	.0300
42.28	.0722	.0240
45.56	.0108	.0210
48.84	.0866	.0260
52.12	.0469	.0250
55.40	.0180	.0170

RECOIL MASS = 12 A.M.U.

EXCITATION ENERGY = 4.44 (MEV)

SYMMETRIC ANGLE = 22 DEG.

T3 (MEV)	SIGMA (MB/((SR)**2*MEV)	STAT. ERROR (MB/((SR)**2*MEV)
25.88	.0632	.0170
29.16	.0517	.0180
32.44	.0575	.0180
35.72	.0546	.0190
39.00	.0287	.0130
42.28	.0345	.0170
45.56	.0747	.0200
48.84	.0661	.0190
52.12	.1322	.0260
55.40	0.	-0.

RECOIL MASS = 12 A.M.U.

EXCITATION ENERGY = 4.44 (MEV)

SYMMETRIC ANGLE = 25 DEG.

T3 (MEV)	SIGMA (MB/((SR)**2*MEV)	STAT. ERROR (MB/((SR)**2*MEV)
25.88	.0309	.0130
29.16	.0841	.0200
32.44	.0785	.0200
35.72	.0561	.0180
39.00	.1038	.0240
42.28	.0701	.0180
45.56	.0533	.0200
48.84	.0841	.0210
52.12	.0505	.0200
55.40	.0112	.0090

RECOIL MASS = 12 A.M.U.

EXCITATION ENERGY = 4.44 (MEV)

SYMMETRIC ANGLE = 28 DEG.

T3 (MEV)	SIGMA (MB/((SR)**2*MEV)	STAT. ERROR (MB/((SR)**2*MEV)
21.20	.0370	.0071
24.36	.0438	.0078
27.53	.0521	.0085
30.69	.0438	.0078
33.85	.0562	.0088
37.02	.0575	.0089
40.18	.0630	.0093
43.34	.0479	.0081
46.50	.0493	.0082
49.67	.0384	.0073
52.83	.0260	.0060

RECOIL MASS = 12 A.M.U.

EXCITATION ENERGY = 4.44 (MEV)

SYMMETRIC ANGLE = 35 DEG.

T3 (MEV)	SIGMA (MB/((SR)**2*MEV)	STAT. ERROR (MB/((SR)**2*MEV)
21.20	.0470	.0070
24.36	.0261	.0052
27.53	.0355	.0061
30.69	.0230	.0049
33.85	.0261	.0052
37.02	.0282	.0054
40.18	.0209	.0047
43.34	.0240	.0050
46.50	.0292	.0055
49.67	.0250	.0051
52.83	.0324	.0058

RECOIL MASS = 12 A.M.U.

EXCITATION ENERGY = 4.44 (MEV)

SYMMETRIC ANGLE = 41 DEG.

T3 (MEV)	SIGMA (MB/((SR)**2*MEV)	STAT. ERROR (MB/((SR)**2*MEV)
21.20	.0146	.0055
24.36	.0063	.0036
27.53	.0126	.0051
30.69	.0188	.0063
33.85	.0230	.0069
37.02	.0084	.0042
40.18	.0146	.0055
43.34	.0146	.0055
46.50	.0146	.0055
49.67	.0063	.0036
52.83	.0042	.0030

RECOIL MASS = 12 A.M.U.

EXCITATION ENERGY = 4.44 (MEV)

SYMMETRIC ANGLE = 42 DEG.

T3 (MEV)	SIGMA (MB/((SR)**2*MEV)	STAT. ERROR (MB/((SR)**2*MEV)
21.20	.0127	.0035
24.36	.0137	.0037
27.53	.0049	.0022
30.69	.0117	.0034
33.85	.0117	.0034
37.02	.0215	.0046
40.18	.0098	.0031
43.34	.0068	.0026
46.50	.0098	.0031
49.67	.0078	.0028
52.83	.0088	.0029

RECOIL MASS = 12 A.M.U.

EXCITATION ENERGY = 4.44 (MEV)

SYMMETRIC ANGLE = 47 DEG.

T3 (MEV)	SIGMA (MB/((SR)**2*MEV)	STAT. ERROR (MB/((SR)**2*MEV)
21.20	.0088	.0029
24.36	.0068	.0026
27.53	.0029	.0017
30.69	.0020	.0014
33.85	.0049	.0022
37.02	.0068	.0026
40.18	.0039	.0020
43.34	.0049	.0022
46.50	.0010	.0010
49.67	.0029	.0017
52.83	.0029	.0017

RECOIL MASS = 20 A.M.U.

EXCITATION ENERGY = 0. (MEV)

SYMMETRIC ANGLE = 28 DEG.

T3 (MEV)	SIGMA (MB/((SR)**2*MEV)	STAT. ERROR (MB/((SR)**2*MEV)
21.20	.0085	.0020
24.36	.0081	.0020
27.53	.0265	.0035
30.69	.0265	.0035
33.85	.0422	.0045
37.02	.0455	.0046
40.18	.0630	.0055
43.34	.0517	.0050
46.50	.0545	.0051
49.67	.0341	.0040
52.83	.0237	.0034
55.99	.0033	.0013
59.16	.0005	.0005

RECOIL MASS = 20 A.M.U.

EXCITATION ENERGY = 0. (MEV)

SYMMETRIC ANGLE = 35 DEG.

T3 (MEV)	SIGMA (MB/((SR)**2*MEV)	STAT. ERROR (MB/((SR)**2*MEV)
21.20	.0121	.0026
24.36	.0132	.0027
27.53	.0094	.0023
30.69	.0166	.0030
33.85	.0298	.0041
37.02	.0385	.0057
40.18	.0828	.0068
43.34	.0773	.0065
46.50	.0574	.0056
49.67	.0342	.0043
52.83	.0215	.0034
55.99	.0072	.0020
59.16	.0005	.0005

RECOIL MASS = 20 A.M.U.

EXCITATION ENERGY = 0. (MEV)

SYMMETRIC ANGLE = 41 DEG.

T3 (MEV)	SIGMA (MB/((SR)**2*MEV)	STAT. ERROR (MB/((SR)**2*MEV)
21.20	.0158	.0020
24.36	.0117	.0018
27.53	.0099	.0016
30.69	.0083	.0015
33.85	.0192	.0023
37.02	.0288	.0028
40.18	.0414	.0033
43.34	.0315	.0029
46.50	.0200	.0023
49.67	.0083	.0015
52.83	.0117	.0018
55.99	.0043	.0011
59.16	-.0003	.0003

RECOIL MASS = 20 A.M.U.

EXCITATION ENERGY = 0. (MEV)

SYMMETRIC ANGLE = 47 DEG.

T3 (MEV)	SIGMA (MB/((SR)**2*MEV)	STAT. ERROR (MB/((SR)**2*MEV)
21.20	.0048	.0011
24.36	.0043	.0010
27.53	.0020	.0007
30.69	.0013	.0006
33.85	.0015	.0006
37.02	.0045	.0011
40.18	.0025	.0008
43.34	.0045	.0011
46.50	.0023	.0008
49.67	0.	0.
52.83	.0015	.0006
55.99	.0013	.0006
59.16	0.	0.

RECOIL MASS = 20 A.M.U.

EXCITATION ENERGY = 1.63 (MEV)

SYMMETRIC ANGLE = 28 DEG.

T3 (MEV)	SIGMA (MB/((SR)**2*MEV)	STAT. ERROR (MB/((SR)**2*MEV)
21.20	.0019	.0009
24.36	.0009	.0007
27.53	.0071	.0018
30.69	.0014	.0008
33.85	.0052	.0016
37.02	.0038	.0013
40.18	.0014	.0008
43.34	.0066	.0018
46.50	-.0005	.0005
49.67	.0038	.0013
52.83	0.	0.
55.99	-.0005	.0005

RECOIL MASS = 20 A.M.U.

EXCITATION ENERGY = 1.63 (MEV)

SYMMETRIC ANGLE = 35 DEG.

T3 (MEV)	SIGMA (MB/((SR)**2*MEV)	STAT. ERROR (MB/((SR)**2*MEV)
21.20	.0033	.0013
24.36	.0017	.0010
27.53	.0005	.0005
30.69	.0017	.0010
33.85	.0011	.0008
37.02	.0017	.0010
40.18	.0033	.0013
43.34	.0033	.0013
46.50	.0088	.0022
49.67	.0050	.0017
52.83	.0055	.0018
55.99	0.	0.

RECOIL MASS = 20 A.M.U.

EXCITATION ENERGY = 1.63 (MEV)

SYMMETRIC ANGLE = 41 DEG.

T3 (MEV)	SIGMA (MB/((SR)**2*MEV)	STAT. ERROR (MB/((SR)**2*MEV)
21.20	.0032	.0009
24.36	.0037	.0010
27.53	.0027	.0008
30.69	.0008	.0005
33.85	.0024	.0008
37.02	.0024	.0008
40.18	.0021	.0008
43.34	.0032	.0009
46.50	.0027	.0008
49.67	.0013	.0006
52.83	.0043	.0011
55.99	.0003	.0003

RECOIL MASS = 20 A.M.U.

EXCITATION ENERGY = 1.63 (MEV)

SYMMETRIC ANGLE = 47 DEG.

T3 (MEV)	SIGMA (MB/((SR)**2*MEV)	STAT. ERROR (MB/((SR)**2*MEV)
21.20	.0013	.0006
24.36	.0010	.0005
27.53	.0013	.0006
30.69	.0008	.0004
33.85	.0010	.0005
37.02	.0003	.0003
40.18	0.	0.
43.34	.0018	.0007
46.50	.0010	.0005
49.67	.0018	.0007
52.83	.0018	.0007
55.99	0.	0.

RECOIL MASS = 22 A.M.U.

EXCITATION ENERGY = 0. (MEV)

SYMMETRIC ANGLE = 28 DEG.

T3 (MEV)	SIGMA (MB/((SR)**2*MEV)	STAT. ERROR (MB/((SR)**2*MEV)
21.20	.0084	.0025
24.36	.0130	.0032
27.53	.0238	.0043
30.69	.0276	.0046
33.85	.0429	.0057
37.02	.0307	.0048
40.18	.0452	.0059
43.34	.0552	.0065
46.50	.0429	.0057
49.67	.0314	.0049
52.83	.0192	.0038
55.99	-.0008	.0008

RECOIL MASS = 22 A.M.U.

EXCITATION ENERGY = 0. (MEV)

SYMMETRIC ANGLE = 35 DEG.

T3 (MEV)	SIGMA (MB/((SR)**2*MEV)	STAT. ERROR (MB/((SR)**2*MEV)
21.20	.0191	.0030
24.36	.0168	.0028
27.53	.0065	.0018
30.69	.0163	.0028
33.85	.0280	.0036
37.02	.0392	.0043
40.18	.0541	.0050
43.34	.0393	.0053
46.50	.0453	.0046
49.67	.0317	.0039
52.83	.0182	.0029
55.99	.0037	.0013

RECOIL MASS = 22 A.M.U.

EXCITATION ENERGY = 0. (MEV)

SYMMETRIC ANGLE = 41 DEG.

T3 (MEV)	SIGMA (MB/((SR)**2*MEV)	STAT. ERROR (MB/((SR)**2*MEV)
21.20	.0114	.0019
24.36	.0089	.0016
27.53	.0071	.0015
30.69	.0055	.0013
33.85	.0083	.0016
37.02	.0230	.0027
40.18	.0221	.0026
43.34	.0166	.0023
46.50	.0120	.0019
49.67	.0077	.0015
52.83	.0098	.0017
55.99	.0021	.0008

RECOIL MASS = 22 A.M.U.

EXCITATION ENERGY = 0. (MEV)

SYMMETRIC ANGLE = 47 DEG.

T3 (MEV)	SIGMA (MB/((SR)**2*MEV)	STAT. ERROR (MB/((SR)**2*MEV)
21.20	.0026	.0008
24.36	.0023	.0009
27.53	.0007	.0004
30.69	.0018	.0006
33.85	.0013	.0005
37.02	.0022	.0007
40.18	.0024	.0007
43.34	.0020	.0007
46.50	.0015	.0006
49.67	.0018	.0006
52.83	.0024	.0007

RECOIL MASS = 22 A.M.U.

EXCITATION ENERGY = 1.28 (MEV)

SYMMETRIC ANGLE = 28 DEG.

T3 (MEV)	SIGMA (MB/((SR)**2*MEV)	STAT. ERROR (MB/((SR)**2*MEV)
21.20	.0054	.0020
24.36	.0031	.0015
27.53	.0084	.0025
30.69	.0046	.0019
33.85	.0023	.0013
37.02	.0054	.0020
40.18	.0031	.0015
43.34	.0069	.0023
46.50	.0038	.0017
49.67	.0046	.0019
52.83	.0038	.0017

RECOIL MASS = 22 A.M.U.

EXCITATION ENERGY = 1.28 (MEV)

SYMMETRIC ANGLE = 35 DEG.

T3 (MEV)	SIGMA (MB/((SR)**2*MEV)	STAT. ERROR (MB/((SR)**2*MEV)
21.20	.0093	.0021
24.36	.0051	.0016
27.53	.0028	.0011
30.69	.0042	.0014
33.85	.0023	.0010
37.02	.0037	.0013
40.18	.0061	.0017
43.34	.0079	.0019
46.50	.0070	.0018
49.67	.0056	.0016
52.83	.0023	.0010
55.99	.0005	.0005

RECOIL MASS = 22 A.M.U.

EXCITATION ENERGY = 1.28 (MEV)

SYMMETRIC ANGLE = 41 DEG.

T3 (MEV)	SIGMA (MB/((SR)**2*MEV)	STAT. ERROR (MB/((SR)**2*MEV)
21.20	.0021	.0008
24.36	.0024	.0009
27.53	.0024	.0009
30.69	.0018	.0008
33.85	.0046	.0012
37.02	.0021	.0008
40.18	.0031	.0010
43.34	.0015	.0007
46.50	.0012	.0006
49.67	.0009	.0005
52.83	.0043	.0011

RECOIL MASS = 22 A.M.U.

EXCITATION ENERGY = 1.28 (MEV)

SYMMETRIC ANGLE = 47 DEG.

T3 (MEV)	SIGMA (MB/((SR)**2*MEV)	STAT. ERROR (MB/((SR)**2*MEV)
21.20	.0037	.0009
24.36	.0022	.0007
27.53	.0028	.0008
30.69	.0013	.0005
33.85	.0009	.0004
37.02	.0011	.0005
40.18	.0022	.0007
43.34	.0031	.0008
46.50	0.	0.
49.67	.0024	.0007
52.83	.0022	.0007

RECOIL MASS = 24 A.M.U.

EXCITATION ENERGY = 0. (MEV)

SYMMETRIC ANGLE = 28 DEG.

T3 (MEV)	SIGMA (MB/((SR)**2*MEV)	STAT. ERROR (MB/((SR)**2*MEV)
21.20	.0057	.0018
24.36	.0057	.0018
27.53	.0143	.0029
30.69	.0263	.0039
33.85	.0298	.0041
37.02	.0361	.0045
40.18	.0338	.0044
43.34	.0453	.0051
46.50	.0344	.0044
49.67	.0232	.0044
52.83	.0218	.0035
55.99	.0006	.0006

RECOIL MASS = 24 A.M.U.

EXCITATION ENERGY = 0. (MEV)

SYMMETRIC ANGLE = 35 DEG.

T3 (MEV)	SIGMA (MB/((SR)**2*MEV)	STAT. ERROR (MB/((SR)**2*MEV)
21.20	.0187	.0029
24.36	.0143	.0025
27.53	.0076	.0018
30.69	.0116	.0023
33.85	.0196	.0030
37.02	.0392	.0042
40.18	.0432	.0044
43.34	.0406	.0043
46.50	.0379	.0041
49.67	.0232	.0032
52.83	.0174	.0028
55.99	.0027	.0011

RECOIL MASS = 24 A.M.U.

EXCITATION ENERGY = 0. (MEV)

SYMMETRIC ANGLE = 41 DEG.

T3 (MEV)	SIGMA (MB/((SR)**2*MEV)	STAT. ERROR (MB/((SR)**2*MEV)
21.20	.0114	.0021
24.36	.0090	.0019
27.53	.0059	.0015
30.69	.0063	.0016
33.85	.0102	.0020
37.02	.0232	.0030
40.18	.0188	.0027
43.34	.0188	.0027
46.50	.0110	.0021
49.67	.0094	.0019
52.83	.0067	.0016
55.99	.0059	.0015
59.16	.0004	.0004

RECOIL MASS = 24 A.M.U.

EXCITATION ENERGY = 0. (MEV)

SYMMETRIC ANGLE = 47 DEG.

T3 (MEV)	SIGMA (MB/((SR)**2*MEV)	STAT. ERROR (MB/((SR)**2*MEV)
21.20	.0027	.0009
24.36	.0024	.0008
27.53	.0005	.0004
30.69	.0021	.0008
33.85	0.	0.
37.02	.0046	.0011
40.18	.0048	.0011
43.34	.0029	.0009
46.50	.0013	.0006
49.67	.0035	.0010
52.83	.0019	.0007
55.99	0.	0.
59.16	-.0003	.0003

RECOIL MASS = 24 A.M.U.

EXCITATION ENERGY = 1.37 (MEV)

SYMMETRIC ANGLE = 28 DEG.

T3 (MEV)	SIGMA (MB/((SR)**2*MEV)	STAT. ERROR (MB/((SR)**2*MEV)
21.20	.0080	.0021
24.36	.0063	.0019
27.53	.0086	.0022
30.69	.0080	.0021
33.85	.0057	.0018
37.02	.0051	.0017
40.18	.0063	.0019
43.34	.0080	.0021
46.50	.0115	.0026
49.67	.0069	.0020
52.83	.0046	.0016

RECOIL MASS = 24 A.M.U.

EXCITATION ENERGY = 1.37 (MEV)

SYMMETRIC ANGLE = 35 DEG.

T3 (MEV)	SIGMA (MB/((SR)**2*MEV)	STAT. ERROR (MB/((SR)**2*MEV)
21.20	.0062	.0017
24.36	.0031	.0012
27.53	.0036	.0013
30.69	.0045	.0014
33.85	.0013	.0008
37.02	.0080	.0019
40.18	.0049	.0015
43.34	.0053	.0015
46.50	.0058	.0016
49.67	.0049	.0015
52.83	.0049	.0015
55.99	0.	0.

RECOIL MASS = 24 A.M.U.

EXCITATION ENERGY = 1.37 (MEV)

SYMMETRIC ANGLE = 41 DEG.

T3 (MEV)	SIGMA (MB/((SR)**2*MEV)	STAT. ERROR (MB/((SR)**2*MEV)
21.20	.0051	.0014
24.36	.0020	.0009
27.53	.0039	.0012
30.69	.0035	.0012
33.85	.0020	.0009
37.02	-.0004	.0004
40.18	.0004	.0004
43.34	0.	0.
46.50	0.	0.
49.67	.0039	.0012
52.83	.0059	.0015
55.99	-.0004	.0004

RECOIL MASS = 24 A.M.U.

EXCITATION ENERGY = 1.37 (MEV)

SYMMETRIC ANGLE = 47 DEG.

T3 (MEV)	SIGMA (MB/((SR)**2*MEV)	STAT. ERROR (MB/((SR)**2*MEV)
21.20	.0008	.0005
24.36	.0005	.0004
27.53	0.	0.
30.69	.0005	.0004
33.85	0.	0.
37.02	.0011	.0005
40.18	.0024	.0008
43.34	.0016	.0007
46.50	-.0003	.0003
49.67	.0013	.0006
52.83	.0008	.0005

RECOIL MASS = 26 A.M.U.

EXCITATION ENERGY = 0. (MEV)

SYMMETRIC ANGLE = 28 DEG.

T3 (MEV)	SIGMA (MB/((SR)**2*MEV)	STAT. ERROR (MB/((SR)**2*MEV)
25.74	.0043	.0021
29.02	.0321	.0059
32.30	.0225	.0049
35.58	.0150	.0040
38.86	.0182	.0044
42.14	.0236	.0050
45.42	.0107	.0034
48.70	.0182	.0044
51.98	.0064	.0026
55.26	.0043	.0021
58.54	.0032	.0019
61.82	0.	0.

RECOIL MASS = 26 A.M.U.

EXCITATION ENERGY = 0. (MEV)

SYMMETRIC ANGLE = 35 DEG.

T3 (MEV)	SIGMA (MB/((SR)**2*MEV)	STAT. ERROR (MB/((SR)**2*MEV)
25.74	.0027	.0019
29.02	.0148	.0045
32.30	.0162	.0047
35.58	.0202	.0052
38.86	.0265	.0070
42.14	.0283	.0062
45.42	.0224	.0066
48.70	.0175	.0049
51.98	.0081	.0033
55.26	.0095	.0036
58.54	.0013	.0013
61.82	0.	0.

RECOIL MASS = 26 A.M.U.

EXCITATION ENERGY = 0. (MEV)

SYMMETRIC ANGLE = 41 DEG.

T3 (MEV)	SIGMA (MB/((SR)**2*MEV)	STAT. ERROR (MB/((SR)**2*MEV)
25.74	.0015	.0011
29.02	.0070	.0023
32.30	.0023	.0013
35.58	.0179	.0037
38.86	.0171	.0037
42.14	.0117	.0030
45.42	.0194	.0039
48.70	.0047	.0019
51.98	.0047	.0019
55.26	.0039	.0017
58.54	0.	0.

RECOIL MASS = 26 A.M.U.

EXCITATION ENERGY = 0. (MEV)

SYMMETRIC ANGLE = 47 DEG.

T3 (MEV)	SIGMA (MB/((SR)**2*MEV)	STAT. ERROR (MB/((SR)**2*MEV)
25.74	.0009	.0009
29.02	.0026	.0015
32.30	.0034	.0017
35.58	.0017	.0012
38.86	.0034	.0017
42.14	.0068	.0024
45.42	.0017	.0012
48.70	.0017	.0012
51.98	.0017	.0012
55.26	.0009	.0009
58.54	0.	0.

RECOIL MASS = 26 A.M.U.

EXCITATION ENERGY = 1.81 (MEV)

SYMMETRIC ANGLE = 28 DEG.

T3 (MEV)	SIGMA (MB/((SR)**2*MEV)	STAT. ERROR (MB/((SR)**2*MEV)
25.74	.0011	.0011
29.02	.0064	.0026
32.30	.0054	.0024
35.58	0.	0.
38.86	.0021	.0013
42.14	.0096	.0032
45.42	.0064	.0026
48.70	.0086	.0030
51.98	.0075	.0028
55.26	.0054	.0024
58.54	0.	0.

RECOIL MASS = 26 A.M.U.

EXCITATION ENERGY = 1.81 (MEV)

SYMMETRIC ANGLE = 35 DEG.

T3 (MEV)	SIGMA (MB/((SR)**2*MEV)	STAT. ERROR (MB/((SR)**2*MEV)
25.74	.0013	.0013
29.02	.0013	.0013
32.30	.0013	.0013
35.58	.0068	.0030
38.86	.0040	.0023
42.14	.0027	.0019
45.42	.0068	.0030
48.70	.0040	.0023
51.98	.0040	.0023
55.26	.0040	.0023
58.54	0.	0.

RECOIL MASS = 26 A.M.U.

EXCITATION ENERGY = 1.81 (MEV)

SYMMETRIC ANGLE = 41 DEG.

T3 (MEV)	SIGMA (MB/((SR)**2*MEV)	STAT. ERROR (MB/((SR)**2*MEV)
25.74	0.	0.
29.02	.0031	.0016
32.30	.0031	.0016
35.58	.0023	.0013
38.86	.0031	.0016
42.14	.0062	.0022
45.42	.0016	.0011
48.70	.0023	.0013
51.98	.0039	.0017
55.26	.0023	.0013
58.54	0.	0.

RECOIL MASS = 36 A.M.U.

EXCITATION ENERGY = 0. (MEV)

SYMMETRIC ANGLE = 28 DEG.

T3 (MEV)	SIGMA (MB/((SR)**2*MEV)	STAT. ERROR (MB/((SR)**2*MEV)
25.74	.0009	.0007
29.02	.0100	.0022
32.30	.0166	.0028
35.58	.0199	.0031
38.86	.0242	.0034
42.14	.0218	.0032
45.42	.0128	.0025
48.70	.0157	.0027
51.98	.0066	.0018
55.26	.0043	.0014
58.54	.0033	.0013
61.82	.0005	.0005
65.10	.0005	.0005

RECOIL MASS = 36 A.M.U.

EXCITATION ENERGY = 0. (MEV)

SYMMETRIC ANGLE = 32 DEG.

T3 (MEV)	SIGMA (MB/((SR)**2*MEV)	STAT. ERROR (MB/((SR)**2*MEV)
25.74	.0020	.0010
29.02	.0109	.0023
32.30	.0179	.0030
35.58	.0328	.0040
38.86	.0233	.0034
42.14	.0263	.0036
45.42	.0169	.0029
48.70	.0084	.0020
51.98	.0050	.0016
55.26	.0035	.0013
58.54	.0035	.0013
61.82	.0020	.0010
65.10	.0005	.0005

RECOIL MASS = 36 A.M.U.

EXCITATION ENERGY = 0. (MEV)

SYMMETRIC ANGLE = 42 DEG.

T3 (MEV)	SIGMA (MB/((SR)**2*MEV)	STAT. ERROR (MB/((SR)**2*MEV)
25.74	0.	0.
29.02	.0038	.0011
32.30	.0026	.0009
35.58	.0093	.0017
38.86	.0067	.0015
42.14	.0064	.0014
45.42	.0157	.0022
48.70	.0051	.0013
51.98	0.	0.
55.26	.0019	.0008
58.54	0.	0.
61.82	0.	0.

RECOIL MASS = 36 A.M.U.

EXCITATION ENERGY = 0. (MEV)

SYMMETRIC ANGLE = 47 DEG.

T3 (MEV)	SIGMA (MB/((SR)**2*MEV)	STAT. ERROR (MB/((SR)**2*MEV)
25.74	.0003	.0003
29.02	.0009	.0005
32.30	0.	0.
35.58	.0006	.0004
38.86	.0006	.0004
42.14	.0009	.0005
45.42	.0012	.0006
48.70	.0009	.0005
51.98	.0003	.0003
55.26	0.	0.
58.54	.0006	.0004
61.82	.0003	.0003

RECOIL MASS = 36 A.M.U.

EXCITATION ENERGY = 1.97 (MEV)

SYMMETRIC ANGLE = 28 DEG.

T3 (MEV)	SIGMA (MB/((SR)**2*MEV)	STAT. ERROR (MB/((SR)**2*MEV)
25.74	.0029	.0012
29.02	.0100	.0022
32.30	.0104	.0022
35.58	.0123	.0024
38.86	.0114	.0023
42.14	.0138	.0025
45.42	.0152	.0027
48.70	.0142	.0026
51.98	.0147	.0026
55.26	.0100	.0022
58.54	.0047	.0015
61.82	0.	0.

RECOIL MASS = 36 A.M.U.

EXCITATION ENERGY = 1.97 (MEV)

SYMMETRIC ANGLE = 32 DEG.

T3 (MEV)	SIGMA (MB/((SR)**2*MEV)	STAT. ERROR (MB/((SR)**2*MEV)
25.74	.0060	.0017
29.02	.0124	.0025
32.30	.0124	.0025
35.58	.0084	.0020
38.86	.0094	.0022
42.14	.0114	.0024
45.42	.0070	.0019
48.70	.0065	.0018
51.98	.0084	.0020
55.26	.0089	.0021
58.54	.0099	.0022

RECOIL MASS = 36 A.M.U.

EXCITATION ENERGY = 1.97 (MEV)

SYMMETRIC ANGLE = 42 DEG.

T3 (MEV)	SIGMA (MB/((SR)**2*MEV)	STAT. ERROR (MB/((SR)**2*MEV)
25.74	.0029	.0010
29.02	0.	0.
32.30	.0016	.0007
35.58	.0038	.0011
38.86	.0048	.0012
42.14	.0067	.0015
45.42	.0035	.0011
48.70	.0029	.0010
51.98	.0032	.0010
55.26	.0026	.0009
58.54	.0035	.0011
61.82	.0006	.0005

RECOIL MASS = 36 A.M.U.

EXCITATION ENERGY = 1.97 (MEV)

SYMMETRIC ANGLE = 47 DEG.

T3 (MEV)	SIGMA (MB/((SR)**2*MEV)	STAT. ERROR (MB/((SR)**2*MEV)
25.74	0.	0.
29.02	.0006	.0004
32.30	.0003	.0003
35.58	.0006	.0004
38.86	.0006	.0004
42.14	.0012	.0006
45.42	.0003	.0003
48.70	.0003	.0003
51.98	.0009	.0005
55.26	.0012	.0006
58.54	.0006	.0004
61.82	0.	0.

RECOIL MASS = 40 A.M.U.

EXCITATION ENERGY = 0. (MEV)

SYMMETRIC ANGLE = 28 DEG.

T3 (MEV)	SIGMA (MB/((SR)**2*MEV)	STAT. ERROR (MB/((SR)**2*MEV)
21.20	.0016	.0011
24.36	.0024	.0014
27.53	.0102	.0028
30.69	.0118	.0030
33.85	.0189	.0039
37.02	.0212	.0041
40.18	.0267	.0046
43.34	.0236	.0043
46.50	.0244	.0044
49.67	.0259	.0045
52.83	.0134	.0032
55.99	.0039	.0018
59.16	-.0008	.0008

RECOIL MASS = 40 A.M.U.

EXCITATION ENERGY = 0. (MEV)

SYMMETRIC ANGLE = 42 DEG.

T3 (MEV)	SIGMA (MB/((SR)**2*MEV)	STAT. ERROR (MB/((SR)**2*MEV)
21.20	.0023	.0011
24.36	.0029	.0010
27.53	.0025	.0010
30.69	.0018	.0008
33.85	.0033	.0011
37.02	.0047	.0013
40.18	.0088	.0018
43.34	.0055	.0014
46.50	.0033	.0011
49.67	.0015	.0007
52.83	.0029	.0010
55.99	.0025	.0010
59.16	0.	0.

RECOIL MASS = 40 A.M.U.

EXCITATION ENERGY = 0. (MEV)

SYMMETRIC ANGLE = 47 DEG.

T3 (MEV)	SIGMA (MB/((SR)**2*MEV)	STAT. ERROR (MB/((SR)**2*MEV)
21.20	.0009	.0005
24.36	.0003	.0003
27.53	0.	0.
30.69	.0009	.0005
33.85	0.	0.
37.02	.0009	.0005
40.18	.0003	.0003
43.34	.0017	.0007
46.50	0.	0.
49.67	.0006	.0004
52.83	.0017	.0007
55.99	.0006	.0004

RECOIL MASS = 62 A.M.U.

EXCITATION ENERGY = 0. (MEV)

SYMMETRIC ANGLE = 28 DEG.

T3 (MEV)	SIGMA (MB/((SR)**2*MEV)	STAT. ERROR (MB/((SR)**2*MEV)
25.74	.0025	.0010
29.02	.0047	.0013
32.30	.0083	.0017
35.58	.0134	.0022
38.86	.0199	.0027
42.14	.0199	.0027
45.42	.0145	.0023
48.70	.0076	.0017
51.98	.0069	.0016
55.26	.0029	.0010
58.54	.0018	.0008
61.82	.0036	.0011
65.10	.0011	.0006
68.38	0.	0.

RECOIL MASS = 62 A.M.U.

EXCITATION ENERGY = 0. (MEV)

SYMMETRIC ANGLE = 35 DEG.

T3 (MEV)	SIGMA (MB/((SR)**2*MEV)	STAT. ERROR (MB/((SR)**2*MEV)
25.74	.0038	.0011
29.02	.0072	.0016
32.30	.0045	.0012
35.58	.0096	.0018
38.86	.0182	.0025
42.14	.0240	.0029
45.42	.0236	.0029
48.70	.0168	.0024
51.98	.0082	.0017
55.26	.0045	.0012
58.54	.0051	.0013
61.82	.0051	.0013
65.10	.0017	.0008

RECOIL MASS = 62 A.M.U.

EXCITATION ENERGY = 0. (MEV)

SYMMETRIC ANGLE = 43 DEG.

T3 (MEV)	SIGMA (MB/((SR)**2*MEV)	STAT. ERROR (MB/((SR)**2*MEV)
25.74	.0021	.0008
29.02	.0029	.0009
32.30	.0029	.0009
35.58	.0024	.0008
38.86	.0030	.0010
42.14	.0070	.0014
45.42	.0059	.0013
48.70	.0013	.0006
51.98	.0029	.0009
55.26	.0029	.0009
58.54	.0029	.0009
61.82	.0019	.0007
65.10	.0005	.0004

RECOIL MASS = 62 A.M.U.

EXCITATION ENERGY = 1.17 (MEV)

SYMMETRIC ANGLE = 28 DEG.

T3 (MEV)	SIGMA (MB/((SR)**2*MEV)	STAT. ERROR (MB/((SR)**2*MEV)
25.74	.0022	.0009
29.02	.0014	.0007
32.30	.0022	.0009
35.58	.0033	.0011
38.86	.0043	.0013
42.14	.0036	.0011
45.42	.0043	.0013
48.70	.0029	.0010
51.98	.0029	.0010
55.26	.0047	.0013
58.54	.0004	.0004
61.82	.0004	.0004

RECOIL MASS = 62 A.M.U.

EXCITATION ENERGY = 1.17 (MEV)

SYMMETRIC ANGLE = 35 DEG.

T3 (MEV)	SIGMA (MB/((SR)**2*MEV)	STAT. ERROR (MB/((SR)**2*MEV)
25.74	.0014	.0007
29.02	.0010	.0006
32.30	.0021	.0008
35.58	.0017	.0008
38.86	.0034	.0011
42.14	.0021	.0008
45.42	.0021	.0008
48.70	.0017	.0008
51.98	.0007	.0005
55.26	0.	0.
58.54	.0014	.0007
61.82	.0021	.0008
65.10	0.	0.

RECOIL MASS = 62 A.M.U.

EXCITATION ENERGY = 1.17 (MEV)

SYMMETRIC ANGLE = 43 DEG.

T3 (MEV)	SIGMA (MB/((SR)**2*MEV)	STAT. ERROR (MB/((SR)**2*MEV)
25.74	.0008	.0005
29.02	.0013	.0006
32.30	.0016	.0007
35.58	.0003	.0003
38.86	.0003	.0003
42.14	0.	0.
45.42	.0013	.0006
48.70	0.	0.
51.98	.0011	.0005
55.26	.0005	.0004
58.54	.0005	.0004
61.82	.0011	.0005
65.10	0.	0.

Appendix V. This appendix gives a summary of the $^{12}C(\alpha, 2\alpha)^{8}Be$ and $^{16}O(\alpha, 2\alpha)^{12}C$ asymmetric triple differential cross sections. One detector was fixed at 42° while the other alpha detector varied angular position on the opposite side of the beam. Again all quantities are given in the laboratory frame, and the triple differential cross section is given as a function of T_3.

RECOIL MASS = 8 A.M.U.

EXCITATION ENERGY = 0. (MEV)

ASYMMETRIC ANGLE = 25 DEG.

T3 (MEV)	SIGMA (MB/((SR)**2*MEV)	STAT. ERROR (MB/((SR)**2*MEV)
25.74	.1023	.0091
29.02	.1829	.0121
32.30	.1434	.0107
35.58	.1386	.0106
38.86	.1063	.0093
42.14	.0789	.0080
45.42	.0661	.0073
48.70	.0314	.0050
51.98	.0145	.0034
55.26	.0113	.0030
58.54	.0032	.0016
61.82	0.	0.

RECOIL MASS = 8 A.M.U.

EXCITATION ENERGY = 0. (MEV)

ASYMMETRIC ANGLE = 28 DEG.

T3 (MEV)	SIGMA (MB/((SR)**2*MEV)	STAT. ERROR (MB/((SR)**2*MEV)
25.74	.0633	.0068
29.02	.1065	.0088
32.30	.1411	.0101
35.58	.1360	.0099
38.86	.1454	.0102
42.14	.1331	.0098
45.42	.1231	.0094
48.70	.0489	.0059
51.98	.0417	.0055
55.26	.0295	.0046
58.54	0.	0.
61.82	0.	0.

RECOIL MASS = 8 A.M.U.

EXCITATION ENERGY = 0. (MEV)

ASYMMETRIC ANGLE = 31 DEG.

T3 (MEV)	SIGMA (MB/((SR)**2*MEV)	STAT. ERROR (MB/((SR)**2*MEV)
25.74	.0695	.0064
29.02	.0712	.0065
32.30	.0940	.0074
35.58	.0835	.0070
38.86	.1058	.0080
42.14	.1244	.0085
45.42	.1185	.0083
48.70	.0607	.0060
51.98	.0671	.0063
55.26	.0274	.0040
58.54	.0064	.0019
61.82	0.	0.

RECOIL MASS = 8 A.M.U.

EXCITATION ENERGY = 0. (MEV)

ASYMMETRIC ANGLE = 35 DEG.

T3 (MEV)	SIGMA (MB/((SR)**2*MEV)	STAT. ERROR (MB/((SR)**2*MEV)
25.74	.0993	.0082
29.02	.1200	.0090
32.30	.0818	.0074
35.58	.0617	.0064
38.86	.0369	.0050
42.14	.0349	.0048
45.42	.0389	.0051
48.70	.0536	.0060
51.98	.0677	.0067
55.26	.0530	.0060
58.54	.0147	.0032
61.82	.0013	.0009

RECOIL MASS = 8 A.M.U.

EXCITATION ENERGY = 0. (MEV)

ASYMMETRIC ANGLE = 38 DEG.

T3 (MEV)	SIGMA (MB/((SR)**2*MEV)	STAT. ERROR (MB/((SR)**2*MEV)
25.74	.0688	.0063
29.02	.0873	.0071
32.30	.0838	.0070
35.58	.0948	.0074
38.86	.0827	.0069
42.14	.0387	.0047
45.42	.0168	.0031
48.70	.0110	.0025
51.98	.0497	.0054
55.26	.0595	.0059
58.54	.0260	.0039
61.82	.0006	.0006

RECOIL MASS = 8 A.M.U.

EXCITATION ENERGY = 0. (MEV)

ASYMMETRIC ANGLE = 42 DEG.

T3 (MEV)	SIGMA (MB/((SR)**2*MEV)	STAT. ERROR (MB/((SR)**2*MEV)
25.74	.0116	.0024
29.02	.0378	.0043
32.30	.0223	.0033
35.58	.0276	.0037
38.86	.0626	.0055
42.14	.0810	.0063
45.42	.0907	.0066
48.70	.0209	.0032
51.98	.0141	.0026
55.26	.0276	.0037
58.54	.0223	.0033
61.82	.0034	.0013

RECOIL MASS = 8 A.M.U.

EXCITATION ENERGY = 0. (MEV)

ASYMMETRIC ANGLE = 47 DEG.

T3 (MEV)	SIGMA (MB/((SR)**2*MEV)	STAT. ERROR (MB/((SR)**2*MEV)
25.74	.0052	.0016
29.02	.0081	.0020
32.30	.0119	.0024
35.58	.0071	.0018
38.86	.0114	.0023
42.14	.0223	.0033
45.42	.0332	.0040
48.70	.0318	.0039
51.98	.0185	.0030
55.26	.0294	.0037
58.54	.0062	.0017
61.82	.0005	.0005

RECOIL MASS = 8 A.M.U.

EXCITATION ENERGY = 2.90 (MEV)

ASYMMETRIC ANGLE = 25 DEG.

T3 (MEV)	SIGMA (MB/((SR)**2*MEV)	STAT. ERROR (MB/((SR)**2*MEV)
25.74	.0491	.0063
29.02	.0596	.0069
32.30	.0435	.0059
35.58	.0338	.0052
38.86	.0403	.0057
42.14	.0387	.0056
45.42	.0709	.0076
48.70	.0709	.0076
51.98	.0717	.0076
55.26	.0218	.0042
58.54	0.	0.

RECOIL MASS = 8 A.M.U.

EXCITATION ENERGY = 2.90 (MEV)

ASYMMETRIC ANGLE = 28 DEG.

T3 (MEV)	SIGMA (MB/((SR)**2*MEV)	STAT. ERROR (MB/((SR)**2*MEV)
25.74	.0554	.0063
29.02	.0741	.0073
32.30	.0446	.0057
35.58	.0425	.0055
38.86	.0439	.0056
42.14	.0374	.0052
45.42	.0461	.0058
48.70	.0626	.0067
51.98	.0741	.0073
55.26	.0266	.0044
58.54	0.	0.
61.82	0.	0.

RECOIL MASS = 8 A.M.U.

EXCITATION ENERGY = 2.90 (MEV)

ASYMMETRIC ANGLE = 31 DEG.

T3 (MEV)	SIGMA (MB/((SR)**2*MEV)	STAT. ERROR (MB/((SR)**2*MEV)
25.74	.0648	.0061
29.02	.0747	.0066
32.30	.0520	.0055
35.58	.0315	.0043
38.86	.0339	.0045
42.14	.0420	.0050
45.42	.0642	.0061
48.70	.0502	.0054
51.98	.0747	.0066
55.26	.0310	.0043
58.54	.0006	.0006

RECOIL MASS = 8 A.M.U.

EXCITATION ENERGY = 2.90 (MEV)

ASYMMETRIC ANGLE = 35 DEG.

T3 (MEV)	SIGMA (MB/((SR)**2*MEV)	STAT. ERROR (MB/((SR)**2*MEV)
25.74	.0657	.0066
29.02	.1060	.0084
32.30	.0805	.0073
35.58	.0389	.0051
38.86	.0201	.0037
42.14	.0288	.0044
45.42	.0376	.0050
48.70	.0570	.0062
51.98	.0570	.0062
55.26	.0389	.0051
58.54	.0020	.0012

RECOIL MASS = 8 A.M.U.

EXCITATION ENERGY = 2.90 (MEV)

ASYMMETRIC ANGLE = 38 DEG.

T3 (MEV)	SIGMA (MB/((SR)**2*MEV)	STAT. ERROR (MB/((SR)**2*MEV)
25.74	.0416	.0049
29.02	.1058	.0078
32.30	.0821	.0069
35.58	.0497	.0054
38.86	.0439	.0050
42.14	.0243	.0038
45.42	.0358	.0045
48.70	.0347	.0045
51.98	.0445	.0051
55.26	.0370	.0046
58.54	.0023	.0012
61.82	.0012	.0008

RECOIL MASS = 8 A.M.U.

EXCITATION ENERGY = 2.90 (MEV)

ASYMMETRIC ANGLE = 42 DEG.

T3 (MEV)	SIGMA (MB/((SR)**2*MEV)	STAT. ERROR (MB/((SR)**2*MEV)
25.74	.0209	.0032
29.02	.0359	.0042
32.30	.0461	.0047
35.58	.0364	.0042
38.86	.0412	.0045
42.14	.0408	.0045
45.42	.0291	.0038
48.70	.0291	.0038
51.98	.0369	.0042
55.26	.0296	.0038
58.54	.0044	.0015

RECOIL MASS = 8 A.M.U.

EXCITATION ENERGY = 2.90 (MEV)

ASYMMETRIC ANGLE = 47 DEG.

T3 (MEV)	SIGMA (MB/((SR)**2*MEV)	STAT. ERROR (MB/((SR)**2*MEV)
25.74	.0180	.0029
29.02	.0204	.0031
32.30	.0360	.0041
35.58	.0289	.0037
38.86	.0332	.0040
42.14	.0275	.0036
45.42	.0289	.0037
48.70	.0337	.0040
51.98	.0451	.0046
55.26	.0427	.0045
58.54	.0066	.0018
61.82	.0005	.0005

RECOIL MASS = 12 A.M.U.

EXCITATION ENERGY = 0. (MEV)

ASYMMETRIC ANGLE = 25 DEG.

T3 (MEV)	SIGMA (MB/((SR)**2*MEV)	STAT. ERROR (MB/((SR)**2*MEV)
25.74	.0787	.0100
29.02	.1307	.0129
32.30	.1066	.0116
35.58	.0825	.0102
38.86	.0698	.0094
42.14	.0254	.0057
45.42	.0165	.0046
48.70	.0025	.0018
51.98	.0063	.0028
55.26	.0025	.0018
58.54	.0025	.0018
61.82	0.	0.

RECOIL MASS = 12 A.M.U.

EXCITATION ENERGY = 0. (MEV)

ASYMMETRIC ANGLE = 28 DEG.

T3 (MEV)	SIGMA (MB/((SR)**2*MEV)	STAT. ERROR (MB/((SR)**2*MEV)
25.74	.0495	.0077
29.02	.0809	.0099
32.30	.1014	.0111
35.58	.0929	.0106
38.86	.0748	.0095
42.14	.0748	.0095
45.42	.0447	.0073
48.70	.0193	.0048
51.98	.0085	.0032
55.26	.0193	.0048
58.54	.0060	.0027
61.82	0.	0.

RECOIL MASS = 12 A.M.U.

EXCITATION ENERGY = 0. (MEV)

ASYMMETRIC ANGLE = 31 DEG.

T3 (MEV)	SIGMA (MB/((SR)**2*MEV)	STAT. ERROR (MB/((SR)**2*MEV)
25.74	.0375	.0065
29.02	.0535	.0078
32.30	.0671	.0087
35.58	.0512	.0076
38.86	.0626	.0084
42.14	.0728	.0091
45.42	.0569	.0080
48.70	.0421	.0069
51.98	.0432	.0070
55.26	.0171	.0044
58.54	.0159	.0043
61.82	.0023	.0016

RECOIL MASS = 12 A.M.U.

EXCITATION ENERGY = 0. (MEV)

ASYMMETRIC ANGLE = 35 DEG.

T3 (MEV)	SIGMA (MB/((SR)**2*MEV)	STAT. ERROR (MB/((SR)**2*MEV)
25.74	.0586	.0073
29.02	.1099	.0100
32.30	.0898	.0091
35.58	.0577	.0073
38.86	.0256	.0048
42.14	.0192	.0042
45.42	.0266	.0049
48.70	.0366	.0058
51.98	.0220	.0045
55.26	.0339	.0056
58.54	.0211	.0044
61.82	.0028	.0016

RECOIL MASS = 12 A.M.U.

EXCITATION ENERGY = 0. (MEV)

ASYMMETRIC ANGLE = 38 DEG.

T3 (MEV)	SIGMA (MB/((SR)**2*MEV)	STAT. ERROR (MB/((SR)**2*MEV)
25.74	.0210	.0047
29.02	.0712	.0086
32.30	.0828	.0093
35.58	.1110	.0108
38.86	.0576	.0078
42.14	.0262	.0052
45.42	.0136	.0038
48.70	.0136	.0038
51.98	.0272	.0053
55.26	.0283	.0054
58.54	.0356	.0061
61.82	.0042	.0021
65.10	.0011	.0011

RECOIL MASS = 12 A.M.U.

EXCITATION ENERGY = 0. (MEV)

ASYMMETRIC ANGLE = 42 DEG.

T3 (MEV)	SIGMA (MB/((SR)**2*MEV)	STAT. ERROR (MB/((SR)**2*MEV)
25.74	.0130	.0049
29.02	.0111	.0045
32.30	.0204	.0061
35.58	.0270	.0083
38.86	.0574	.0103
42.14	.0759	.0119
45.42	.0241	.0067
48.70	.0259	.0069
51.98	.0130	.0049
55.26	.0092	.0041
58.54	.0204	.0061
61.82	.0111	.0045

RECOIL MASS = 12 A.M.U.

EXCITATION ENERGY = 0. (MEV)

ASYMMETRIC ANGLE = 47 DEG.

T3 (MEV)	SIGMA (MB/((SR)**2*MEV)	STAT. ERROR (MB/((SR)**2*MEV)
25.74	.0118	.0033
29.02	.0100	.0030
32.30	.0091	.0029
35.58	.0045	.0020
38.86	.0055	.0022
42.14	.0236	.0046
45.42	.0236	.0046
48.70	.0236	.0046
51.98	.0182	.0041
55.26	.0091	.0029
58.54	.0118	.0033
61.82	.0091	.0029

RECOIL MASS = 12 A.M.U.

EXCITATION ENERGY = 4.44 (MEV)

ASYMMETRIC ANGLE = 25 DEG.

T3 (MEV)	SIGMA (MB/((SR)**2*MEV)	STAT. ERROR (MB/((SR)**2*MEV)
25.74	.0152	.0044
29.02	.0304	.0062
32.30	.0368	.0068
35.58	.0241	.0055
38.86	.0178	.0048
42.14	.0152	.0044
45.42	.0279	.0060
48.70	.0228	.0054
51.98	.0178	.0048
55.26	.0152	.0044
58.54	0.	0.

RECOIL MASS = 12 A.M.U.

EXCITATION ENERGY = 4.44 (MEV)

ASYMMETRIC ANGLE = 28 DEG.

T3 (MEV)	SIGMA (MB/((SR)**2*MEV)	STAT. ERROR (MB/((SR)**2*MEV)
25.74	.0241	.0054
29.02	.0193	.0048
32.30	.0253	.0055
35.58	.0290	.0059
38.86	.0193	.0048
42.14	.0290	.0059
45.42	.0169	.0045
48.70	.0060	.0027
51.98	.0157	.0043
55.26	.0097	.0034

RECOIL MASS = 12 A.M.U.

EXCITATION ENERGY = 4.44 (MEV)

ASYMMETRIC ANGLE = 31 DEG.

T3 (MEV)	SIGMA (MB/((SR)**2*MEV)	STAT. ERROR (MB/((SR)**2*MEV)
25.74	.0296	.0058
29.02	.0364	.0064
32.30	.0250	.0053
35.58	.0228	.0051
38.86	.0319	.0060
42.14	.0216	.0050
45.42	.0239	.0052
48.70	.0068	.0028
51.98	.0136	.0039
55.26	.0080	.0030
58.54	.0011	.0011

RECOIL MASS = 12 A.M.U.

EXCITATION ENERGY = 4.44 (MEV)

ASYMMETRIC ANGLE = 35 DEG.

T3 (MEV)	SIGMA (MB/((SR)**2*MEV)	STAT. ERROR (MB/((SR)**2*MEV)
25.74	.0137	.0035
29.02	.0256	.0048
32.30	.0220	.0045
35.58	.0165	.0039
38.86	.0192	.0042
42.14	.0220	.0045
45.42	.0229	.0046
48.70	.0192	.0042
51.98	.0137	.0035
55.26	.0192	.0042

RECOIL MASS = 12 A.M.U.

EXCITATION ENERGY = 4.44 (MEV)

ASYMMETRIC ANGLE = 38 DEG.

T3 (MEV)	SIGMA (MB/((SR)**2*MEV)	STAT. ERROR (MB/((SR)**2*MEV)
25.74	.0147	.0039
29.02	.0126	.0036
32.30	.0126	.0036
35.58	.0178	.0043
38.86	.0115	.0035
42.14	.0147	.0039
45.42	.0136	.0038
48.70	.0126	.0036
51.98	.0126	.0036
55.26	.0084	.0030
58.54	0.	0.

RECOIL MASS = 12 A.M.U.

EXCITATION ENERGY = 4.44 (MEV)

ASYMMETRIC ANGLE = 42 DEG.

T3 (MEV)	SIGMA (MB/((SR)**2*MEV)	STAT. ERROR (MB/((SR)**2*MEV)
25.74	.0092	.0041
29.02	.0074	.0037
32.30	.0130	.0049
35.58	.0167	.0055
38.86	.0111	.0045
42.14	.0055	.0032
45.42	.0055	.0032
48.70	.0111	.0045
51.98	.0092	.0041
55.26	.0130	.0049
58.54	0.	0.

RECOIL MASS = 12 A.M.U.

EXCITATION ENERGY = 4.44 (MEV)

ASYMMETRIC ANGLE = 47 DEG.

T3 (MEV)	SIGMA (MB/((SR)**2*MEV)	STAT. ERROR (MB/((SR)**2*MEV)
25.74	.0073	.0026
29.02	.0073	.0026
32.30	.0036	.0018
35.58	.0018	.0013
38.86	.0055	.0022
42.14	.0018	.0013
45.42	.0055	.0022
48.70	.0027	.0016
51.98	.0027	.0016
55.26	.0009	.0009

RECOIL MASS = 12 A.M.U.

EXCITATION ENERGY = 7.66 (MEV)

ASYMMETRIC ANGLE = 28 DEG.

T3 (MEV)	SIGMA (MB/((SR)**2*MEV)	STAT. ERROR (MB/((SR)**2*MEV)
25.74	.0012	.0012
29.02	0.	0.
32.30	.0048	.0024
35.58	.0024	.0017
38.86	.0024	.0017
42.14	.0024	.0017
45.42	.0024	.0017
48.70	0.	0.
51.98	.0024	.0017

RECOIL MASS = 12. A.M.U.

EXCITATION ENERGY = 7.66 (MEV)

ASYMMETRIC ANGLE = 31 DEG.

T3 (MEV)	SIGMA (MB/((SR)**2*MEV)	STAT. ERROR (MB/((SR)**2*MEV)
25.74	.0011	.0011
29.02	0.	0.
32.30	.0023	.0016
35.58	.0045	.0023
38.86	.0045	.0023
42.14	.0080	.0030
45.42	.0034	.0020
48.70	.0023	.0016
51.98	.0023	.0016

RECOIL MASS = 12 A.M.U.

EXCITATION ENERGY = 7.66 (MEV)

ASYMMETRIC ANGLE = 35 DEG.

T3 (MEV)	SIGMA (MB/((SR)**2*MEV)	STAT. ERROR (MB/((SR)**2*MEV)
25.74	.0018	.0013
29.02	.0028	.0016
32.30	.0018	.0013
35.58	.0028	.0016
38.86	.0009	.0009
42.14	.0009	.0009
45.42	0.	0.
48.70	.0055	.0022
51.98	.0046	.0020

Acknowledgements

For assistance in the completion of this thesis I gratefully acknowledge:

Dr. Bernard Harvey for encouragment and support throughout this work;

Dr. David Hendrie for countless conversations and many valuable suggestions in both experimental and theoretical matters;

Dr. Michael Zisman, Dr. Dennis Kovar, and Dr. Fredrick Becchetti for giving valuable assistance in the experimental data acquisition;

Dr. Alain Giorni, Dr. Fredrick Becchetti, and Dr. Phil Deutchman for several conversations and suggestions concerning various theoretical problems encountered in this work;

Professor Joseph Cerny and Dr. Homer Conzett for encouragement and several helpful discussions;

Mr. Jack Walton and the detector lab for providing Si detectors which were virtually trouble free;

Dr. George Goth and Miss Jeannette Mahoney for assistance in programing the PDP-5 on-line computer program;

The accelerator technicians, Mr. John Bowen, and the cyclotron crew for providing the alpha particle beams;

Mr. Matt Renkas, Mr. Manny Enos, and Mr. Roy Burton for help in designing and installing a second movable counter mount in the 36 in. scattering chamber;

Mr. Ted Reynolds and his crew for support in maintenance of the vacuum pumps and other mechanical equipment;

Mr. Claude Ellsworth for preparing the many and varied targets used in these experiments;

Mr. John Meng and Mr. Ed Lampo and other members of the electronics development and maintenance staff who provided both educational experiences and reliable electronic equipment;

Mr. Dick Perkins for advice and tutelage in the use of shop equipment;

The friendship and help of my fellow graduate students, Dr. Michael Zisman, Dr. John Esterl, Dr. Creve Maples, Dr. Joel Moss, Dr. George Goth, Mr. Gordon Wozniak, Mr. John Macdonald, Mr. Kenneth Wilcox, Mr. Robert Weisenmiller, Mr. Wolfram Dahme, and in particular, my office mate Mr. Richard Sextro who kept me informed on practically every subject, and who was very tolerant of my piles of computer output;

My wife Barbara for typing the first draft and revisions of this thesis;

My parents, sister, and the Cone family for providing encouragement and confidence in the successful completion of this work;

My family, Barbara and Patrick, whose cheerfulness and affections brightened many difficult days.

Work done under the auspices of the U. S. Atomic Energy Commission.

References

Ahl 66 Lars V. Ahlfors, Complex Analysis, Second Edition, McGraw Hill Book Co., (1966).

Ajz 68 F. Ajzenberg-Selove and T. Lauritson, Nucl. Phys. A114, 1 (1968).

Ajz 72 F. Ajzenberg-Selove, Nucl. Phys. A190, 1 (1972)

Amos 66 K. A. Amos, Nucl. Phys. 77, 225 (1966).

Ari 71 A. Arima and V. Gillet, Ann. of Phys. 66, 117 (1971).

Ari 72 A. Arima, H. Horiuchi, K. Kubodera, and N. Takigawa, Adv. in Nucl. Phys. 5, 345 (1972).

Bach 71 A. D. Bacher, et al., Nucl. Phys. A181, 453 (1971).

Bach 73 D. Bachelier, et al., Phys. Rev. (C) 7, 165 (1973).

Bal 68 V. V. Balashov and J. V. Meboniya, Nucl. Phys. A107, 369 (1968).

Ball 69 J. B. Ball, A. W. Fairhall, and I. Halpern, Phys. Rev. 114, 305 (1959).

Bar 71 N. Baron, R. F. Leonard, and W. M. Stuart, Phys. Rev. (C) 4, 1159 (1971).

Bed 72 M. Bedjidian, et al., Nucl. Phys. A189, 403 (1972).

Ber 65 P. Beregi, et al., Nucl. Phys. 66, 513 (1965).

Bet 70 K. Bethge, Annual Reviews of Nucl. Sci., 255 (1970).

Bohr 69 A. Bohr and B. R. Mottelson, Nuclear Structure, W. A. Benjamin, Inc., Vol. I, 13 (1969).

Bred 59 D. J. Bredin, et al., Proc. Roy. Soc. (London) A251, 143 (1959).

Bri 66 D. M. Brink, Proc. of the Int. School of Physics, XXXVI, 247 (1966).

Chat 72 A. K. Chatterjee and P. A. Deutchman, Nucl. Phys. A189, 20 (1972).

Conz 60 H. E. Conzett, et al., Phys. Rev. 111, 1075 (1960).

Darr 65 P. Darriulat, et al., Phys. Rev. 137, 315 (1965).

Dec 68 Introduction to Programing, Digital Equipment Corporation, C-1 (1968).

Den 66 L. J. Denes, W. W. Daehnick, and R. M. Drisko, Phys. Rev. 148, 1097 (1966).

Det 70 C. Detraz, et al. Nucl. Phys. A147, 488 (1970).

Det 72 C. Detraz, et al., Phys. Rev. Lett. 28, 117 (1972).

Deu 68 P. A. Deutchman and I. E. McCarthy, Nucl. Phys. A112, 399 (1968).

DeV 73 R. M. DeVries, Phys. Rev. Lett. 30, 666 (1973).

Dol 69 V. K. Dolinov, et al., Nucl. Phys. A129, 577 (1969).

Dol 69a V. K. Dolinov, et al., Nucl. Phys. A129, 597 (1969).

Eber 70 K. A. Eberhard, Phys. Lett. 33B, 343 (1970).

Eic 72 J. Eichler and M. Yamamura, Nucl. Phys. A182, 33 (1972).

Eid 62 W. W. Eidson and J. G. Cramer, Jr., Phys. Rev. Lett. 9, 497 (1962).

Eis 58 L. Eisenbud and E. P. Wigner, Nuclear Structure, Princeton University Press, 44 (1958).

Eisb 59 R. M. Eisberg, I. E. McCarthy, and R. A. Spurrier, Nucl. Phys. 10, 571 (1959).

Elt 67 L. R. B. Elton and D. F. Jackson, Phys. Rev. 155, 1070 (1967).

End 67 P. M. Endt and C. Van Der Leun, Nucl. Phys. A105, 1 (1967).

Eps 68 M. Epstein, et al., Phys. Rev. 178, 1698 (1968).

Fai 70 J. C. Faivre, et al., Phys. Rev. Lett. 24, 1188 (1970).

Gail 70 P. Gaillard, et al., Phys. Rev. Lett. 25, 593 (1970).

Gam 28 G. Gamow, Z. Phys. 51, 204 (1928).

Gau 69 G. Gaul, H. Ludecke, R. Santo, H. Schmeing, and R. Stock, Nucl. Phys. A137, 177 (1969).

Gott 70 B. Gottschalk and S. Kannenberg, Phys. Rev. (C) 2, 24 (1970).

Gou 66 F. S. Goulding, Nucl. Inst. and Methods 43, 1 (1966).

Gou 67 F. S. Goulding, D. A. Landis, and R. H. Pehl, UCRL-17560 (1967).

Gui 71 A. Guichard, et al., Phys. Rev. (C) 4, 700 (1971).

Gut 71 H. H. Gutbrod, H. Yoshida, and R. Bock, Nucl. Phys. A165, 240 (1971).

Hau 72 G. Hauser, et al., Nucl. Phys. A182, 1 (1972).

Hin 69 R. E. Hintz, et al., Nucl. Inst. and Methods 72, 61 (1969).

Holm 69 H. D. Holmgren, Int. Conf. on Clustering Phenomena in Nuclei, Bochum, 17 (1969).

Igo 63 G. Igo, L. F. Hansen, and T. J. Gooding, Phys. Rev. 131, 337 (1963).

Jac 65 D. F. Jackson and T. Berggren, Nucl. Phys. 62, 372 (1965).

Jac 65a D. F. Jackson, Nuovo Cimento XL N. 1, 109 (1965).

Jac 67 D. F. Jackson, Nucl. Phys. A90, 209 (1967).

Jac 67a D. F. Jackson, Phys. Rev. 155, 1065 (1967).

Jack 71 D. F. Jackson, Adv. in Nucl. Phys. 4, 1 (1971).

Jam 63 A. N. James and H. G. Pugh, Nucl. Phys. 42, 441 (1963).

Kann 68 S. L. Kannenberg, Thesis, unpublished, (1968).

Kene 73 R. Kenefick, private communication.

Krom 62 A. J. Kromminga and I. E. McCarthy, Nucl. Phys. 31, 678 (1962).

Kubo 72 K. I. Kubo and M. Hirata, Nucl. Phys. A187, 186 (1972).

Kudo 65 Y. Kudo, Prog. Theor. Phys. 34, 942 (1965).

Kur 73 D. Kurath, preprint (1973).

La 55 A. M. Lane and D. H. Wilkinson, Phys. Rev. 97, 1199 (1955).

Lau 66 T. Lauritsen and F. Ajzenberg-Selove, Nucl. Phys. 78, 1 (1966).

Led 67 C. M. Lederer, J. M. Hollander, and I. Perlman, Table of Isotopes, Sixth Ed. (1967).

Lim 62 K. L. Lim, Direct Interactions and Nuclear Reaction Mechanisms, ed. Clementel and Villi, Gordon and Breach, 180 (1962).

Lim 64 K. L. Lim and I. E. McCarthy, Phys. Rev. 133, B 1006 (1964).

Lim 64a K. L. Lim and I. E. McCarthy, Phys. Rev. Lett. 13, 446 (1964).

Lim 66 K. L. Lim and I. E. McCarthy, Nucl. Phys. 88, 433 (1966).

Lipp 67 E. P. Lippincott and A. M. Bernstein, Phys. Rev. 163, 1170 (1967).

Mah 72 J. V. Maher, et al., Phys. Rev. Lett. 29, 291 (1972).

Mar 41 H. Margenau, Phys. Rev. 59, 37 (1941).

McC 59 I. E. McCarthy, Nucl. Phys. 10, 583 (1959).

McC 59a I. E. McCarthy, Nucl. Phys. 11, 574 (1959).

McC 61 I. E. McCarthy and D. L. Pursey, Phys. Rev. 122, 578 (1961).

McC 62 I. E. McCarthy, Direction Interactions and Nuclear Reaction Mechanisms, ed. Clementel and Villi, Gordon and Breach, 94 (1962).

McC 65 I. E. McCarthy, Rev. Mod. Phys. 37, 388 (1965).

McC 68 I. E. McCarthy, An Introduction to Nuclear Theory, Wiley, (1968).

McF 66 L. McFadden and G. R. Satchler, Nucl. Phys. 84, 177 (1966).

McG 71 R. L. McGrath, et al., Phys. Lett. 34B, 289 (1971).

Meb 69 J. V. Meboniya, Phys. Lett. 30B, 153 (1969).

Meri 70 J. Meriwether, private communication.

Mit 72 B. Mithra and R. Laverriere, Nucl. Phys. A184, 321 (1972).

Moss 66 J. Moss and G. C. Ball, Energy Resolution in Cyclotron Experiments, UCRL-17124 (1966).

Moss 69 J. Moss, Ph. D. Thesis, UCRL-18902 (1969).

Mun 72 P. Braun-Munzinger, et al., Phys. Rev. Lett. 29, 1261 (1972).

Neo 72 P. Neogy, R. Middleton, and W. Scholz, Phys. Rev. (C) 6, 885 (1972).

Nils 56 R. Nilson, et al., Phys. Rev. 104, 1673 (1956).

Oes 72 H. Oeschler, et al., Phys. Rev. Lett. 28, 694 (1972).

Park 68 A. E. Parker, et al., Phys. Rev. 174, 1093 (1968).

Phi 60 G. C. Phillips and T. A. Tombrello, Nucl. Phys. 19, 555 (1960).

Pli 69 R. D. Plieninger, W. Eichelberger, and E. Velten, Nucl. Phys. A137, 20 (1969).

Pugh 67 H. G. Pugh, D. L. Hendrie, M. Chabre, E. Boschitz, and I. E. McCarthy, Phys. Rev. 155, 1054 (1967).

Pugh 69 H. B. Pugh, et al., Phys. Rev. Lett. 22, 408 (1969).

Reb 72 H. Rebel, et al., Nucl. Phys. A182, 145 (1972).

Reed 68 M. Reed, Ph. D. Thesis, UCRL-18414 (1968).

Riou 65 M. Riou, Rev. Mod. Phys. 37, 375 (1965).

Riou 70 M. Riou and Ch. Ruhla, Prog. in Nucl. Phys. 11, 195 (1970).

Rob 68 L. B. Robinson, F. Gin, and F. S. Goulding, Nucl. Inst. and Meth. 62, 237 (1968).

Rob 72 D. Robson, Comm. in Nucl. and Part. Phys. 5, 18 (1972).

Rob 67 L. S. Rodberg and R. M. Thaler, Introduction to the Quantum Theory of Scattering, Academic Press, 202 (1967).

Roos 68 P. G. Roos, et al., Phys. Rev. 176, 1246 (1968).

Rot 68 I. Rotter, Fortschr. Phys. 16, 195 (1968).

Rot 69 I. Rotter, Nucl. Phys. A135, 378 (1969).

Rot 73 I. Rotter, preprint.

Sat 65 G. R. Satchler, Nucl. Phys. 70, 177 (1965).

Sch 70 N. C. Schmeing, Nucl. Phys. A142, 449 (1970).

Scho 72 W. Scholz, P. Neogy, K. Bethge, and R. Middleton, Phys. Rev. (C) 6, 893 (1972).

Skj 64 O. Skjeggestad, Easter School for Physicists, Herceg-novi, vol. II (1964).

Sol 60 V. G. Soloviev, Nucl. Phys. 18, 161 (1960).

Sto 72 R. Stock, et al., Phys. Rev. (C) 6, 1226 (1972).

Tay 72 J. R. Taylor, Scattering Theory, John Wiley and Sons, Inc., 361 (1972).

TMC 65 Practical Guide to Semiconductor Detectors, Technical Measurement Corporation, 1965.

Tob 61 W. Tobocman, Theory of Direct Nuclear Reactions, Oxford University Press, 3 (1961).

Tom 63 T. A. Tombrello and L. S. Senhouse, Phys. Rev. 129, 2252 (1963).

Wat 71 J. W. Watson, et al., Nucl. Phys. A172, 513 (1971).

Whe 37 J. A. Wheeler, Phys. Rev. 52, 1083 (1937).

Will 71 W. S. C. Williams, Introduction to Elementary Particles, Academic Press, 499 (1971).

Zaf 71 C. D. Zafiratos, et al., Phys. Rev. Lett. 27, 437 (1971).

Zaf 72 C. D. Zafiratos, Scien. Amer. 227, 100 (1972).

Zup 67 C. Zupančič, Les Reactions Nucleaires A Trois Corps, Universite de Grenoble, 15 (1967).

TECHNICAL INFORMATION DIVISION
LAWRENCE BERKELEY LABORATORY
UNIVERSITY OF CALIFORNIA
BERKELEY, CALIFORNIA 94720